博士論文

Study of site effects and its applications to understanding seismic damage

（サイト効果とその地震被害解釈への応用の研究）

バッタライ　ムクンダ

Bhattarai　Mukunda

Abstract

Earthquakes are the most destructive geological phenomena in the Himalaya. The seismic waves that cause destruction on the ground depend on source effect, path effect, and site effect. Among them, site effect is usually the most important therefore, the amplification of seismic waves due to local geological and geomorphological conditions in sedimentary basins is one indispensable component for seismic hazard assessment. Nepal, situated in the boundary between the Eurasian and Indian tectonic plates, has a long history of about 20 destructive earthquakes since 1255, with the 2015 Gorkha earthquake being the most recent one. The Kathmandu valley, where the capital city of Nepal is located, falls in the lesser Himalaya of central Nepal, is characterized by flat-topped terraces. Its northern part is dominated by clay, silt, sand, and gravel whereas that of the southern part is mainly rich in clay and silt. Exposed bedrocks are abundant only in the surrounding mountain/hill slopes. The sediments in the valley were transported from these slopes forming the undulated pattern above the basement. The sediments in the valley were transported from these slopes forming the undulated pattern above the basement. The valley is also probably prone to earthquake disasters due to the presence of complex subsurface structures, and infilled quaternary sediments of lacustrine origin. The unconsolidated sediments of the valley mainly consist of fluvial and lacustrine sequence, causing large local variations on ground motions. Therefore, the site effect is the most important, and studies are needed for the shear wave velocity structures up to the basement for the evaluation of seismic hazard.

Studies on the variation of ground motion at different site conditions had begun in the Kathmandu valley by installing an accelerometric network since 2009. The first accelerograph was installed at the central part of the Kathmandu valley (DMG), whereas the other (KKA) was at a distance of 10 km north-west of the valley center on rock. This network is used to evaluate the site effects caused by the valley sediments with reference to the rock site and also complement the short-period pre-existing seismic network to prevent over saturation. Results from early records showed that the low gain channel of the KKA velocimetric station collocated with KKA perfectly complements the high gain channels when they get saturated. The site over reference spectral ratio for the 17 October 2010, Xizang, China earthquake (M_L 5.7) shows that DMG exhibits higher amplification at lower frequencies below 4 Hz; however, KKA shows clear trough in the frequency range from 4 to

10 Hz. These phenomena might misestimate the site amplification of the valley in the mentioned frequency range. It is also observed that there are no *S*-waves on the vertical component at DMG suspecting some sedimentary effects.

The same method is applied to confirm the site effect of DMG with reference to KKA in the mentioned frequency range using 9 earthquakes of $M_L \geq 5$. The non-flat feature on the spectral ratio of DMG with KKA in the frequency range from 0.5 to 4 Hz shows that all curves are between unity and 10 whereas those fall below unity from 4 to 10 Hz supporting the same trend as before. To better estimate the site amplification of DMG another rock site PKIN located about 15 km south-east of the valley center is used as a proxy of KKA and the same analyses are repeated. It is obtained that the spectral ratios of DMG with reference to PKIN show site amplification from 1 to at most 10 times in the given frequency range. Based on the comparative studies it is proposed that PKIN should be considered as a more reliable reference site for site effect studies in the Kathmandu valley. This has been confirmed by installing an accelerograph PKI nearby PKIN after the Gorkha earthquake. The long-period site response due to the thick sediments of the Kathmandu valley is evidenced by the spectral ratios of the 18 September 2011, Taplejung-Sikkim earthquake (M_L 6.8) which is also supported by the analyses of the aftershocks of the Gorkha earthquake.

The behavior of the site effects in the Kathmandu valley is analyzed using the main-shock and few aftershocks of the Gorkha earthquake recorded at DMG. The results from the time history analysis of the mainshock reveal high amplification in the horizontal components at around 0.25 Hz in the total record of 100 s. Its significant relative duration in the horizontal component is about 42 s. The spectral acceleration of the mainshock shows long-period amplification in comparison to the predicted ones even though the PGA is lower considering the Ground Motion Prediction Equation (GMPE) of Boore and Atkinson (2008). However, the observed value is suppressed taking into account the basin effect using the GMPE of Abrahamson and Silva (2008). The spiky pulses observed at the second negative and positive peaks in the north-south component of ground motion at the DMG site in the mainshock was suspected as an effect of liquefaction or source effects; however, no field study and comparision with the nearby NQ.KATNP confirmed this phenomenon. The time history of the largest aftershock shows a total record of 70 s having a significant relative duration in the horizontal component about 32 s. The high amplification was observed at around 0.3 Hz and polarization characteristics were evident which were not visible in the mainshock and the

other aftershocks. The observed and predicted ground motions of the largest aftershock are consistent with the GMPE of Boore and Atkinson (2008). The aftershock in the east of the Kathmandu valley follows the same trend of Fourier amplitude spectra and H/V spectral ratios of the mainshock and the largest aftershock; however, the small aftershock that has occurred inside the Kathmandu valley shows a different trend.

In addition to these basic observations, we have explored the shear wave velocity (V_S) structure of the deep sediments in the Kathmandu valley, where long-period amplification at around 0.25 Hz was observed during the Gorkha earthquake. The four seismographs used consist of the broadband seismometers CMG40T and data loggers LS8800. Three sites in the central part of the valley are selected as pilot sites for applying the SPatial Auto Correlation (SPAC) method. The array geometry consists of few equilateral triangles and mainly with irregular shapes (2ST-SPAC). The appropriateness of the latter was supported by the isotropic characteristics of the coherence functions checked using the records of regular shape array in site 1. The frequency range of analysis covers from 0.2 Hz to around 1.0 Hz. Particularly for two sites 2 and 3, the dispersion curves have a winding part in the frequency range from 0.25 Hz to 0.35 Hz, where clear peaks are manifested both in the power spectra and horizontal to vertical spectral ratio. This winding part is due to the sags of the coherence functions. The cause was; however, left for future works, as the presence of higher mode of Rayleigh wave cannot explain this strange phenomenon. Results from inversion show that V_S > 2,000 m/s is determined deeper than 600 m at three sites. V_S is roughly 200 m/s or slower at the shallowest layer, then gradually increases. The layer of V_S 400 m/s appears at depths from 160 to 180 m. V_S then reaches over 550 m/s from 260 to 300 m. Bedrock depth of over 750 m is obtained at site 1; however, at sites 2 and 3 structural parameters at the deeper part and the layer above it have uncertainties.

To grasp the dispersion curve in the broad frequency range we re-analyzed the same data, some additional, and other existing ones using the Centerless Circular Array (CCA) method and the L-shape SPAC method. The disturbance in the sags of coherence function at sites 2 and 3 was suppressed when CCA was applied, but detectable. Then, we obtained broadband dispersion curves from 0.2 Hz to the frequency higher than 5 Hz at the three sites. Good consistency was confirmed between the SPAC and CCA methods in the lower frequency range. The performance of seismic interferometry was tested by applying joint inversion of phase and group velocities and shows better accuracy of velocity structure in the

higher frequency range. To obtain the dispersion curve in the lower frequency range below 0.2 Hz, a temporary continuous observation system was set at four locations in the Kathmandu valley since 2018. The regional and teleseismic earthquakes of various magnitudes greater than 4.0 were observed. The surface wave component of the records is used for the estimation of the Rayleigh-wave phase velocities in the lower frequency range. It shows the dispersive nature in the frequency range from 0.01 to 0.13 Hz. The phase velocity obtained from microtremor in the higher frequency side (> 2.0 Hz) is related to the phase velocity derived from the records of earthquakes at the lower frequency side. However, the gap in the dispersion curves exist from 0.1 to 0.2 Hz. It is confirmed that the estimated V_S are comparable with those derived from the newly proposed seismic velocity structure model of Nepal; however, they are smaller than those obtained from the existing velocity structure model at the shallower depth, but are larger below 10 upto 30 km. Microtremor array exploration is extended to the Tribhuvan International Airport (TIA), National Academy of Science and Technology (NAST), the exposed limestone site Chobhar (CHB), and many more sites. The bedrock detected at TIA and NAST from microtremor, resulted in greater depth than the previously obtained depth at site 1. The results of the gravity survey at TIA shows the basement at about 400 m depth which is supported by the high impedance contrast obtained from seismic reflection survey.

We apply the simulated ground motions to building damage analysis. The non-specific 1-, 2-, 3-, 6-, 18-, and 40-story RC buildings using horizontal components of ground motions at site 2 simulated based on the rock site motions of KKA, KTP, and PKI. Also, the ground motions at site 1 and site 3 are simulated. Structural performance factor K = 1, 2, 3, and 4 are used for all the considered buildings. Building damage caused by the Xizang, China earthquake in the 1-story and then Taplejung-Sikkim earthquake in 1-, 2-, and 3-story buildings are analyzed using the KKA-base ground motion at site 2. None of the states of collapse and damage result using either of the horizontal components, which are consistent with the observed damage. A totally collapsed state results using both the components of observed mainshock ground motion at DMG. The result of building damage analysis using ground motions at site 2 simulated based on rock site motions of PKI shows all states of collapse for 18-story buildings; however, a 6-story building was collapsed particularly for K = 1 using the EW component of ground motion. Only moderate and minimal damage has resulted from the NS component of ground motion. None of the states of collapse occurred

using the largest aftershock ground motion at site 2 simulated based on rock site motions of KTP. The analysis using the mainshock ground motion at site 2 simulated based on KTP rock site motion shows several states of collapse and severe damage in 18-story buildings mainly for K = 1 and 2; however, collapse state is observed for K = 1 in the 3-story building only using the NS component of ground motion. Several states of collapse are observed at sites 1 and 3 in 18-story buildings mainly with K = 1 and 2 using both the components of ground motion. However, only moderate and minimal damage result using other buildings and K values. It is confirmed that the mainshock of the Gorkha earthquake is severe with both the components of ground motion for low and high-rise buildings at site 2; however, it is severe for 18-story buildings at sites 1 and 3. Similarly, the largest aftershock was severe only with the EW component of ground motion for 6-story buildings with K = 1 and 18-story buildings with all values of K. This study shows the possibility of building damage analyses, at particular domains where no ground motion records but shear wave velocity structures exist.

The results obtained in this study will provide the basis to revisit the seismic hazard in Nepal, and in particular in the Kathmandu valley. It is suggested that the descripancies between expected and observed building damage will need to be addressed taking into account the three-dimensional nature of accelerometric response as well as basin structures.

Acknowledgments

I would like to express my sincere gratitude to my advisors Professor Kazuki Koketsu, Professor Hiroe Miyake, and Dr. Toshiaki Yokoi for their encouragement, guidance, and support during all steps of my study and research. I am grateful to Dr. Takumi Hayashida for his support during various steps of my study. I am deeply grateful to Professor Koichi Kusunoki for his guidance.

I am greatly benefited to have inspired comments and discussions from Professor Tsuyoshi Takada and Professor Tatsuya Itoi.

I am very thankful to Dr. Yadab Prasad Dhakal, Dr. Shakti P. C., Dr. Subeg Man Bijukhhen, Dr. Santosh Shrestha, Dr. Rishi Ram Parajuli, Dr. Trevor Yeow, and Dr. Rami Ibrahim to be benefited from their experiences and feedback.

I am grateful to Mr. Parkirna Tuladhar, and Mr. Manoj Nakarmi, Senior Divisional Engineers from DUDBC, for providing me information regarding to the Nepalese Building code (NBC, 1994) and observed damage.

I am indebted to Er. Thierry Héritier, Dr. Laurent Bollinger, Dr. Bruno Hernandez, Dr. V. Boutin, Dr. A. Laurendeau, Dr. C. Labonne, Dr. R. Hoste-Colomer, and Dr. O. Sebe for their support and technical assistance for installing GeoSIG AC 23 accelerometers, its accessories and data analysis software in Nepal since 2009 under the technical cooperation between the Governments of France and Nepal.

I would like to thank our former Director Generals Mr. Sarbjit Prasad Mahato, Mr. Rajendra Prasad Khanal, Director General Dr. Soma Nath Sapkota, Deputy Director Generals Mr. Ram Prasad Ghimire, Mr. Sudhir Rajaure, and Dr. Rajendra Prasad Bhandari, Superintendent Geologist, Mr. Dinesh Nepali, Senior Divisional Seismologists Mr. Lok Bijaya Adhikari, and Mr. Bharat Prasad Koirala from the Department of Mines and Geology, for the various support during my study.

Further thank goes to my seniors/colleagues Mr. Dilli Ram Tiwari, Mr. Umesh Prasad Gautam, Mr. Thakur Prasad Kandel, Mr. Ratna Mani Gupta, Mr. Chintan Timsina, Mr. Ashim Babu Shrestha, Mr. Nabin B. K., Mr. Rajesh Sharma and French co-operant at NSC Mr. Wendling-Vazquez Nicolas for their various supports during my research.

Acknowledgments are addressed to the Japan Society of Promotion of Science (JSPS) for providing financial support to affiliate me at the Earthquake Research Institute, University of Tokyo.

I am grateful to the Science and Technology Research Partnership for sustainable Development (SATREPS) project, Japan Science and Technology Agency (JST), and Japan International Cooperation Agency (JICA) for their various supports.

At last but not least I would like to thank my father Prem Narayan Bhattarai, mother Rama Bhattarai, spouse Manvi Bhattarai, daughter Nitika Bhattarai, son Sarthak Bhattarai, relatives, and friends for their continuous support, encouragement, and patience during my study period.

Contents

Chapter 1

Introduction

1.1 Background

Earthquakes are unavoidable and devastative for humankind among various geological phenomena all over the world. The seismic waves that can cause destruction on the ground depend on the source effect including magnitude, rupture process, etc., the path effect governed by the propagation from the source, and the site effect controlled by ground conditions around sites. Each new destructive earthquake gives further proof of the importance of the site conditions in parallel with the other two. This site effect, i.e., how local geological or geomorphological conditions amplify the seismic waves, can be prospected before the disaster occurrence. The local amplification of seismic waves, especially in a sedimentary basin, has been one of vital research targets in the world, as one of the indispensable components of the seismic hazard assessment.

A review of the early history of site effect studies was given by Sanchez-Sesma and Crouse (2015). The disparity of ground motion with depth at various soil conditions were first investigated in Japan using ground displacement records (Milne, 1887). Later, Sekiya and Omori (1892) continued this work. The *M* 7.9 great California earthquake of 1906, which occurred on the San Andreas fault (U.S.), caused limited devastation, whereas the resulting fire overwhelmed the city (Lawson, 1969; Reid, 1910). The *M* 7.9 Kanto earthquake of 1923 caused massive disaster in southeastern Japan together with the fire devastation induced by ground shaking. Kanai (1983) had reported the details of damage, whereas Imamura (1924) and Ishimoto (1932) had described the site effects. These studies show some correlation between the damage and soil type. The site amplification effects were also considered in the Soviet Union while preparing the seismic microzonation map of major cities during the late 1920s and early 1930s (Madvedev and Sponheuer, 1999). The *M* 6.4 Long Beach, California earthquake of 1933 was the first major acceleration record captured by the accelerographs in the U.S. (Martel, 1936). However, the site effects cannot be studied being the sensors located inside the buildings. The *M* 6.6 San Fernando earthquake in Los Angeles of the U.S. generated huge accelerograms which could be convinent to obtain the geological effects on various scales caused by ground motion records (Hounser, 1978). The requirement of site

effects on building code becomes a topic of dialogue after this earthquake. The *M* 6.4 Venezuela earthquake of 1967 in the Caracus showed a strong influence on non-uniform subsurface terrain covered by the sediments (Esteva *et al*., 1968; Seed *et al*., 1972). The *M* 8.1 Michoacan earthquake of 1985 in the Mexico City exibited the effect of soft clay deposits in the strong motion records. The *M* 6.9 Loma Prieta earthquake of 1989 in the Sanfrancisco resulted remarkable damage in the various parts of the city in particular, Okland and high intensity areas e.g., bay mud, infill sites, etc. (Hanks and Brady, 1991). The quantitative estimate of the site effects based on studies of engineering seismology is one of the demanding issues in seismic hazard assessment (e.g., Borcherdt, 1970). The classical method for describing such effects is composed of recording earthquakes at several sites and comparing each record with that at the reference site (e.g., Borcherdt and Gibbs, 1976; Field and Jacob, 1995; Bard, 1998, etc.). However, the history of instrumentally recorded earthquakes is rather short, and the spatial distribution of observed ground motions is extremly irregular. Seismic surface waves of long-periods and high amplitudes in deep sedimentary basins, can cause damage to large scale structures, e.g., high-rise buildings and oil storage tanks (Koketsu and Miyake, 2008). Therefore, an accurate estimate of such long-period seismic waves that can be affected by sedimentary layers in basin structures is necessary for reliable seismic safety evaluation of these structures.

Over the last decades, microtremors (ambient noises) have been used as an efficient tool for the spatial variability of seismic site response as it is convenient and affordable for usage in urbanized areas as well as more advanced array exploration technique. The horizontal to vertical Fourier amplitude spectral ratio (HVSR) is used to evaluate site response parameters. After the pioneering work by Nogoshi and Igarashi (1971) the HVSR ratio technique came into existence. Later its potentiality has been frequently shown (Nakamura, 1989; Lachet and Bard, 1994; Kudo; 1995; Bard 1998). Moreover, Arai and Tokimatsu (2004) introduced proposals for microtremor H/V spectra taking in to account the consequences of fundamental and higher modes. They approximated the V_S profile of subsurface soils by an inverse analysis of H/V spectra assuming either the V_S is and thickness of shallow soil layers are known. Later Sanchez-Sesma (2011) introduced a theory for microtremor H/V spectral ratios appropirate for a layered medium assuming the diffused seismic field. Furthermore, Kawase *et al*. (2011) showed the optimal use of HVSR for ground motions to derive a velocity structure based on the diffuse-field theory for plane waves.

The array exploration techniques were first to derive the dispersion curve of surface waves included in microtremors by array measurement of microtremor and to derive subsurface *S*-wave velocity profiles by inverting the dispersion curve. Such studies started in the later 1950s and successively resulted in the quantification and qualitification of the array techniques (e.g., Aki, 1957, 1965; Asten and Henstridge; 1984; Horike, 1985, 1996; Kudo *et al*., 2002, Ohori *et al*., 2002; Okada, 2003; Asten, 2004; Yamanaka *et al*., 2004; Chavez-Gracia *et al*., 2005, 2006, Shiraishi *et al*., 2006; Okada, 2006; Cho *et al*., 2008; Asten *et al*., 2014; Hayashi and Craig, 2017). Among the studies mentioned above, Hayashi and Craig (2017) recently showed a successful example of *S*-wave velocity profile at eleven sites in east San Francisco Bay area, California by the SPatial Auto Correlation (SPAC) method with two stations (2ST-SPAC) using long-period microtremors, where the maximum inter-station distance was targeted from several hundred meters to several kilometers within the frequency range from 0.2 to 2 Hz depending on sites.

Nepal Himalaya occupies one third arc length, about 800 km of the whole Himalayan range extending from Myanmar in the east to Afghanistan in the west. The Indian plate in the south is moving northward at a convergent rate of about 40 mm/yr (Lavé and Avouac, 2000; Jouanne *et al*., 2004; Bettinelli *et al*., 2006; Ader *et al*., 2012). However, its continental lithosphere is too buoyant to subduct so that it is colliding with the Eurasian plate in the north generating large earthquakes and forming steep mountains in the Himalayan region including Mount Everest (8,848 m). Urban areas in Nepal are mostly located in few basins such as the Kathmandu valley. The Kathmandu valley is a tectonic basin formed by the rapid uplift of the southern rim dammed by the proto-Bagmati river (Sakai *et al*., 2002) and created a paleo-Kathmandu lake (Fuji and Sakai, 2002). It comprises mainly fluvio-lacustrine deposits of the Quaternary age with varying thickness. A simplified geological cross-section through central Nepal indicating the Kathmandu valley is shown in Figure 1.1. The 1934 Bihar-Nepal earthquake (M_W 8.1) was one of the unfavourable earthquakes in the present-day history of Nepal. The epicenter of this earthquake was in the eastern Nepal-India (Bihar) border at about 200 km south-east of the Kathmandu valley. However, the destruction in the Kathmandu valley was particularly severe. This earthquake affirmed 8,519 fatalities in total including 4,296 in the Kathmandu valley (Rana, 1935). An intensity from I to X was reported to some parts of the Kathmandu valley whereas from I to IX to the rest (Pandey and Molnar, 1988). In 1920 there were 66,440 houses in the Kathmandu valley among them, 12,397

(nearly 19%) were completely destroyed whereas 25,658 (38%) were badly fractured (Rana, 1935; Dunn *et al*., 1936). Moreover, the buildings built on the bedrock survived better than young sediment, in particular, three temples Boudhanath, Pashupatinath, and Swayambhunath escaped from significant damage (Dunn *et al*., 1939). Since the subsidence of ground was not reported, tilting and slumping of buildings and structures were not observed. Most of the buildings built on unconsolidated sediments were affected due to the amplification of ground motion in the sediment-filled valley (Dunn *et al*., 1939). In addition to this instrumental earthquake and resulting devastation, historical chronicles reported significant earthquakes observed in 1255, 1408, 1681, 1803, 1810, 1833, and 1866 (e.g., Chitrakar and Pandey, 1986). However, despite those descriptions suggesting their contributions to events with various magnitudes at various distances, most of these historical earthquakes' sources are still unknown. Site-specific studies in the valley conducted in the past are: (gravity survey) Moribayasi and Maruo (1980); (earthquake disaster assessment) JICA (2002); generation of geological database Piya (2004); short-period microtremor survey Pandey (2000); Kukidome *et al*. (2009); Mugnier *et al*. (2011); Paudyal *et al*. (2012; 2012a; 2012b); Bhandary *et al*. (2014); Bhattarai *et al*. (2011), etc. These studies are mainly focused on gravity survey, borehole logs, geological cross-section, short-period microtremor analysis, and observed ground motion records. However, none of these studies have derived the shear wave velocity structures for the deeper part and their applications to building damage analysis in the Kathmandu valley.

The 2010 Xizang, Tibet earthquake (M_L 5.7) is the first felt earthquake in the Kathmandu valley that has been co-recorded by the NSC seismic and accelerometric networks. The epicenter of this earthquake in the background of accelerometers in and around the Kathmandu valley is shown in Figure (1.2a). Such a moderate magnitude earthquake with epicentral distances above 100 km form DMG and KKA recorded by the seismic network get saturated (Figure 1.2b). The earthquake was occurred outside the seismic network; however, recorded by all the seismic as well as accelerometric network. Figure 1.2c shows the manual processing of earthquake by the NSC seismic network. The saturated signals in the seismic network are well complemented by the strong motion data recorded at DMG and KKA. Acceleration waveform of this earthquake recorded in the premises of DMG and its acceleration response spectra processed by ViewWave (Kashima, 2009) are shown in Figures (1.3a and b). Hereafter ViewWave is used to analyze the acceleration waveform.

The Kathmandu valley was well shaken by the 2011 Taplejung-Sikkim border earthquake (M_L 6.8). The epicenter of this earthquake was in the border region of eastern Taplejung district of Nepal and the western Sikkim of India and followed by many aftershocks (NSC, 2011). In total 111 fatalities were reported including 97 from India, 7 from China, 6 from Nepal, and 1 from Bhutan (MoHA, 2011). The epicenter map of this earthquake including the immediate aftershocks is shown in Figure 1.4. The acceleration waveform and acceleration response spectra recorded at DMG are shown in Figures (1.5a and b). This earthquake was also felt in Nepal, India, China, Pakistan, Bangladesh, and Bhutan. Many non-specific, non-code compliances buildings in the eastern region of Nepal has been collapsed during this earthquake. However, in the Kathmandu valley the retaining wall of British embassy in the Lainchour area nearby DMG collapsed resulting 3 people spot death. The long-period shaking was felt in the Kathmandu valley even though the epicenter was about 300 km east from it. The intensity map of this earthquake is shown in Figure 1.6 (USGS, 2011).

The current seismic observation network of Nepal is shown in Figure 1.7. This network has two autonomous centers for recording earthquakes. Each center is equipped with a seismic and technical alert system for immediate response in case of an earthquake or technical failure. The seismic stations are deployed mainly in lesser and sub-Himalayan terrain with an average interstation distance about 100 km. The Gorkha earthquake (M_W 7.8) is the most recent disastrous earthquake hitting Nepal since the 1934 Nepal-Bihar earthquake (Goda *et al.*, 2015; NPC, 2015), regarding its magnitude and losses. The waveform and acceleration response spectra recorded at DMG are shown in Figures (1.8a and b). The intensity distribution in the Kathmandu valley (Martin *et al.*, 2015) is shown in Figure 1.9. The death toll in the Kathmandu valley was reported to 1,738 among the total 8,979 (MoHA, 2015). The spatial distribution of the aftershocks from the epicentral region towards east about 150 km suggested that the fault rupture propagated from the west to the east resulting severe devastation in the Kathmandu valley (Koketsu *et al.*, 2016).

The detail rupture imaging using teleseismic *P*-waves is described by Fan and Shearer (2015). Together with notable aftershocks of 25, 26 April, and 12 May 2015, the Gorkha earthquake destroyed 498,582 buildings whereas 256,697 were partially affected. Among the damaged ones, the majority of low-strength masonry buildings are 474,025 as comprising 95% of the damaged buildings, while 173,867 accounted for 67.7% of the partially damaged

buildings. By comparision, 18,214 cement-mortared masonry buildings accounted for about 3.7% of fully damaged building and 25.6% of the partially damaged buildings (65,859). This data clearly demonstrates the structural damage during the Gorkha earthquake to the low-strength masonry buildings (NPC, 2015).

During the Gorkha earthquake in the central part of the Kathmandu valley, high-rise structures with the long natural period (e.g., Bhimsen tower commonly known as Dharahara, built in 1832) collapsed. Moreover, those outside the Kathmandu ring road, the Park View Horizon apartment and Sunrise apartment, etc. also suffered heavy damage in the masonry infill walls. The damage was mainly concentrated on centuries-old buildings and monuments in the Kathmandu valley, e.g., Kathmandu, Patan, and Bhaktapur Durbar Squares, ancient and historic towns of Sankhu and Khokana but also in recently growing urbanized areas Sitapaila, Balaju, etc. Outside the valley the heavily damaged sites are distributed from the hypocenter to the east, e.g., Sindhupalchowk, Dolakha, etc. Some damaged examples of typically sampled buildings and structures in the Kathmandu valley are Dharahara (Figure 1.10a), Park View horizon apartment building (Figure 1.10b), and some private buildings in Balaju (Figure 1.10c), (Hashash *et al*., 2015). The Gorkha earthquake brought singular facts in low input motion and soil non-linearity (JICA, 2016). Although the actual conditions of individual buildings varied, the soil/ground condition did affect the damage of them. Therefore, after this earthquake many studies were concentrated regarding to site effect studies and damage distribution e.g., Parajuli and Kiyono, 2015; Okamura *et al*., 2015; Hashash *et al*., 2015; Bhattarai *et al*., 2015, 2016; JICA 2016; Dhakal *et al*., 2016; Takai *et al*., 2016; Hough *et al*., 2016; Dixit *et al*., 2015; Yamada *et al*., 2016; Williams *et al*., 2016; Gautam *et al*., 2016; Ohsumi *et al*., 2016; Shakya and Kawan, 2016; Koketsu *et al*., 2016; Bijukchhen *et al*., 2017; Rajaure *et al*., 2017; Poovarodom *et al*., 2017; Molnar *et al*., 2017; etc. Two factors caused the disparity of damage in the Kathmandu valley: The basin underneath the Kathmandu, filled with a half kilometer of soft sediments, amplifies the shaking of taller buildings. Secondly the source characteristics of the earthquake would have affected shorter buildings (Avouac *et al*., 2015).

The Kathmandu valley is exposed to high seismic hazard due to its tectonic environment and local site conditions. Furthermore, unplanned land use, rapid urbanization, and poor earthquake resistant constructions make this area highly vulnerable. For the seismic protection of lives and properties for approximately 3.0 million urban agglomerations across

the valley, it is required to evaluate the seismic hazard and risk using the newest methods of engineering seismology. Estimation of local site effects based on the shear wave velocity structure of sedimentary layers is the indispensable process for this aim. An efficient and affordable method to do it is the microtremor array exploration which does not pose any environmental problem even in the densely populated Kathmandu valley. Thus, it is necessary and possible to model both shallow and deep parts of the sedimentary layers which is important for the ground motion prediction as well as building damage evaluation. The pilot sites chosen in the Kathmandu valley at different geological environments for the long-period microtremor exploration are shown in Figure 1.11.

1.2 Objectives

This thesis presents studies that address site effects on seismic ground motions and simulations based on velocity structure models derived from long-period microtremor arrays observations. Results from the former are used to differentiate the networks, strong motion site characterization, understand the behavior of the site effects in the Kathmandu valley, and its comparison with the conventional approaches whereas those from the latter are used to understand the damage of RC buildings in the Kathmandu valley during the past earthquakes. Also, we explain the derivation process and physical meaning of SPatial Auto Correlation (SPAC) method for microtremor exploration and validate the velocity structure models by re-analyzing the same database and some additional ones based on different exploration techniques. We mainly simulate ground motions at arbitrary sites that exist the velocity structure models and evaluate the building damage in the Kathmandu valley sited on the lake sediment bed and its vicinity of the ancient paleo Kathmandu lake based on the ductility demand and the ductility capacity required for the building collapse specified by the building code.

Nepal's national building code was formulated in 1994 and most of the ancient buildings constructed before have suffered much more damage during the Gorkha earthquake in comparison to recently constructed code compliance RC buildings of various configurations. However, some high raise buildings suffered severe damage during the mainshock and the largest aftershock. In the mainshock of the Gorkha earthquake, the Peak Ground Acceleration observed at DMG (Bhattarai *et al*., 2015), Kantipath (USGS, 2015b),

and others (Takai *et al*., 2015) are smaller than predicted by GMPEs without considering the basin effect. However, the PGV's observed are higher than the predicted ones.

Before the Gorkha earthquake researchers had been concentrated in the Kathmandu valley (KTV) to study the sediment depth (gravity survey) and predominant response period of sites using single tri-axial sensors (short-period microtremor survey). However, the deep shear wave velocity structures of the lake-bed sediments and its applications to analyze building damage have not been studied yet.

The general objective of this research is to develop the deep 1-D velocity structure models of the Kathmandu valley and their applications to building damage analysis.

The specific objectives are,

(1) To review the earthquake monitoring system in Nepal and grasp the difference between the networks.

The new accelerometric network is used to complement the existing seismic network and characterize the local site conditions. The traditional magnitude scale such as local magnitude (M_L) used by NSC for routine data processing and scaling of large earthquakes at short and large, epicentral distances suffers from saturation. The site amplification and building damage studies at and around the DMG site are examined (Chapter 2).

(2) To establish a reference rock site.

Reference site is needed at least 2 or 3 points in the Kathmandu valley from which we can evaluate the site amplification at arbitrary sites. The site amplification estimated from the rock site having its own response will pose a problem for the evaluation of damage at the site of interest (Chapter 3).

(3) To obtain the behavior of site effects and compare them with the conventional approach (Chapter 4).

Deep sedimentary basins like the Kathmandu valley generates large amplification at a long-period which is clearly evidenced during the Gorkha earthquake. Conventional EMPEs do not account for the soil and site conditions. The spectral acceleration of the observed

ground motions is compared with the conventional approaches e.g., Boore and Atkinson, 2008 and Abrahamson and Silva, 2008 with and without taking in to account the basin effect. The spiky pulses observed at the second negative and positive peaks at DMG in the EW component are suspected as a non-stationary effect which is carefully checked with the nearby site and presented. The effect of the long-period ground motion in the sedimentary basin and resulting damage in RC buildings are discussed in Chapter 7.

(4) To construct the shear wave velocity structure for the ground motion prediction and hazard evaluation (Chapter 5).

The study of the sub-surface velocity structures in the Kathmandu valley from the previous studies is very poor or almost lacking. A deep velocity structure is needed to address the long-period ground motion like the Gorkha earthquake. Also, shallow velocity structures are important to study the significance of the earthquake in the buildings and structures and the inclusion of site effects in the building codes. The complex underground structure of the sedimentary basin poses a problem to accurately estimate the structural parameters which might influence the ground motion simulation.

(5) To refine, validate, tune, and expand the velocity structure model towards the deeper part based on different analyses (Chapter 6).

To reduce and confirm the uncertainty of the structural parameters and validate the results from the same data, some existing, and additionally measured data are re-analyzed with various exploration techniques. The bias in the deeper structure will cause the problem in the hazard evaluation and building damage analysis. The lack of the dispersion curve in the frequency below 0.2 Hz from microtremor analyses are determined by analyzing the earthquakes at regional and teleseismic distances.

(6) To use shear wave velocity structures for analyzing building damage based on simulated ground motions and comparison of the calculated damage with the observed one (Chapter 7).

The rock site motions from the past earthquakes (e.g., 2010 Xizang, China, earthquake, 2011 Taplejung-Sikkim earthquake, 2015 Gorkha earthquake, and its largest aftershock) are simulated at the sedimentary sites. The investigation is performed first by considering the observed records both at the sedimentary and rock sites and taking in to

account the shear wave velocity structures. Then the damage is evaluated at the specific domain using the simulated ground motion at the sites where only the shear wave velocity structures exist but seismic observation system does not then an extension of this method is recommended to apply arbitrary sites. The simulated ground motions are used for building damage analyses and the results obtained from the analysis are compared with the observed building damage.

1.3 Organization

The thesis consists of eight chapters as follows:

In Chapter 1, we present the background, objectives, and organization of this thesis as an introduction.

In Chapter 2, we briefly review the earthquake monitoring system of Nepal and explain the difference between the existing seismic network and the newly established accelerometric network of NSC. The limitation of short-period seismic network during large magnitude earthquakes at short and large epicentral distances is discussed. Site amplification at DMG with reference to KKA is analysed using spectral ratios and some anomaly is detected at the rock site KKA while using the magnitude (M_L 5.7) Xizang, China earthquake. The time series in the vertical component at DMG does not show *S*-onset suspecting the sedimentary site effect. The damage analysis using this earthquake is discussed in Chapter 7.

In Chapter 3, we analyzed nine earthquakes of ($M_L \geq 5.0$) simultaneously recorded from various azimuths and epicentral distances in DMG and KKA to ascertain the anomaly detected in Chapter 2. The anomaly re-appeared for all of the analyzed earthquake records. The anomoly is re-examined considering PKIN as a proxy to the KKA rock site for all the earthquakes used. The long-period site response in the Kathmandu valley was observed during 2011 Taplejung-Sikkim earthquake (M_L 6.8). After the Gorkha earthquake, an accelerometer PKI has been installed nearby the PKIN site and its reliability as a reference rock site is confirmed with DMG examining with the largest aftershock and other aftershocks of the Gorkha earthquake. The rock motion at the PKI station is used for the numerical simulation in Chapter 7. The damage analysis using this earthquake is discussed in Chapter 7.

In Chapter 4, the behavior (time series, frequency content, polarization, etc.) of the ground motion in the Kathmandu valley using the mainshock, the largest aftershock, and some other aftershocks are discussed. The acceleration response spectrum of the observed ground motion is compared with the conventional approaches with or without considering basin effects. The damage analysis using these earthquakes is discussed in Chapter 7.

In Chapter 5, taking into account the nature of the long-period ground motion at the sedimentary site DMG in Chapter 4 and others in the Kathmandu valley during the Gorkha earthquake long-period microtremor arrays in the central part of KTV at various sites including DMG is observed. The deep shear wave velocity structure model is constructed using inversion techniques from the dispersion curve obtained from the SPAC coefficients of microtremor records. Some uncertainties in the structural parameters is detected due to the presence of sags in the SPAC coefficients. The revised and extended structural model in the next chapter is realized for ground motion simulation and building damage analysis as shown in Chapter 7.

In Chapter 6, we derived the dispersion curve in the broad frequency range by re-analyzing the data obtained from Chapter 5 with some existing, and additional observations using various analysis techniques (e.g., CCA, seismic interferometry, analysis of teleseismic records, etc.). Results from these analyses are used for ground motion simulation in Chapter 7. The maximum explored depth at around the explored sites is used in the GMPE (Abraham and Silva, 2008) in Chapter 4 to account for the basin effect.

In Chapter 7, we conduct damage analysis of RC buildings using simulated ground motion caused by Xizang, China earthquake, Taplejung-Sikkim earthquake, the most recent Gorkha earthquake, and its largest aftershock. The Xizang earthquake and Taplejung-Sikkim earthquake are simulated using the rock motions at KKA. The mainshock and the largest aftershock of the Gorkha earthquake are simulated using the rock motion at the KTP and PKI sites. The ground motion of the mainshock during the Gorkha earthquake at SDB and TEKU is simulated using mathematical approach taking in to account the observed records at the DMG and KTP sites. The simulated ground motion mainly at DMG, SDB, and TEKU are used for building damage analysis using Capacity Spectrum Method. We analyzed the damage taking in to account the various types of code compliance RC buildings in the Kathmandu valley, e.g., 1-, 2-, 3-, 6-, 18-, and 40-story buildings with different values of

structural performance factor K = 1, 2, 3, and 4. The observed damage is also compared with the results from analyses. We also compared the design response spectrum of the building code (NBC, 1994) with the acceleration response spectra of the mainshock and the largest aftershock of the Gorkha earthquake for the judgment of the code limit.

In Chapter 8, we present a discussion on the main conclusions of this thesis and possible extension of future studies.

1.4 References

Abrahamson, N., and W. Silva (2008). Summary of the Abrahamson and Silva NGA Ground-Motion Relations, Earthquake Spectra, 24(1), 67-97, doi: 10.1193/1.2924360.

Ader, T., J. -P. Avouac, J. -L. Jing, L. -C. Helene, L. Bollinger, J. Galetzka, J. Generich, M. Thomas, K. Chanard, S. N. Sapkota, S. Rajaure, P. Shrestha, L. Ding, and M. Flouzat (2012). Convergence rate across the Nepal Himalaya and interseismic coupling on the Main Himalaya Thrust, Implications for seismic hazard, *J. Geophys. Res.*, **117**, B04403.

Aki, K. (1957). Space and time spectra of stationary stochastic waves, with special reference to microtremor, *Bull. Earthq. Res. Inst*., Tokyo Univ., **35**, 415-456.

Aki, K. (1965). A note on the use of microseisms in determining the shallow structures of the earth's crust, *Geophysics*, **30**, 665-666.

Arai, H., and K. Tokimatsu (2004). *S*-wave velocity profiling by inversion of microtremor H/V spectrum, *Bull. Seismol. Soc. Am*., **94**, 53-63.

Asten, M. W. (2004). Method for site hazard zonation, Santa Clara valley, Thickness and shear-velocity mapping of Holocene-Pleistocene sediments by array studies of microtremors. Presented at *First Annual Northern California Earthquake hazard workshop*, Jan. 13-14, USGS, Menlo park.

Asten, M. W., A. Askan, E. E. Ekincioglu, F. N. Sisman, and B. Ugurhan (2014). Site Characterization in north-western Turkey based on SPAC and HVSR analysis of microtremors noise, *Exploration Geophysics*, **45**, 74-85, doi: 10.1071/EG12026.

Asten, M. W., and J. D., Henstridge (1984). Array estimators for the use of microseisms for reconnaissance of sedimentary basins, *Geophysics*, **49(11)**, 1828-1837.

Avouac, J. -P., L. Meng, S. Wei, T. Wang, and J. -P. Ampureo (2015). Lower edge of locked Main Himalayan Thrust unzipped by the 2015 Gorkha Earthquake, *Nat. Geosci*., **8(9)**, 708-711.

Bard, P. Y. (1998). Microtremor Measurement: a tool for site effect estimation? In: K., Irikura, K. Kudo, H., Okada and T., Sasatani (Eds.), the effect of Surface geology in seismic motion, *Balkema,* 1251-1259.

Bettinelli, P., J. -P. Avouac, M. Flouzat, F. Jouanne, L. Bollinger, P. Willis, and G. R. Chitrakar (2006). Plate motion of India and interseismic strain in the Nepal Himalaya from GPS and DORIS measurements, *J. Geodesy*, **80**, 567-589.

Bhandary, N. P., R. Yatabe, K., and Y. R. Paudyal (2014). Use of a Sparse Geo-Info Database and Ambient Ground Vibration Survey in Earthquake Disaster Risk Study, A Case of Kathmandu Valley, *J. Civil Eng. Res.*, **4(3A)**, 20-30, doi: 10.5923/c.jce.201402.03.

Bhattarai, M., L. B. Adhikari, U. P. Gautam, L. Bollinger, B. Hernandez, T. Yokoi, and T. Hayashida (2016). Establishing a reference rock site for the site effect study in and around the Kathmandu valley, Nepal, *Earth Planets Space*, doi: 10.1186/s40623-016-0454-9.

Bhattarai, M., L. B. Adhikari, U. P. Gautam, A. Laurendeu, C. Labonne, R. Hoste-Colomer, O. Sebe, and B. Hernandez (2015). Overview of the large 25 April Gorkha, Nepal, earthquake from accelerometric perspectives, *Seismol. Res. Lett*., **86**, 40-48.

Bhattarai, M., U. Gautam, R. Pandey, L. Bollinger, B. Hernandez, and V. Boutin (2011). Capturing first records at the Nepal NSC accelerometric network, *J. Nepal Geol. Soc*., **43**, 15-22.

Bijukchhen, S. M., N. Takai, M. Shigefuji, M. Ichiyanagi, T. Sasatani, and Y. Sugimura (2017). Estimation of 1-D velocity models beneath the strong motion sites in the Kathmandu Valley using strong motion records from moderate-sized earthquakes, *Earth Planets Space*, doi: 10.1186/s40623-017-0685-4.

Borcherdt, R. D., and J. F. Gibbs (1976). Effects of local geological conditions in the San Francisco Bay region on ground motions and intensities of the 1906 earthquake, *Bull. Seismol. Soc. Am.*, **66(2)**, 467-500.

Borcherdt, R. D. (1970), Effects of local geology on ground motion near San Francisco Bay. *Bull. Seismol. Soc. Am.*, **60(1)**, 29-61.

Boore, D., and G. Atkinson (2008). Ground-motion prediction equations for the average horizontal component of pga, pgv, and 5% damped psa at spectral periods between 0.01 s and 10.0 s, *Earthquake Spectra*, **24(1)**, 99-138, doi: 10.1193/1.2830434.

Chavez-Garcia, F. J., M. Rodriguez, and W. R. Stephenson (2006). Subsoil structure using SPAC measurements along a line, *Bull. Seismol. Soc. Am.*, **96**, 729-737.

Chavez-Garcia, F. J., M. Rodriguez, and W. R. Stephenson (2005). An alternative approach to the SPAC analysis of microtremors: Exploiting stationarity of noise, *Bull. Seismol. Soc. Am*., **95**, 277-293.

Cho, I., T. Tada, and Y. Shinozaki (2008). Assessing the applicability of the spatial autocorrelation method: A theoretical approach, *Geophys. J. Int.*, **113**, B06307, doi:10.1029/2007JB005245.

Chitrakar, G. R., and M. R. Pandey (1986). Historical Earthquake of Nepal, News *Bull. Geol. Soc., Nepal*, **4**, 7-8.

Dhakal, Y. P., H. Kubo, W. Suzuki, T. Kunugi, S. Aoi, and H. Fujiwara (2016). Analysis of strong ground motions and site effects at Kantipath, Kathmandu, from 2015 Mw 7.8 Gorkha, Nepal earthquake and its aftershocks, *Earth Planets Space*, **68(1)**, doi: 10.11.86/s40623-016-0432-2.

Dixit, A. M., A. T. Ringler, D. F. Sumy, E. S. Cochran, S. E. Hough, S. S. Martin, S. Gibbons, J. H. Luetgert, J. Galetzka, S. N. Shrestha, S. Rajaure, and D. E. McNamara (2015). Strong-Motion Observations of the M 7.8 Gorkha, Nepal, Earthquake Sequence and Development of the N-SHAKE Strong-Motion Network, *Seismol. Res. Lett*., **86(6)**, 1533-1539.

Dunn, J. A., J. B. Auden, A. M. N. Ghosh, and D. N. Wadia (1939). The Bihar-Nepal earthquake of 1934, *Geol. Survey India Mem*., 73.

Esteva, L., R. Díazde de Cossio, and J. Elorduy (1968). El temblor de Caracas, Julio de 1967, *Ingeniería*, **38**, 289-314, also at *Inst. Ing*., 168.

Fan, WY., and PM. Shearer (2015). Detail rupture imaging of the 25 April 2015 Nepal earthquake using P waves, *Geophys. Res. Lett*., **42(14)**, 5744-5742, doi: 101002/2015g1064587.

Field, E. H., and K. H. Jacob (1995). A comparison and test of various site-response estimation techniques, including three that are not reference-site dependent. *Bull. Seismol. Soc. Am*., **85**, 1127-1143.

Fujii, R., and H. Sakai (2002). Paleoclimatic changes during the last 2.5 myr recorded in the Kathmandu Basin, Central Nepal Himalayas, *J. Asian Earth Sci.*, **20**, 255-266.

Gautam, D. (2017). Unearthed lessons of 25 April 2015 Gorkha earthquake (MW 7.8), geotechnical earthquake engineering perspectives, *GEOMATICS, NATURAL HAZARDS AND RISK*, **8(2)**, 1358-1382.

Gautam, D., and D. Chaulagain (2016). Preliminary assessment of seismic site effects in the fluvio-lacustrine sediments of the Kathmandu valley Nepal, *Nat*., *Hazards*, **81**, 1745-1759.

Goda, K., T. Kiyota, R. M. Pokhrel, G. Chairo, T. Katagiri, and K. Sharma (2015). The 2015 Gorkha Nepal Earthquake: insights from earthquake damage survey, *Front. Built Environ*., 1, 8, doi: 10.3389/fbuil.2015.00008.

Hashash, Y., B. Tiwari, R. Moss, D. Asimaki, K. Chalan, D. Kieffer, D. Dreger, A. Macdonald, C. Madugo, H. Mason, M. Pehlivan, D. Rajamajhi, I. Acharya, and B. Adhikari (2015). Geotechnical field Reconnaissance: Gorkha (Nepal) earthquake of April 25, 2015 and related shaking sequence, *Geotechnical Extreme Event Reconnaissance GEER Association*, Report No. GEER-040.

Hanks, TC., and AG. Brady (1991). The Loma Prieta earthquake ground motion and damage in Oakland, Treasure Island, and San Franscisco, *Bull. Seismol. Soc. Am*., **81**, 2019-2047.

Hayashi, K., and M. Craig (2017). *S*-wave velocity measurement and the effect of basin geometry on site response, east San Francisco Bay area, California, USA, *Physics and Chemistry of the Earth*, **98**, 49-61.

Horike, M. (1996). Geophysical exploration using microtremor measurements, *Proc. 11th World Conf. Earthq. Eng*., Paper No. 2033.

Horike, M. (1885). Inversion of phase velocity of long-period microtremors to S-wave velocity structure down to the basement in urbanized areas, *J. Phys. Earth*, **33**, 59-96.

Hounser, GW. (1978). A challenge to Earthquake Research. *Bull. Seismol. Soc. Am*., **68**, 1181-1185.

Hough, S. E., S. S. Martin, V. Gahalaut, A. Joshi, M. Landes, and R. Bossu (2016). A comparison of observed and predicted ground motions from the 2015 *Mw* 7.8 Gorkha, Nepal, Earthquake, *Nat. Hazards*, **84(3)**, 1661-1684.

Imamura, A. (1924). Preliminary note on great earthquake of southeastern Japan on September 1, 1923, *Bull. Seismol. Soc. Am*., **14,** 136-149.

Ishimoto, M. (1932). Comparison acceleromtrique des secousses sismiques dans deux parties de la ville de Tokyo, *Bull. Earthq. Res. Inst.*, **10**, 171-187.

Japan International Cooperation Agency (2016). The project for assessment of Earthquake Disaster Risk for the Kathmandu valley in Nepal (Progress report).

Japan International Cooperation Agency (2002). *The study on earthquake disaster mitigation in the Kathmandu valley, Kingdom of Nepal*, Vols. I-III.

Jouanne, F., J. L. Mugnier, J. F. Gamond, P. L. Fort, M. R. Pandey, L. Bollinger, M. Flouzat, and J. -P. Avouac (2004). Current shortening across the Himalayas of Nepal, *Geophys. J. Int.*, **157**, 1-14.

Kanai, K. (1983). Engineering Seismology, Tokyo university, Tokyo.

Kashima, T. (2009). View Wave, http://smo.kenken.go.jp/~kashima/viewwave, accessed on 20 May 2015.

Koketsu, K., H. Miyake, Y. Guo, H. Kobayashi, T. Matsuda, S. Davuluri, M. Bhattarai, L. B. Adhikari, and S. N. Sapkota (2016). Widespread ground motion distribution caused by

rupture directivity during the 2015 Gorkha, Nepal earthquake, *Scientific reports*, **6(28356)**, doi: 10.1038/srep28356.

Koketsu, K., and H. Miyake (2008). A seismological overview of long-period ground motion, *J. Seismol*., **12**, 133-143.

Kudo, K., T. Kanno, H. Okada, O. Ozel, and M. Erdik (2002). Site-specific issues for strong ground motions during the Kocaeli, Turkey, earthquake of 17 August 1999, as inferred from array observations of microtremors and aftershocks, *Bull. Seismol. Soc. Am*., **92**, 448-465.

Kudo, K. (1995). Practical estimates of site response, state of art report, in 5th *International Conference on seismic zonation*, Nice France.

Kawase, H., F. J. Sanchez-Sesma, and S. Matsushima (2011). The optimal use of horizontal-to-vertical spectral-ratios of earthquake motions for velocity inversions based on diffuse-field theory for plane waves, *Bull. Seismol. Soc. Am*., **101(5)**, 2001-2014.

Kukidome, T., T. Mori, and N. P. Bhandary (2009). Distribution of predominant period of ground across Kathmandu valley based on microtremor measurement, Proc. *44th Annual Conf. Japan Geotec. Soc.*, 1543-1544 (In Japanese).

Lave, J., and J. -P. Avouac (2000). Fluvial incision and tectonic uplift across the Himalayas of central Nepal, *J. Geophys. Res*., Solid Earth, **98(B4)**, 6755-6804.

Lawson, AC. (1969). The California earthquake of April 18, 1906. *Report of the state Earthquake Investigation Commission*, Carnegie Institute of Washington,1908 (Reprinted).

Lachet, C., and P. Y. Bard (1994). Numerical and theoretical investigations on the possibilities and limitations of the "Nakamura's technique", *J. Phys. Earth*, **42**, 377-397.

Martel, RR. (1936). A report on earthquake damage to type III buildings in Long Beach, Earthquake investigations in California, 1934-1935, U.S., *Dept. commerce, Coast and Geodetic Survey*, 143-162 (Special publication).

Martin, S. S., S. E. Hough, R. Bilham, and C. Hung (2015). Ground motions from the 2015 Mw 7.8 Gorkha Nepal, Earthquake, constrained by the detailed assessment of Macro seismic data, *Seismol. Res. Lett*., **86(6)**, doi: 10.1785/0220150138.

Medvedev, SV., and W. Sponheur (1969). Scale of seismic intensity, *Proc. 4th world conf. Earthq. Eng.*, Santiago Chile, **1**, 143-153.

Milne, J. (1887). On a seismic survey made in Tokio in 1884 and 885, Transactions of the *Seismol. Soc. Japan*, **10**, 1-36.

Ministry of Home Affairs, Government of Nepal (MoHA, 2015), http://www.moha.gov.np.

Ministry of Home Affairs, Government of Nepal (MoHA, 2011), http://www.moha.gov.np.

Molnar, S., J. Onwuemeka, and S. R. Adhikari (2017). Rapid post-earthquake microtremor measurements for site amplification and shear wave velocity profiling in Kathmandu, Nepal, *Earthquake Spectra*, 33, doi: 10.1193/121916EQS245M.

Moribayashi, S., and Y. Maruo (1980). Basement Topography of the Kathmandu valley, Nepal, An application of gravitational method of the survey of the tectonic basin in the Himalayas, *J. Japan Soc. Eng. Geol*., **21(2)**, 30-37.

Mugnier, J. L., P. Hyughe, A. Gajurel, B. N. Upreti, and F. Jouanne (2011). Seismites in the Kathmandu basin and seismic hazard, *Tectonophysics*, **9**, 33-49.

Nakamura, Y. (1989). A method for dynamic characteristics estimation of subsurface using microtremor on the ground surface, *QR of TREI*, **30(1)**, 25-33.

National Seismological Centre (NSC, 2011), http://www.seismonepal.gov.np/, accessed on 20 Sep. 2011.

NPC (2015). Nepal Earthquake, Post Disaster Needs Assessment Vol. A: key findings, Government of Nepal, National Planning Commission, Kathmandu.

Nogoshi, M., and T. Igarashi (1971). On the amplitude characteristics of microtremor (part 2). *J. Seismol. Soc. Japan*, **24**, 26-40 (In Japanese with English abstract).

Ohori, M., A. Nobata, and K. Wakamatsu (2002). A comparison of ESAC and FK methods of estimating phase velocity using arbitrarily shaped microtremor arrays, *Bull. Seismol. Soc. Am.*, **92(6)**, 2323-2332.

Ohsumi, T., M. Yoichi, and H. Fujitani (2016). Investigation of damage in and around Kathmandu valley related to the 2015 Gorkha, Nepal Earthquake and beyond, *Geotech. Geol. Eng*., **34(4)**, doi: 10.1007/s10706-016-0023-9.

Okamura, M., N. P. Bhandary, S. Mori, N. Marasini, and H. Hazarika (2015). Report on reconnaissance survey of damage in Kathmandu caused by the 2015 Gorkha Nepal earthquake, *Soils and Foundations,* **55(5)**, 1015-1029.

Okada, H. (2006). Theory of efficient array observations of microtremors with special reference to the SPAC method, *Exp. Geophysics*, **37**, 73-85.

Okada, H. (2003). The Microtremor Survey Method, translated by Koya Suto, Geophysical Monograph Series, no 12, *Soc. Exp. Geophysics*.

Pandey, M. R. (2000). Ground response of Kathmandu Valley using microtremor, *12th World Conf. Earthq. Eng.*, Auckland, New Zealand.

Pandey, MR., and P. Molnar (1988). "The distribution of Intensity of the Bihar-Nepal Earthquake 15 January 1934 and the bounds of the extent of the Rupture Zone", *J. Nepal Geol. Soc*., 5, 22-44.

Parajuli, R. R., and J. Kiyono (2015). Ground motion characteristics of the 2015 Gorkha earthquake, survey of damage to stone masonry structures and structural field tests, *Front. Built. Invinon*., https://doi.org/10.3389/fbuil.2015.00023.

Paudyal, Y. R., N. P. Bhandary, and R. Yatabe (2012). Seismic microzonation of densely populated area of Kathmandu Valley of Nepal using microtremor observations, *J. Earthq. Eng*., **16**, 1208-1229.

Paudyal, Y. R., R. Yatabe, N. P. Bhandary, and R. K. Dahal (2012a). A study of local amplifications effects of soil layers on ground motion in the Kathmandu Valley using microtremor analysis, *Earthq. Eng. Eng. Vib.*, **11(2)**, 257-286.

Paudyal, Y. R., R. Yatabe, N. P. Bhandary, and R. K. Dahal (2012b). Basement topography of the Kathmandu Basin using microtremor observation, *J. Asian Earth Sci.*, **62**, 627-637.

Piya, B. K. (2004). Generation of a geological database for the liquefaction hazard assessment in Kathmandu valley, M. Sc. Thesis, International Institute for Geo-information science and Earth Observation, Enschede, the Netherlands.

Poovarodom, N., D. Chamlagain, A. Jirasakjamroonsri, and P. Warnitchal (2017). Site characteristics of Kathmandu valley form array microtremor observations, *Earthquake Spectra*, **33**, 85-93.

Rajaure, S., D. Asimaki, E. M. Thompson, S. Hough, S. Martin, J. P. Ampuero, M. R. Dhital, A. Inbal, N. Takai, M. Shigefuji, S. M. Bijukchhen, M. Ichiyanagi, T. Sasatani, and L. Paudel (2017). Characterizing the Kathmandu Valley response through strong motion recordings of the 2015 Gorkha earthquake sequence, *Tectonophysics*, http://dx.doi.org/10.1016/j.tecto.2016.09.030.

Rana, Maj. Gen. Braham Sumsher (1935). Nepal ko Bhukampa (The great earthquake of Nepal), Second ed., *Jorganesh press,* 1-250 (in Nepali).

Ried, HF. (1910). The California earthquake of April 18, 1906. *Report of the state Earthquake Investigation Commission,* Vol II, The Mechanics of the Earthquake, Carnegie Institute of Washington.

Sanchez-Sesma, F. J., and C. B. Crouse (2015). Effects of site geology on seismic ground motion, early history, *Earthq. Eng. Struct. Dyn*., **44**, 1099-1113.

Sanchez-Sesma, F. J., M. Rodriguez, U. Iturranan-Viveros, F. Luzon, M. Campillo, L. Margerin, A. Garcia-Jerez, M. Suarez, M. A. Santoyo, and A. Rodriguez-Catellanos (2011). A theory for microtremor H/V spectral ratio, application for a layered medium, *Geophys. J. Int*., **186**, 221-225.

Sakai, H., R. Fujii, and R. Kuwahara (2002). Changes in the depositional system of the Paleo-Kathmandu Lake caused by the uplift of the Nepal Lesser Himalayas, *J. Asian Earth Sci.*, **20(3)**, 267-276.

Sekiya, S., and F. Omori (1892). Comparisons of earthquake measurements made in a pit and on the surface ground, Transactions of the *Seismol. Soc. Japan*, **16**, 19-45.

Seed, HB., RV. Whitman, H. Dezfulian, R. Dobry, and IM. Idress (1972). Soil conditions and building damage in 1967 Caracas earthquake, *Journal of Soil Mechanics and Foundations Division*, ASCE, **98**, 787-806.

Shakya, M., and C. K. Kawan (2016). Reconnaissance based damage survey of buildings in Kathmandu valley: An aftermath of 7.8 M_W 25 April Gorkha (Nepal) earthquake, *Eng. Failure Analysis*, **59**, 161-184.

Shiraishi, H., T. Matsuoka, and H. Asanuma (2006). Direct estimation of the Rayleigh wave phase velocity in microtremor, *Geophys. Res. Lett*., **33**, L18307.

Stöcklin, J., and K. D. Bhattarai (1981). Geological map of Kathmandu area and central Mahabharat Range (1:250.000); Department of Mines and Geology, His Majesty's Government of Nepal.

Takai, N., M. Shigefuji, S. Rajaure, S. M. Bijukchhen, S. Ichiyanagi, M. R. Dhital, and T. Sasatani (2016). Strong Ground Motion in the Kathmandu valley during the 2015 Gorkha, Nepal, Earthquake, *Earth Planets Space*, **68(10)**, doi: 10.1186/s40623-016-0383-7.

USGS (2015b). United States Geological Survey, Net QuakesStation KATNP_NQ_01, 25 April 2015, http://earthquake.usgs.gov/monitoring/netquakes/station/KATNP_NQ_01/20150425061138.

USGS (2011). United States Geological Survey, http://earthquake.usgs.gov.

Williams, S., B. Gosh, S. Wilkinson, C. Fenton, P. Burton, M. Whitworth, S. Dalta, G. Franco, A. Trieu, M. Dejong, V. Novellis, T. White, and T. Lloyd (2016). Site Amplification in the Kathmandu Valley during the 2015 M 7.6 Gorkha, Nepal earthquake, *Bull. Earthq. Eng.*, **14(12)**, 3301-3315.

Yamanaka, H. (2004). Application of the heuristic search methods to phase velocity inversion in microtremor array observation, *Proc. of the 13th World Conf. Earthq. Eng.*, Paper 1161.

Yamada, M., T. Hayashida, J. Mori, and W. D. Mooney (2016). Building damage survey and microtremor measurements for the source region of the 2015 Gorkha, Nepal earthquake, *Earth Planets Space*, **68**, 117.

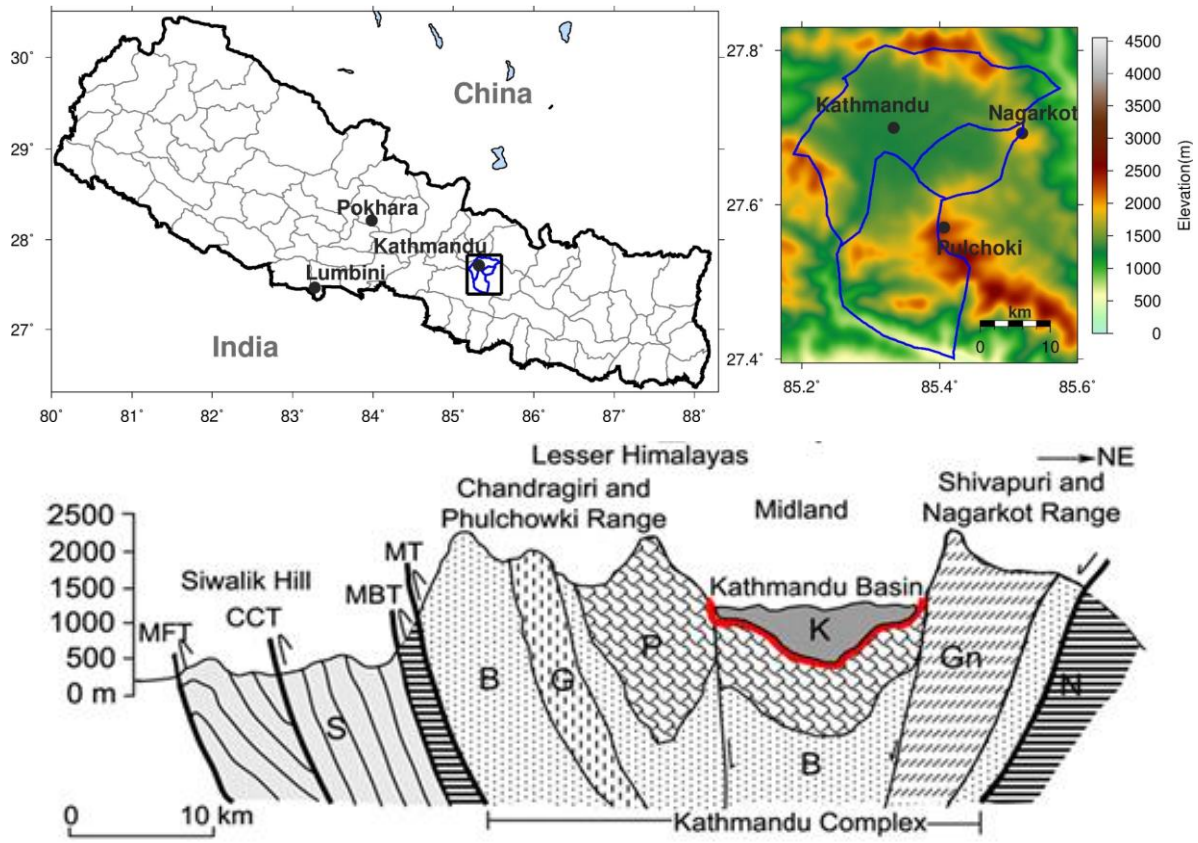

Figure 1.1 A simplified geological cross-section through central Nepal (after Stöcklin and Bhattarai, 1981 and Sakai *et al*., 2002). S: Siwalik Group, B: Bhimphedi Group, P: Phulchauki Group, N: Nawakot Complex, G: Granite, Gn: Gneiss Complex, K: Kathmandu Complex, MFT: Main Fontal Thrust, CCT: Central Churia Thrust, MBT: Main Boundary Thrust, MT: Mahabharat Thrust. The geological cross-section can be plotted in the location map of the Kathmandu valley (upper left) by rotating counter clock wise about 45 degree in reference with the geographical map of the Kathmandu valley (upper right).

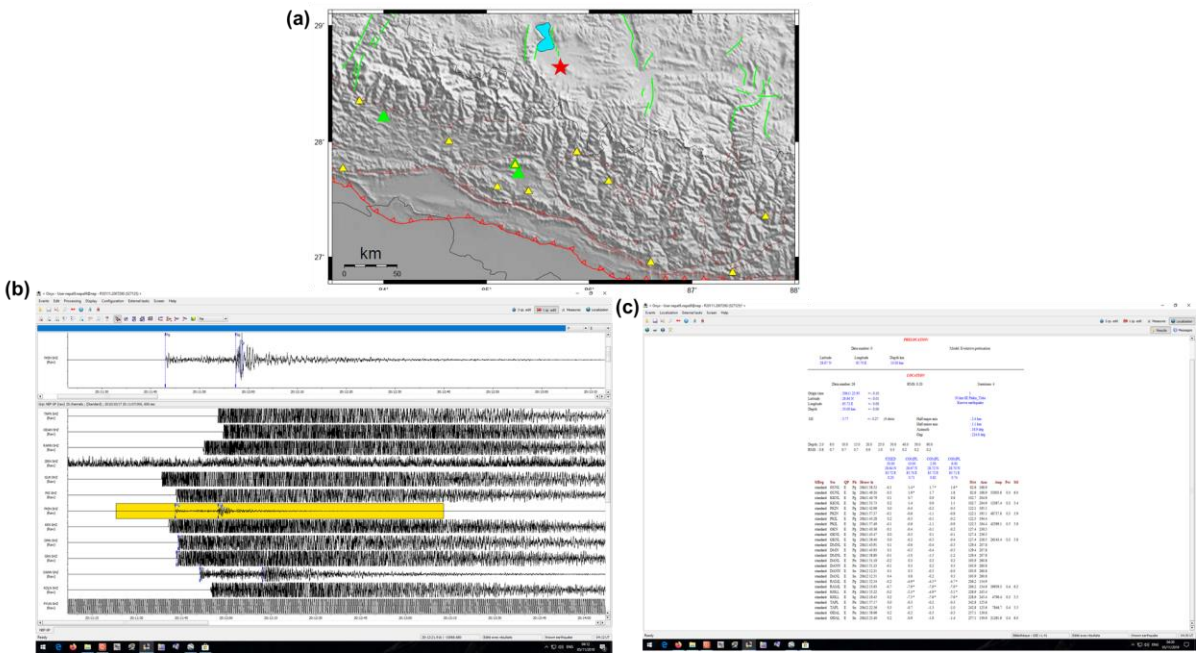

Figure 1.2 (a) Green triangles indicates the location map of accelerometers DMG and KKA (center), and PKR (west) in and outside the Kathmandu valley. Red star denotes the epicenter of the 2010 October 17 (M_L 5.7) Xizang earthquake occurred in the northern Tibet region. (b) Saturated seismograms recorded by the NSC seismic network. (c) Routine data processing and earthquake parameter determination by the existing seismic network.

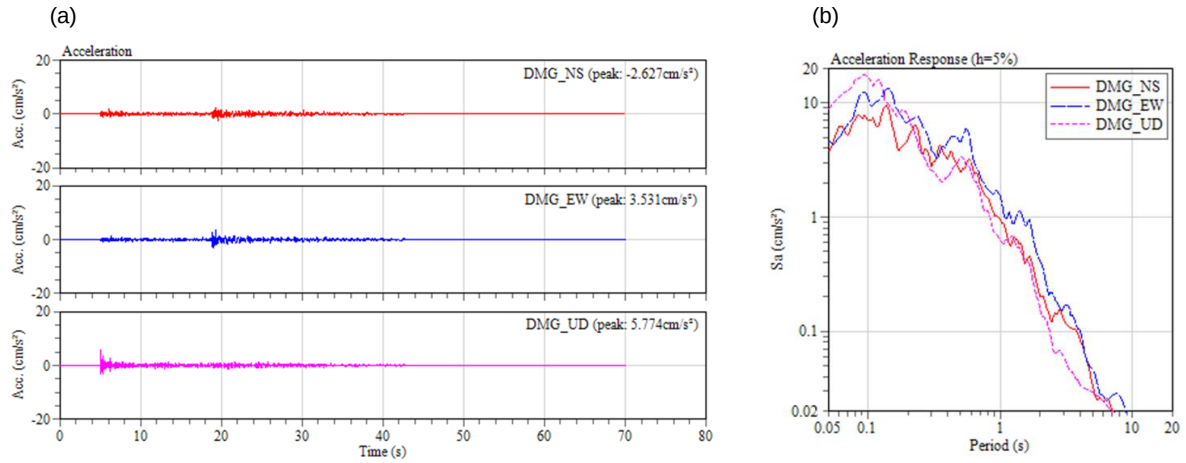

Figure 1.3 (a) Acceleration waveform of the 2010 October 17 (M_L 5.7) Xizang, Tibet earthquake recorded in the central part of the Kathmandu valley (DMG). (b) Acceleration response spectra. Note that epicenter of this earthquake was about 110 km north of the Kathmandu valley and recorded by both the seismic and accelerometric networks. The records are analyzed and plotted using the ViewWave (Kashima, 2009).

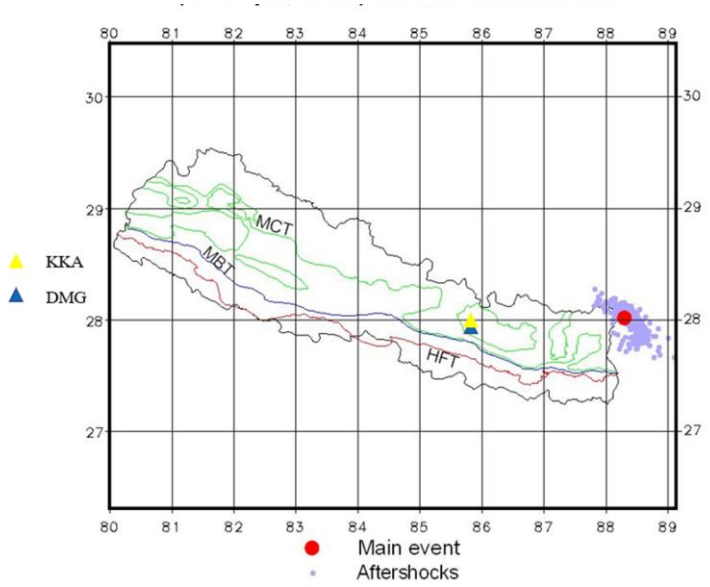

Figure 1.4 Epicenter (red close circle) of the mainshock of 2011 September 18 (M_L 6.8) Taplejung-Sikkim earthquake. The purple dot denotes their early aftershocks. The Main Central Thrust (MCT), Main Boundary Thrust (MBT), and Himalayan Frontal Thrust (HFT) denote the east-west trending thrust faults from north to south (NSC, 2011).

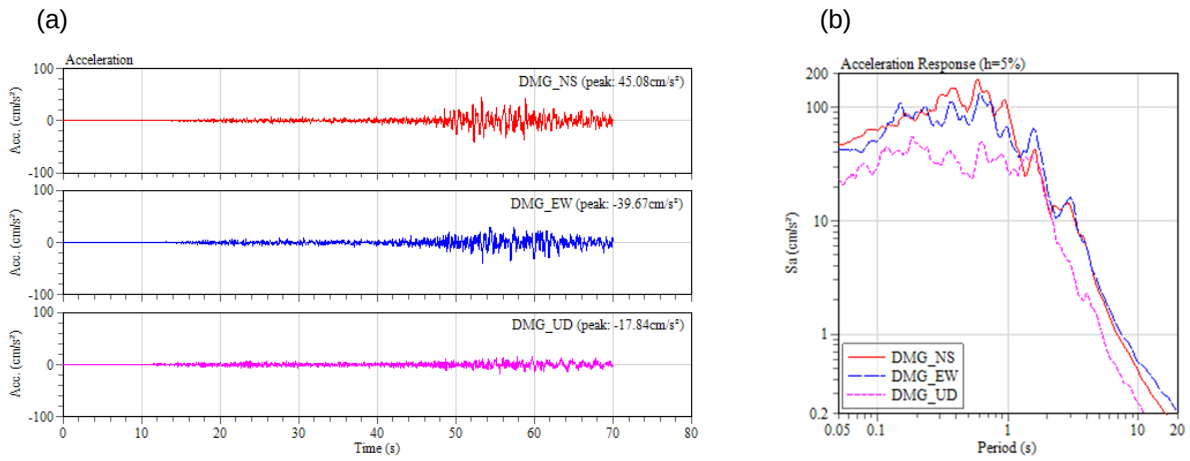

Figure 1.5 (a) Acceleration waveform of the 2011 September 18 (M_L 6.8) Taplejung-Sikkim earthquake recorded in the central part of the Kathmandu valley at DMG. (b) Its acceleration response spectra. The records are analyzed and plotted using the ViewWave (Kashima, 2009). Note that the epicenter of this earthquake was about 300 km east of the Kathmandu valley.

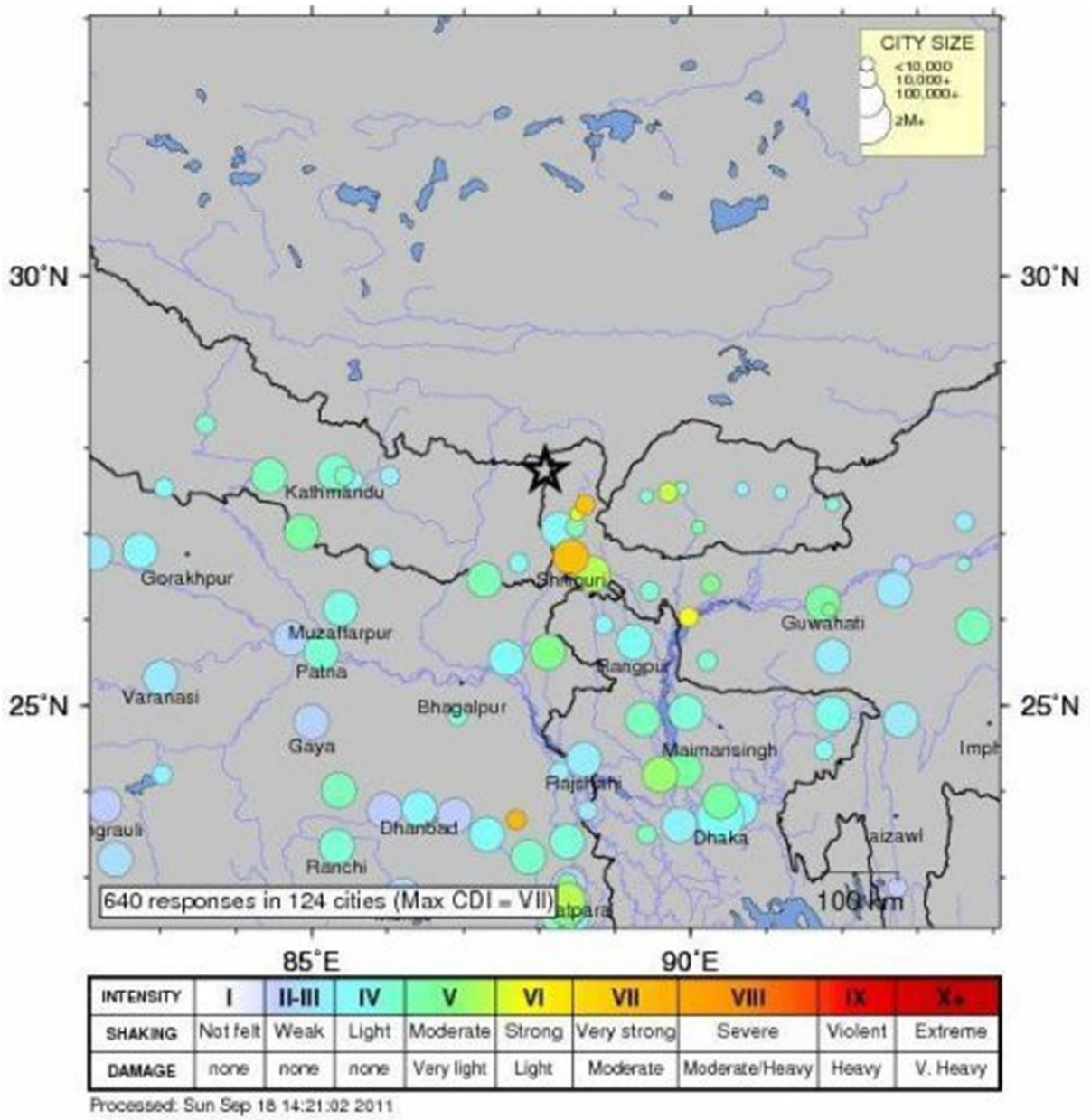

Figure 1.6 Intensity map of the 2011, Taplejung-Sikkim earthquake (USGS, 2011)**.**

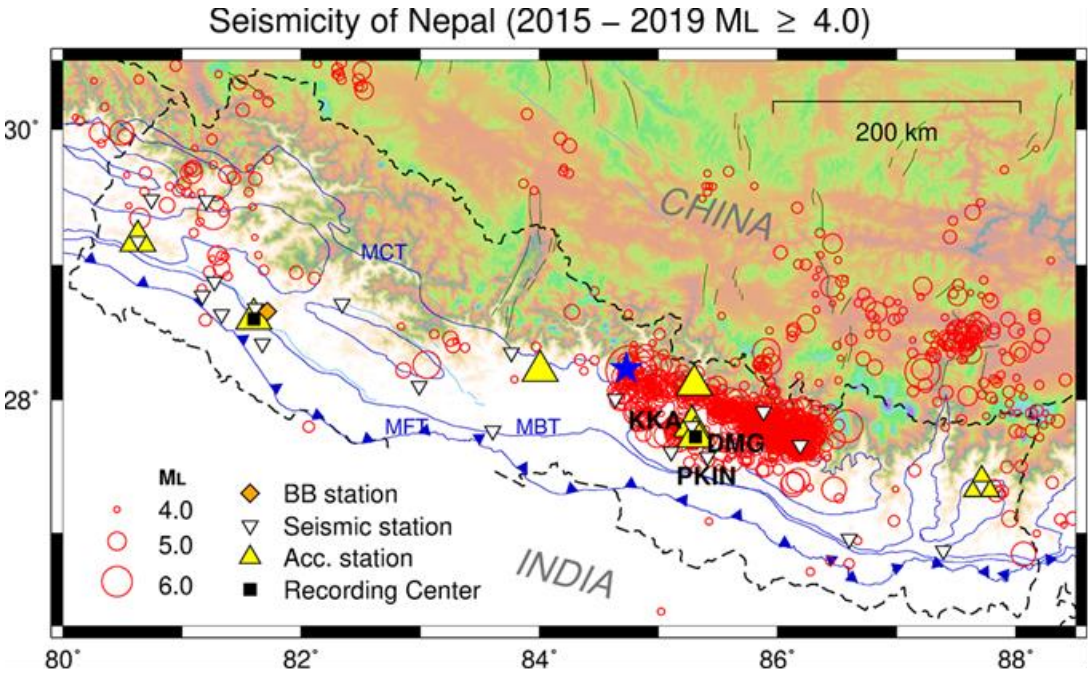

Figure 1.7 The national seismic network of Nepal (white open triangles) in the background seismicity (2015-2019, $M_L \geq 4.0$). Yellow triangles denote the accelerometric stations, black squares indicate the earthquake recording centers, blue star denotes the epicenter of the Gorkha earthquake, and red circles towards the east and north denote its aftershocks.

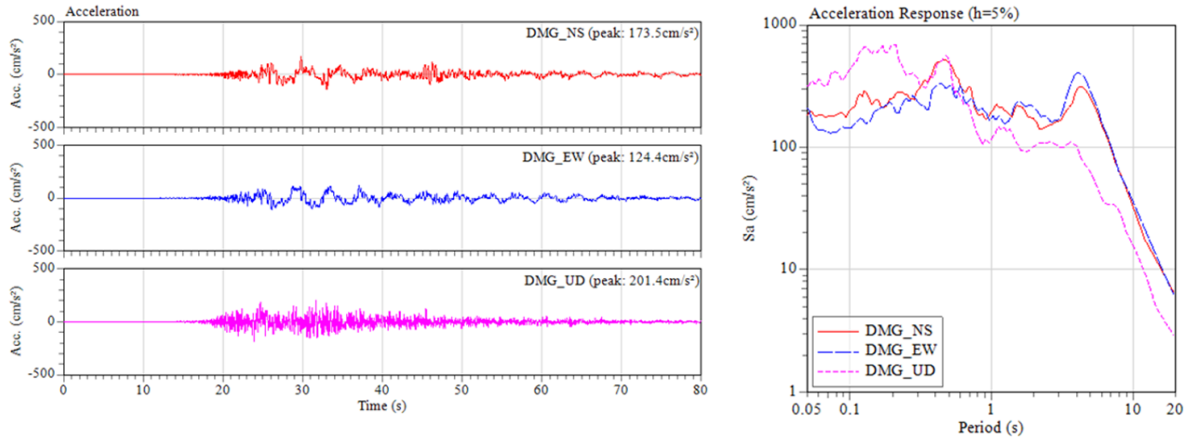

Figure 1.8 Acceleration waveform of the Gorkha earthquake recorded in the premises of DMG in the central part of the Kathmandu valley (left) and its acceleration response spectra (right).

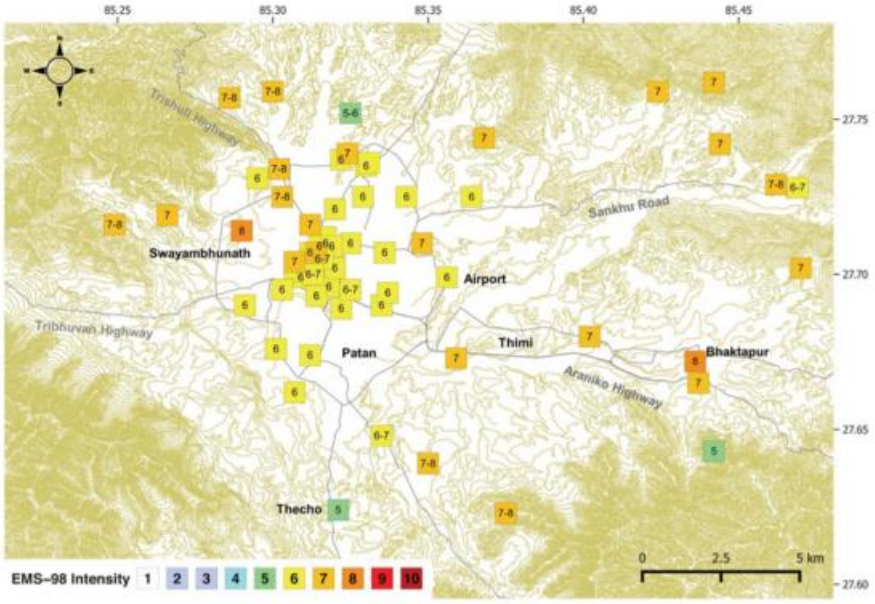

Figure 1.9 Intensity distribution of the Gorkha earthquake in and around the Kathmandu valley (Martin *et al*., 2015).

Figure 1.10 (a) Residuals of the sixty-meter-high 9-story historical Bhimsen tower (Dharahara) in the central part of the Kathmandu valley after the Gorkha earthquake (Hashash *et al*., 2015).

Figure 1.10 (b) Structural and non-structural damage in the Park View Horizon apartment building at Dhapasi, northern part of the Kathmandu valley (Hashash *et al*., 2015).

Figure 1.10 (c) Soft-story collapse of a 6-story building in Balaju near the Gongabu bus terminal (new bus park) one of the heavily damaged areas in the Kathmandu valley killed over 20 people in the neighbourhood (Hashash *et al*., 2015).

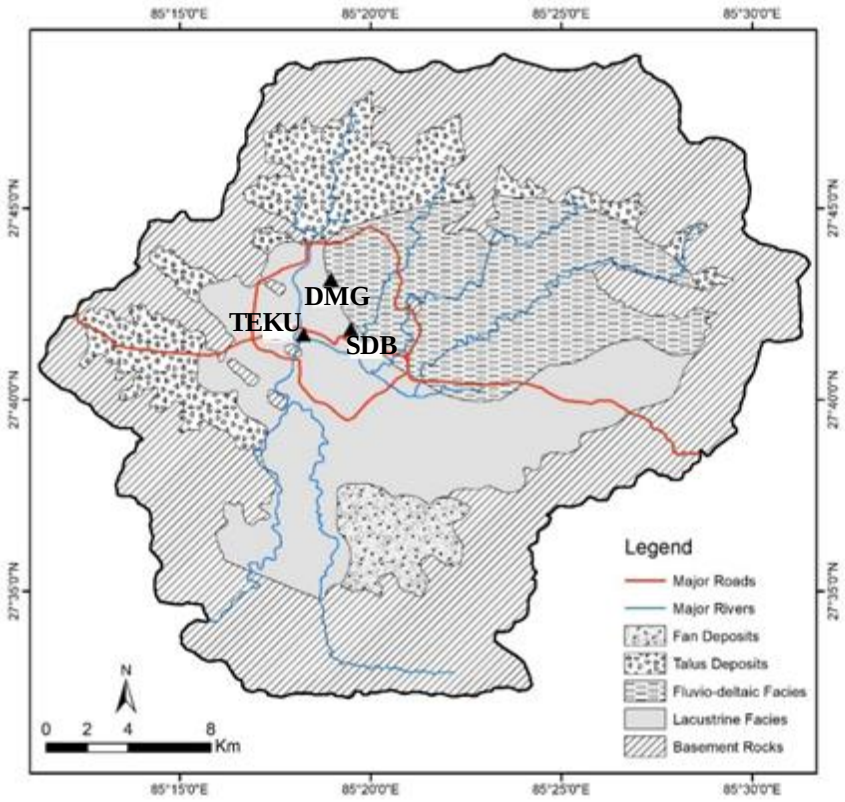

Figure 1.11 Long-peroid microtremor survey locations in the central part of the Kathmandu valley in the background of geological map of the Kathmandu valley. The black triangles SDB, DMG, and TEKU represent the sites 1, 2, and 3 respectively (observed sites are added after Fujii and Sakai, 2002 and Paudyal *et al*., 2012).

Chapter 2

Seismic observation network in Nepal for site effect studies

2.1 Introduction

National Earthquake Monitoring and Research Center under the Department of Mines and Geology (DMG) is the only one responsible government authority to monitor earthquake and conduct earthquake-related research in Nepal. Instrumental recording had begun monitoring earthquakes since 1978 from a network of short-period stations operated by the National Seismological Centre (NSC) under DMG, the government of Nepal. The international technical collaboration was first established with Département Analyse et Surveillance de l'Environnement (DASE), the government of France. Currently, this network is composed of 17 vertical short-period velocimetric stations, 4 broad-band stations, and one 3-component long-period and short-period stations with data acquisition and processing facilities at both the centers. The one is the NSC located in the Kathmandu valley, and the other is the Seismological Centre Surkhet (RSC) located in the Birendranagar municipality of western Nepal (Figure 2.1). The seismic network allows perceving and locating earthquakes with magnitudes M_L greater than 2.2 within Nepal (Pandey *et al*., 1999). Furthermore, it ensures the trigger of a seismic alert for every seismic event above M_L 4.0 within the country and above magnitude 5.5 worldwide. Only the local and regional earthquake informations are disseminated as soon as possible to the public through the responsible authorities. However, the dynamic range of the velocimetric stations operated by NSC/RSC for the routine processing and scaling of large earthquakes is not adequate to cover the whole range of velocities from very small to large earthquakes respectively at long and short distances. Therefore, most of the stations at short distances from the large earthquakes suffer from over-saturation and a proper ground velocity measure or ground acceleration conversion cannot be performed. As a result, Nepal attenuation law lacks some strong motion records at short distances and does not work as a necessary input for seismic hazard assessment studies.

Some solutions may help to overcome that limitation. One of them is the use of attenuation laws calibrated from strong motion data acquired in similar contexts (e.g. Singh *et al*., 1996; Sharma, 1998; Kumar *et al*., 1997; Pandey *et al*., 2002; Nath *et al*., 2008). However, the scarcity of strong motion available in the Himalaya, as well as the large uncertainity within these data delight for the installation of some strong-motion stations in Nepal.

In spite of deducting at short distances attenuation laws limited by the weak motion database only, NSC/DMG decided to acquire a strong-motion database with the installation of three accelerometric stations since 2009. The beginning installation was DMG (sediment) and KKA (rock) in the vicinity of the Kathmandu valley whereas PKR (sediment) at a distance of about 200 km west of the Kathmandu valley.

In addition to the existing seismic, accelerometric, and cGPS network, NSC/DMG has extended its potentiality in the field of earthquake monitoring and research after the Gorkha earthquake. Some of the newly established existing international collaborations are Japan International Cooperation Agency (JICA), China Earthquake Administration (CEA), and Regional Integrated Multi-Hazard Early Warning System in Asia and Africa (RIMES) based on Thailand. However, besides the earthquake monitoring by installing a network of 8 broadband seismometers/accelerometers, 10 cGPS in the central and western Nepal in collaboration with JICA, strong ground motion monitoring by installing 10 accelerometers and subsurface explorations by microtremor, gravity, and seismic reflection surveys are focused in the vicinity of the Kathmandu valley only. Figure 2.2a designates the most recent seismic network of Nepal under the data integration procedure. Blue hexagons represent seismic stations established in collaboration with Japan, black triangles denote the pre-existing seismic stations in collaboration with France, red stars represent seismic station installed in collaboration with China, and yellow triangles are seismic stations installed in collaboration with RIMES, based on Thailand. However, red circle denotes the broad band seismic station installed in the Ev-K2-CNR pyramid international laboratory-observatory (Mount-Everest) on the way to Mount Everest region by Italian research Institutions. DMG do not have any collaboration with it. Figure 2.2b shows the accelerometers under operation before the Gorkha earthquake in and around the Kathmandu valley. Figure 2.2c shows the seismicity induced in and around the Kathmandu valley followed by the aftershocks of the Gorkha earthquake and the blue triangles are the accelerometers under operation after the Gorkha earthquake in and around the Kathmandu valley.

The purpose of Chapter 2 is to review the history of earthquake monitoring in Nepal, differentiate the existing seismic network, newly established accelerometric network, and site effect studies using strong motion instruments installed until 2011 in the Kathmandu, Kakani, and Pokhara regions. Kathmandu (DMG) and Kakani (KKA) are placed in the proximity of the Kathmandu valley whereas Pokhara (PKR) is located in the Pokhara valley at a distance of about 200 km west of the Kathmandu valley. We then describe some specific softwares that have been developed to allow NSC to quickly analyze the accelerograms and translate them into seismic aggressiveness parameters. We finally describe some preliminary results of site effects that have been observed from the interpretation of early records (e.g., Xizang, China earthquake M_L 5.7).

This study focuses on site effect studies and damage analyses based on the records mainly at DMG and KKA in the vicinity of Kathmandu. The damage analysis due to this earthquake is described in Chapter 7.

2.2 Instrument setting

Three strong-motion instruments have been installed in Kathmandu (DMG), Kakani (KKA), and Pokhara (PKR) in 2009. The station is composed of 3-components accelerometric sensor (GeoSIG AC 23) connected to a 24-bit digitizer (GeoSIG GSR 24), whose sampling is set at 200 Hz. The dynamic range of the instruments is larger than 125 dB within from 0.1 to 35 Hz band. The full scale is set at ± 1 G. The stations are not currently telemetered. Only signals with acceleration peaks significantly larger than the background noise or larger than a fixed threshold are stored on a local memory card.

Because the variations of the noise level at DMG and PKR are large due to a very high level of social noises, a STA/LTA (short time average/long time average) trigger mode has been chosen and the trigger level is set at 20dB. The advantage of this trigger mode over an absolute threshold trigger method is that it allows recording events with relatively low acceleration peaks and avoiding the overload of the memory card due to an increase of background noise. The background noise level being lower at KKA, an absolute threshold is set at 0.001 G (0.1% of the full scale). This threshold is theoretically sufficient for the accelerometers to be triggered by M_L 5, M_L 4, and M_L 3 events within about 100 km, 30 km, and 10 km, respectively. This is according to an attenuation relationship calibrated in France

using a similar M_L as the one calculated by NSC (Marin *et al*., 2004). The threshold also corresponds to the triggers by *M*4, *M*3, and *M*2 events within about 100 km, 55 km, and 30 km, respectively according to one of the most recent Garwhal ground motion prediction equations expressed as a function of the M_W (Nath *et al*., 2005, 2008).

Background noise is not the only difference between the stations, since one of the stations (KKA) is installed on rock of weathered granite, while the DMG and PKR stations are installed in the Kathmandu and Pokhara sedimentary basins. The pre- and post-events recording time windows set for all instruments from 5 to 10 s up to September 2010 were not sufficient and have been changed from 10 to 40 s.

2.3 Data analysis

Once the accelerograms are collected following an earthquake, the DIAMANT software (Hernandez *et al*., 2011) is used to rapidly assess the aggressiveness of the seismic ground motion. This software computes several parameters of aggressiveness and produces graphical representations used for risk applications. The aggressiveness parameters computed, which are the most commonly used in the engineering domain at present, such as peak amplitudes, time duration, spectral amplitudes, energetic values and so on. These parameters are described hereafter but the output of the software will be shown in the next section.

The peak amplitudes of the ground motion are the peak ground acceleration (PGA), the peak ground velocity (PGV), and the peak ground displacement (PGD). The PGA is a primary measure of earthquake aggressiveness; however, used alone, is not reliable for damage estimation. The examination of recorded ground motion shows that these with large PGA's did not always produce appreciable structural damage, while some earthquakes producing rather small PGA can produce an excessive degree of destruction (Cosenza and Manfredi, 2000). The PGV appears to be a better representative measure of earthquake aggressiveness as it is linked with the energy (e.g., Housner *et al*., 1982; Betbeder-Matibet, 2003).

All the parameters estimated from time series rely upon the duration. The duration is a parameter difficult to predict near the seismic source. However, experience from various earthquakes indicate that the duration of ground motion has a major impact on the extent of structural damage. Records with large acceleration and spectral values can produce slight

damage if the duration is short; however, some records with moderate acceleration and long duration can be very destructive (Cosenza and Manfredi, 2000). It is difficult to describe strong motion duration in terms of main energy content. In this regard, Trifunac and Brady (1975) have defined the Trifunac duration as the time in the Husid diagram, which express the main part of the energy in the seismic signal that has elapsed between 5% and 95%.

DIAMANT defines two parameters based on energy of time series. These parameters determined from time series are inherently much more relevant than peak amplitudes or duration to quantify the aggressiveness of a seismic signal. The Arias intensity (AI) is the integral of the square of the ground acceleration normalized by π divided by twice the gravity value at the observation site (Arias, 1970). Often measured is the cumulative absolute velocity (CAV) defined as the integral of the time series of the absolute acceleration. AI and CAV are useful in predicting the possible onset of structural damage and liquefaction of saturated soils (Kayen and Mitchell, 1997).

Several damages estimated from the seismic signals are based on parameters related to the response of a linear elastic single-degree-of-freedom system. Spectra of the Acceleration, velocity, and displacement response represent the responses of the elastic single-degree-of-freedom system. The fundamental frequency and the damping factor are the only parameters required to dynamically characterize the system. It can be assumed that Spectral shape and amplitudes are fundamental measures of seismic potential. The maximum pseudo-acceleration for an earthquake is a measure of maximum demand of strength. It is proportional to the structure's maximum seismic force. The maximum pseudo-velocity is a measure of seismic motion's kinetic energy. The maximum displacement of the response spectrum is a measure of the maximum displacement demand. It controls the structural damage caused by lateral displacement of the multi-story buildings (Cosenza and Manfredi, 2000).

The Acceleration Displacement Response Spectrum (ARDS) format can also be displayed by using the DIAMANT software in the spectral acceleration versus displacement domain. The implementation of the Capacity spectrum technique allows both the demand response spectra and the structural capacity (or pushover curves) to be plotted together (Freeman, 2004). A spectrum plotted in this way is known as the ADRS representation.

Finally, the intensity of the Housner spectrum (Housner, 1952) is also calculated. It is an integral part of the pseudo-velocity spectrum from 0.4 to 10 Hz (frequency range of interest in earthquake engineering) and can be viewed as an integral measure of the energy demand.

2.4 Results and discussion

During the first months of NSC more than 4000 accelerometric events were detected. Although most of them correspond to social noise events, some have been generated by earthquakes. The Kakani strong motion station (KKA) recorded 7 events with M_L within the range of 3.4 to 5.8 at epicentral distances of 25 to 105 km (Figure 2.3). This station is co-located with a short-period vertical component velocimetric seismograph (ZM 500) with low and high gain channels, insuring a wide dynamic range. The absolute threshold set at 0.001 G for the strong motion instrument guarantees a significant overlap between the accelerometric and low gain velocimetric components at the site (Figure 2.3).

As a first example of signal recorded at KKA, we focus on an event on 15 July 2010 with M_L 3.4. It was recorded at a very short distance (25 km) from the epicentre determined by NSC using the seismic network. Note that the time delay between the *P*- and *S*-wave arrivals is about 4 s, in accordance to the distance estimate (Figure 2.4). The mean horizontal PGA for this event is 0.853 cm/s^2, larger than 0.3 to 0.4 cm/s^2 predicted by the French attenuation law (Marin *et al*., 2004) but smaller than 3.6 to 4.6 cm/s^2, 9.7 to 11.4 cm/s^2 and 16.7 to 18.8 cm/s^2 estimated using respectively Nath *et al*.'s (2008), Nath *et al*.'s (2005) and Singh *et al*.'s (1996) ground motion prediction equations calibrated in other regions of the Himalayas. Note that these values M_W, m_b, and M_L have been estimated assuming that the laws can be extrapolated to such small magnitude events and are equal to each other

The theoretical PGV of 24 to 28 cm/s calculated using Singh *et al.*'s (1996) attenuation law also overestimates significantly the recorded value of 0.021 cm/s suggesting that either the assumptions taken into account here are not valid, and that the ground motion prediction equations calibrated in other regions of the Himalayas are not valid. Figures 2.4 and 2.5 also illustrate the output of the other aggressiveness parameters introduced in section 2.3. Note that most of the parameters calculated here are out of the range within which they have been calibrated or are usually used. In particular, because the PGD and displacement seismogram are not reliable enough because the signal is too weak.

Further examination of larger events recorded at more than one station is needed. Although the number of events recorded is still very small, some intriguing results appear. Overall horizontal to vertical component ratios of the strong motion records are systematically lower for the two stations within basins (DMG and PKR) than at KKA on the hard rocks (Figure 2.6). This characteristic might be due to sedimentary site effects at DMG and PKR. It may also be induced by a topographical effect at the KKA station, the instrument being installed on the top side of a ridge, at a place where waves refracted by the topography might constructively interfere with direct arrival (Bouchon, 1973). It may also be only coincidental given the very small number of events recorded at the basin station.

To go further into the understanding of that result, we look for events recorded at several stations. The 3 strong-motion instruments were triggered by an event on 17 October 2010. This earthquake of M_L 5.7 was felt in Kathmandu. Recorded at all the NSC velocimetric stations, it has been located on the south-eastern end of the Gyirong graben active fault system at epicentral distances to PKR, DMG, and KKA of 174, 110, and 103 km, respectively. The depth of the event appears uncertain. It is poorly constrained by the sole NSC stations because of the location of the event outside the seismic network, roughly constrained by depth phase (*pP*) that have been picked about 17 to 21 s after the *P*- at teleseismic distances, suggesting a depth of about 80 km.

The inspection of the signal at DMG shows that there are almost no *S*-waves but strong *P* in the vertical component, which is not the case at all at KKA, a few kilometers north-west (Figure 2.7). This could be due to basin effect. Hard rocks, gneisses and granites, with high seismic wave velocities and high density, underlie the Kathmandu valley and the KKA station. The Kathmandu valley is filled with soft sediments and rocks characterized also by lower seismic waves velocities and densities. This juxtaposition of the two geological media generates a strong impedance decrease. The incidence of the seismic ray is therefore, steeper than elsewhere as illustrated in (Figure 2.8). Further analysis of the site over reference spectral ratio put in evidence higher amplitudes at low frequencies for DMG (Figure 2.9). These characteristics suggest a basin effect; the energy present at high frequencies at the rock site could be redistributed and present at low frequencies within the valley. It seems that the characteristic resonance of the Kathmandu valley at DMG is of the order from 1 to 2 Hz, this is consistent with the depth and composition of the valley at this site.

For the moment, none of the interpretations proposed can be ascertained on the sole basis of the few data available. Several complementary records, including signals coming from various source-stations azimuth, distances, depths, and focal mechanisms will be needed to properly characterize some particular site effects and differentiate them from path or topographical effects.

2.5 Conclusions

The strong motion instruments that had installed at Kathmandu (DMG), Kakani (KKA), and Pokhara (PKR) complemented well the pre-existing seismic network. They first offer the benefit of a large dynamic range (±1 G full scale). The potentials of the instruments, with the low gain and then high gain velocimetric channels overlap very well. The low gain channel will perfectly complement the high gain channels when they get saturated. Accelerometers increase the dynamic range of the signal recorded by DMG up to about 100 m/s^2 and there is no gap between the velocimetric and accelerometric data.

These records could be used in order to constrain the ground motion prediction equation of Nepal. The short-period stations installed at the NSC network are single components whereas, the accelerometers are 3 components. The new records acquired at these stations will, therefore, help to work on the body waves' incidences, as well as may be used for the characterization of body wave arrival azimuth for location purposes. Also, the higher sampling rates will help better capture the peak ground acceleration, as well as better, characterize the potential response of the buildings and equipment, sensitive to high frequencies seismic waves. The site over reference spectral ratios of DMG with reference to KKA suggests the long-period amplification of the basin sediment in the lower frequency range below 4 Hz. However, a wide trough has been detected in the spectral ratio from 4 to 10 Hz. The instrument characteristics, as well as presented automatic signal analysis toolboxes specifically to meet the demand for quick signal analysis and seismic aggressiveness characterization. To complement the existing weak-motion data a strong-motion database is needed and will help to restrict the attenuation law for ground motion as well as to characterize the site effects in the Kathmandu valley (Bhattarai *et al.*, 2011; Rai (2011)).

2.6 References

Arias, A. (1970). A measure of earthquake intensity, In seismic design for nuclear power plants, Cambridge MA: *MIT press*, 438-468.

Betbeder-Matibet, J. (2003). Essai sur l'état de l'art et le sens des ordres de grandeur en génie parasismique, *Hermès Sciences Publications,* Vols. 1-3 (in French).

Bhattarai, M., U. Gautam, R. Pandey, L. Bollinger, B. Hernandez, and V. Boutin (2011). Capturing first records at the Nepal NSC accelerometric network, *J. Nepal Geol. Soc*., **43**, 15-22.

Bouchon, M. (1973). Effect of topography on surface motion, *Bull. Seismol. Soc. Am*., **63**, 615-632.

Cosenza, E., and G. Manfredi (2000). Damage indices and damage measures, *Prog. Struct. Eng. Mat*., **2 (1)**, 50-59.

Freeman, S. A. (2004). REVIEW OF THE DEVELOPMENT OF THE CAPACITY SPECTRUM MEHOD, ISET Journal of Earthquake Technology, **41**, 1-13.

Hernandez, B., L. Bollinger, and V. Boutin (2011). DIAMANT. Traitement des données accélérométriques et calcul d'indicateur de nocivité sismique. Guide d'utilisation. CEA/DIF/DASE/LDG/2011/DO, 1-34.

Housner, G. W., and P. C. Jennings (1982). Earthquake design criteria, *EERI Monograph Series* Berkeley, CA, Earthquake Engineering Research Institute.

Housner, G. W. (1952). Intensity of ground motion during strong earthquakes, *Technical Report, CaltechEERL*, 1952.EERL, 1952.001.

Kayen, R. E., and J. K. Mitchell (1997). Assessment of liquefaction potential during earthquakes by Arias intensity, *J. Geotec.Geoenv. Eng.*, 1162-1174.

Kumar (1997). Assessment of Liquefaction Potential During Earthquakes by rias Intensity, *J. Geotech. Geoenviron. Eng*, **123(12)**, 1162-1174.

Marin, S., J. P. Avouac, M. Nicolas, and A. Schlupp (2004). A probabilistic approach to seismic hazard in metropolitan France, *Bull. Seismol. Soc. Am*., **94(6)**, 2137-2163.

Nath, S. K., K. Shukla, and M. Vyas (2008). Seismic hazard scenario and attenuation model of the Garhwal Himalaya using near-field synthesis from weak motion seismometry, *J. Earth Syst. Sci*., **117**, 649-670.

Nath, S. K., M. Vyas, I. Pal, and P. Sen Gupta (2005). A seismic hazard scenario in the Sikkim Himalaya from seismotectonics, spectral amplification, source parameterization and spectral attenuation laws using strong motion seismometry, *J. Geophys. Res*., **110**, B01301, doi: 10.1029/2004/2004JB003199.

Pandey, M. R., G. R. Chitrakar, B. Kafle, S. N. Sapkota, S. Rajaure, and U. Gautam (2002). Seismic hazard map of Nepal, *Bull. Department of Mines and Geology*.

Pandey, M. R., R. P. Tandukar, J. -P. Avouac, J. Vergne, and T. Héritier (1999). Seismotectonics of the Nepal Himalayas from a local seismic network, *J. Asian Earth Sci*., **17**, 703-712.

Sharma, M. L. (1998). Attenuation relationship for estimation of peak ground horizontal acceleration using data from strong motion arrays in India, *Bull. Seismol. Soc. Am*., **88**, 1063-1069.

Singh, R. P., M. Ashutosh, and Y. J. J. Prasad (1996). Attenuation relations for strong seismic ground motion in the Himalayan Region, *Pure and Applied Geophysics*, **147 (1)**, 161-180.

Trifunac, M. D. and A. G. Brady (1975). On the correlation of seismic intensity scales with the peaks of recorded ground motion, *Bull. Seismol. Soc. Am*., **6**, 5139-5162.

Rai, S. (2011). "Abstract Volume of Sixth Nepal Geological Congress on Geology, Natural Resources, Infrastructures, Climate Change and Natural Disasters, 15-17 November 2010, Kathmandu, Nepal", *Nepal Geol. Soc*., **43**, 1-175 (Special issue).

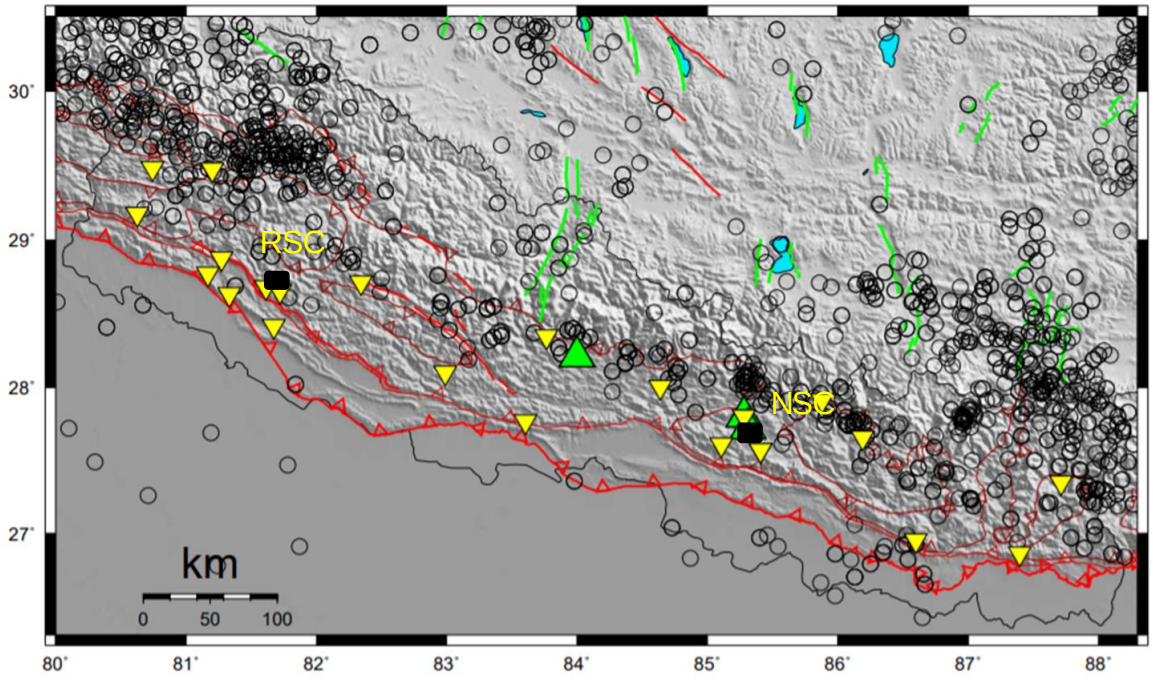

Figure 2.1 Seismicity recorded between 1995 and 2010 by National Seismological Centre, Department of Mines and Geology. Events with M_L greater than 4.0 are shown. These earthquakes correspond to events triggering the seismic alert. The yellow down triangles correspond to the short-period stations of the seismic network, the green up triangles correspond to the accelerometric stations installed in 2009. The black square in the west represents recording centre RSC and that in east represents NSC (Bhattarai *et al*., 2011).

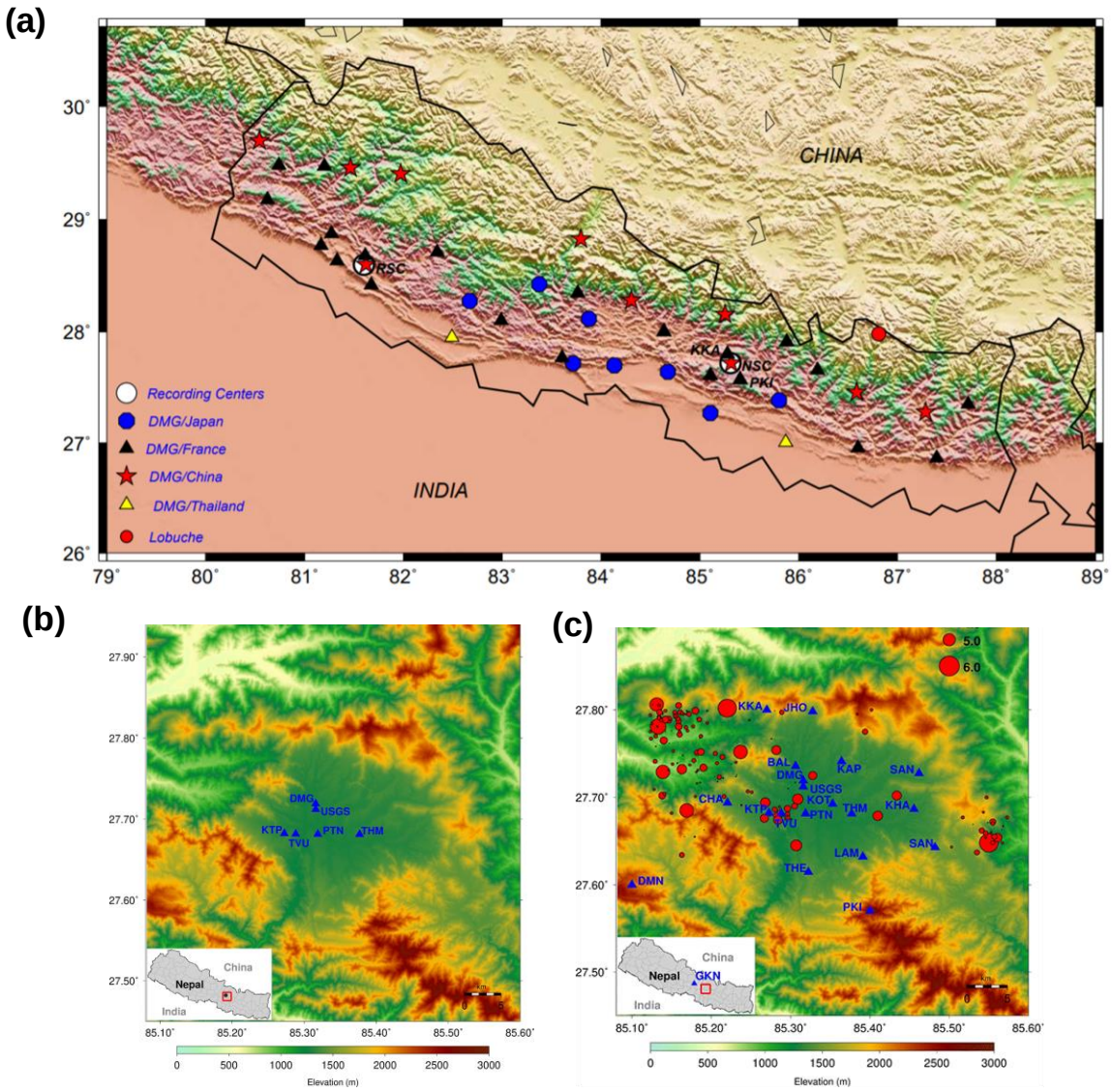
(a)
CHINA
INDIA
RSC
KKA
JNSC
PKI
Recording Centers
DMG/Japan
DMG/France
DMG/China
DMG/Thailand
Lobuche
30°
29°
28°
27°
26°
79°
80°
81°
82°
83°
84°
85°
86°
87°
88°
89°
(b)
DMG
USGS
KTP
PTN
THM
TVU
China
Nepal
India
27.90°
27.80°
27.70°
27.60°
27.50°
85.10°
85.20°
85.30°
85.40°
85.50°
85.60°
0
500
1000
1500
2000
2500
3000
Elevation (m)
(c)
5.0
6.0
KKA
JHO
BAL
DMG
KAP
SAN
USGS
CHA
KOT
KTP
TVU
PTN
THM
KHA
LAM
THE
DMN
PKI
GKN
China
Nepal
India
27.80°
27.70°
27.60°
27.50°
85.10°
85.20°
85.30°
85.40°
85.50°
85.60°
0
500
1000
1500
2000
2500
3000
Elevation (m)

Figure 2.2 (a) The most recent seismic network of Nepal under data integration procedure. Blue hexagon denotes seismic stations installed in collaboration with JICA, Japan, black triangle represents pre-existing seismic stations in collaboration with DASE, France, red stars are stations installed in collaboration with CEA, China, yellow triangle are stations installed in collaboration with RIMES based on Thailand, and the red circle indicates the broad-band seismic station installed in the Ev-K2-CNR pyramid international laboratory-observatory (Mount-Everest) by Italian researchers which is not owned by DMG. The closed white circles indicate the recording centers at NSC and RSC. (b) Accelerometers under operation in the Kathmandu valley during the Gorkha earthquake. (c) Accelerometers under operation in and around the Kathmandu valley established after the Gorkha earthquake in the background of aftershocks. KKA, PKI, and KTP are the stations established on rock site.

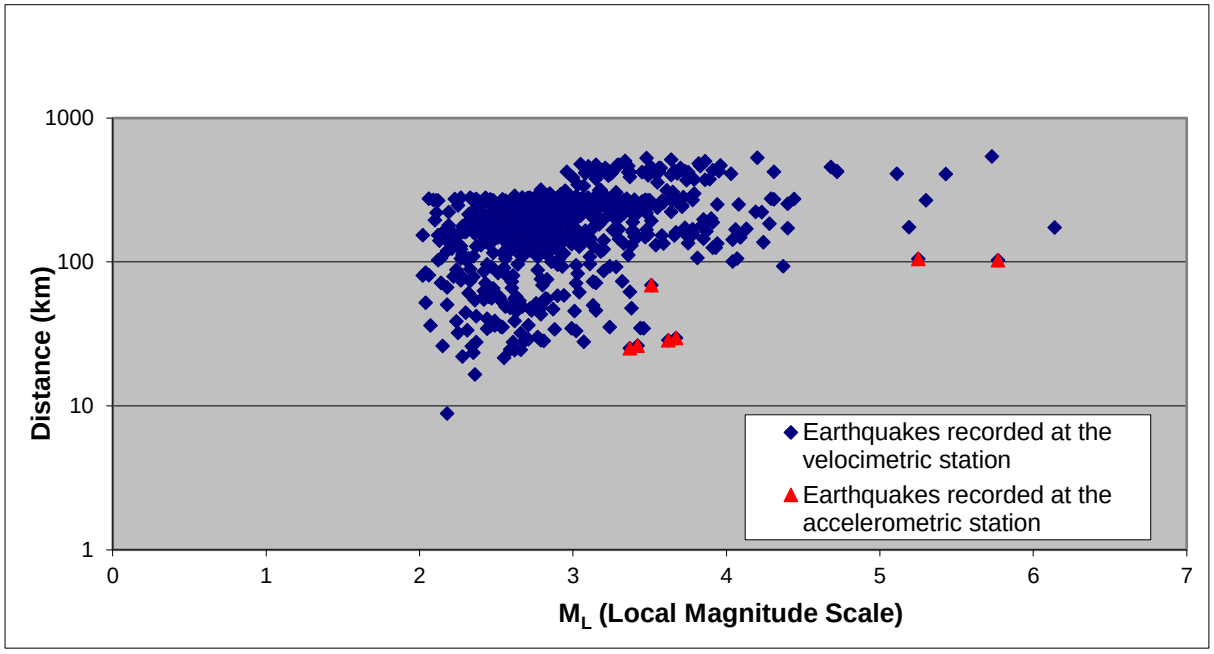

Figure 2.3 Earthquakes recorded by the KKA velocimetric station between 1 January to 18 October, 2010 as a function of their magnitudes and distances to the station. The blue diamond indicates the events that triggered in the accelerometric station whereas the red triangles are the earthquake records collocated in both stations (modified from Bhattarai *et al.*, 2011).

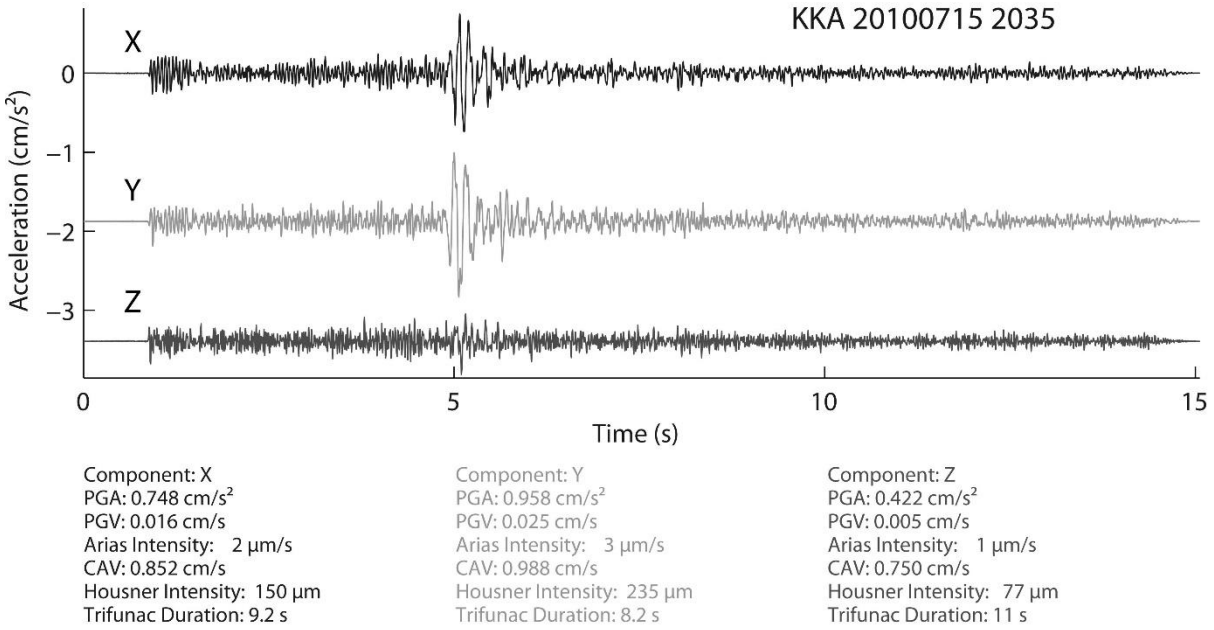

Figure 2.4 An example of accelerometric signal recorded at KKA station at 20:35 on July 15, 2010 which was from an earthquake of M_L 3.4 recorded at 25 km away (Bhattarai *et al*., 2011).

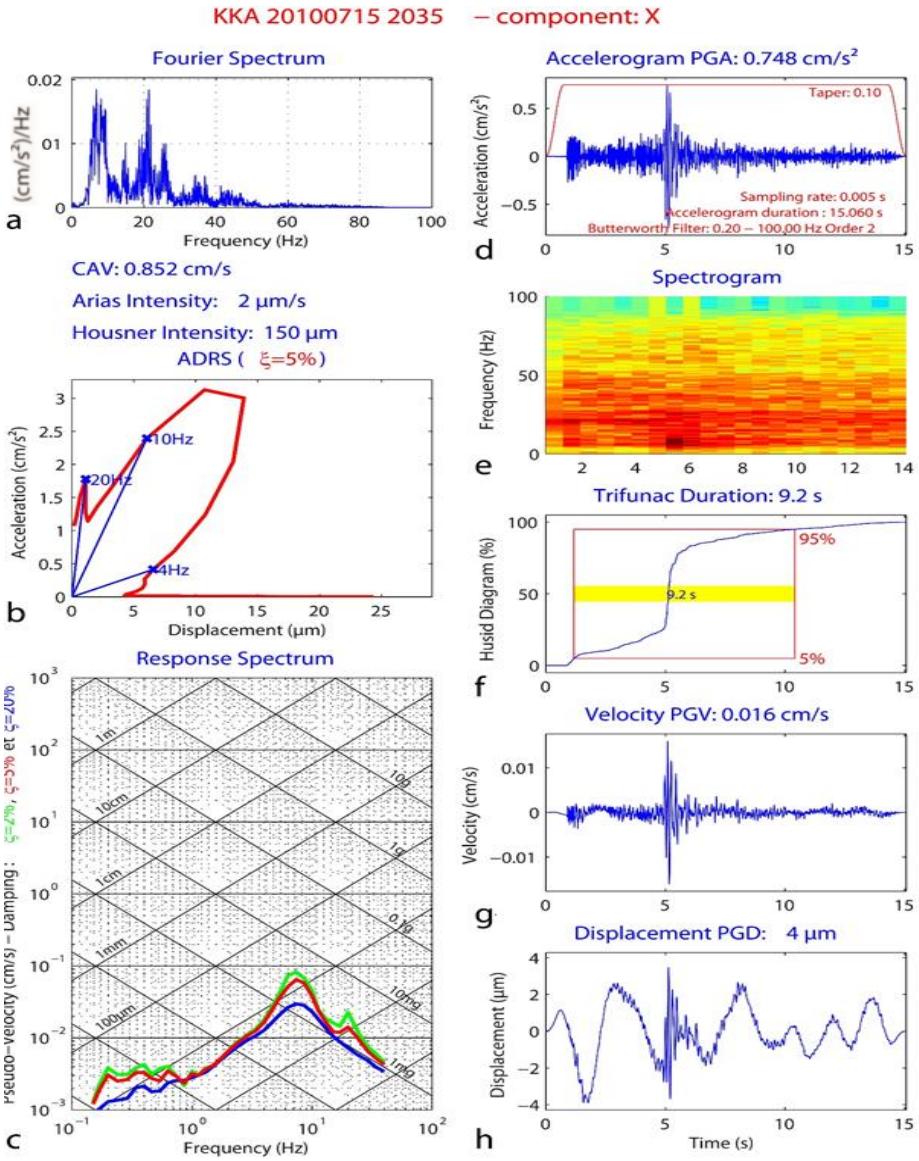

Figure 2.5 An example of accelerometric signal analysis executed using Diamant software (Hernandez *et al*., 2011). Here, the seismic motion is induced by an earthquake of (M_L 3.4) recorded at KKA (Kakani) station 25 km away at 20:35 on 15 July 2010. (a) Fourier amplitude spectra. (b) Acceleration displacement response spectra representation (c) Response spectra on a trilogy diagram for 3 values of damping (d) Accelerogram (e) Spectrogram between 0 and half of the sampling frequency (100 Hz) (f). Husid diagram, (g) Velocity seismogram (h) Displacement seismogram (Bhattarai *et al*., 2011).

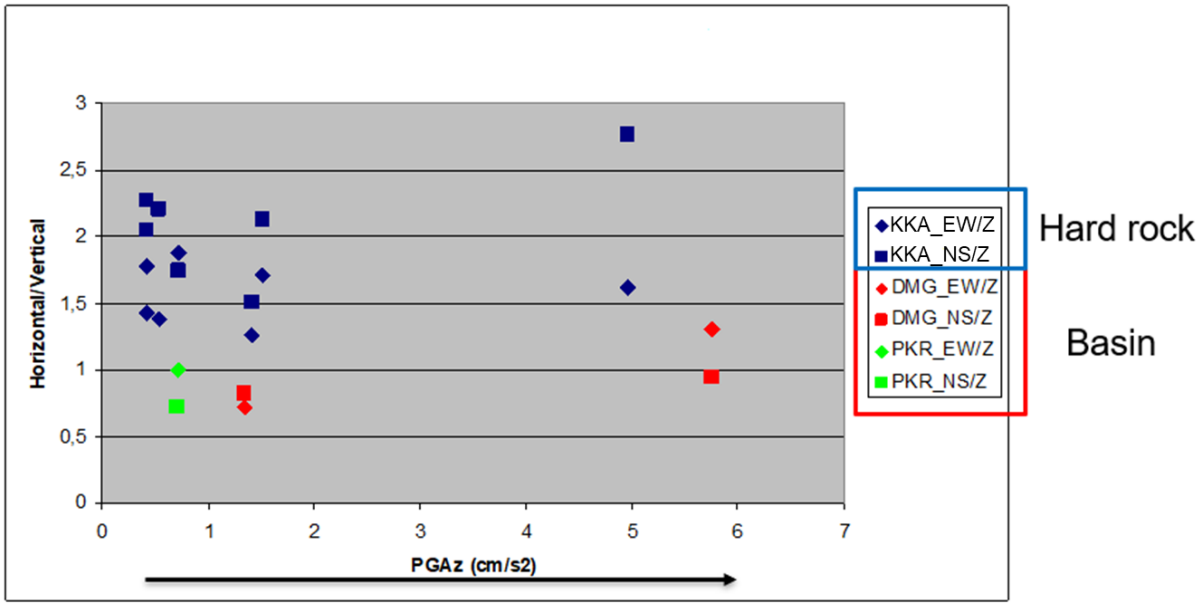

Figure 2.6 Horizontal over vertical component ratio as a function of the PGA (cm/s^2) for all stations used. Note that both Kathmandu (DMG) and Pokhara (PKR) are sediment sites, while Kakani (KKA) is a rock site (Bhattarai *et al*., 2011).

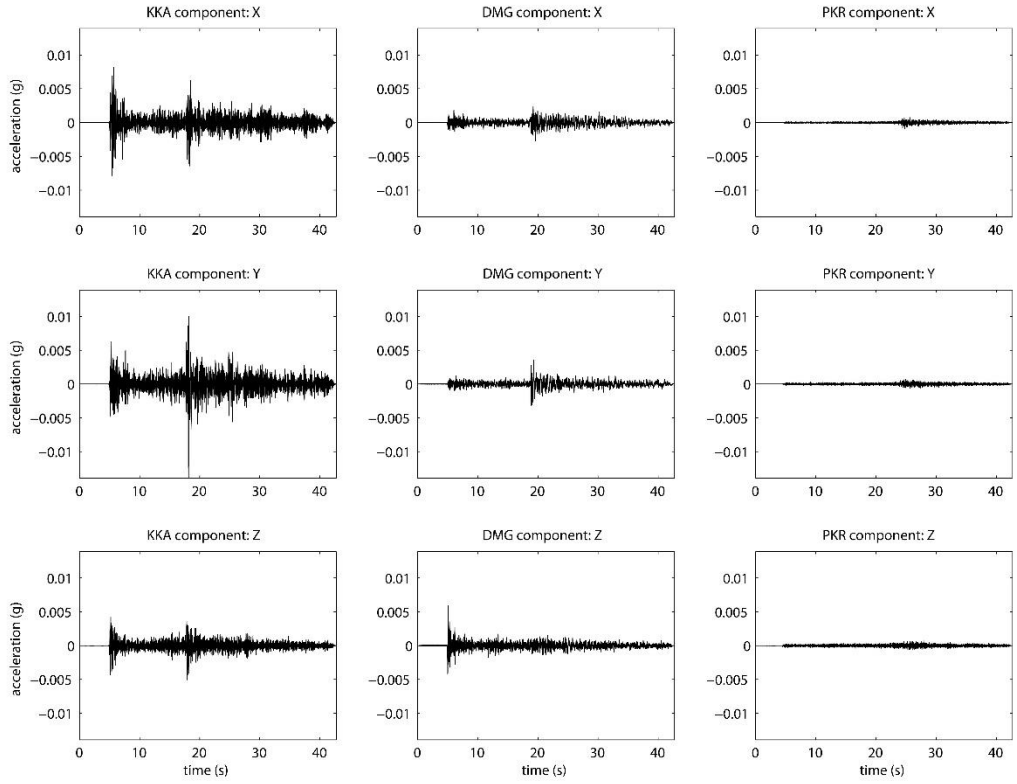

Figure 2.7 Accelerograms in the north-south, east-west, and vertical components on the 17 October 2010 (M_L 5.7) Xizang, China earthquake recorded by KKA, DMG, and PKR stations at distances of 103, 110, and 174 km respectively (Bhattarai *et al*., 2011).

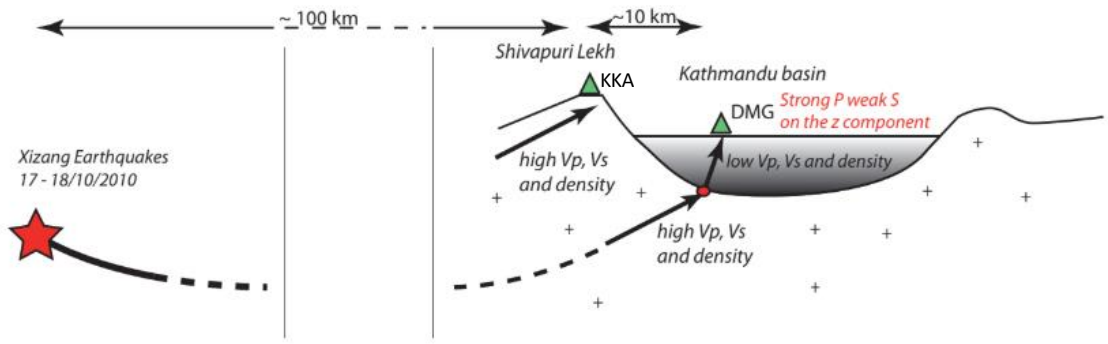

Figure 2.8 Schematic representation of the basin effect (Bhattarai *et al*., 2011).

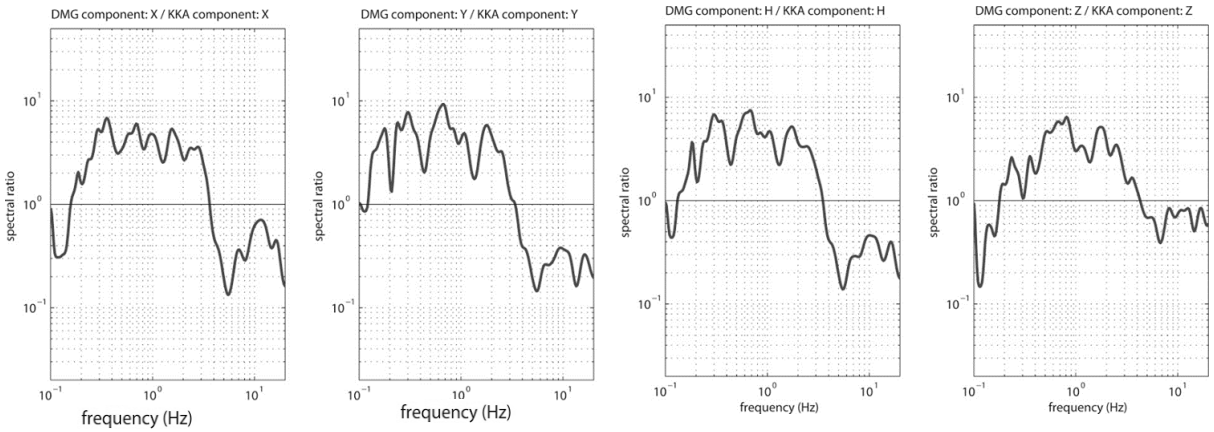

Figure 2.9 Spectral ratios at DMG and KKA for the 17 October 2010 Xizang earthquake (M_L 5.7) (Bhattarai *et al*., 2011).

Chapter 3

Establishing a reference rock site for site effect studies

3.1 Introduction

Kathmandu, the capital city of Nepal, as well as its sister cities, were located in a fluvio-lacustrine valley at the foot of the high Himalayan range, which is one of the most active and the highest mountain range of the world (Figure 3.1). The valley is severely impacted by large earthquakes due to the high tectonic activity of nearby faults, which also contribute to the growth of the mountain range. Local site conditions in the valley have large effects on the ground motion at the surface. Therefore, the disaster mitigation from damaging earthquakes is a major concern for the approximately 2.6 million people who live there. The use of observed strong ground motion records is a crucial component for seismic hazard assessment since they provide information of local site effect that plays a major role in seismic ground motion and its influences, i.e., damage caused by large earthquakes.

The Kathmandu valley is a tectonic basin formed by the uplift of the Himalayan frontal range, and filled by thick lacustrine, alluvial fan, and fluvial deposits of the paleo-Kathmandu lake in Pleistocene and Quaternary that overlay meta-sedimentary Precambrian to Paleozoic bedrock (e.g., Yoshida and Igarashi 1984, Sakai 2001, Sakai *et al*., 2006, Piya, 2004). Moribayasi and Maruo (1980) mapped the basement topography based on their result of gravity survey and estimated the maximum depth of sediment to be about 650 m. The depth at the strong motion observation station DMG that is located in the main office building of the Department of Mines and Geology, the Government of Nepal (Figure 3.1) is estimated to be 500 m that is consistent with the information obtained by drillings nearby (Sakai, 2001). In the valley, the average shear wave velocity in the upper most 30 m is spread from 180 to 310 m/s (Japan International Cooperation Agency, 2002). Paudyal *et al*. (2012) derived the predominant period of the ground from the horizontal to vertical spectral ratios of ambient noise (so-called Nakamura's method, Nakamura, 1989) at the DMG station and estimated it to be between 1 and 2 s period. The intensity distribution during the 1934 Nepal-

Bihar earthquake (Rana, 1935; Roy *et al*., 1939) suggests that velocity structure in the valley is not simple (Figure 3.1). During the Gorkha earthquake (Kobayashi *et al*., 2015; Kubo *et al*., 2016) clear predominant period around 5 s was observed at the DMG station (Bhattarai *et al*., 2015), at the KATNP site maintained by USGS (Dixit *et al*., 2015), and also at some temporary stations in the Kathmandu valley (Takai *et al*., 2016). These show necessity of further studies such as geological and geophysical surveys, and strong and weak motion observations, especially on velocity structures and on the shape of bedrock that will be used for seismic hazard assessment.

In Nepal the permanent seismic network has been established under the technical cooperation between Departement Analyse Surveillance de l'Environnement (DASE) under Commissariat Energie Atomique (CEA) of the Government of France, and Department of Mines and Geology, of the Government of Nepal since 1978. Within the cooperation, the National Seismological Centre under Department of Mines and Geology (NSC/DMG) has been jointly working with DASE since 2009 in deploying accelerographs in order to study the strong ground motion and its variability in different site conditions. The DMG station is located in the central part of the Kathmandu valley (DMG) and the other stations lie in other major cities such as Pokhara (PKR) and Surkhet (SKT), or are collocated with velocimetric stations Ghanteshwor (GHA), Kakani (KKA), and Taplejung (TAP). DMG, KKA, and PKR were installed earlier then the network was extended to SKT and Dhunche (DHU) in 2011. After the Taplejung-Sikkim earthquake in 2011, three temporary stations were deployed in eastern Nepal. One of them was later converted to the permanent station TAP.

In and around the Kathmandu valley NSC/DMG had maintained only two accelerographs DMG and KKA and KKA would have been considered as a reference site. Bhattarai *et al*. (2011); however, have pointed out the problem that in the frequency range from 4 to 10 Hz there was significant amplification at the rock site KKA located on the weathered granite and gneisses of Shivapuri Lekh in comparison with the soil site DMG on thick fluvio-lacustrine sediments using the records of 17 October 2010 Xizang, China earthquake (Event No.1 in Table 3.1). Then, the appropriateness of KKA as a reference rock site is left in doubt.

To understand this problem data simultaneously recorded by the short-period velocimetric station PKIN located at a distance of 15 km south-east from the Kathmandu

valley before the Gorkha earthquake detailed in Tables 3.1 and 3.3 is used. After the Gorkha earthquake an accelerometer PKI has been installed nearby the PKIN station. PKI has recorded the aftershocks of the Gorkha earthquake including the largest aftershock. Tables 3.2 and 3.4 show earthquake and the instrument details at PKI.

Site response analyses at the surface using the data from at least two stations are usually performed by comparing ground motion records at a site of interest to that of nearby rock site commonly known as reference motion. A site that has a flat transfer function with an amplitude of one is known as a reference. It plays a vital role in estimating the site amplification at the site of interest. Site amplification is generally considered unity for the reference rock site; however, none of the sites can be treated as perfect ideal site. Studies from previous earthquakes have shown that ground motions have variation on site wise and earthquake wise. This causes uncertainty on the evaluated site response and therefore, reference site should be selected carefully (Steid *et al*., 1996).

It is well known that soft soil amplifies ground motions in comparison to stiff soil or bedrock. This variation is evident in the damage pattern during large earthquakes. Selection of a reliable reference site is basis for studies of the site effects including basin and basin-edge effects, and then shall be completed with the highest priority. Therefore, this chapter is aimed to review the process taken to propose a more reliable reference rock site that shall be used for site effect studies at the arbitrary sites in and around the Kathmandu valley and to examine the impact of this site for site effect studies using some aftershocks of the Gorkha earthquake.

3.2 Method

One of the experimental indicators that are commonly used to determine site effects at an arbitrary site is H/H_{ref} spectral ratio (Borcherdt, 1970). It is defined as the ratio of the Fourier amplitude spectra of horizontal components of a soil site (site of interest) and rock site (reference site) records from the same earthquake. This technique has been applied for practical use, on the assumption that ground motion at the rock site is equivalent to the input motion on the basin bedrock. The H/H_{ref} ratio is thus the representative of the transfer function of the sedimentary layers at the soil site. This is valid only if the difference of source radiation and propagation effects between the two sites can be neglected. It is also necessary to let the distance between the source and site must be sufficiently large compared with the

distance between the sites. Since *S*-waves are very sensitive to site conditions and are the origin of most of the damage, this technique is generally applied to *S*-waves. This method requires finding a good reference site (Steidl *et al*., 1996). The specific procedure is described in the next section.

3.3 Data and analysis

In addition to the two accelerographs at DMG and KKA we used the velocity waveform data from the station situated in the Phulchwoki tunnel (PKIN) to the south-east of Kathmandu maintained by NSC/DMG in (Figure 3.1). Altogether we used the digital waveform data obtained during nine earthquakes of different magnitudes equal to or larger than 5.0 recorded at the three stations, simultaneously (Table 3.1, Figure 3.2). It is noticed that in some accelerograms *P*-phase or the later part of *S*-phase was missing due to the choice of insufficient pre- or post-event window in the setup of the instrument. It is also found that some of the velocity seismograms at PKIN were saturated due to the limited dynamic range of the sensor and some breakage occurs before and after *P*- or *S*-phase onset in some components. For the selection of earthquakes, those with epicentral distances from DMG larger than 60 km were taken to prevent the influence of the difference in radiation and propagation effects between the stations. Therefore, we could use a limited number of the records as shown in Table 3.1. The signal to noise ratio (S/N*)* of the available records is above two consequently. For the convenience, the earthquakes are numbered as shown in Table 3.1.

The instruments and site conditions of the stations are summarized in Table 3.3 with their station codes. PKIN has a short-period velocity seismograph of which natural frequency is 1 Hz. Its velocity records are converted to accelerograms by numerical differentiation and the instrumental correction is applied in the frequency domain as described below. Therefore, a careful consideration is required on S/N in the frequency range lower than 1 Hz, especially in the case of weak ground motion.

The strong motion seismographs GeoSIG AC 23 at DMG and KKA are accelerometers but not of the force balanced type. This accelerometer is based on a geophone mass-spring system with a velocity transducer of the natural frequency 4.5 Hz and electronic corrector that over-damps the geophone by applying a voltage with opposite polarity. Then the output response is flat and proportional to the acceleration in the frequency range from 0.1 to 100 Hz

(GeoSIG Ltd., 2015). Therefore, for these two accelerometric stations, an attention is required on S/N for very small amplitude signals in the low-frequency range. However, a quantitative discussion related with PKIN is possible within the target frequency range of this study, i.e., over 0.5 Hz and also the consideration is possible on the relation of DMG with KKA for frequencies over 0.3 Hz as explained below.

The second largest earthquake, No. 8, was used as an example in order to explain the data processing using the software ViewWave (Kashima, 2009). The accelerograms of earthquake No. 8 (Table 3.1) at the KKA, DMG, and PKIN stations are shown in Figures 3.3a, b, and c respectively. Especially, those shown in Figure 3.3c were obtained by the numerical differentiation of the original velocity seismograms, but the instrumental correction was not yet applied. A time window of the twenty seconds was chosen for the calculation of Fast Fourier Transform (FFT). Prerequisites for FFT that are removal of DC trend, cosine taper, and zero padding, were applied and Fourier amplitude spectra were calculated and smoothed using the Parzen's window of bandwidth 0.2 Hz.

The thing to be considered in this chapter is not the individual behaviors of *SH*- and *SV*-waves, but the overall behaviors of the entire *S*-waves. The displacement particle motions on the horizontal plane for the event No. 8 recorded at KKA, DMG, and PKIN are shown in Figures 3.4a, b, and c respectively. No clear polarity and similarity in the Fourier amplitudes of the two horizontal components suggest an isotropic feature of *S*-waves. Therefore, two horizontal components were combined into their Euclidian mean, i.e., the square root of the sum of the squares of NS and EW components as shown in Figures 3.5a, b, and c respectively. Then, an instrumental correction is applied to the PKIN records in the frequency domain. The broken and solid curves in Figure 3.5c shows those before and after the instrumental correction, respectively, and the gray curve shows the normalized instrumental response that is used for the instrumental correction. Hereafter, the name PKIN_Cor is used for the signals obtained at PKIN but after conversion to acceleration and removal of the instrumental response.

The strange behavior of the solid curve of Figure 3.5c in the frequency range below 0.5 Hz is interpreted as the noise amplified by the instrumental correction. The flat part of the broken curve in the same frequency range shows the noise level. This clearly indicate that any discussion based on the spectral ratios DMG/PKIN_Cor or KKA/PKIN_Cor in the

frequency ranges below 0.5 Hz is not considered relevant and shall be excluded from the analyses. Similar flat parts are observed below 0.2 Hz in Figure 3.5a and below 0.3 Hz in Figure 3.5b. This implies that any discussion on the spectral ratio DMG/KKA cannot be fully reliable in the frequency range below 0.3 Hz.

Finally, the spectral ratios DMG/KKA, DMG/PKIN_Cor, and KKA/PKIN_Cor for the earthquake No. 8 are calculated as shown in Figures 3.6a, b, and c respectively. All three curves do not asymptote to the unity at low frequencies due to the effect of the noise dominating the records of KKA, DMG, and PKIN_Cor in the frequency ranges below 0.2, 0.3 and 0.5 Hz, respectively. Namely, the noise makes the denominator spectra too big in the mentioned frequency ranges.

The same procedure is applied for other earthquakes' records. Finally, all available spectral ratios are plotted together, their combined trend is analyzed and interpreted in the next section. In order to take the elongation of *S*-wave trains during the propagation via long distance and also their difference depending on the earthquake magnitude into account, different values of the duration of the time window for FFT were used: 10 s for the earthquakes No. 2 and No. 9; 20 s for No. 3, No. 5, No. 6 and No. 8; 40 s for No. 4 and No. 7. Due to the setting of post-event time window the captured *S*-waves parts are shorter than 10 s for No. 1; 7 s for DMG; 8 s for KKA; and 10 s for PKIN. Besides PKIN records are saturated during No. 4 and partly lost during No. 6 and No. 7 due to trouble of data acquisition system. Therefore, these three events are not used in discussions below.

The procedure mentioned above is used to analyze the data recorded at PKI. From Table 3.2, No. 1 indicates the largest aftershock of the Gorkha earthquake. No. 2, 3, and 4 are the aftershocks occurred after the largest aftershock around the epicenter region whereas No. 5 is an aftershock that occurred in the Kathmandu valley. A total time window of 22 s is used for data processing.

For the sake of convenience, three frequency ranges were set as follows: Range -1: lower than about 0.5 Hz, Range -2: from about 0.5 Hz to about 4 Hz, Range -3: from about 4 Hz to 10 Hz and higher.

3.4 Results

The observations for the representative earthquake DMG/KKA, DMG/PKIN_Cor, and KKA/PKIN_Cor in the previous section can also be seen even for other events. The spectral ratio curves of all earthquake are plotted in Figures 3.7a, b, and c, respectively. For most of the earthquakes, the ratios show similar trends.

The most notable one is the non-flat feature of the spectral ratio DMG/KKA. In Range -2, all curves are between the unity and 10, whereas in Range -3 below the unity. Namely, a rock site KKA more amplification was performed than at DMG in the center of the valley, in Range -3, consistently with Bhattarai *et al*. (2011). This is supported by the spectral ratio DMG/PKIN_Cor in Figure 3.7b where a dratic contrast is found between Range -2 and Range -3. Also, in Figure 3.7c, the spectral ratio KKA/PKIN_Cor takes values around the unity in Range -2 and over 10 up to 25 in Range -3. Thus, it was confirmed that KKA has its own particular site response at Range -3. However, its mechanism is left unknown.

On the other hand, DMG/PKIN_Cor shows the amplification around 4 or 5 in Range -2 and in Range -3 with narrow peaks and troughs. All the signals converged towards unity at higher frequencies above 10 Hz. The sharp peak exceeding 10 in Range -3 is particular only to the earthquake No. 9. This clearly shows the site amplification at DMG is, at maximum, 10 times higher than that at PKIN. Additionally, it is clearly observed that for the largest earthquake No. 4 exhibited a significant peak at 0.3 and also 0.6 Hz in Figure 3.7a.

Figure 3.8a shows simultaneously recorded earthquakes used to compare KKA and PKIN with DMG before Gorkha earthqake; however, Figure 3.8b shows the aftershocks recorded at PKI nearby the PKIN staion used to compare with DMG after the Gorkha earthquake. It is clearly observed in Figure 3.9 that DMG shows clear site amplification in all Ranges of frequencies mentioned above. Long-period amplification caused by the largest afershock of the Gorkha earthquake at around 0.3 Hz and others is clearly evident in Figure 3.9.

3.5 Conclusions

This study aims to resolve an issue discovered in the previous study by Bhattarai *et al.* (2011) and to propose a better reference site for the investigation of site effect in and around the Kathmandu valley. The problem is that in the frequency range from 4 to 10 Hz there is significant amplification at the rock site KKA in comparison with the soil site DMG.

This anomaly is re-checked using the acceleration data of nine earthquakes obtained at these stations, and also velocity seismograms of another rock site PKIN on the southern slope of Phulchwoki Hill. The anomaly reappears for all of the analyzed earthquake records, and the amplification of KKA in comparison with DMG is confirmed. It is also confirmed, using the spectral ratio of the ground motions of DMG and PKIN for the same earthquakes, that the DMG site has amplification ranging from 1 to at most 10 times in the frequency range of 0.5 to 10 Hz. On the other hand, the spectral ratios of KKA compared to PKIN showed that the KKA site has amplification in the frequency range from 4 to 10 Hz, with a peak value at most 10. This means that site amplification in and around the Kathmandu valley that is estimated by spectral ratios with reference to KKA will be underestimated in the frequency range from 4 to 10 Hz. The mechanism or reason for the amplification in this frequency range at KKA is left unknown. Further studies, parallel measurement of ambient noise and/or geophysical exploration are needed. In the frequency range higher than 1 Hz, the mentioned data show the amplification at the DMG site, but it is confirmed only for linear response range.

Additionally, amplification due to thick sediments in the valley has been suggested by the spectral ratio of DMG compared to KKA using the records of the Taplejung-Sikkim earthquake M_L 6.8 on 18 September 2011. In the frequency range lower than 0.5 Hz, the power of the used records of DMG and KKA was not enough to reveal it clearly. Only this M_L 6.8 earthquake has power there and the long-period response is observed, but its reliability does not seem enough due to the poor S/N in the frequency range lower than 0.3 Hz at DMG and KKA. A drastic site effect in the frequency range lower than 0.5 Hz has been shown during the 2015 Gorkha, Nepal earthquake (Bhattarai *et al.*, 2015), not only in DMG but also other stations (Takai *et al.*, 2016; Kubo *et al.*, 2016). However, further studies on additional strong motion records of the mainshock and aftershocks of the Gorkha earthquake will be required to understand and quantify the effect.

Based on the analysis and interpretation in this chapter, we have proposed that the station PKIN should be considered as a reliable reference site for the estimation of seismic hazards in and around the Kathmandu valley.

In addition to the velocity seismograph PKIN an accelerograph PKI has been installed nearby the station PKIN in May 2015, after the Gorkha, earthquake. Aftershocks simultaneously recorded at PKI together with DMG shows clear site amplification at DMG in all frequency ranges mentiond above supporting the reference site. It is also clearly evident that long-period amplification at around 0.3 Hz exibits clear peak with the largest aftershock as well as some other aftershocks under consideration. A rock site motion recorded at PKI is also used for the numerical simulation of ground motion in Chapter 7.

3.6 References

Bhattarai, M., U. Gautam, R. Pandey, L. Bollinger, B. Hernandez, and V. Boutin (2011). Capturing first records at the Nepal NSC accelerometric network, *J. Nepal Geol. Soc*., **43**, 15-22.

Bhattarai, M., L. B. Adhikari, U. P. Gautam, A. Laurendeau, C. Labonne, R. Hoste-Colomer, O. Sèbe, and B. Hernandez (2015). Overview of the large April 25 Gorkha, Nepal earthquake from accelerometric perspectives, *Seismol. Res. Lett*., **86**, 40-48.

Borcherdt, R. D. (1970). Effect of Geology in ground motion near San Francisco bay, *Bull. Seismol. Soc. Am.*, **60**, 29-61.

Dixit, A. M., A. T. Ringler, D. F. Sumy, E. S. Cochran, S. E. Hough, S. S. Martin, S. Gibbons, J. H. Luetgert, J. Galetzka, S. N. Shrestha, S. Rajaure, and D. E. McNamara (2015). Strong-motion observations of the *M* 7.8 Gorkha, Nepal, earthquake sequence and development of the N-SHAKE strong-motion network, *Seismol. Res. Lett*., **86**, 1533-1539.

Dunn, J. A., J. B. Auden, A. M. N. Ghosh, and D. N. Wadia (1939). The Bihar-Nepal earthquake of 1934, *Geol. Survey India Mem*., 73.

GeoSIG Ltd. (2015). AC 23 Accelerometer Manual, downloadable from www.geosig.com/productfile2.html?productid=10359, accessed 18 December 2015.

Japan International Cooperation Agency (2002). *The study on earthquake disaster mitigation in the Kathmandu valley, Kingdom of Nepal*, Vols. I-III.

Kashima, T. (2009), View Wave Software (version 1.56), http://iisee.kenken.go.jp/staff/kashima/software_en.shtml, accessed on 18 September 2015.

Kobayashi T., Y. Morishita, and H. Yarai (2015). Detailed crustal deformation and fault rupture of the 2015 Gorkha earthquake, Nepal, revealed from ScanSAR-based interferograms of ALOS-2, *Earth Planets Space*, **67**, 201, doi: 10.1186/s40623-015-0359-z.

Kubo H., Y. Dhakal, W. Suzuki, T. Kunugi, S. Aoi, H. Fujiwara (2016). Estimation of the source process of the 2015 Gorkha, Nepal, earthquake and simulation of long-period ground

motions in the Kathmandu basin using a one-dimensional basin structure model, *Earth Planets Space*, **68**, 16, doi: 10.1186/s40623-016-0393-5.

Moribayasi, S., and Y. Maruo (1980). Basement topography of the Kathmandu valley, Nepal, an Application of Gravitational Method to the Survey of a tectonic basin in the Himalayas, *J. Japan Soc. Eng. Geol*., **21**, 30-37.

Nakamura, Y. (1989). A method for dynamic characteristics estimation of subsurface using microtremor on the ground surface, *Q. Rep. Railway Tech. Res. Inst*., **30**, 25-33.

National Seismological Centre (NSC): http://www.seismonepal.gov.np/, accessed on 18 Sep 2015.

Paudyal, Y. R., N. P. Bhandary, and R. Yatabe (2012). Seismic microzonation of densely populated area of Kathmandu Valley of Nepal using microtremor observations, *J. Earthq. Eng*., **16**, 1208-1229.

Piya, B. K. (2004). Generation of a Geological data base for the Liquefaction hazard assessment in Kathmandu valley, M. Sc. thesis, International Institute for Geo-Information Science and Earth Observation, Enschede, The Netherlands.

Rana, MG Braham Sumsher J. B. (1935). Nepalko Bhukampa, (The Great Earthquake of Nepal), Second ed., *Jorganesh press* Kathmandu, 1-250, (in Nepali).

Sakai, H., W. Yahagi, R. Fujii, T. Hayashi, and B. N. Upreti (2006). Pleistocene rapid uplift of the Himalayan frontal ranges recorded in the Kathmandu and Siwalik basins, *Paleogeography, Paleoclimatology, Paleoecology*, **241**, 16-27.

Sakai, H. (2001). Stratigraphic division and sedimentary facies of the Kathmandu basin sediments, *J. Nepal Geol. Soc*., **25**, 19-32.

Steidl H., G. Tumarkin, and J. Archuleta (1996). What is a reference site? *Bull. Seismol. Soc. Am*., **86,** 33-48.

Takai, N., M. Shigefuji, S. Rajaure, S. Bijukchhen, M. Ichiyanagi, M. Dhital, and T. Sasatani (2016). Strong ground motion in the Kathmandu Valley during the 2015 Gorkha, Nepal, earthquake, *Earth Planets Space*, **68**,10.

Yoshida M., and Y. Igarashi (1984). Neogene to Quaternary Lacustrine Sediments in the Kathmandu Valley, *J. Nepal. Geol. Soc*., **4**, 73-100 (Special issue).

Table 3.1 Earthquake parameters used before the Gorkha earthquake

Event ID	Date (UTC)	Latitude	Longitude	D_{epi} from DMG (km)	Magnitude (M_L)
1	20101017	28.64	75.71	110.55	5.7
2	20101018	28.65	85.73	112.5	5.2
3	20110815	27.44	86.27	100.13	5
4	20110918	27.71	88.3	296.23	6.8
5	20111112	28.18	84.93	63.63	5.3
6	20130628	28.47	82.67	272.74	5.5
7	20130715	28.75	87.59	252.99	5.6
8	20130830	28.43	86.02	106.17	6.1
9	20130830	28.48	86.03	111.17	5.2

*D_{epi} denotes an epicentral distance.

Table 3.2 Earthquake parameters used after the Gorkha earthquake

Event ID	Date	Time (UTC)	Latitude	Longitude	D_{epi} from NSC	Magnitude (M_L)
1	20150512	7:05:20	27.78	86.14	80.23	6.9
2	20150512	7:12:54	27.8	86.29	96.21	5.2
3	20150512	8:13:55	27.79	85.82	52.2	5.4
4	20150512	8:21:10	27.77	86.14	83.17	5.3
5	20150512	20:22:14	27.69	85.3	1.2	4.3

*D_{epi} denotes an epicentral distance.

Table 3.3 Instruments and site details before the Gorkha earthquake

Station code	Type of Instrument	Sampling rate	Latitude (deg.)	Longitude (deg.)	Altitude (m)	Geology	Remarks
PKIN	ZM, 500 HM- 500 (1 Hz, h =0.7) Velocity Seismograph	50 Hz	27.57	85.39	2320	Rocks of Phulchauki Group dominated byhematite in Phulchwoki tunnel	~15 km southeast of Kathmandu
DMG	GeoSIG AC 23 Accelerograph GeoSIG-GSR24 digitizer	200 Hz	27.72	85.31	1340	Lacustrine deposit	~Central part of Kathmandu
KKA	GeoSIG AC 23 Accelerograph GeoSIG-GSR24 digitizer	200 Hz	27.80	85.27	2043	Granite and gneiss rock	~10 km northwest of Kathmandu

Table 3.4 Instruments and site details after the Gorkha earthquake

Station code	Type of Instrument	Sampling rate	Latitude (deg.)	Longitude (deg.)	Altitude (m)	Geology	Remarks
PKI	GeoSIG AC 23 Accelerograph GeoSIG GSR 24 digitizer	200 Hz	27.72	85.31	2320	Lacustrine deposit	About 15 km south-east of Kathmandu
DMG	GeoSIG AC 23 Accelerograph GeoSIG GSR 24 digitizer	200 Hz	27.72	85.31	1340	Lacustrine deposit	~Central part of Kathmandu

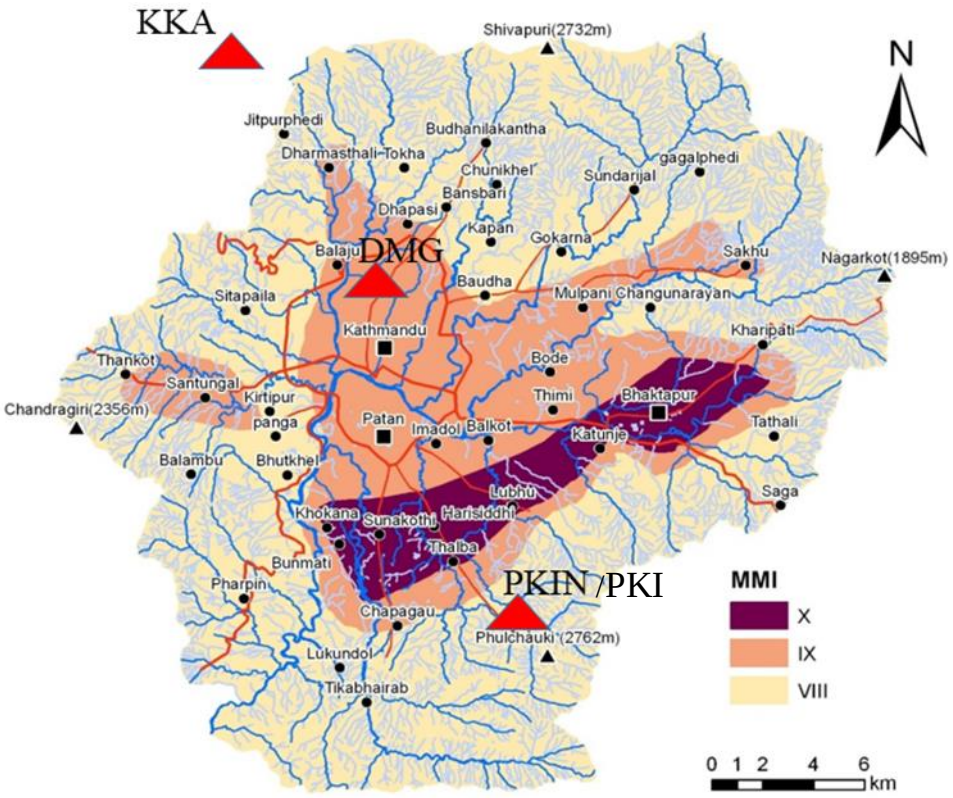

Figure 3.1 The locations of the stations (red triangles) in the background of intensity map of the 1934 Bihar-Nepal earthquake in the Kathmandu valley based on the description in Dunn *et al*. (1939) from Rana (1935) (Bhattarai *et al*., 2016).

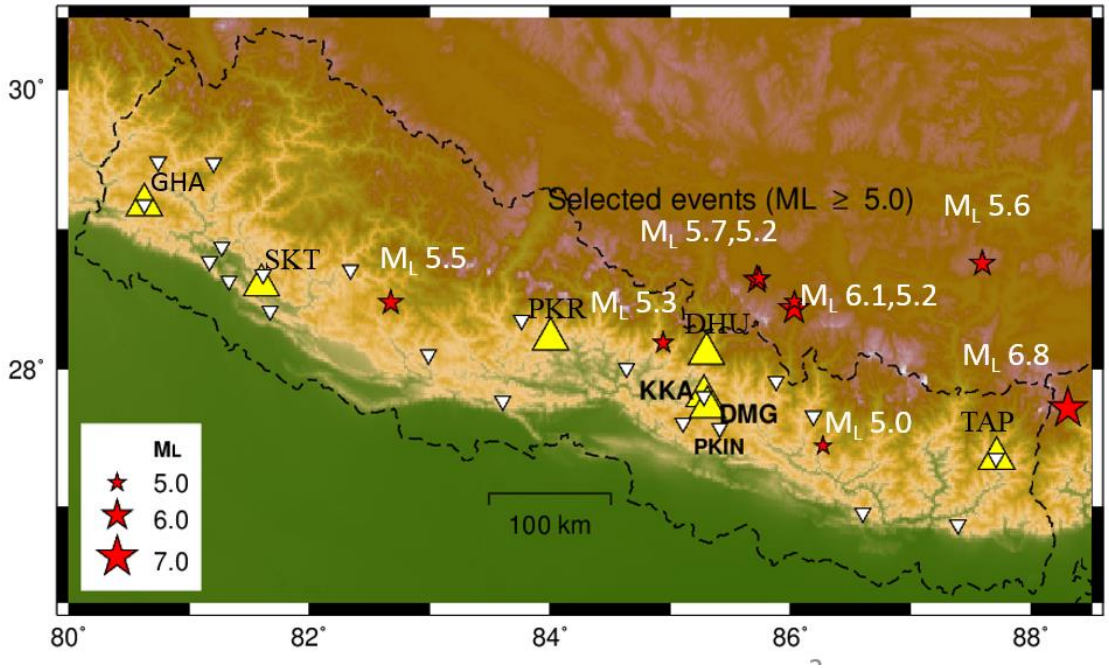

Figure 3.2 Stations and earthquakes used in the analyses. They are shown with station codes (Bhattarai *et al*., 2016).

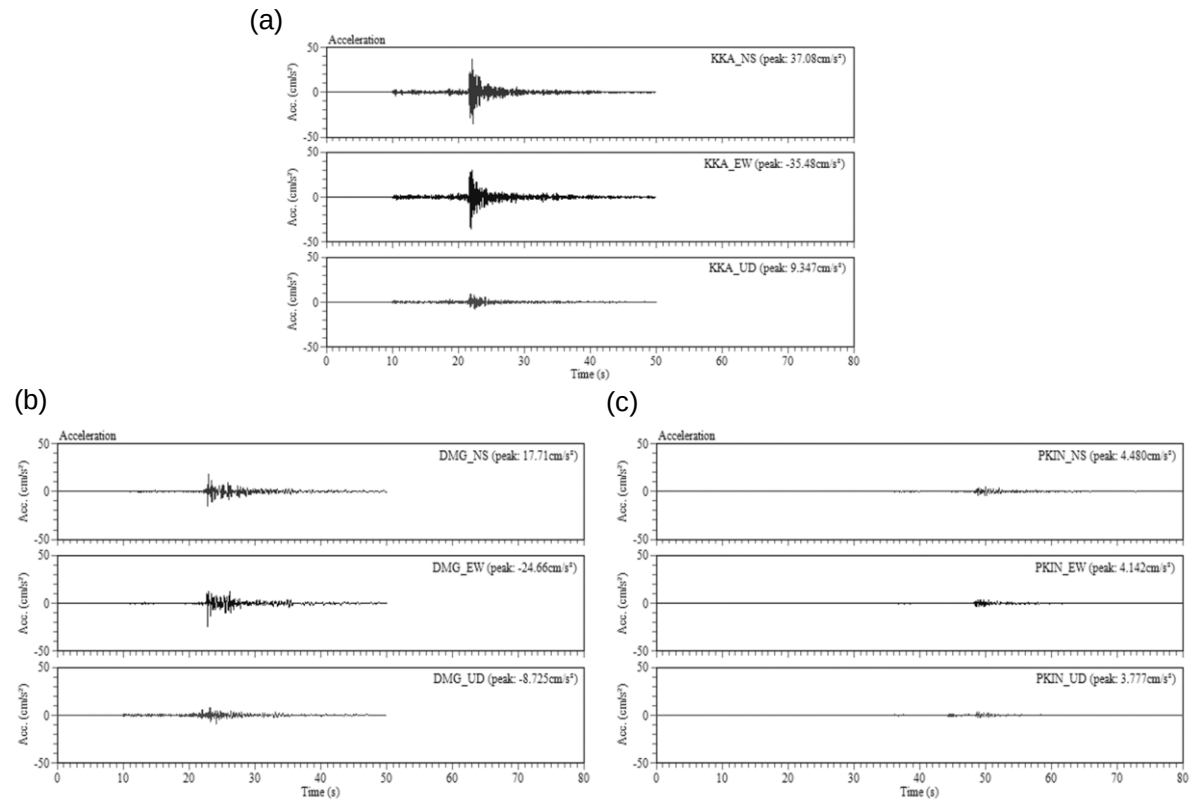

Figure 3.3 Accelerograms of the earthquake No. 8 in Table 3.1 recorded at (a) KKA, (b) DMG, and (c) PKIN. The last one was obtained by the numerical differentiation of the original velocity seismograms, but without instrumental correction (modified from Bhattarai *et al*. (2016)).

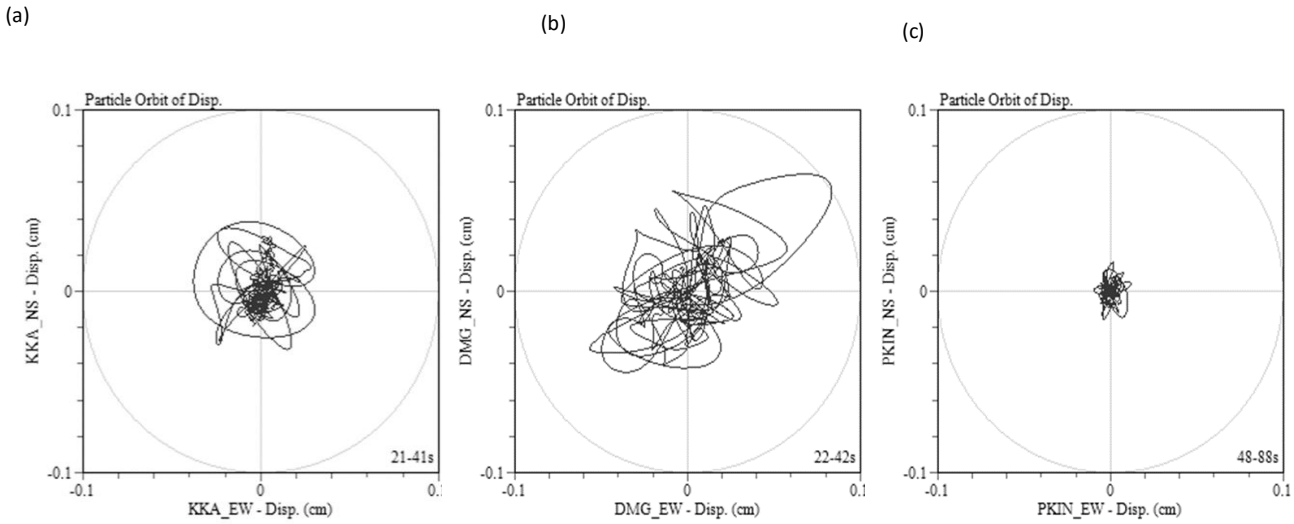

Figure 3.4 Displacement particle motions on the horizontal plane of the earthquake No. 8 in Table 3.1 recorded at (a) KKA, (b) DMG, and (c) PKIN. Low-cut filter is applied at 0.5 Hz to prevent the influence of noise (modified from Bhattarai *et al*. (2016)).

(a)

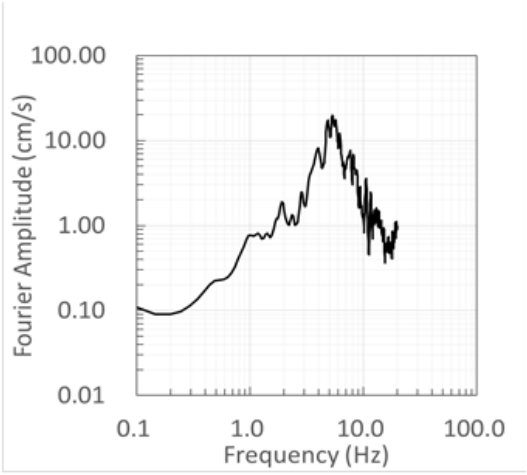

(b)

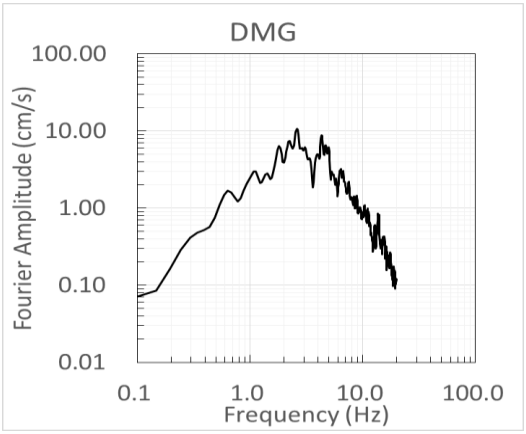

(c)

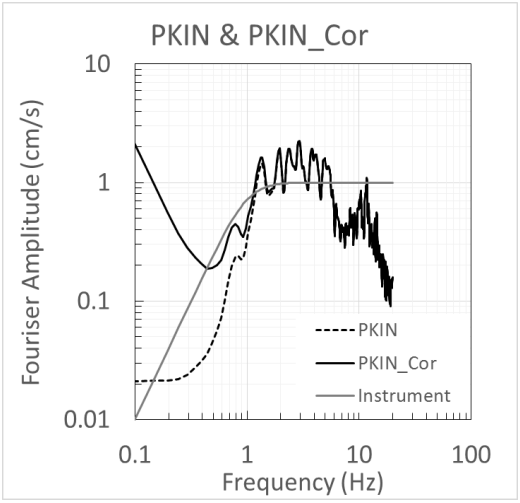

Figure 3.5 Fourier amplitude spectra of the horizontal component (Euclidian mean of NS and EW components) of the earthquake No. 8 in Table 3.1 at (a) KKA, (b) DMG and (c) PKIN (dotted curve, before the instrumental correction), PKIN_Cor (solid curve, after the instrumental correction) and the instrumental response used for correction (gray curve). The Fourier amplitude spectra of three components are calculated applying the time window of duration 20 s to 21, 22, and 46 s after the beginnings of the records of KKA, DMG, and PKIN, respectively (Bhattarai *et al*., 2016).

.

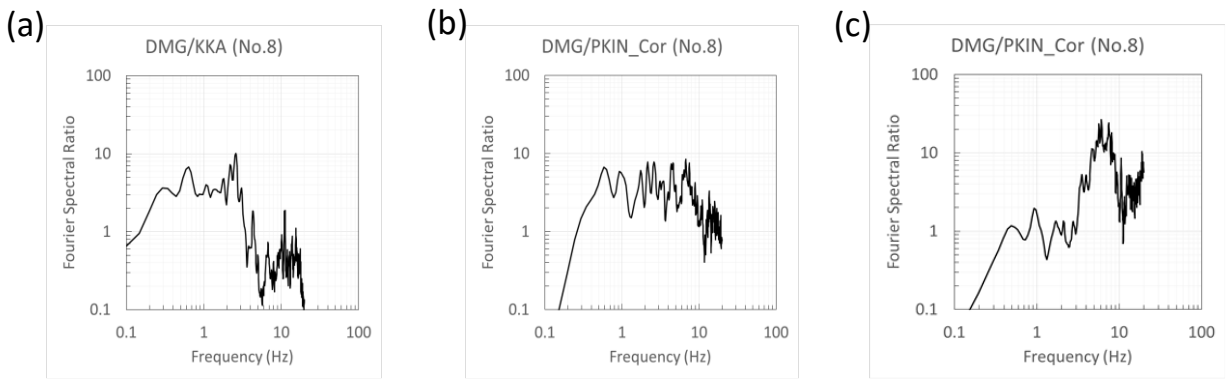

Figure 3.6 Spectral ratios (a) DMG/KKA, (b) DMG/PKIN_Cor, and (c) KKA/PKIN_Cor of the earthquake No. 8 in Table 3.1 (Bhattarai *et al*., 2016).

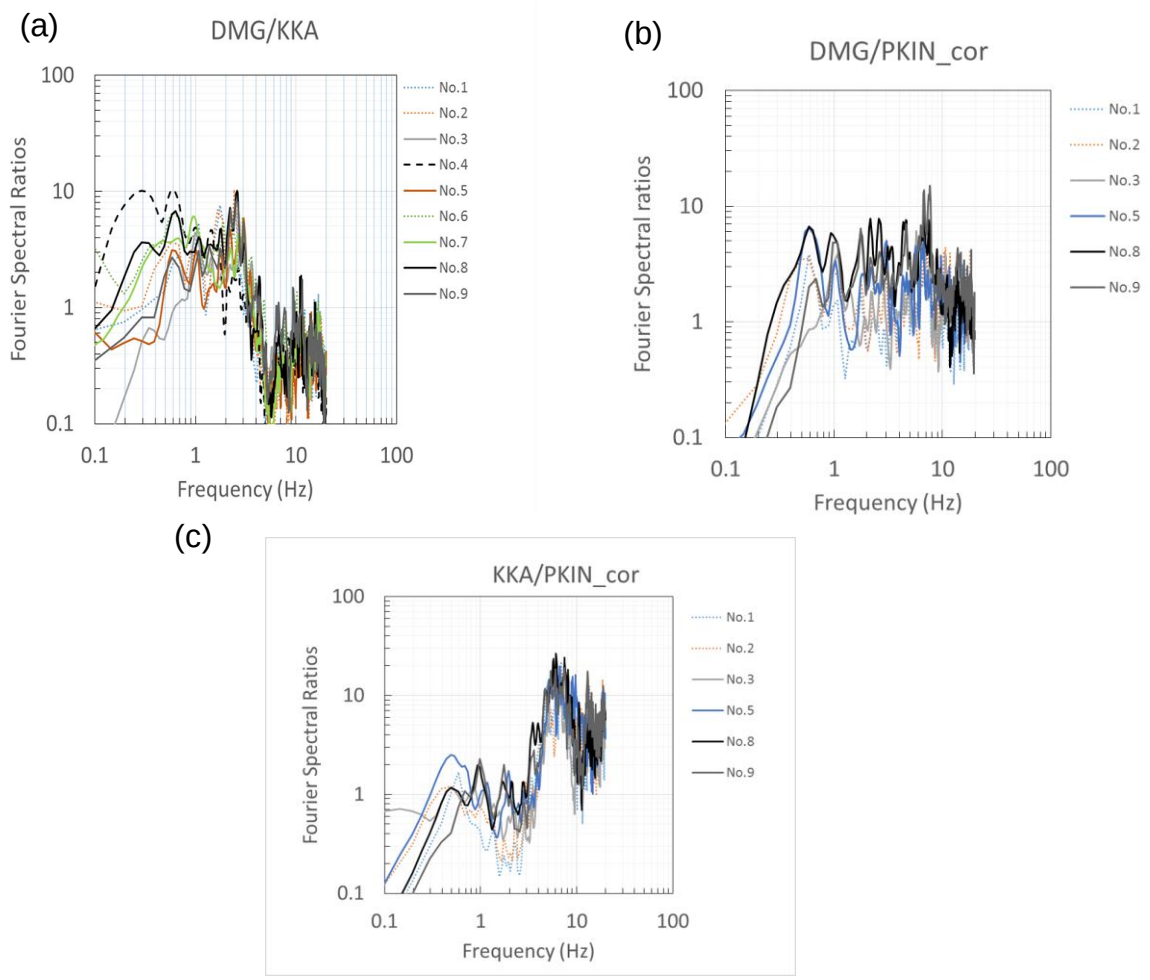

Figure 3.7 Spectral ratios (a) DMG/KKA, (b) DMG/PKIN_Cor, and (c) KKA/PKIN_Cor for all available records among the nine earthquakes in Table 3.1 (Bhattarai *et al*., 2016).

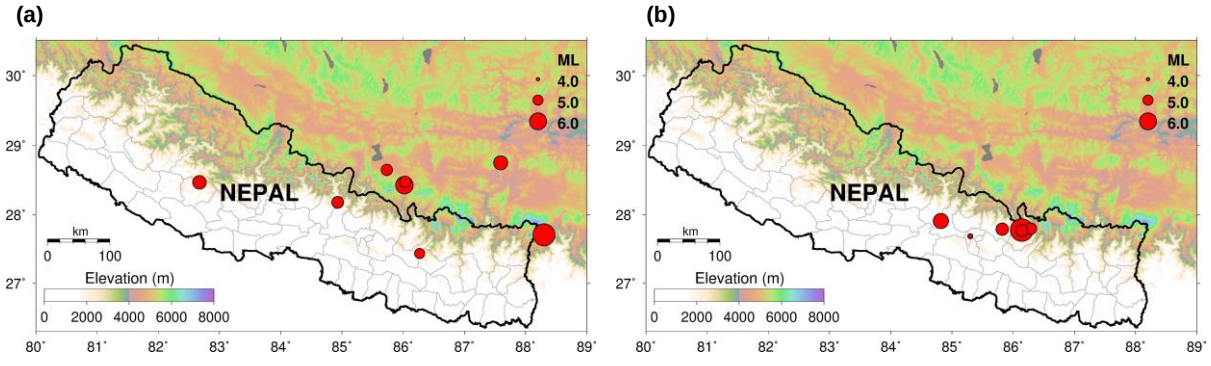

Figure 3.8 (a) Location map of the epicenters before the Gorkha earthquake. (b) The largest aftershock including the aftershock inside the Kathmandu valley and others after the Gorkha earthquake.

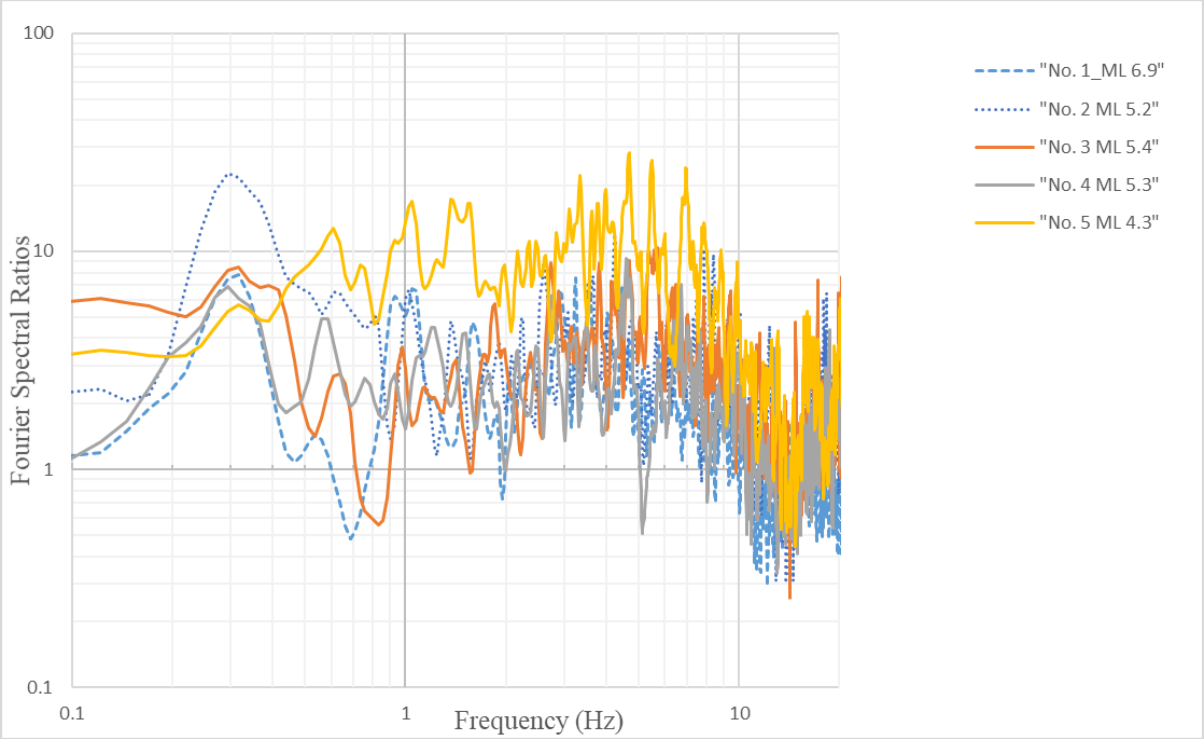

Figure 3.9 (H/H_{ref}) spectral ratios between the DMG sedimentary site and the PKI reference rock site the latter was installed nearby the PKIN site after the Gorkha earthquake.

Chapter 4

Site effects in ground motions of the 2015 Gorkha earthquake

4.1 Introduction

An earthquake of local magnitude M_L 7.6 given by the National Seismological Center (NSC) struck the Gorkha district of central Nepal on 25 April 2015 at 11:56 NST. The moment magnitude of this earthquake as reported by the United States Geological Survey (USGS) was M_W 7.8. The epicenter region, locally known as Barpak village of the Gorkha district is located at a distance of about 80 km NW from the Kathmandu valley. This interplate earthquake has occurred on the thrust interface between the south lying Indian and north lying Eurasian plates rupturing a locked segment of the Main Himalayan Thrust (MHT) fault. This plate boundary megathrust accommodates about 20 mm/yr of the convergence between India and Eurasia about 40 mm/yr (Lavé and Avouac, 2000; Bettinelli *et al*., 2006; Jouanne *et al*., 2004; Ader *et al*., 2012). While the rupture was propogeted towards east rupturing about 140 km WNW-ESE long fault segment (Adhikari *et al*., 2015). Low-frequency surface waves consistent with the fundamental frequency of the valley were generated in the Kathmandu valley after few seconds exciting Kathmandu valley as a whole. This shallow focused earthquake displays a low angle displacement consistent with the reverse fault motion of the Main Himalayan Thrust (MHT) (CEA, 2015). The mainshock rupture zone is delineated by the aftershocks; it is consistent with preliminary finite source modelings using InSAR, seismic data, and cGPS (Avouac *et al*., 2015; Galetzka *et al*., 2015).

Numerous aftershocks are still following the mainshock. Till 10 January 2020, NSC has reported 537 aftershocks issuing seismic alerts $M_L \geq 4.0$ to the public through media. Out of those four were major aftershocks above $M_L > 6.5$ and 12 May 2015, Dolakha earthquake M_L 6.9 (M_W 7.3) has been reported as one of the major aftershocks. It was initiated at the eastern tip of the ruptured segment about a distance of 80 km NE from the Kathmandu valley. However, over 50 thousand aftershocks above the detection capability ($M_L \geq 2.2$) and below the alert threshold ($M_L \geq 3.5$) of the seismic network have been associated in the micro-seismicity database of NSC. This number is approximately larger than the total number of

local earthquakes recorded by the NSC network from its establishment to just before the Gorkha earthquake. Aftershocks with $M_L \geq 4.0$ from the early records have described in Adhikari *et al*. (2015). The epicenter map of the mainshock, the largest, and other aftershocks is shown in Figure 4.1.

The Gorkha earthquake is the most severe devastating seismic event to strike Nepal and new experience for mass population in Nepal after 81 years since the great Bihar-Nepal earthquake 1934 (M_W 8.1). The total duration of the mainshock recorded at DMG in the central Kathmandu valley was over one minute; however, the strong shaking has lasted about 40 s. It was widely felt in central, eastern, and some parts of western Nepal and the neighboring countries (e.g., India, Pakistan, China, Bangladesh, Bhutan, etc.). In total 18 districts of Nepal including the Kathmandu valley were severely affected by this earthquake. The macroseismic intensities of this earthquake were reported between VI-VII in the EMS scale (Martin *et al*., 2015) at the various locations of the Kathmandu valley resulting in 8,778, fatalities and 22,303 injuries within the affected areas. In addition, more than 790,000 buildings were fully or partially damaged in Nepal (MoHA, 2015). It triggered secondary effects e.g., landslide, avalanche, and rockslide in Nepal. Liquefaction and soil non-linearity have also been detected in the Kathmandu valley after this earthquake mainly on the bank of the river (liquefaction) and close to the strong motion recording sites (non-linearity).

Attenuation relationships, recently known as Ground Motion Prediction Equations (GMPEs) are empirical ground-motion models need to be treated with certain characteristics of the ground motion data. Earthquake type, depth to the rupture, hanging wall effect, scattering, site dependence (e.g., basin depth, soil non-linearity), removal of the distance dependence, regional variation in the distance dependence, change of amplitude with distance for fixed magnitude, etc. are considered in most of the cases. Since GMPEs are conventional approaches that cannot be created without enough data and most of these approaches are limited by the scarcity of large earthquake at short distances. The conventional GMPEs do not account for the soil and site conditions. GMPEs provide a means of predicting the level of ground shaking based on earthquake magnitude, source-to-site distance, local soil conditions, fault mechanisms, etc. and associated with uncertainty at any given site or location.

Boore and Atkinson, 2008 (BA08) model was developed based on the Pacific Earthquake Engineering Center's (PEER) Next Generation Attenuation (NGA) database from

active crustal regions worldwide. The equations are applicable for moment magnitude M_W (5-8), time-averaged shear wave velocity from the surface to 30 m V_S30 (180-1300 m/s), closest horizontal distance to the surface projection of the fault plane < 200 km, Peak Ground Acceleration (PGA), Peak Ground Velocity (PGV), and 5% damped Peak Spectral Acceleration (PSA) at periods between 0.01 s and 10 s. However, it does not account for the basin effect.

To account for the basin effect Abraham and Silva, 2008 (AS08) model is used. The equations are applicable for moment magnitude M_W 4.0 upto from 7.5 to 8.5, closest horizontal distance to the surface projection of the fault plane from 0 to 200 km, peak ground acceleration (PGA), peak ground velocity (PGV), peak ground displacement (PGD), and 5% damped pseudo-absolute response spectral acceleration (PSA) at periods between 0.01 s and 10 s. Magnitude saturation, magnitude-dependent attenuation, style of faulting, rupture depth, hanging-wall geometry, linear and non-linear site response, 3-D basin response, and inter-event and intra-event are also considered in this model.

In this chapter we describe the behavior of the site effects caused by the mainshock, largest aftershock and some other aftershocks observed in the central part of the Kathmandu valley recorded by the DMG accelerometric station owned and maintained by NSC/DMG. The results at DMG are compared with the records of nearby the NQ.KATNP station owned by USGS. The spectral acceleration is compared with the GMPEs BA08, and AS08 the former does not account basin effect whereas the latter does it. The damage analyses using the mainshock and the largest aftershock are described in Chapter 7.

4.2 The DMG accelerometric station

One accelerometric station (DMG) installed in the premises of the Department of Mines and Geology in Lainchaur, Kathmandu (85.3166° E, 27.7193° N) recorded the mainshock and the aftershocks. The accelerometric station considered here was installed to complement the existing National seismic network (Figure 4.1). The station, installed on a concrete slab at the ground floor of a 1-story building, is instrumented with a Geosig AC 23 sensor and a GSR 24 digitizer (Bhattarai *et al*., 2011). Complementary non-telemetered stations have been deployed in the past (Bhattarai *et al*., 2011). However, some were out of service before and during the Gorkha earthquake.

The DMG station is located at the center of the Kathmandu valley, which is filled by Pleistocene and Quaternary lacustrine, alluvial fan, and fluvial deposits. The sediments reach a depth of 500 m at DMG and are lying on a meta-sedimentary Pre-Cambrian to Paleozoic bedrock (Sakai, 2001). Bore-holes drilled nearby corroborate this subsurface geology. However, to our knowledge, no geophysical data characterizing the local shear wave velocity or the site response at DMG are presently available. Because of this lack, we use later estimates of the average shear wave velocity over the upper 30 m (V_S30) derived from a relationship between the topographic slope and V_S30 (Wald and Allen, 2007). The V_S30 maps in the world are available on the USGS website (http://earthquake.usgs.gov/data/V_S30/). At the location of DMG, V_S30 is estimated about 250 m/s. We are aware of the limitations of this method; however, the V_S30 value is consistent with the range of V_S30 values estimated by JICA (2002) to be between 180 and 310 m/s for the Kathmandu valley. In addition, Paudyal *et al*. (2012) have measured the horizontal-to-vertical spectral ratios from microtremors (method introduced by Nakamura (1989)) for a grid of 171 points in and around the Kathmandu valley. Athough there was sensor limitation for frequencies below 0.5 Hz these authors estimated dominant periods to be from about 0.5 to 1 Hz in the vicinity of DMG.

4.3 Ground motion observation of the 2 major events at DMG

In this section, we describe the strong ground motion records at DMG for the Gorkha M_W 7.8 mainshock and the 12 May, 2015 M_W 7.3 largest aftershock by considering the time histories, the frequency content, the time-frequency decomposition, and the polarization. For the other aftershocks with $M_L > 6.5$, the strong motion parameters are computed following Bhattarai *et al*. (2011) and are given in Table 4.1 where the duration is calculated using (Trifunac and Brady, 1975). Another accelerometric station NQ.KATNP had been installed by USGS in the Kathmandu valley and it recorded the seismic sequence. The accelerograms recorded at this station, publicly available (http://www.strongmotioncenter.org), have been analyzed by Goda *et al*. (2015) and Dixit *et al*. (2015). A similar analysis to DMG is performed for this station and is presented in the following sections (Figures 4.7, 4.8, and 4.9).

4.4 Time history analysis

A simple processing is applied to the raw acceleration time histories recorded at DMG. The first 100 s and 70 s of the signal (the length of the time history record during the largest

aftershock is 70 s only) are extracted for the mainshock and the aftershock, respectively. Duration of the window, *Td* is reflected directly to the sampling interval of period/frequency axis as ($\Delta f = 1/T_d$) to keep T_d constant zeros are padded after the observed records in case the observation is shorter than others same sampling interval over frequency axis. The signal is tapered with a 5% cosine taper. Then, the acceleration time histories are analyzed and the strong motion parameters are computed. Horizontal and vertical acceleration time histories are shown in Figure 4.2 (left panel for the mainshock, right panel for the largest aftershock).

The mainshock records have a peak ground acceleration (PGA) of 0.15 g for the geometrical mean of the two horizontal components, and a larger PGA of 0.21 g on the vertical component. Thus, the vertical-to-horizontal ratio is 1.4. Figure 4.2 presents a quantification of the strong ground motion duration using the normalized Husid diagram (Husid, 1969), which represents the cumulative Arias intensity (AI) over time, a measure of the signal energy by Arias (1970). A common duration parameter is the significant relative duration Dsr(5-95%) (e.g., Bommer *et al*., 2009), which is the time interval between 5% and 95% of the cumulative AI over time. Dsr(5-95%) is around 42 s for the horizontal components and around 35 s for the vertical one. The energy is mainly accumulated between 21 s and 37 s. The horizontal components are mainly characterized by low frequency signal from 23 s.

Time histories of the aftershock recorded at DMG show PGAs of 0.10 g and 0.06 g for the horizontal and the vertical components respectively. Dsr(5-95%) is around 32 s for the horizontal components and around 35 s for the vertical one. The energy is mainly accumulated between 13 s and 26 s. For both the mainshock and the largest aftershock, a second energy pulse in the *S*-waves part is observed on the north component. It arrived at about 44 s for the mainshock and at about 32 s for the largest aftershock. This is observable especially with the Husid plots, which present a rapid increase at these times. The NQ.KATPN records reveal the same arrivals (Figure 4.7).

4.5 Spectral content

Figure 4.3 shows the Fourier Amplitude Spectra (FAS) for each component. For the mainshock, the predominant frequency of the horizontal component is about 0.23 Hz. The vertical spectrum is flatter and more consistent with a Brune model spectrum (Brune, 1970) with an apparent corner frequency slightly above 0.1 Hz. The large amplitudes on the

horizontal component at about 0.23 Hz may be related to site effects of the Kathmandu valley and/or properties of the source. A classical way to estimate site effects is to consider spectral ratios of ground motion recordings. The horizontal-to-vertical spectral ratio (HVSR) potentially highlights the predominant frequencies of amplification resulting from strong impedance contrasts (*e.g.*, Lermo and Chavez-Garcia, 1993). The HVSR of the mainshock exhibits a clear peak at 0.2 Hz (Figure 4.3).

For the 12 May aftershock, we also observed amplification at frequencies between 0.2 and 0.3 Hz, but the peak is less sharply defined. These HVSRs also reveal amplification around from 2 to 3 Hz which are not visible in the mainshock HVSRs. For the FAS, the predominant frequency is around 1 Hz. The vertical component reveals a corner frequency of about 0.4 Hz. We also note that, in the vertical component, FAS presents larger amplitude at high frequencies for both events.

4.6 Time-frequency decomposition and polarization analysis

An analysis of 3-component signals can provide an estimate of polarization characteristics of seismic wavefields. The polarization characteristics helps with understanding the seismic wavefield composition and discriminating between the different types of waves based on their degree of ellipticity, or the orientation of their polarization plane. Here the time-frequency representation is incorporated in the polarization analysis and the polarization attributes are estimated directly from the three components (Figure 4.4).

Using 3-component accelerometric DMG data, the characteristics of the wavefield are analyzed, in Figures 4.4a, b, f, and g, using Stockwell *et al.*'s (1996) decomposition called S-spectrum and, in Figures 4.4c, d, e, h, i, and j, using the polarization attribute spectra of Pinnegar (2006). It is assumed that the ground motion, at a specific time and frequency, can be considered as an elliptical motion confined in a plane. The polarization attributes used in this study to characterize the elliptical motion are the ellipticity and the orientation of the polarization plane. The ellipticity is defined as the ratio between the minor axis and the major axis of the main ellipse motion. The ellipticity values range from 0 to 1.0 corresponding to pure linear motion and 1 to pure circular motion (Figures 4.4c and h). The azimuth and the dip describe the orientation of the polarization plane. The azimuth (Figure 4.4d and i) represents the orientation from north and the dip (Figures 4.4e and j) is the angle from the

horizontal plane (0° corresponds to a horizontal plane and 90° to a vertical plane). Opacity is used to highlight significant amplitudes.

Considering the mainshock (Figures 4.4), two separate frequency behaviors can be distinguished below and above 1 Hz. The low frequency part below 1 Hz on the horizontal components of the S-spectrum is dominated by a peak of amplitude around 0.25 Hz (Figure 4.4a). This peak is less energetic on the vertical component (Figure 4.4b). Around this frequency of 0.25 Hz, the ellipticity is close to one from 12 to 40 s (Figure 4.4c), meaning that the particle motion is almost circular. After 40 s, the ellipticity becomes close to 0 corresponding to a linear particle motion.

At high frequencies above 1 Hz, the large amplitude is mainly concentrated on the vertical component (Figure 4.4b). The waves are all close to linearly polarized motion (ellipticity around 0), but it is difficult to determine the actual nature of the wavefield (body or surface waves) without velocity information. Three large high frequency energetic arrivals appear around 2 Hz at 26 s, 32 s, and 44 s (Figures 4.4c, d, and e). The first two arrivals at 26 s and 32 s are confined in nearly vertical polarization planes with an azimuth of 40° from the north. The polarization of the last arrival at 44 s is nearly horizontal. This last energetic arrival at 44 s on the horizontal component corresponds to the pulse observed only on the north-south component of the acceleration time history (Figure 4.2).

The rupture surface of the largest aftershock was located at a larger distance from Kathmandu than the rupture surface of the mainshock, therefore, *P*- and *S*-wave arrivals become distinguishable from each other. The *P*-waves, arriving around 10 s, mainly appear on the vertical component and are dominated by high frequency from 2 to 10 Hz (Figures 4.4f and g). The *S*-waves arrive around 20 s and have broader frequency content from 0.25 Hz to 10 Hz. The time-frequency representations are dominated by two peaks of energy both around 22 s at 1 Hz and 3 Hz (Figures 4.4h, i, and j). The peak of energy at 3 Hz is concentrated on the horizontal component whereas the peak at 1 Hz is polarized with a dip of 45° and with an azimuth of 60°. This peak at 1 Hz is noticeable on the three components and not observable on the mainshock, meaning that it is probably due to a source effect.

4.7 Response spectra and comparison with prediction

The reference papers for the seismic hazard assessment in Nepal are NSET (2001) and JICA (2002). A recent global PSHA study of Chaulagain *et al*. (2015) predicts, for the Kathmandu metropolitan city, a PGA around 0.3 g and a maximum response spectrum of 0.65 g around 0.2 s, with 10% probability of exceedance in 50 years.

The acceleration response spectra with a damping of 5% are computed and compared to prediction from the empirical GMPE of Boore and Atkinson (2008) (Figure 4.5). The Boore and Atkinson (2008) GMPE was developed using the Next Generation Attenuation (NGA) database, composed of worldwide data from active crustal regions. This model has the advantage to well represent the physics of the phenomenon (e.g., non-linearity with the magnitude, non-linearity of the geometric attenuation, non-linearity of the site) with only few input parameters (M_W, R_{JB}, V_S30, and the style of faulting). The Joyner and Boore distance (R_{JB}) parameter, defined as the shortest distance from a site to the surface projection of the rupture surface, must be determined. A distance of 15 km is used for the mainshock following the rupture model of Galetzka *et al*. (2015) and a distance of 65 km is used for the aftershock following the DASE rupture model (CEA, 2015). A GMPE, when obtained from different types of sites, represents an average spectral acceleration for a given V_S30. The comparison of a GMPE with a real response spectrum highlights the characteristics of a specific site. The two horizontal observed response spectra are generally in good agreement with the prediction within ± 1 sigma (Figure 4.5). For the mainshock, the observed PGA (0.15 g) occurs in the lowest part of the predicted distribution, i.e., lower than the predicted median (0.27 g). Thus, this comparison indicates that mainshock was only moderate for the magnitude and distance. However, the response spectra from DMG reveal some amplification peaks with amplitudes larger than the Boore and Atkinson (2008) GMPE. For example, the response spectra of the mainshock show huge amplification at 0.25 Hz. Boore and Atkinson (2008) does not take into account the deep sedimentary effect; however, the other two attenuation relationships mentioned below account it. The former one is Abrahamson and Silva (2008) AS08, there is a soil depth model, the sediment thickness is parametrized by the depth to the shear wave velocity horizon where V_S = 1 km/s. The latter one is Campbell and Bozorgnia (2008) CB08, there is a basin response term where the sediment thickness is parameterized by the depth to the shear wave velocity horizon where V_S = 2.5 km/s. Considering the velocity structure model (V_S and depth) so far derived in the Kathmandu

valley at around 1 km/s is about 770 m at the site 1 the AS08 seems only possible in this regard. The huge amplification at 0.25 Hz (4 s) in the response spectra of the mainshock using BA08 (Figure 4.6a) is suppressed in the time domain from 0.01 to 10 s using the AS08 (Figure 4.6b) when considering the basin effect.

4.8 Analysis of the records at the NQ.KATNP station

In the main part of this chapter, only the records of the DMG station are analyzed. Here we perform a similar analysis of the signals recorded at the NQ.KATNP station. NQ. KATNP and DMG stations are separated by a distance of about 800 m. Figure 4.7 presents the acceleration time histories, Figure 4.8 the Fourier Amplitude Spectra (FAS) and the horizontal-to-vertical ratios (HVSR), and Figure 4.9 the time-frequency analysis and the results of polarization.

The acceleration time histories at NQ.KATNP (Figure 4.7) are quite similar to the records of the DMG station which also provides a confirmation of the fidelity of both recordings. As for DMG records, a predominant peak of 0.2 Hz is observed for the mainshock and the aftershock from HVSR (Figure 4.8). Based on polarization analysis results (Figure 4.9), for this frequency of 0.2 Hz, the motion is mainly concentrated on the horizontal component, for the mainshock and for the aftershock as well (dip value around 0° in Figures 4.9d and i), in a similar way to the DMG station. This similarity also provides a confirmation of the results.

4.9 Analysis of two aftershocks of the Gorkha earthquake

Two aftershocks, one in the eastern part of the Kathmandu valley that occurred on 25 April 2015 at 08:05 with M_L 4.9 and the other inside the Kathmandu valley occurred on 26 April 2015 at 00:15 with M_L 4.1 are also analyzed as the same process before. The location map of the aftershocks analyzed is shown in Figure 4.1. The time histories recorded at DMG, their Husid plots, Fourier acceleration spectra and HVSR are shown in Figures 4.11 and 4.12 respectively. The results of time-frequency analysis are shown in Figure 4.13. In this figure the frequency changes are noticed with the passage of time. The change from higher to lower frequencies can be clearly seen for the first event in the left panel of Figure 4.13. For the second in the right panel of Figure 4.13 the change is not clear and mainly high frequency contents are observed around the *S*-wave arrival because it is a smaller event. It is interesting

to see in Figures 4.13 that the smaller event has the small duration. The polarization characteristics cannot be seen in either of the events, probably because of small magnitudes (Figures 4.13). It is also seen that the Fourier acceleration spectra of M_L 4.9 follows the same trend of the mainshock and largest aftershock of the Gorkha earthquake; however, M_L 4.1 was completely different even though the epicenter was in the southern part of the valley in the vicinity of the KTP rock site. It might be due to less energy in the smaller aftershock to activate the thick sediments of the Kathmandu valley.

4.10 Preliminary discussion about site effects

Previously, the work of Paudyal *et al*. (2012) discussed site effects in the Kathmandu basin. Unfortunately, in their method signal processing choices did not allow investigation of signals below 0.5 Hz. In this chapter, the analysis reveals large low frequency amplification i.e., a clear peak at 0.2 Hz for the mainshock and slightly more diffuse frequency amplification between 0.2 Hz and 0.3 Hz for the largest aftershock. The observed predominant frequencies are consistent both with site response estimates of Galetzka *et al*. (2015) and Dixit *et al*. (2015), and with the dominant frequency observed for NQ.KATPN (Figures 4.7 and 4.8).

The different predominant frequency between the mainshock and the largest aftershock could be explained by geometric effects (*e.g*., Kawase *et al*., 1996). Indeed, the Kathmandu valley has a complex geometric shape (Sakai, 2001). These two events have two different azimuths and for the aftershock, HVSRs display differences between the two horizontal components. In addition, the second pulse observed mainly on the north component for the two events and at the two stations (DMG and NQ.KATPN) could be diffracted waves. Otherwise, the observed differences in terms of frequency could indicate some potential non-linear site effects, as suggested by Dixit *et al*. (2015) and as has been inferred for other large earthquakes (e.g., Chin and Aki, 1991; Field *et al*., 1999; Bonilla *et al*., 2011). Non-linear site effects are characterized by a decrease in frequency of the predominant peak with the PGA (Beresnev and Wen, 1996).

A more advanced study is required to understand fully the nature of site effects. It seems necessary to process a larger number of events with different characteristics in terms of magnitude, distance, PGA, and azimuth to detect any potential basin effects and/or non-linear effects.

4.11 Discussion on liquefaction

During the Gorkha earthquake liquefaction has been detected in the Kathmandu valley at 5 locations as indicated by Okumura *et al*. (2015) in the liquefaction susceptibility map prepared by UNDP (1994) (Figure 4.14). Most of these locations fall on the bank of the river and none of these are closely located from the seismic observation system. The observed records in the central part of the Kathmandu valley on the NS component at DMG exhibits the spiky pulses at the second positive peak and the second negative peak etc. that look like caused by the cyclic mobility (lower panel) (Figure 4.15). This is because the cyclic mobility is regarded as an evidence of liquefaction. However, the phenomena did not appear in the EW component. The high-frequency component in the NS component did not disappear suddenly after these spiky pulses and observed in the coda part. On the other hand, any eye-witness of sand boil or crack by the field observation was not obtained around the DMG site. Therefore, it is guessed that liquefaction did not take place in DMG during the mainshock. Comparison with the strong motion records at the NQ.KATNP station (upper panel) (Figure 4.15) about 800 m south from DMG these pulses are not the effect of the seismic source. There is not overlapping between the liquefaction occurrences reported during the 1934 M_W 8.4 Bihar earthquake and the Gorkha earthquake in the central part of the Kathmandu valley.

4.12 Conclusions

This chapter presents the analyses of the acceleration time histories of the 25 April mainshock (M_W 7.8) of its 12 May largest aftershock (M_W 7.3), and of other aftershocks. These time histories are mainly recorded in the Kathmandu valley at the DMG station, installed and maintained by NSC/DMG. These results are compared with the records observed at the nearby NQ.KATNP station under the responsibility of USGS.

Time history analysis of the mainshock shows that the value of PGA recorded on the vertical component is greater than the horizontal components. A high-level amplitude peak observed in low frequency at around 0.25 Hz in the horizontal components of the mainshock is consistent with the fundamental frequency of the basin. The H/V spectral ratio also shows the peak at around 0.25 Hz. Which reveals excitation of the basin as a whole; however, this peak is not visible in the vertical component. At high frequency, the amplitude is larger in the vertical component. In contrast, the high-frequency energy observed on the accelerometric signal was quite moderate for such a large magnitude and short epicentral distance

earthquake. Time-frequency decomposition analyses for the mainshock show that, around frequency 0.25 Hz, ellipticity is close to one from 12 to 40 s, showing circular particle motion. After 40 s, ellipticity becomes close to 0, showing linear particle motion.

Time history analysis of the largest aftershock shows that the value of PGA recorded on the horizontal component is greater than vertical components. The amplification at frequencies from 0.2 to 0.3 Hz, shows a less sharp peak. The H/V spectral ratio also reveals amplification at around from 2 to 3 Hz and the vertical component reveals a corner frequency of around 0.4 Hz.

The energy peak at 1 Hz is polarized on the horizontal components of the aftershock; however, this peak is not visible in the mainshock which might have affected due to source effect. Analyses from the two small aftershocks one inside the Kathmandu valley and the other towards east does not show any polarization. However, HVSR and FAS of an event that occurred inside the Kathmandu valley shows different trend in comparison to other.

A comparison with the NQ.KATNP record provides the confirmation of the fidelity of both recordings. To better understand the frequency content associated with these two major events, a more detailed numerical analysis of the site response would be required.

The spiky pulses observed at the second positive and negative peaks recorded in the NS component during the mainshock at DMG look like caused by the cyclic mobility. This is because cyclic mobility is regarded as an evidence of liquefaction. However, it is not supported by the records at the nearby NQ.KATNP station and field observations.

When comparing with Boore and Atkinson (2008) GMPE, the two horizontal observed response spectra are in good agreement with the prediction, in general within $\pm$ 1 sigma. The observed PGA of the mainshock occurs in the lowest part of the predicted distribution which is lower than the predicted median. This indicates that the Gorkha earthquake shows high amplification in the lower frequency range around 0.25 Hz than the predicted ones; however, the PGA was smaller. For the largest aftershock the observed peak in the east-west component exceeds the median at around 1 Hz. This phenomenon shown in the mainshock is suppressed taking in to account with the basin effect using the GMPE (Abrahamson and Silva, 2008).

The Kathmandu valley is composed, at the DMG station, of soft sediments with a thickness of about 500 m. The contrast between sediments and the bedrock has contributed to amplify the low frequency ground motion which was evidenced during the Gorkha earthquake. This earthquake shows the necessity and importance of further studies on deep velocity structures of the basin for the seismic hazard assessment.

4.13 References

Abrahamson, N., and W. Silva (2008). Summary of the Abrahamson and Silva NGA Ground-Motion Relations, Earthquake Spectra, *Earthquake Spectra*, **24(1)**, 67-97, doi: 10.1193/1.2924360.

Ader, T., J. -P. Avouac, J. -L. Jing, L. -C. Helene, L. Bollinger, J. Galetzka, J. Generich, M. Thomas, K. Chanard, S. N. Sapkota, S. Rajaure, P. Shrestha, L. Ding, and M. Flouzat (2012). Convergence rate across the Nepal Himalaya and interseismic coupling on the Main Himalaya Thrust, Implications for seismic hazard, *J. Geophys. Res.*, **117**, B04403.

Adhikari, L. B., U. P. Gautam, B. Koirala, M. Bhattarai, T. Kandel, R. M. Gupta, C. Timsina, N. Maharjan, K. Maharjan, T. Dahal, R. Hoste-Colomer, Y. Cano, M. Dandine, A. Guilhem, S. Merrer, P. Roudil, and L. Bollinger (2015). The aftershock sequence of the April 25, 2015 Gorkha-Nepal earthquake, *Geophys. J. Int.*, **203(3)**, 2119-2124, doi:10.1093/gji/ggv412.

Arias, A. (1970). A measure of earthquake intensity, seismic design for nuclear power plants, 438-483.

Avouac, J. -P., L. Meng, S. Wei, T. Wang, J. -P. Ampuero (2015). Unzipping lower edge of locked Main Himalayan Thrust during the 2015, M_W 7.8 Gorkha earthquake, Nepal, *Nat. Geosci.*, **8**, 708-711.

Beresnev, I. A., and K. L. Wen (1996). Nonlinear site responsea reality? *Bull. Seismol. Soc. Am.*, **86**, 1964-1978.

Bettinelli, P., J. -P. Avouac, M. Flouzat, F. Jouanne, L. Bollinger, P. Willisand, and G. R. Chitrakar (2006). Plate motion of India and interseismic strain in the Nepal Himalaya from GPS and DORIS measurements, *J. Geodesy*, **80**, 567-589.

Bhattarai, M., L. B. Adhikari, U. P. Gautam, A. Laurendeu, C. Labonne, R. Hoste-Colomer, O. Sebe, and B. Hernandez (2015). Overview of the large 25 April Gorkha, Nepal, earthquake from accelerometric perspectives, *Seismol. Res. Lett.*, **86**, 40-48.

Bhattarai, M., U. Gautam, R. Pandey, L. Bollinger, B. Hernandez, and V. Boutin (2011). Capturing first records at the Nepal NSC accelerometric network, *J. Nepal Geol. Soc.*, **43**, 15-22.

Bommer, J., P. Stafford, and J. Alarcon (2009). Empirical equations for the prediction of the significant, bracketed, and uniform duration of earthquake ground motion, *Bull. Seismol. Soc. Am*., **99 (6)**, 3217-3233, doi: 10.1785/0120080298.

Bonilla, L. F., K. Tsuda, N. Pulido, J. Régnier, and A. Laurendeau (2011). Non-linear site response evidence of K-NET and KiK-net records from the 2011 off the Pacific coast of Tohoku Earthquake, *Earth Planets Space*, **63**, 785-789.

Boore, D., and G. Atkinson (2008). Ground-motion prediction equations for the average horizontal component of PGA, PGV, and 5% damped psa at spectral periods between 0.01 s and 10.0 s, *Earthquake Spectra*, **24 (1)**, 99-138, doi: 10.1193/1.2830434.

Brune, J. (1970). Tectonic stress and the spectra of seismic shear waves from earthquakes. *J. Geophys. Res.*, **75(26),** 4997-5009.

Campbell, K., and Y. Bozorgnia (2008). NGA Ground Motion Model for Geometric Mean Horizontal Component of PGA, PGV, PGD and 5% Damped Linear Elastic Response Spectra for Periods Ranging from 0.01 to 10 s, *Earthquake Spectra*, **24(1)**, 139-171, doi: 10.1193/1.2857546.

Chaulagain, H., H. Rodrigues, V. Silva, E. Spacone, and H. Varum (2015). Seismic risk assessment and hazard mapping in Nepal, *Nat. Hazards*, 1-20.

Chin, B. H., and K. Aki (1991). Simultaneous determination of source, path and recording site effects on strong ground motion during the Loma Prieta earthquake - a preliminary result on pervasive non-linear site effect, *Bull. Seismol. Soc. Am*., **81,** 1859-1884.

CEA (2015). Direction des applications militaires, Sciences de la Terre et de l'environnement, http://www-dase.cea.fr/actu/dossiers_scientifiques/2015-05-12/index.html, accessed on 12 June, 2015.

Dixit A. M., A. T. Ringler, D. F. Sumy, E. S. Cochran, S. E. Hough, S. S. Martin, S. Gibbons, J. H. Luetgert, J. Galetzka, S. N. Shrestha, S. Rajaure, and D. E. McNamara (2015). Strong-motion observations of the *M* 7.8 Gorkha, Nepal, earthquake sequence and development of the N-SHAKE strong-motion network, *Seismol. Res. Lett.*, **86**, 1533-1539.

Field, E. H., P. A. Johnson, I. A. Beresnev, and Y. Zeng (1997). Non linear ground motion amplification by sediments during the 1994 Northridge earthquake, *Nature*, **390(6660)**, 599-602.

Galetzka, J., D. Melgar, J. F. Genrich, J. Geng, S. Owen, E. O. Lindsey, X. Xu, Y. Bock, J. -P. Avouac, L. B. Adhikari, B. N. Upreti, B. Pratt-Sitaula, T. N. Bhattarai, B. P. Sitaula, A. Moore, K. W. Hudnut, W. Szeliga, J. Normandeau, M. Fend, M. Flouzat, L. Bollinger, P. Shrestha, B. Koirala, U. Gautam, M. Bhattarai, R. Gupta, T. Kandel, C. Timsina, S. N. Sapkota, S. Rajaure, and N. Maharjan (2015). Slip pulse and resonance of Kathmandu basin during the 2015 Gorkha earthquake, Nepal, *Science*, **349(6252)**, 1091-1095, doi:10.1126/science.aac6383.

Goda, K., T. Kiyota, R. Pokhrel, G. Chiaro, T. Katagiri, K. Sharma, and S. Wilkinson (2015). The 2015 Gorkha Nepal Earthquake: Insights from Earthquake Damage Survey, *Front. Built Environ*, 1, 8, doi: 10.3389/fbuil.2015.00008.

Husid, R. (1969). Analisis de terremotos: analisis general, Revista del IDIEM, **8(1)**.

Japan International Cooperation Agency (2002). *The study on earthquake disaster mitigation in the Kathmandu valley Kingdom of Nepal*, Vols. I-III.

Jouanne, F., J. L. Mugnier, J. F. Gamond, P. L. Fort, M. R. Pandey, L. Bollinger, M. Flouzat, and J. -P. Avouac (2004). Current shortening across the Himalayas of Nepal, *Geophys. J. Int.*, **157**, 1-14.

Kawase, H. (1996). The cause of the damage belt in Kobe: "The basin-edge effect," constructive interference of the direct *S*-wave with the basin-induced diffracted/Rayleigh waves, *Seismol. Res. Lett.*, **67(5)**, 25-34.

Konno, K., and T. Ohmachi (1998). Ground-motion characteristics estimated from spectral ratio between horizontal and vertical components of microtremor, *Bull. Seismol. Soc. Am.*, **88(1)**, 228-241.

Lavé, J., and J. P. Avouac (2000). Active folding of fluvial terraces across the Siwaliks Hills, Himalayas of central Nepal, *J. Geophys. Res.*, **105**, 5735-5770.

Lermo J., and F. J. Chavez-Garcia (1993). Site effect evaluation using spectral ratios with only one station, *Bull. Seismol. Soc. Am.*, **83(5)**, 1574-1594.

Martin, S. S., S. E. Hough, R. Bilham, and C. Hung (2015). Ground motions from the 2015 Mw 7.8 Gorkha, Nepal, earthquake, constrained by a detailed assessment of macroseismic data, *Seismol. Res. Lett.*, **86(6)**, 1524-1532.

Nakamura, Y. (1989). A method for dynamic characteristics estimation of subsurface using microtremor on the ground surface, *Quarterly Report* of the Railway Technical Research, Japan.

MoHA (2015). Nepal Disaster Risk Reduction Portal, Ministry of Home Affairs, Government of Nepal, http://drrportal.gov.np/, accessed on 12 June 2015.

NSET (2001). *The Kathmandu valley earthquake risk management action plan*, The Kathmandu valley Earthquake Risk Management Project.

NSC (National Seismological Centre), http://www.seismonepal.gov.np/, accessed on 25 April 2015.

Okamura, M., N. P. Bhandary, S. Mori, N. Marasini, and H. Hazarika (2015). Report on reconnaissance survey of damage in Kathmandu caused by the 2015 Gorkha Nepal earthquake, *Soils and Foundations*, **55(5),** 1015-1029.

Paudyal, Y. R., N. P. Bhandary, and R. Yatabe (2012). Seismic Microzonation of densely populated area of Kathmandu Valley of Nepal using microtremor observations, *J. Earthq. Eng.*, **16 (8)**, 1208-1229.

Pinnegar, C. R. (2006). Polarization analysis and polarization filtering of the three-component signals with the time-frequency S-transform, *Geophy. Jour. Int.*, **165**, 596-606.

Sakai, H. (2001). Stratigraphic division and sedimentary facies of the Kathmandu Basin sediments, *J. Nepal Geol. Soc*., **25**, 19-32.

Stockwell, R. G., L. Mansinha, and R. P. Lowe (1996). Localization of the complex spectrum: the S-transform, Signal Processing, IEEE *transactions on signal processing*, **44 (4)**, 998-1001.

Trifunac, M. D., and A. G. Brady (1975). On the correlation of seismic intensity scales with the peaks of recorded ground motion, *Bull. Seismol. Soc. Am*., **65**, 139-162.

Wald, D. J., and T. I. Allen (2007). Topographic slope as a proxy for seismic site conditions and amplification, *Bull. Seismol. Soc. Am*., **97(5)**, 1379-1395.

UNDP (1994). "Seismic Hazard Mapping and Risk Assessment for Nepal", His Majesty's Government of Nepal, Ministry of Housing and Physical Planning, UNDP/ UNCHS (Habitat), Subproject NEP/88/054/21.03.

USGS (United-State Geological Survey), http://earthquake.usgs.gov/earthquakes/eventpage/us20002926/general_summary, accessed on June 12, 2015.

Table 4.1 Ground motion parameters of the mainshock, the largest aftershock, and other aftershocks with $M_L > 6.5$

Date and Time (UTC)	Station ID	M_L/M_W	Epi. Dist. (km)	Comp.	PGA (cm/s²)	PGV (cm/s)	AI (m/s)	CAV (m/s)	HI (cm)	Dsr(5-95%) (s)
20150425 : 0611	DMG	7.6/7.8	80	NS	174	58.7	1.02	16.9	95.7	48
20150425 : 0611	DMG	7.6/7.8	80	EW	124	62.7	1.12	18.2	102.0	46
20150425 : 0611	DMG	7.6/7.8	80	UD	202	30.1	1.38	17.2	66.8	36
20150425 : 0645	DMG	6.6/6.6	85	NS	63.7	5.56	4.98	2.96	33.2	34
20150425 : 0645	DMG	6.6/6.6	85	EW	62.2	11.1	9.92	3.98	56.1	27
20150425 : 0645	DMG	6.6/6.6	85	UD	32.3	3.74	2.54	2.27	22.7	35
20150426 : 0709	DMG	6.9/6.7	73	NS	57.4	6.86	12.3	6.04	34.7	48
20150426 : 0709	DMG	6.9/6.7	73	EW	58.4	9.42	14.8	6.70	39.8	47
20150426 : 0709	DMG	6.9/6.7	73	UD	44.3	3.65	6.22	4.39	24.2	48
50150512 : 0705	DMG	6.9/7.3	80	NS	82.7	10.4	23.3	8.61	50.1	45
50150512 : 0705	DMG	6.9/7.3	80	EW	120	17.7	33.2	9.65	82.5	36
50150512 : 0705	DMG	6.9/7.3	80	UD	54.9	8.57	10.5	5.73	36.7	41

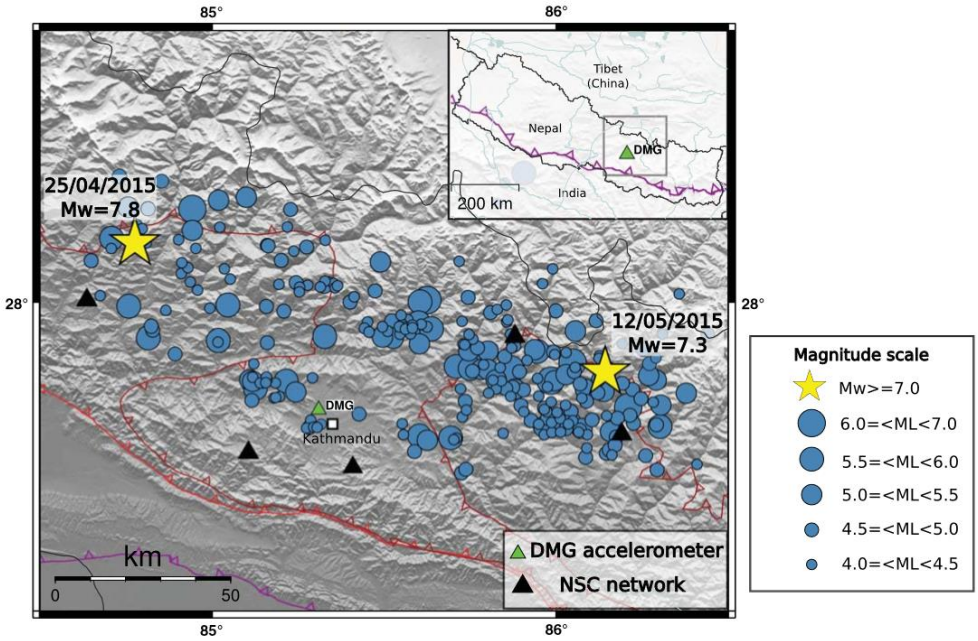

Figure 4.1 DMG accelerograph (green triangle) in the background of NSC seismic network (black triangles). Yellow stars show the locations of the mainshock and the largest aftershock. Blue circles show the locations of the early aftershocks with $M_L > 4$ (Bhattarai *et al*., 2015).

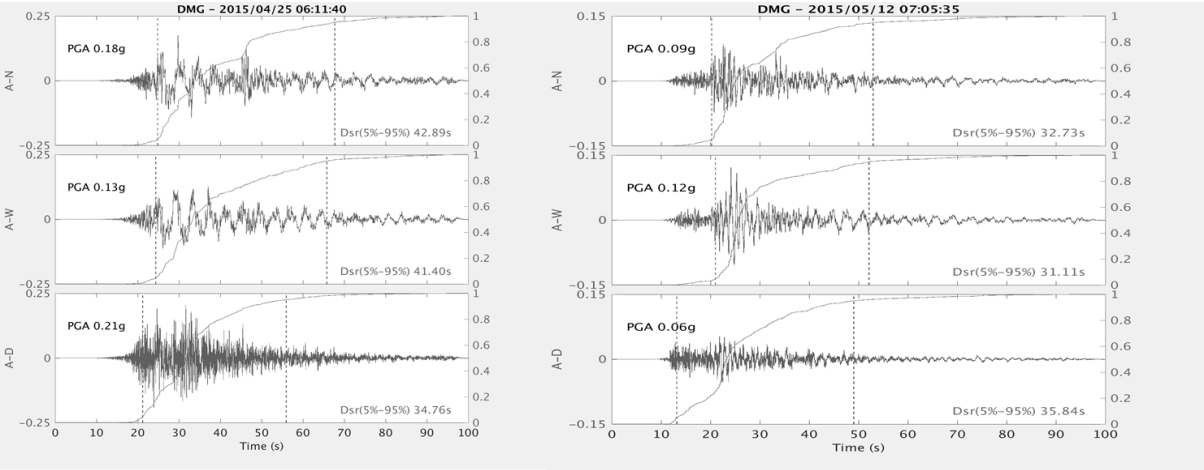

Figure 4.2 Acceleration time histories in g at the DMG station (left panel) for the 25 April mainshock (M_W 7.8) and (right panel) for the 12 May aftershock (M_W 7.3). We also show the normalized Husid diagrams (grey solid lines) and the time intervals corresponding to 5 and 95% of the cumulative Arias intensity (dashed grey lines). The peak ground acceleration PGA and the significant relative duration Dsr(5-95%) are also indicated for each component (modified from Bhattarai*et al.*, 2015).

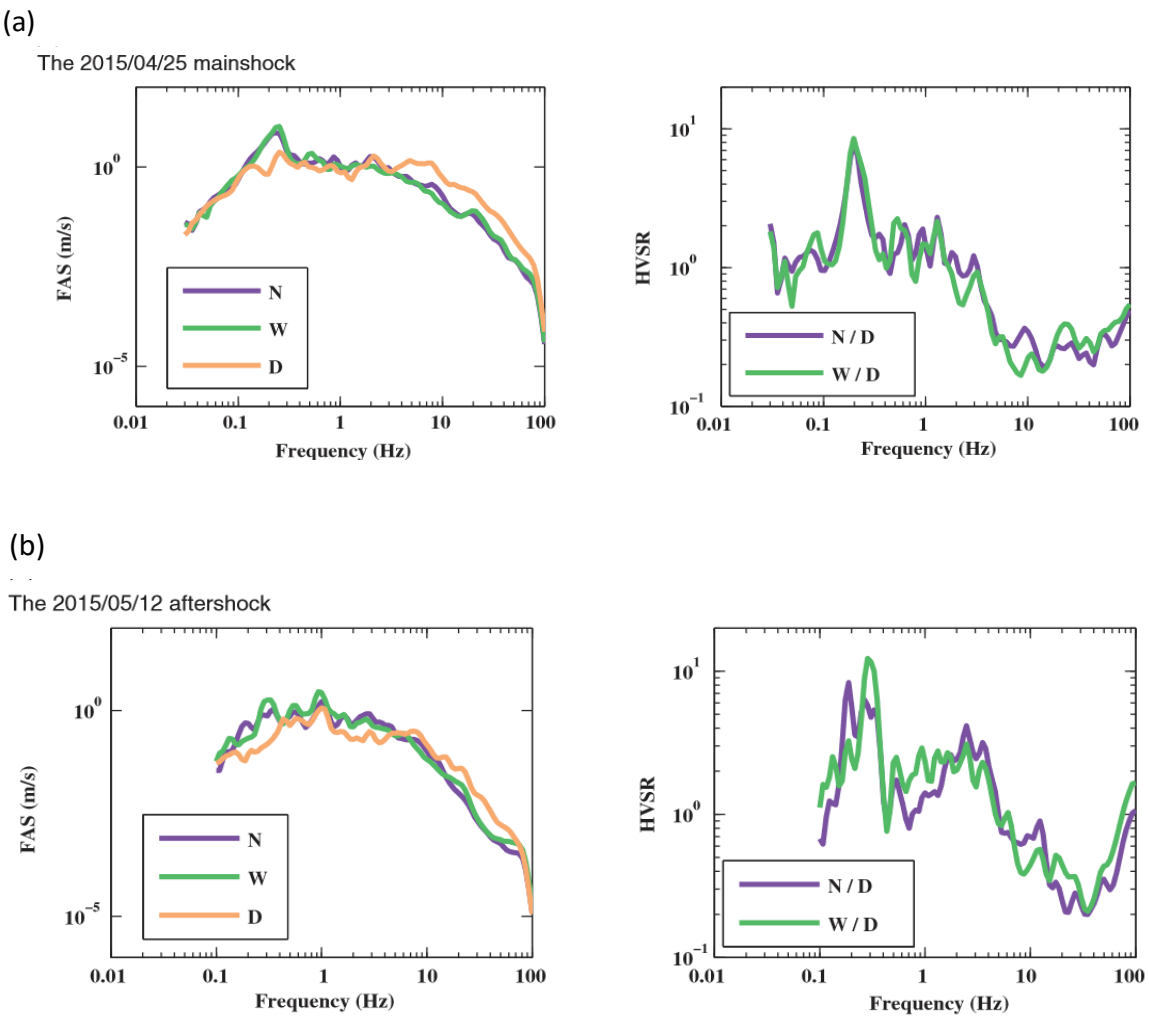

Figure 4.3 Fourier amplitude spectra (FAS) (left) and horizontal-to-vertical spectral ratios (HVSR) (right) for the mainshock (upper) and the largest aftershock (lower). FAS are smoothed using the filter Konno and Ohmachi (1998) with b = 30. FAS and HVSR are represented on the frequency band for which the signal is larger than the noise (Bhattarai *et al.*, 2015).

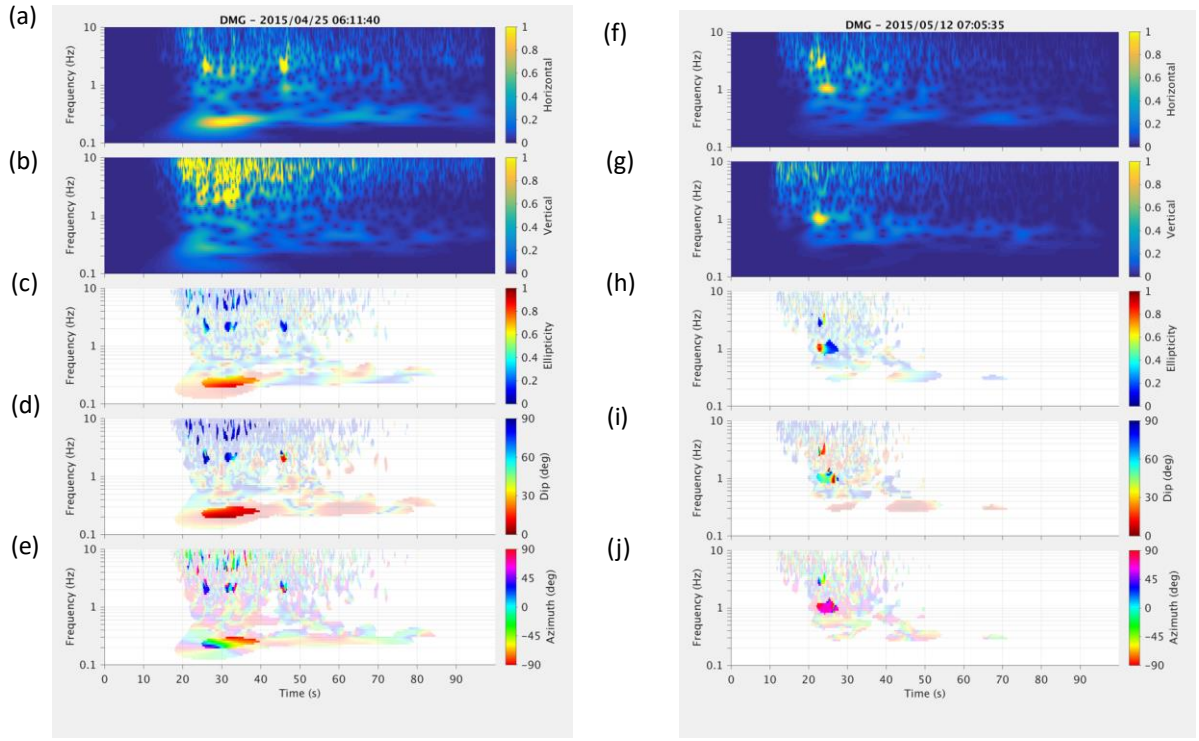

Figure 4.4 Analysis of the mainshock (left panel) and the largest aftershock (right panel). (a) and (f) Amplitude of S- spectrum of the horizontal components normalized by the maximum of the total amplitude defined as $ST_{max} max_{t,f} [\frac{1}{3}\sqrt{ST_N(t,f)^2 + ST_W(t,f)^2 + ST_D(t,f)^2}]$; (b) and (g) amplitude of the ST of the vertical component normalized by ST_{max} (note that the amplitude values above 1 may be clipped by the color scale in some places leading to some yellow patches. (c) and (h) filtered ellipticity attribute; (d) and (i) filtered dip attribute; (e) and (j) filtered azimuth attribute. In plots c, d, e, h, i and j, opacity has been used to filter the different attributes and highlight the values at which the total S-spectrum amplitude is larger than an arbitrary threshold. Lighter colors for values between 0.1 and 0.5 and brighter colors are for values above 0.5 (modified from Bhattarai *et al.*, 2015).

.

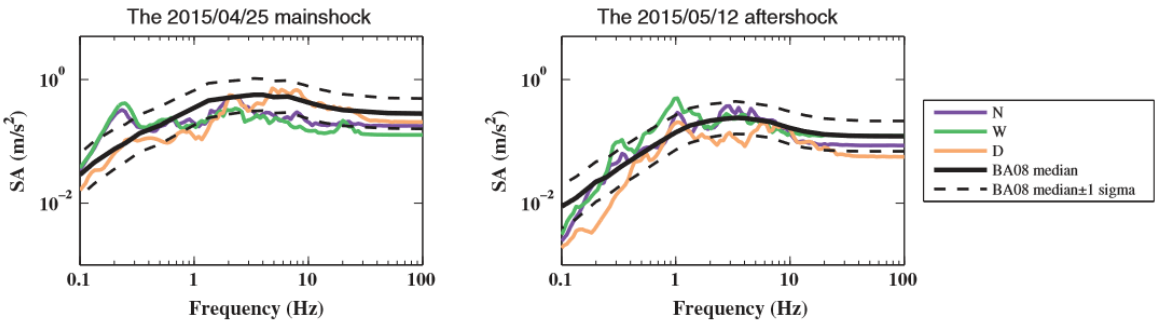

Figure 4.5 Spectral accelerations with 5% damping of the mainshock (M_W 7.8) (left panel) and that of the largest aftershock (M_W 7.3) (right panel). Response of these accelerations are compared with the GMPE Boore and Atkinson (2008). The following input parameters are used for the mainshock (left): M_W 7.8, R_{JB} 15 km, V_S 30 250 m/s, and RS 1; and for the aftershock (right): M_W 7.3, R_{JB} 65 km, V_S30 250 m/s, and *RS* 1 (Bhattarai *et al.*, 2015).

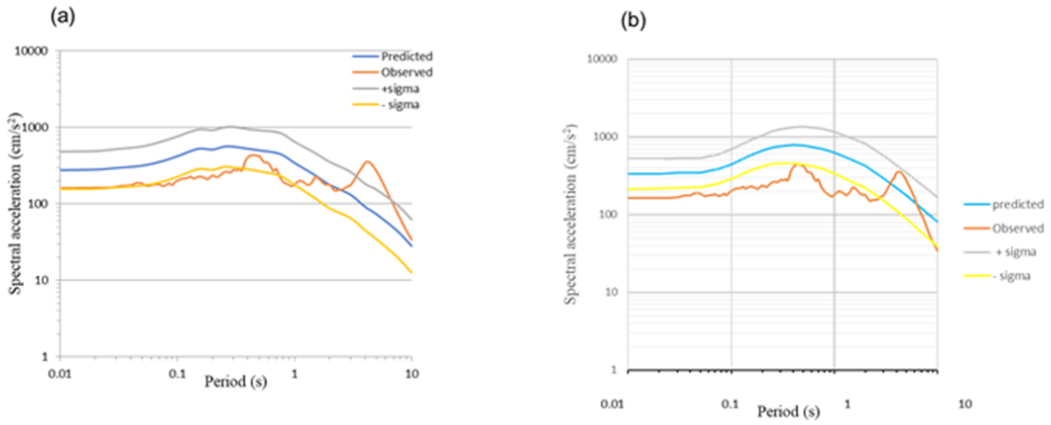

Figure 4.6 (a) Spectral accelerations with 5% damping of the mainshock (M_W 7.8) with the GMPE Boore and Atkinson (2008). The average horizontal component is compared with the other ground motion prediction equation, (b) Abrahamson and Silva (2008) which accounts the basin effect. The following input parameters are used for former (4.6a): M_W 7.8, R_{JB} 15 km, V_S30 250 m/s, and RS 1; and for the later (4.6b): M_W 7.8, R_{JB} 15 km, V_S30 250 m/s, $Z_{1.0}$ = 770 m, and RS 1 (modified from Bhattarai *et al*. (2015)).

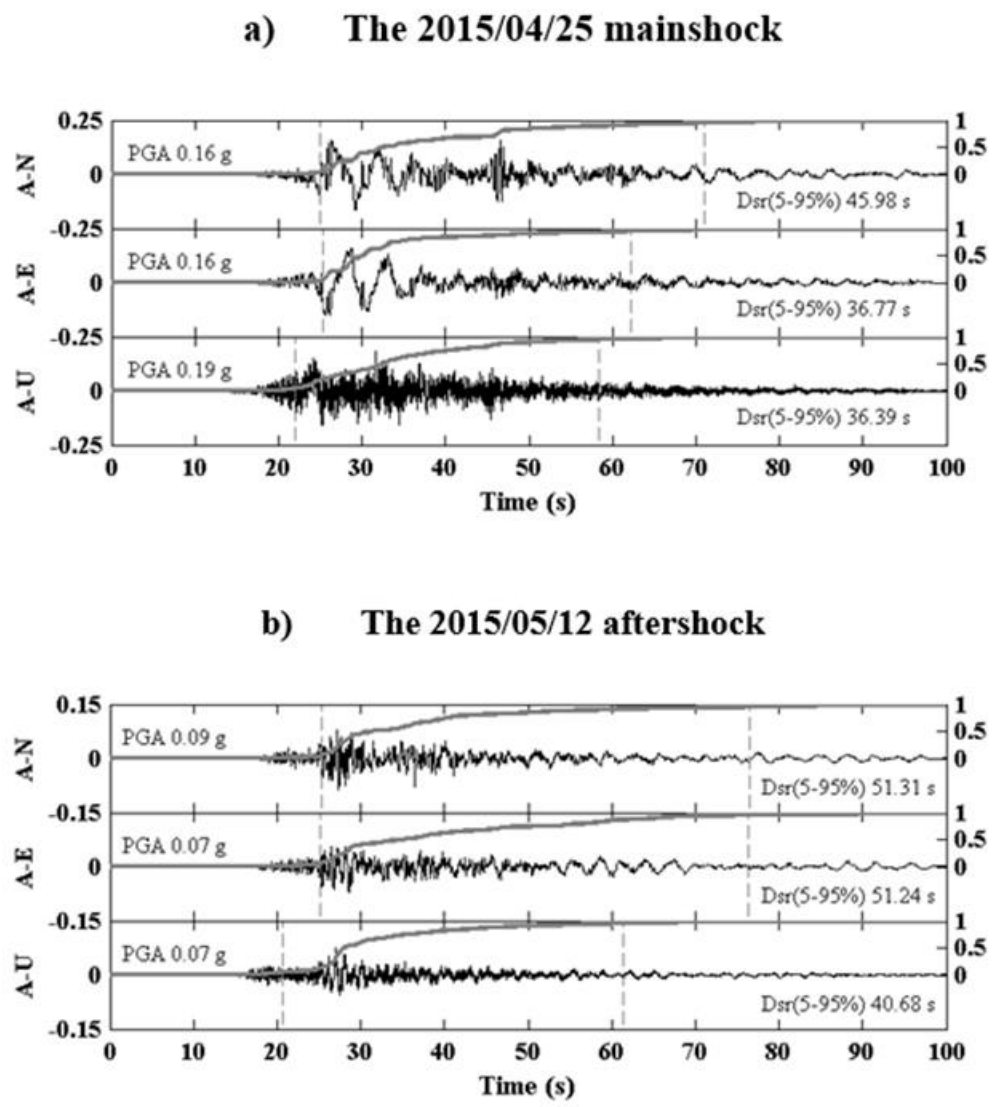

Figure 4.7 (a) Acceleration time histories in g at the station NQ.KATPN of USGS for the mainshock (M_W 7.8) and (b) for the largest aftershock (M_W 7.3). 20 s of pre-event noise are removed from the raw accelerograms. The normalized Husid diagrams are represented by the grey solid lines. The time intervals from 5 to 95% of the cumulative Arias intensity are shown by dashed grey lines. The peak ground acceleration PGA and the significant relative duration Dsr(5-95%) are indicated for each component (Bhattarai*et al.*, 2015).

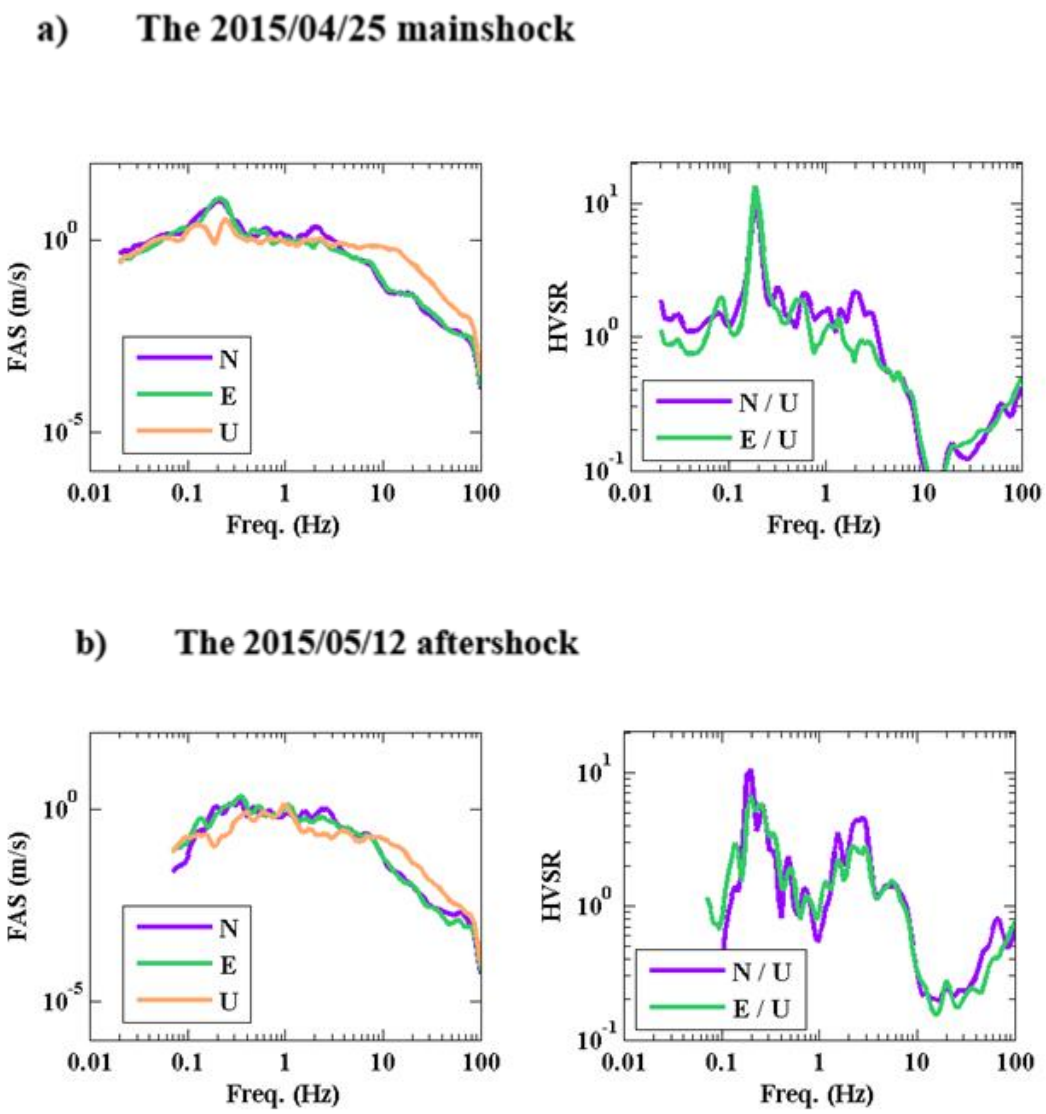

Figure 4.8 (a) Fourier Amplitude Spectra (FAS) (left panel) and horizontal-to-vertical spectral ratios (HVSR) (right panel) for the main shock recorded at NQ.KATNP. (b) That of the largest aftershock. FAS are smoothed according the filter Konno and Ohmachi (1998) with b = 30. FAS and HVSR are represented on the frequency band for which the signal is larger than the noise (Bhattarai *et al.*, 2015).

.

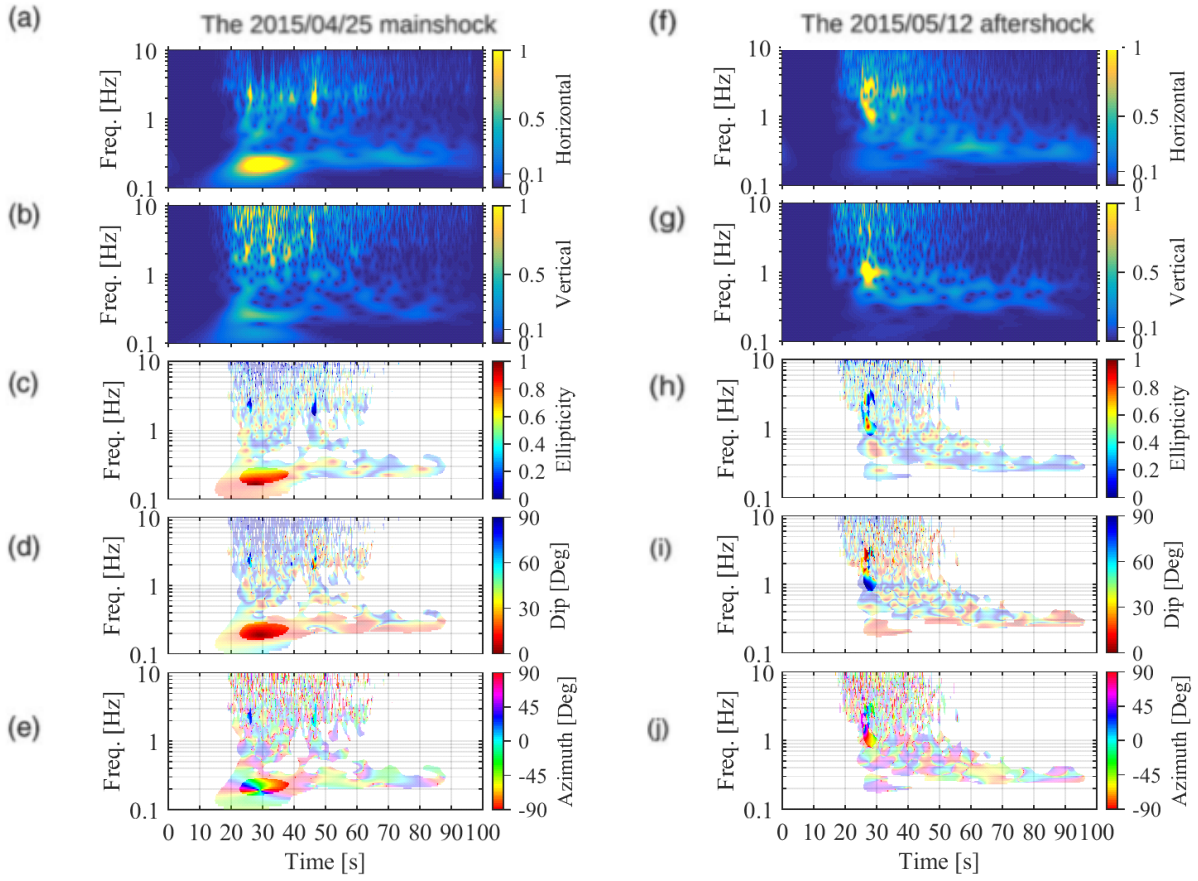

Figure 4.9 Analysis of the mainshock (left panel) and the largest aftershock (right panel) for the the events recorded at NQ.KATNP (a) and (f). S-spectrum of the average horizontal components; (b) and (g) S-spectrum of the vertical component. The spectra are normalized by the maximum total S- spectrum computed using the 3 components (note that the amplitude values above the maximum of the total S-spectrum amplitude in the horizontal and vertical spectra may be clipped by the color scale in some places leading to some yellow patches). (c) and (h) filtered ellipticity attribute; (d) and (i) filtered dip attribute; (e) and (j) filtered azimuth attribute. In plots c, d, e, h, i, and j opacity has been used to filter the different attributes and highlight the values at which the total S-spectrum amplitude is larger than an arbitrary threshold. Lighter colors for values between 0.1 and 0.5 and brighter colors for values above 0.5 (Bhattarai *et al.*, 2015).

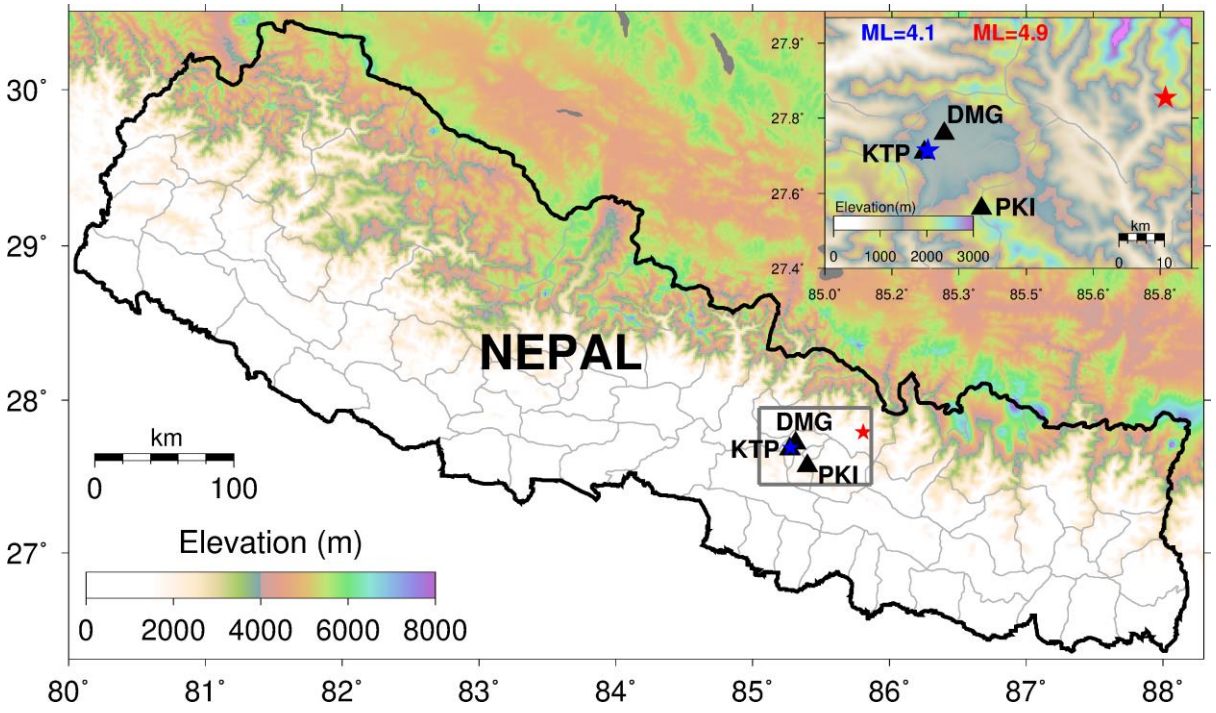

Figure 4.10 Location map of the aftershocks that occurred in the eastern part of Kathmandu valley M_L = 4.9 (red star) with epicentral distance about 110 km from DMG on 25 April 2015 and that of an aftershock of M_L = 4.1 (blue star) that occurred in the Kathmandu valley with epicentral distance about 10 km from DMG on 26 April 2015.

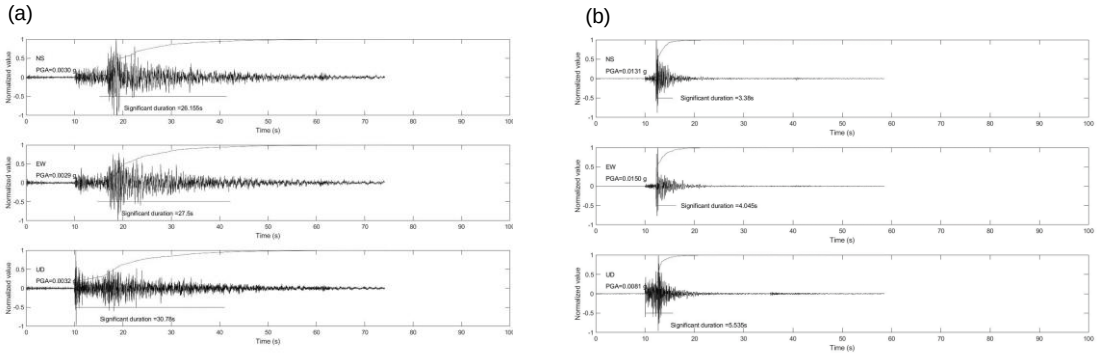

Figure 4.11 (a) Time series of the aftershock that occurred in the eastern part of Kathmandu valley (M_L 4.9) with epicentral distance about 110 km from DMG on 25 April 2015 at 08:05 and (b) that of an aftershock of (M_L 4.1) that occurred in the Kathmandu valley with epicentral distance about 10 km from DMG on 26 April 2015 at 00:15. Their normalized Husid diagrams from 5 to 95% of the cumulative Arias intensity, PGA's, and significant relative duration are also indicated.

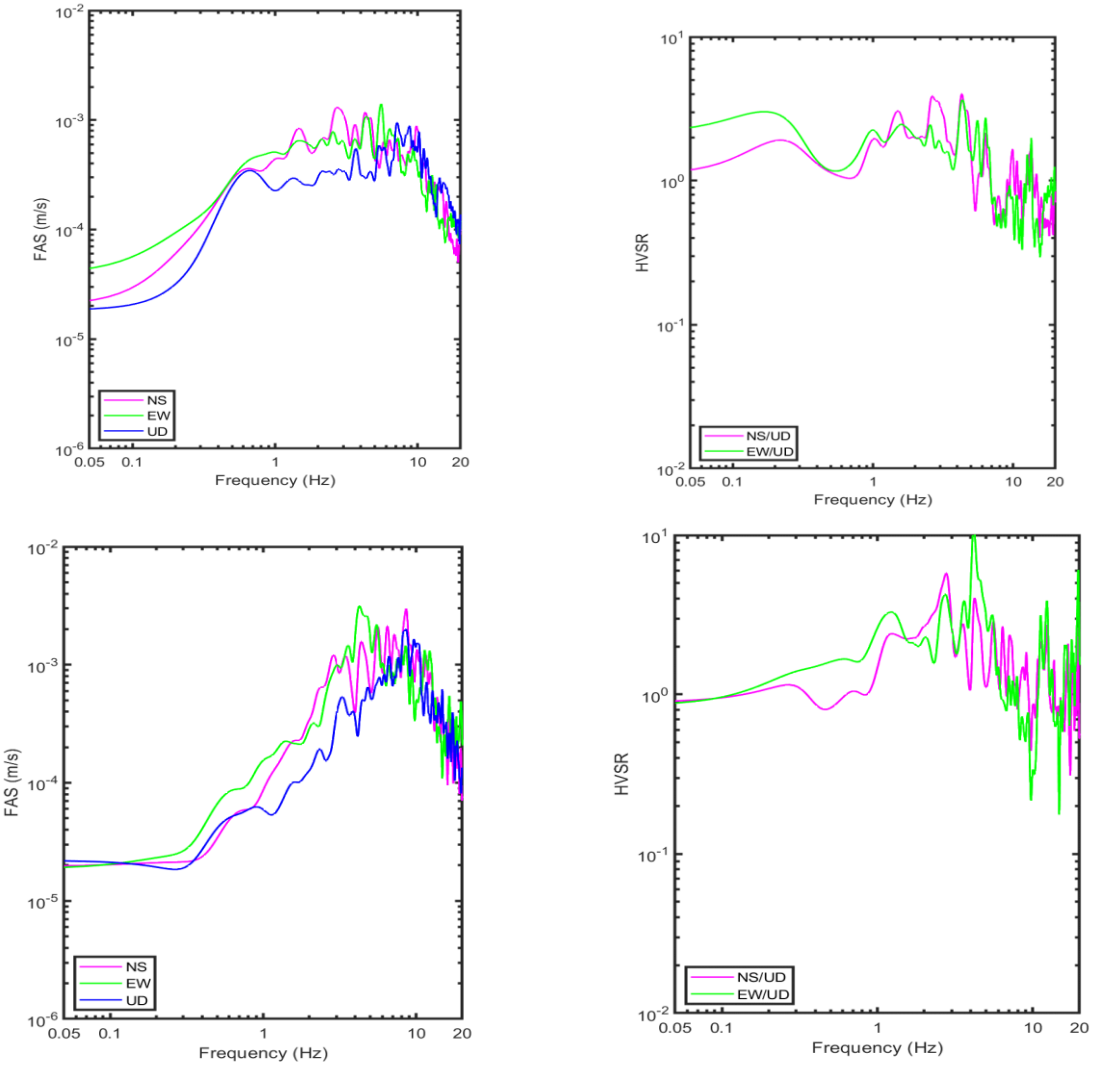

Figure 4.12 Fourier Amplitude spectra (FAS) (left) and horizontal-to-vertical spectral ratios (HVSR) (right) of the (M_L 4.9) aftershock (upper panels) and that of the aftershock (M_L 4.1) (lower panels).

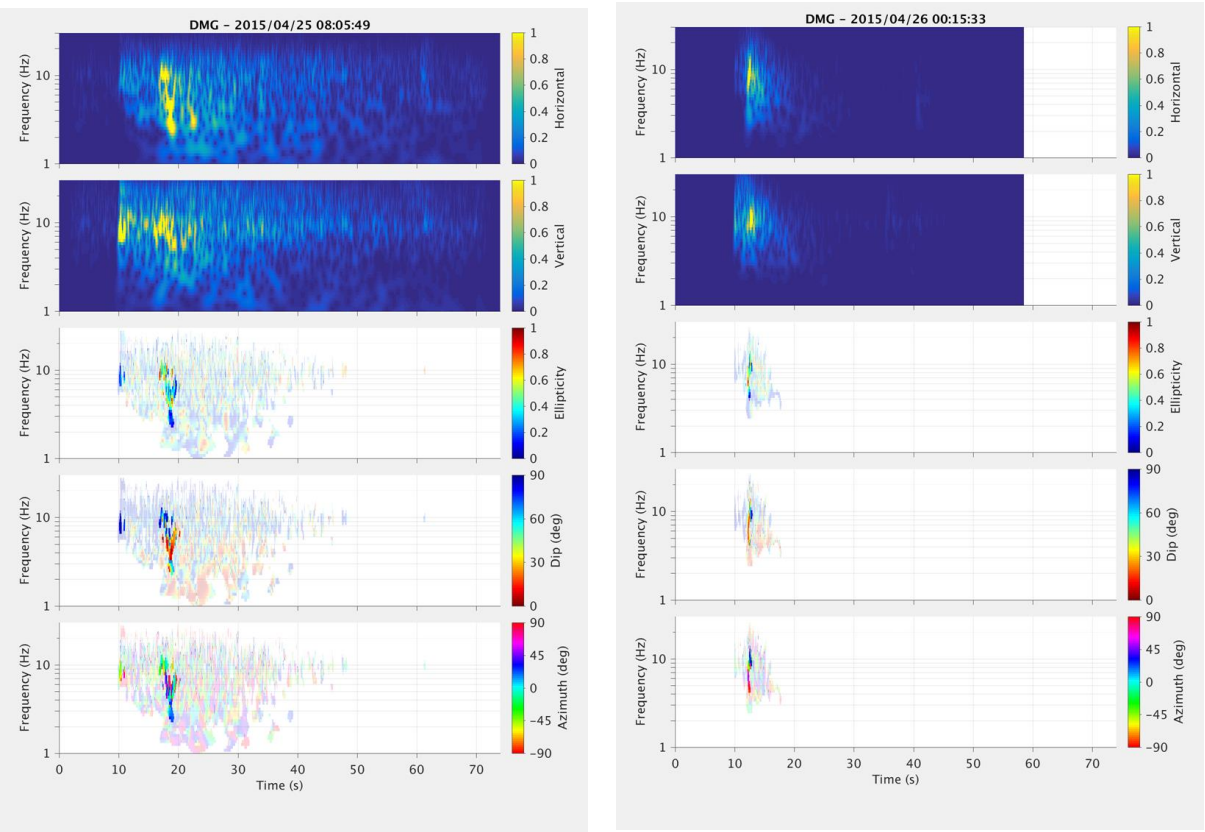

Figure 4.13 Time frequency decomposition and polarization analysis of the aftershocks M_L 4.9 (left panel) and M_L 4.1 (right panel).

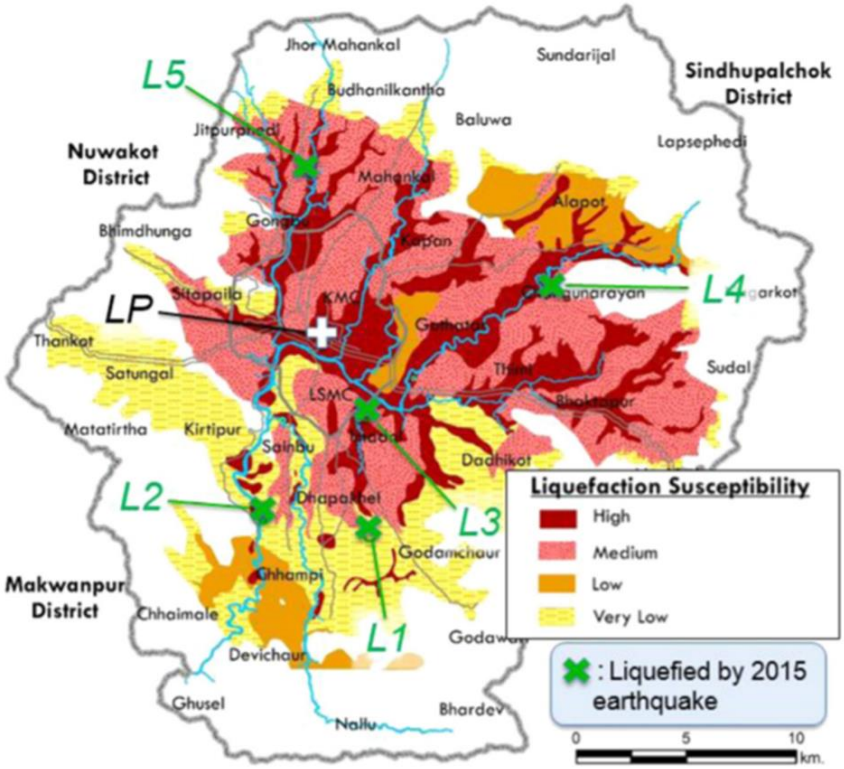

Figure 4.14 Liquefaction susceptibility map of Nepal prepared by UNDP (1994) together with the identified locations of liquefaction by the 2015 Gorkha earthquake (Okamura *et al.*, 2015).

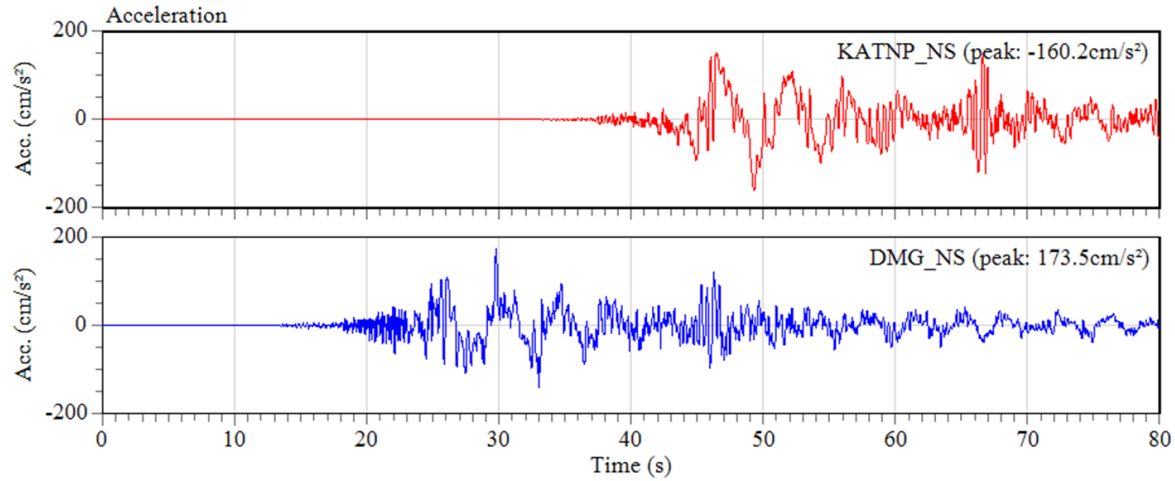

Figure 4.15 Waveform comparison in the NS components from the KATNP (upper panel) and DMG (lower panel) stations. They are located at a distance of about 800 m south in the central Kathmandu valley.

Chapter 5

Microtremor array exploration in the Kathmandu valley, Nepal

5.1 Introduction

The Kathmandu valley, roughly elliptical outline is the largest tectonic basin formed in the lesser Himalaya of central Nepal. Its approximate east-west, and north-south width is 25 km and 20 km respectively. Exposed bedrocks are mainly abundant around the hill slopes of the valley and only a few places on the valley floor. The sediments were transported from the surrounding hills to the valley and varies based on the undulated pattern of the basement. Deep boreholes results (UNDP, 1994) have shown that the shallow basement is located in the north part of the valley at around Bansbari 78 m whereas the deeper part up to 570 m at Bhrikuti Mandap at the central part of the Kathmandu valley. The northern part is influenced by silt, clay, sand, and gravel whereas the southern part is primarily rich in silt and clay (Binny and Partners, 1973). The thickness of the sediments shows variation with the undulated pattern of the basin.

Chronological history shows that recent Kathmandu valley was turned in to an old Kathmandu lake about one million years ago due to tectonic activities. The lake deposits were gradually piled in to Tarebhir, Lukundol, and Kalimati (black clay) layers, etc. after about 50 thousand years ago due to rapid water level changes several terraces face such as Tokha, Gokarna, Thimi, and Patan were formed with each elevation level. Later about 10 thousand years to today the lake water has flown out from Chobar canyon in the south part of the Kathmandu valley and recent river deposits so-called alluvial plain and valley plains were formed (UNDP, 1994). The detailed geology and geomorphology in and around the Kathmandu valley (KTV) can be described as follows (e.g., Sakai *et al*., 2016). With an average elevation of about 1,350 m, the KTV has a basement consisting of Precambrian-Devonian rocks. The rapid uplift of its southern rim dammed the proto-Bagmati River and created the Paleo-Kathmandu Lake. The KTV was then infilled witha thick sequence of semi-consolidated Plio-Pleistocene fluvial and lacustrine sediments (Sakai *et al*., 2012). At present, the surface geology of the central KTV can be divided into three main groups, as shown in

Figure 5.1b (e.g., Sakai *et al*., 2012; Sakai *et al*., 2016). Moribayashi and Maruo (1980) had conducted the gravity survey and showed the complex shape of the basement of KTV. Japan International Cooperation Agency (2018) conducted a seismic risk assessment that was mainly a survey of shallow sediments. They classified the sedimentary layers as follows: weathered rock over 600 m/s; gravelly basin-fill sediment (Tarebhir Formation: *Vs* 400 m/s to 500 m/s); thin marginal lacustrine Lukundol Formation; and black muddy lacustrine deposit under topsoil layer (Kalimati Formation: *Vs* 250 m/s to 320 m/s; Figures 3.4.2 and 3.4.3 of Japan International Cooperation Agency, 2018). The topsoil is sometimes altered with lacustrine delta deposit in the northern parts of the KTV margin, and with an alluvial fan at the southern parts.

In 1988, the Kathmandu Valley Gas project drilled at Bhirkuti-Mandap, located at a few hundred meters to the west from site 1 for the feasibility study of natural gas production (unpublished report of Department of Mines and Geology, the Government of Nepal, compiled by Japan International Cooperation Agency, 2018). They described as follows. Below thin topsoil and a coarse grain sand layer of 20 m thick, layers of clay and coarse sand of a few tens of meters thick appeared alternatively to about 520 m from the ground surface. Below, a layer of gravel with sand and a 20 m thick layer of weathered green phyllite presented, together with the appearance of non-weathered green phyllite at 570 m from the ground surface. In the description of the document of the drilling including the geological column; however, we cannot find any evidence of checking the drilled cores. Therefore, with the consideration on the purpose of the drilling, we guess that the above description of geology was done based on the observation of the cuttings filtered out from slime.

When the sedimentary layers are not horizontal such as Kathmandu valley, site effects are mainly caused by the generation of surface waves due to the lateral heterogeneity (basin edges). This phenomenon may significantly amplify and lengthen the seismic ground motions. Since the surficial sedimentary layers remarkably strength the ground motion, its structure and physical properties should be studied, to evaluate the seismic hazard. The estimation of physical parameters e.g., V_S at different depth of soil layers in the sedimentary filled valley can provide useful information on dynamic properties of soil such as dominant frequencies and site amplification which is important information for ground motion prediction of an area for the seismic hazard estimation.

Microtremors are the vibrations on the ground surface whose displacement amplitude are in the order of 10^{-4} to 10^{-2} mm; far below the human sensing (Okada, 2003). The vibration is spatially and temporally dependent and power variation is connected with atmospheric pressure. In this study long-period microtremor array measurement has been chosen as a tool to study deep shear wave velocity structures of the Kathmandu valley taking into account the source of long-period microtremor coming from the Bay of Bengal, India at a distance of about 700 km far from the Kathmandu valley by deploying the seismographs in a regular/irregular array pattern during over night measurements.

Microtremor exploration for deep sedimentary layers using broadband seismographs at three sites in the central part of the Kathmandu valley (KTV) (Figures 5.1a and b) is performed. Among the three pilot sites chosen site 2 is collocated with the strong motion observation system. Located only within 3 km, site 1 and site 2 are on the margin of the fluvio-deltaic facies where due to the repeated water level change of the Paleo-Kathmandu lake a laterally varying underground structure has been formed. Site 3 is on the soft black clay (lacustrine facies) so called Kalimati in Nepali language (Figure 5.1b).

In the Kathmandu valley strong amplification of long-period waves as 4 s (0.25 Hz) was observed (e.g., Takai *et al*., 2016; USGS, 2015a; Bhattarai *et al*., 2015) during 2015 Gorkha earthquake of M_W 7.8 (United States Geological Survey, 2015b). This notable amplification of long-period seismic waves attracted the interest of researchers of seismology and earthquake engineering, because this local site effect may play an important role again during damaging earthquakes in the future.

After the 2015 Gorkha earthquake, several studies have been focused on the site effect and one-dimensional (1-D) velocity structures below the strong motion stations in the Kathmandu valley. For example, Dhakal *et al*. (2016) tried to estimate the V_S structure of the soil site of USGS's strong motion station. They applied forward modeling of the peak-period of the horizontal to vertical spectral ratio (HVSR) of the coda of the S-waves and estimated a very low V_S structure down to the basement (V_S less than 500 m/s to 470 m depth; Figure 5c of Dhakal *et al*., 2016). They verified this result by simulating vertically propagating *SH* waves. Bijukchhen *et al*. (2017) derived the 1-D velocity model under the seven strong motion stations in the KTV by waveform modeling of long-period *S*-waves using the aftershock data from the stations reported by Takai *et al*. (2016). Their estimated V_S structures vary site by site and consist of surface layers of mainly V_S less than 500 m/s, in sharp contrast to the basement where *Vs* was set at 3,200 m/s, except at a hard rock site.

In this chapter, the results of a microtremor array exploration that have conducted at the three sites in the central part of the Kathmandu valley (Figure 5.1b), using broad band seismograph arrays to construct the 1-D velocity structures of the deep sedimentary layers are shown. The derived velocity structures are validated in the following chapters and used for the ground motion prediction and seismic hazard evaluation.

5.2 Field observation

Tables 5.1 and 5.2 (Bhattarai *et al*., 2017b) present the equipment used for field measurements and the parameter settings for field data acquisition, respectively. At each site, we realized two or three deployments. We conducted overnight measurement for each deployment to capture the long-period components of microtremors installing seismographs temporally at the administrative center site 1 (SDB), a historical museum site 2 (DMG), as well as at a natural gas well site (TEKU) site 3. In the densely built-up urban area with an irregular road pattern, it was impossible to deploy optimally shaped equilateral triangular arrays (*e.g*., Okada, 2006). Therefore, we deployed irregular shape arrays. We explained the rationale above for the analysis using the 2ST-SPAC. The only exceptional equilateral triangular arrays were the S and M arrays at site 1.

Site 1 (5.4a) has two equilateral triangular arrays: S and M Arrays marked by open circles and open diamonds, respectively, consisting of four seismographs; and a trapezium array (L Array) marked by open squares. The minimum and the maximum inter-station distances are in Table 5.2. In Figure 5.4a, a triple concentric circle marks the common central point, named as S4 or M4 of the S or M arrays, respectively.

Site 2 has three irregular fan-shaped arrays (Figure 5.4b). The point of the fans in the DMG included in three deployments is marked by a triple concentric circle. A pair of observation points formed an array (an open circle and a triple concentric circle) that gave the maximum inter-station distance 1,272 m. B and C arrays are marked by open triangles and open diamonds, respectively.

Site 3 has a scalene triangle-shaped array (S array marked by open triangles) and a trapezium array (M array marked by open squares) due to the distribution of secure places (Figure 5.4c). The Teku gas well is generally included in the S and M arrays, named as S4 or M4 and marked by a triple concentric circle. The maximum inter-station distance is 1,331 m.

5.3 Method of data analysis

5.3.1 SPatial Auto Correlation (SPAC) method

We applied the SPAC method (e.g., Aki, 1957, 1965; Okada, 2003) to the records of long-period microtremor captured using broadband seismographs. Aki (1957; 1965) defined for an incoming plane wave, the SPAC coefficient $\rho_{obs}(\omega, r)$ as the real part of the cross-spectra between two positions $\boldsymbol{c}(r = 0, \theta = 0)$ and $\boldsymbol{x}(r,\theta)$, that is normalized by the power spectra at $\boldsymbol{c}$. In the cylindrical coordinate system, it is described as follows,

$$\rho_{obs}(\omega; r) \equiv \frac{1}{2\pi}\int_0^{2\pi} \frac{Re\{S_{cx}(\omega;r,\theta)\}}{S_{cc}(\omega;0,0)} d\theta, \qquad (5.1)$$

where ω denotes angular frequency, and r and θ are the distance and azimuth, respectively, from $\boldsymbol{c}$ to $\boldsymbol{x}$. $\boldsymbol{c}$ represents the center of a circular array, whereas $\boldsymbol{x}$ indicates a position on the peripheral circle of array. $S_{cx}(\omega; r, \theta)$ is the cross-spectra between the ground motion at $\boldsymbol{c}$ and $\boldsymbol{x}$ due to laterally propagating Rayleigh waves, whereas $S_{cc}(\omega; 0, 0)$ is the power spectra at $\boldsymbol{c}$. Aki (1957; 1965) theoretically showed that this $\rho_{obs}(\omega, r)$ becomes $J_0(\omega r/\mathrm{c}(\omega))$, *i.e.*, the 0-th order Bessel function of the first kind with argument $\omega r/\mathrm{c}(\omega)$. Under the assumption that the power spectra of laterally propagating Rayleigh waves are constant within the array $S_{cc}(\omega; 0, 0) = S_{xx}(\omega; r, \theta)$, we can replace $S_{cc}(\omega; 0, 0)$ in the integrand of Equation 5.1 by $\{S_{cc}(\omega; 0, 0)\ S_{xx}(\omega; r, \theta)\}^{1/2}$. Then, the integrand itself becomes the coherence of laterally propagating Rayleigh waves $Coh_{cx}(\omega; r, \theta) = Re\{\ S_{cx}(\omega; r, \theta)\}/\{S_{cc}(\omega; 0, 0)\ S_{xx}(\omega; r, \theta)\}^{1/2}$. This is almost equal to the coherence of the surface ground motion at the two positions $Coh^{obs}{}_{cx}(\omega; r, \theta) = Re\{\ S^{obs}{}_{cx}\ (\omega; r, \theta)\}/\{S^{obs}{}_{cc}(\omega; 0, 0)\ S^{obs}{}_{xx}(\omega; r, \theta)\}^{1/2}$, except the influence of the phase difference due to very local site effect at $\boldsymbol{c}$ and $\boldsymbol{x}$. Under the assumption that this influence can be negligible, we can use $Coh^{obs}{}_{cx}(\omega; r, \theta)$ in place of the integrand of Equation 5.1 as Okada *et al*. (1987) had introduced. The first assumption is probable for a small wavenumber, i.e., long wavelength range, and is useful for the SPAC application, whereas the second one can be fulfilled by a careful site selection.

5.3.2 2-Site SPAC Method (2ST-SPAC)

According to Shiraishi *et al*. (2006) who formulated the coherence function by analyzing the vertical component of single-mode Rayleigh waves emitted from point sources far from ***c*** and ***x***, $Coh_{cx}(\omega; r, \theta)$ can be written $\Sigma^{L}_{l=1}\lambda_{cxl}cos\{krcos(\theta_l-\theta)\}$, where $k = \omega/c(\omega)$ denotes the wavenumber, and λ_{cxl} the rate of the contribution of the *l*-th uncorrelated point source at azimuth θ_l to the power spectra at ***c*** and ***x***. By their assumption of sufficiently far point sources, the λ_{cxl} can be considered a coefficient describing the rate of the contribution of plane waves coming from the azimuth θ_l. The value of λ_{cxl} falls between zero and unity, and its summation over *l* becomes the unity. The mathematical formula $cos(krcos\theta) = J_0(kr)+2\Sigma_{n=1}(-1)^n J_{2n}(kr)cos2n\theta$ shows the notable thing that $J_0(kr)$ is already included in every plane wave $cos(krcos\theta)$ and is enhanced by the summation over *l* because it is always *in-phase*, whereas $\lambda_{cxl}cos2n(\theta_l-\theta)$ in the second term oscillates faster for bigger *n* and their contribution in total is suppressed by the summation over *l*. Then, $Coh_{cx}(\omega; r, \theta)$ can be modified as follows,

$$\sum_{l=1}^{L}\lambda_{cxl}cos\{krcos(\theta_l-\theta)\} = J_0(kr)$$

$$+2\sum_{n=1}^{\infty}[(-1)^n J_{2n}(kr)\times\sum_{l=1}^{L}\lambda_{cxl}\,cos\{2n(\theta_l-\theta)\}], \quad (5.2)$$

where *2n* denotes the even order of the Bessel function of the first kind. Therefore, the 2ST-SPAC is possible simply when the second term of the right member of Equation 5.2 is sufficiently suppressed, i.e., the dependency of λ_{cxl} on $(\theta_l-\theta)$ is sufficiently moderate. We should note that this depends on the characteristics of the microtremor wave field and the 2ST-SPAC is not always possible. In practice, the integration over the azimuth in Equation 5.1 is replaced by the summation of the integrand over the evenly allocated stations along a circle. Okada (2006) showed that the equilateral triangle can give a good approximation, and this is currently considered the optimum way.

From the SPAC coefficients $\rho obs(\omega, r)$ the phase velocity $c(\omega)$ is determined as the value that minimizes the misfit function $(1/Nr)\,\Sigma r\{|\rho obs(\omega,r)-J_0(\omega r/c(\omega))|^2\}$, where the summations are taken over the inter-station distances, Nr the number of $\rho obs(\omega, r)$ considered at each ω. The above-mentioned theories stand for station pairs oriented to few or several azimuths. It has been said that plane waves incoming from various azimuths to a fixed station pair may make

the SPAC application possible. Chavez-Garcia *et al*. (2005; 2006) obtained successful results in a field experiment using linear arrays and measurements over a long duration. In addition, the SPAC is robust against the moderate dependency of the microtremor field on incoming azimuths, as numerically tested by Cho *et al*. (2008). Hayashi and Craig (2016) showed successful examples of real observation using irregular shape arrays, where the coherence of individual station pairs without azimuthal average played the role of the SPAC coefficient. They called the approach the 2ST-SPAC, because of its field application skipping the azimuthal average, and of the way to determine the dispersion curve by fitting to $J_0(\omega r/c(\omega))$ same as the SPAC.

In this study, we first confirmed the isotropic nature of the coherence functions $Cohobscx(\omega; r, \theta)$, using one of the equilateral triangle arrays at site 1, then applied 2ST-SPAC to irregular shape arrays.

5.4 Data Processing

5.4.1 Site 1

Figure 5.5a shows the power spectral density of three components acceleration at M4 (S4) without any spectral smoothing, that have peaks at around 4 s and 0.4 s (2.5 Hz). Despite observation at the ground surface in an urban area, the power of short-period microtremor at night is above the New High Noise Model (NHNM, Peterson, 1993). Power of long period microtremor is between NHNM and the New Low Noise Model (NLNM, Peterson, 1993). The coherence functions for M array in Figure 5.5b are grouped in two: those of inter-station distance 417 m (dashed curves), and those of inter-station distance 241 m (solid curves). These show an approximately isotropic nature of microtremor and give the base of applicability of the 2ST-SPAC skipping azimuthal average which we applied to the L array of site 1 and all deployments at the other two sites. To M and S arrays of site 1 we applied the azimuthal average. On the other hand, their decaying feature at a low frequency side shows the limit of analysis at around 0.2 Hz (5 s). This is observed not only in M array but also in others and directly reflected on the SPAC coefficient curves of site 1 (Figure 5. 5c) that show normal features without any significant disturbance throughout the targeted frequency range above the frequency limit of analysis.

Figure 5.5d shows the misfit function and the determined dispersion curve on

frequency-phase velocity panel. The determined dispersion curve crosses the upper and lower limits of “the reliable range” at 0.9 Hz and 0.54 Hz, respectively, and the lower frequency limits of “the acceptable range” and “critical range” at 0.31 Hz and 0.24 Hz, respectively (e.g., Cornou *et al*., 2006). The maximum phase velocity was around 1,500 m/s at 0.215 Hz. The phase velocity gradually decayed toward the higher frequency, taking the value of 486 m/s at 0.5 Hz. It, then started decaying again, taking a value of 245 m/s at around 0.9 Hz.

In the range of the heuristic search for inversion, a sharp discontinuity was set between the fifth layer and underlying half space with the expectation of fitting this discontinuity to the top of the basement below the KTV (Table 5.4). Figure 5.5f shows that the observed dispersion curve was sufficiently fitted to the theoretical one calculated using the estimated V_S structure in Figure 5.5e and Table 5.5.

5.4.2 Site 2

The analysis was conducted using the 2ST-SPAC. Then, the coherence functions of each station pair were directly used as the SPAC coefficient curve (Figure 5.6a). Some curves show anomalous sag at around 0.3 Hz. The deeper sags weakly tend to appear in the curves of longer inter-station distances, but not exactly follow the order. A clear decay of the SPAC coefficient curves is observed below 0.2 Hz as well as site 1. The determined dispersion curve had a winding part at around 0.3 Hz that was eliminated from the inversion as shown in Figure 5.6c (small grey curve). This part was eliminated from the analysis in the next process. The anomalous phenomenon itself is discussed below.

The inversion was conducted using the search range in Table 5.4. Instead, 700 m/s and 900 m/s were used for the c_{max} of the third and fourth layers, respectively. Figure 6b shows the V_S structure inverted from the determined dispersion curve with the SD of the structural parameters. A sufficiently good fitting of dispersion curves is shown in Figure 5.6c.

5.4.3 Site 3

The analysis was conducted using the 2ST-SPAC. Sharp sags were observed in all SPAC coefficient curves at around 0.3 Hz (Figure 5.7a). A clear decay of the SPAC coefficient curves is observed below 0.2 Hz as well as the other two sites. The determined dispersion curve showed a winding part at around 0.3 Hz that was eliminated from the inversion as well as site 2 (small grey curve in Figure 5.7c). This anomalous phenomenon

itself is discussed below. Inversion was conducted using the search range in Table 4, instead using 600 m/s for the c_{max} of the third layer. The V_S structure was inverted from the determined dispersion curve and the SD of the structural parameters were estimated (Figure 5.7b). The theoretical dispersion curve calculated using the structure in Figure 5.7b sufficiently fits the observed one (Figure 5.7c).

5.4.4 Inversion from Rayleigh waves' dispersion curves

We performed the estimation of the V_S structure from the determined dispersion curves using a heuristic search that was a combination of the very fast simulated annealing (VFSA, Ingbar, 1989) algorithm and the downhill simplex method (DHSM; e.g., Nelder and Mead, 1965; Press *et al*., 2002) with the parameters t_0 =1.0, α = 0.6, and c = 1.3 (Yokoi, 2005). These parameters describe the cooling schedule $t_k = t_0 \exp(-ck^{\alpha}\omega)$, where t_k denotes the temperature at the kth step (Ingber, 1989; Yamanaka, 2004). We used the software package DISPER80 (Saito, 1978) to calculate the phase velocity, energy integral, and eigen function of the Rayleigh waves. We calculated the density and *P*-wave velocity of each layer at each iterative step using the empirical formula of Ludwig *et al*. (1970) for the density, $\rho = 1.2475+0.399V_p-0.026V_p^2$, and Kitsunezaki *et al*. (1990) for the *P*-wave velocity, $Vp = 1.11Vs+1.29$ in Km/s, respectively.

We estimated the standard deviation (SD) of the structural parameters by taking the following steps. We calculated: first the averages of the above mentioned three quantities $S^{obs}_{cc}(\omega; 0, 0)$ $S^{obs}_{xx}(\omega; r, \theta)$, and $Re\{S_{cx}(V_s; r, \theta)\}$ over the time-blocks survived from the screening; their variances and the covariance among them using the deviation of every used time-blocks from the average; the SD of the SPAC coefficient curves from these variances and covariances following the error propagation theory; the SD of the dispersion curve based on the SD of the SPAC coefficient curves using the partial derivatives of the dispersion curves to structural parameters calculated about the solution of the inversion using the finite difference formulation. Finally following Equation 5 of Lai *et al*. (2005) we estimated the SD of the structural parameters from the SD of the dispersion curves and these partial derivatives. To the microtremor data we applied the multiplexing, resampling to a sampling interval of 0.25 s, and division into the time blocks of 1024 samples. Then we screened out time-blocks if they contained impulsive noises caused by traffic or significantly big root mean square (RMS) amplitude. Table 5.3 shows the number of time blocks that survived after screening.

We calculated the cross spectra for the selected inter-station distances with padding zeros to create a sufficiently fine frequency interval. We performed the inversion using VFSA-DHSM for the selected structural parameters: thickness and *Vs* of five surface layers and *Vs* of the underlying half space (Table 5.4).

The dispersion curves determined above for three sites decrease almost monotonically toward the higher frequency, except in the frequency range of the problem of winding as mentioned above (Figures 5.2). These dispersion curves almost fall within the SD of that of site 1 (grey shadow in Figure 5.2). The inversion eliminating the phase velocity data within the frequency range of the problem from the analyses gives us the three V_S structures shown in Figure 5.3, which are almost consistent mutually, even though below 500 m they show a notable deviation. In the next section, we discuss the anomalous winding parts of the determined dispersion curves and the uncertainty of the estimated V_S structure.

5.5 Results and discussion

5.5.1 Anomalous feature of the coherence functions and the dispersion curves

The winding parts of the dispersion curve in the frequency range at around 0.3 Hz for sites 2 and 3 (Figures 5.6c and 5.7c) potentially implies the influence of the higher modes of Rayleigh waves. When the contribution of the first higher mode is not negligible, the apparent phase velocity derived from the usual SPAC application does not represent the true phase velocity, but a mixture of the fundamental and the first higher modes (e.g., Tokimatsu *et al*., 1992; Yokoi 2010; Asten *et al*., 2014). The power partitioning ratio of these two modes controlsthe way of mixing. If the first higher mode dominates a frequency range and the fundamental mode does outside this frequency range, the apparent dispersion curve looks like an anomalous winding part at around this frequency range.

The theoretically calculated power partitioning ratio of the first higher mode to the fundamental mode of Rayleigh waves in the V_S structure of site 3; however, reveals that the power of the first higher mode is not significant over the analyzed frequency range in comparison with that of the fundamental mode. For the frequency range of interest (dashed rectangular in Figure 5.8c), this ratio doesn’t exceed 10%, and cannot cause the migration of the dispersion curve from the fundamental mode to the first higher mode (Figure 5.8c).

Consequently, the influence of the first higher mode could not explain the winding dispersion curve found in this study.

Another potential explanation for the sags in the coherence function (Figure 5.8a) that cause the winding dispersion curves might be the lack of power of the microtremor in the mentioned frequency range. In this study; however, the frequency range of the problem includes the bump of the power spectra (e.g., Figure 5.5a). Therefore, the power of microtremor is sufficiently big in the mentioned frequency range. Moreover, the minimum value of the coherence, -0.637 in Figure 5.8b, doesn't mean the dominance of the incoherent waves that may result from coherence value close to 0.0, but rather coherent ones with a significantly shifted phase in the mentioned frequency range.

We can interpret the winding feature of dispersion curves also like a split of the dispersion curves due to the laterally changing shape of velocity discontinuity. Figure 5.7 of Hayashi and Suzuki (2004) shows a numerical example. As the KTV is a basin in a mountainous area, it is easy to envision a steep lateral variation of the basement. We; however, don't have enough information to ensure that this is the case. We need further careful and quantitative studies to reveal what is going on there.

5.5.2 The uncertainty of deep structure

Here, the uncertainty of estimated structure is considered based on the influence of the standard deviation (SD) and sensitivity of dispersion curve to the structural parameters, using site 1 to simplify the discussion because this site doesn't have the problem of the winding dispersion curve.

The influence of the SD of the dispersion curve is visualized in the following two ways. First, in Figure 5.9 the inverted V_S structure from the average dispersion curve (solid black curve, hereafter, called the Reference) and the SD of the structural parameters (light grey shadow) estimated from the SD of the dispersion curve (grey shadow in Figure 5.2) is discussed. From the ground surface to a depth of about 500 m, the structure is well determined as indicated by the light grey shadow that is narrow both horizontally (V_S) and vertically (depth). In the deepest part; however, this shadow becomes much wider (Figure 5.9). Second, we show the other two structures inverted from the dispersion curves that are the average plus and minus one SD, namely, the upper and lower limit of the grey shadow in

Figure 5.2. These structures fall in the light grey shadow except for the deepest part. Particularly, V_S of the half space deviates outside the light grey shadow (Figure 5.9).

We can interpret this big deviation of V_S in the half space based on the lack of a flat part of the dispersion curve in the low frequency range (Figure 5.3), because we do not know how high the phase velocity can reach in the low frequency range where we could not determine dispersion curves. For example, the maximum determined phase velocity of site 1 is about 1,500 m/s at 0.2 Hz (Figure 5.2), whereas the estimated V_S of the half space was over 2,200 m/s (Table 5.5). This strongly implies that other solutions can fit the dispersion curves in an acceptable way, because of the trade-off relationship between V_S and the depth of the half space. Consequently, the depth of the half space has a big SD, too. This influences the 5-th layer immediately above the half-space, again due to the trade-off relationship between V_S and the layer's thickness. This chain reaction doesn't continue to the 4-th and shallower layers due to the constraint given by the dispersion curve itself. This constraint depending on the depth may have the base in the sensitivity of dispersion curves to the structural parameters of each layer. The uncertainties of V_S and depth are plotted in Figures 5.10a, b, and c.

We test an alternative structure (hereafter, called the Alternative) to consider the influence of sensitivity of dispersion curve to the structural parameters on the uncertainty of estimated structure. For the Alternative, the search range was intentionally set to put the depth of the half space at around 600 m and the V_S of the layers similar to those of the Reference (Figure 5.11a). Therefore, this Alternative doesn't have objectivity, especially at the deepest part. The Alternative roughly traces the upper limit of the grey shadow of the deepest part, i.e., the average structure plus one SD of structural parameters (Figure 5.11a). Figure 5.11b shows an excellent fitting of the calculated dispersion curve of the Alternative to that of the Reference and to the observed curve. The value of the misfit function at the termination of iteration for the Alternative is bigger than that for the Reference. This means that the Alternative is not the solution of the minimum misfit within the search range shown in Table 5.4. Therefore, in the context of minimizing the misfit function, the Reference seems advantageous if additional information such as the geological data from a drilling survey is not available.

The difference between the two calculated dispersion curves is smaller than 3% of the phase velocity of the Reference, except in the frequency ranges lower than 0.217 Hz, where the difference is between 3-4%. This very slight difference shows that dispersion curves are not sensitive enough to distinguish the Alternative from the Reference and other structures between or around them. Figure 5.11c shows the sensitivity of the dispersion curve of the Reference to the structural parameters calculated using the finite difference formulation (e.g., Shen *et al.*, 2016). All shown curves are normalized by the corresponding parameter of the 2nd layer. At the frequency range above 0.3 Hz the sensitivity to the 5-th layer's thickness is less than 0.001 and to V_S less than 0.01. Below 0.3 Hz these sensitivities become comparable with those of shallower layers, but on the other hand the SD of the observed dispersion curve increases in this frequency range. The sensitivity to V_S of the underlying half-space is much less than those of the layers (the right panel of Figure 5.11c). We consider that the absence of dispersion curve below 0.2 Hz causes the uncertainty of the deepest part. The impossibility of determinations there due to the decay of coherency (Figures 5.5c, 5.6a, and 5.7a) may be caused by a low signal to noise ratio (S/N), although the broadband seismic sensor had adequate frequency coverage (from 0.033 to 50 Hz, Table 5.1). We guess that in this frequency range, microtremor waves are not amplified in the KTV, at least within the records used in this study. Further studies using different methods will be needed to determine the dispersion curves below 0.2 Hz or to estimate directly the underground strucutre below about 500 m.

By the above discussion, we recognize a considerable uncertainty in the estimated structures, in particular, in the structural parameters at the deepest part, i.e., below a depth of about 500 m. Above discussion suggests a generalized recommendation that we should check the range of the explorable depth in terms of the sensitivity of dispersion curve to structural parameters when covered frequency range is limited. Especially, dispersion curves without flat part at low frequency side cannot provide accurate information of V_S and the depth of underlying half-space.

5.6 Conclusions

In this chapter microtremor array exploration for the deep sedimentary layers at three sites located in the central part of the KTV is performed. The data are analyzed using the SPAC of regular shape array and the 2ST-SPAC with irregular shape arrays in the frequency range below 1 Hz. The appropriateness of the 2ST-SPAC is supported by the isotropic characteristics of the coherence functions checked using the records of regular shape array at the site 1. A disturbance on the dispersion curve at sites 2 and 3; however, is detected in the frequency range from 0.25 to 0.35 Hz, caused by the anomalous behavior of the coherence function in the same frequency range. A quantitative check of the influence of the first higher mode showed that it could not explain this unusual wave phenomenon. The coincidence of the frequency range of the power spectral peak denied the influence of low S/N in this frequency range. The influence of the lateral variation of the underground structure is then estimated, it is; however, left to further studies to clarify the details.

Especially for site 1 without the disturbance, a virtual blind test is conducted. That is, we calculated the inversion without using the existing geological information from drilling, and estimated bedrock depths of over 750 m, at sites 2 and 3, showing a notable discrepancy with the observed geological information. A detailed consideration of the standard deviation (SD) and sensitivity of dispersion curves; however, showed substantial uncertainty for the V_S of the underlying half space, the layer immediately above, and its thickness. From the sensitivity of the dispersion curve to the structural parameters it is surmised that this uncertainty is caused by the lack of the determined phase velocity below 0.2 Hz. For the other two sites, this uncertainty may present in the same way.

The V_S structures > 2,000 m/s is determined deeper than 600 m at three sites. V_S is roughly 200 m/s or slower at the shallowest layer, then gradually increases. The layer of V_S 400 m/s appears at depths from 160 to 180 m. V_S then reaches over 550 m/s from 260 to 300 m. This V_S structure seems unusually slow and deep among basins in mountainous regions and implies that a rare tectonic process contributed to the formation of the KTV, a steeply deep tectonic basin. Further studies are required using different methods, for example, utilization of tectonic earthquakes' records to determine the dispersion curves below this current frequency limit of analysis.

5.7 References

Aki, K. (1957). Space and time spectra of stationary stochastic waves, with special reference to microtremor, *Bull. Earthq. Res. Inst.*, Tokyo Univ., **35**, 415-456.

Aki, K. (1965). A note on the use of microseisms in determining the shallow structures of the earth's crust, *Geophysics*, **30**, 665-666.

Asten, M. W., A. Askan, E. E. Ekincioglu, F. N. Sisman, and B. Ugurhan (2014). Site Characterization in north-western Turkey based on SPAC and HVSR analysis of microtremor noise, *Exp. Geophysics*, **45**, 74-85.

Bhattarai, M., L. B. Adhikari, U. P. Gautam, A. Laurendeu, C. Labonne, R. Hoste-Colomer, O. Sebe, and B. Hernandez, (2015). Overview of the large 25 April Gorkha, Nepal, earthquake from accelerometric prospectives, *Seismol. Res. Lett*., **86**, 40-48.

Bhattarai, M., D. Nepali, S. Dhakal, S. Shrestha, T. Yokoi, and T. Hayashida (2017a). Microtremor array exploration for deep sedimentary layers in the central part of the Kathmandu valley, Nepal, *13th Annual Meeting of Japan Association for Earthquake Engineering*, Tokyo.

Bhattarai, M., D. Nepali, S. Dhakal, S. Shrestha, T. Yokoi, and T. Hayashida (2017b). On Anomalous Coherence Functions for SPAC Method Applied in Kathmandu, Nepal for Exploring Deep Sedimentary Layers, 137th SEGJ Conference, *Society of Exploration Geophysicists*, Kanagawa.

Bijukchhen, S. M., N. Takai, M. Shigefuji, M. Ichiyanagi, T. Sasatani, and Y. Sugimura (2017). Estimation of 1-D velocity models beneath the strong motion sites in the Kathmandu Valley using strong motion records from moderate-sized earthquakes, *Earth Planets Space*, **69(97)**, doi: 10.1186/s40623-017-0685-4.

Binne and Partners, Inc. (1973). Geology of the Kathmandu valley, Ground water investigations, Kathmandu water supply and sewerage system, WHO project, Nepal 0025, *A report submitted to the Government of Nepal*.

Chavez-Garcia, F. J., M. Rodriguez, and W. R. Stephenson (2006). Subsoil structure using SPAC measurements along a line, *Bull. Seismol. Soc. Am.*, **96**, 729-737.

Chavez-Garcia, F. J., M. Rodriguez, and W. R. Stephenson (2005). An alternative approach to the SPAC analysis of microtremors, Exploiting stationarity of noise, *Bull. Seismol. Soc. Am*., **95**, 277-293.

Cho, I., T. Tada, and Y. Shinozaki (2008). Assessing the applicability of the spatial autocorrelation method, A theoretical approach, *Geophys. J. Int*. 113, B06307, doi: 10.1029/2007JB005245.

Cornou, C., M. Ohrnberger, D. M. Boore, K. Kudo, and P. -Y. Bard (2006). Derivation of structural models from ambient vibration array recordings: results from an international blind test, Proceedings of the Third *International Symposium on the Effects of Surface Geology on Seismic Motion*, NBT, Grenoble, France.

Dhakal, Y. P., H. Kubo, W. Suzuki, T. Kunugi, S. Aoi, and H. Fujiwara (2016). Analysis of strong ground motions and site effects at Kantipath, Kathmandu, from 2015 M_W 7.8 Gorkha, Nepal earthquake and its aftershocks, *Earth Planets Space*, **68(1)**, doi: 10.11.86/s40623-016-0432-2.

Hayashi, K., and M. Craig (2017). *S*-wave velocity measurement and the effect of basin geometry on site response, east San Francisco Bay area, California, USA, *Physics and Chemistry of the Earth*, **98**, 49-61.

Hayashi, K., and H. Suzuki (2004). CMP cross-correlation analysis of multi-channel surface-wave data, *Exp. Geophysics*, **35**, 7-13.

Ingber, L. (1989). Very fast simulated re-annealing, Mathematical and Computer Modelling, **12(8)**, 967-997.

Japan International Cooperation Agency (2018). THE PROJECT FOR ASSESSMENT OF EARTHQUAKE DISASTER RISK FOR THE KATH IN NEPAL FINAL REPORT VOL. 2, MAIN REPORT.

Kitsunezaki, C., N. Goto, Y. Kobayashi, T. Ikawa, M. Horike, T. Saito, T. Kuroda, K. Yamane, and K. Okuzumi (1990). Estimation of P- and S-wave velocities in deep soil deposits for evaluating ground vibrations in earthquake, *J. Japan Soc. Nat. Dis. Sci*., **9**, 1-17 (in Japanese with English abstract).

Lai, C. G., S. Foti, and G. J. Rix (2005). Propagation of data uncertainty in surface wave inversion, *J. Envir. Eng. Geophys.*, **10 (2)**, 219-228.

Ludwig, W. J., J. E. Nafe, and C. L. Drake (1970). Seismic refraction, in Maxwell, A. E. (ed.), The Sea, 4, Wiley-Inter science, New York, 53-84.

Moribayashi, S., and Y. Maruo (1980). Basement Topography of the Kathmandu valley, Nepal, An application of gravitational method of the survey of the tectonic basin in the Himalayas, *J. Japan Soc. Eng. Geol*., **21(2)**, 30-37.

Nelder, J. A., and R. Mead (1965). A Simplex Method for Function Minimization, *Computer J*., **7**, 308-313.

Okada, H. (2006). Theory of efficient array observations of microtremors with special reference to the SPAC method, *Exp. Geophysics*, **37**, 73-85.

Okada, H. (2003). The Microtremor Survey Method, translated by Koya Suto. Geophysical Monograph Series, no 12, *Soc. Exp. Geophysicists*

Okada, H., T. Matsushima, and E. Hidaka (1987). Comparison of Spatial Auto correlation Method and Frequency-Wavenumber Spectral Method of Estimating the Phase Velocity of Rayleigh Waves in Long-Period Microtremor, *Geophys. Bull.* Hokkaido Univ., **49**, 53-62 (in Japanese with English Abstract).

Peterson, J. (1993). Observations and modelling of background seismic noise, Open-file report 93-322, U. S. Geological Survey, Albuquerque, New Mexico.

Press, W. H., A. Teukolsky, W. T. Vetterling, and B. P. Flannery (2002). Numerical recipes multi-language code CD ROM with Windows, DOS, or Macintosh single-screen license, Cambridge University Press.

Saito, M. (1978). An automatic design algorithm for band selective recursive digital filters, *BUTURI-TANSA*, **31**, 112-135 (in Japanese with English abstract).

Sakai, H., R Fujii, M. Sugimoto, R. Setoguchi, and M. R. Paudel (2016). Two times lowering of lake water at around 48 and 38 ka, caused by possible earthquakes, recorded in the Paleo-Kathmandu lake, central Nepal Himalaya, *Earth Planets Space*, **68**, 31.

Sakai, H., T. Sakai, A. P. Gaujrel, and R. Fujii (2012). Guide book for excursion on geology of Kathmandu Valley, *27th Himalaya-Karakoram-Tibet Workshop* (HKT), Kathmandu.

Shen, C., Y. Xu, Y. Pan, A. Wang, and L. Gao (2016). Sensitivities of phase-velocity dispersion curves of surface waves due to high-velocity-layer and low-velocity-layer models, *J. App. Geophysics*, **135**, 367-374.

Shiraishi, H., T. Matsuoka, and H. Asanuma (2006). Direct estimation of the Rayleigh wave phase velocity in microtremor, *Geophys. Res. Lett*., **33**, L18307.

Takai, N., M. Shigefuji, S. Rajaure, S. M. Bijukchhen, S. Ichiyanagi, M. R. Dhital, and T. Sasatani (2016). Strong Ground Motion in the Kathmandu Valley during the 2015 Gorkha, Nepal, Earthquake, *Earth Planets Space*, **68(10)**, doi: 10.1186/s40623-016-0383-7.

Tokimatsu, K., S. Tamura, and H. Kojima (1992). Effects of multiple modes on Rayleigh wave dispersion characteristics, *J. Geotech. Eng*., ASCE, **118**, 1529-1543.

UNDP (1994). "Seismic Hazard Mapping and Risk Assessment for Nepal", His Majesty's Government of Nepal, Ministry of Housing and Physical Planning, UNDP/ UNCHS (Habitat), Subproject NEP/88/054/21.03.

United States Geological Survey, 2015a, Net QuakesStation KATNP_NQ_01, 25 April 2015, http://earthquake.usgs.gov/monitoring/netquakes/station/KATNP_NQ_01/20150425061138, last accessed December 2017.

United States Geological Survey, 2015b, https://earthquake.usgs.gov/earthquakes/eventpage/us20002926/executive, last accessed December, 2017.

Yamanaka, H. (2004), Application of the heuristic search methods to phase velocity inversion in microtremor array observation, *Proc. 13th World Conf. Earthq. Eng.*, Paper, 1161.

Yokoi, T. (2010). New formulas derived from seismic interferometry to simulate phase velocity estimates from correlation methods using microtremor, *Geophysics*, **75(4)**, SA71-SA83.

Yokoi, T. (2005). Combination of Down Hill Simplex Algorithm with Very Fast Simulated Annealing Method, An effective cooling schedule for inversion of surface wave's dispersion curve, *Proc. Fall Meeting Seismol. Soc., Japan*, B049.

Table 5.1 Summary of the equipment used for the microtremor array exploration (Bhattarai *et al*. (2017b))

Seismometer	Data Logger
CMG40T (Guralp Systems Ltd), 3-components, Frequency range: 0.033 Hz (30 s) to 50 Hz (0.02 s), Sensitivity: 2*400 V/m/s	Data Mark LS8800 (Hakusan Co. Ltd Japan), 3-components, GPS synchronized Clock, A/D converter: 24 bits, Dynamic range: 128 dB

Table 5.2 Parameter settings for the field measurements (Bhattarai *et al*., 2017b)

Parameters	Site 1	Site 2	Site 3
Name of Sites	Singhadurbar	DMG-Narayanhiti	Teku-Kalimati
Dates of Measurement	Feb. 12-15, 2017	Dec. 12-15, 2016	Feb. 16-18, 2017
Duration of Measurement	> 1 night/ deployment **(**6**:**00pm-09**:**00am**)**		
Number of Deployments	3	3	2
Min. Interstation Distance	137 m	183 m	209 m
Max. Interstation Distance	829 m	1272 m	1331 m
Equipment	4 Seismographs/deployment		
Sampling Interval	0.01s (100 Hz)		

Table 5.3 Parameter settings for data processing

Parameters	Site 1			Site 2			Site 3	
	L	M	S	A	B	C	M	S
Duration of analyzed data (h)	16.0	12.0	13.0	12.0	19.5	20.5	12.5	14.0
Number of screened time blocks	199	117	163	258	344	302	259	261
Width of Parzen Window (Hz)	0.04	0.04	0.05	0.04	0.05	0.05	0.03	0.05
Number of interstation distance	4	2	2	1	5	5	5	5
Re-sampled interval (s)	0.25 s							
Number of samples/time block	1024							
Number of padded zeros/time block	1024							

Table 5.4 Initial range set for the heuristic search (Bhattarai *et al*. (2017b))

Number of Layers	***h*: *Thickness* (*m*)**		***Vs* (*m/s*)**	
	h_{min}	h_{max}	c_{min}	c_{max}
1	10	300	150	250
2	50	300	200	300
3	50	300	350	500*
4	50	400	400	700+
5	50	400	600	1000
6	*half space*		1,000	3,200

*: 500 m/s, 700 m/s and 600 m/s for site 1, site 2, and site 3, respectively. +: 700 m/s, 900 m/s for site 1 and other two sites, respectively.

Table 5.5 *Vs* structures estimated by the heuristic search at site 1 (Bhattarai *et al*. (2017b))

Number of Layers	***h*: *thickness* (*m*)**	***ρ*** **(*g*/*cm*^{3})**	***V*$_P$** **(*m*/*s*)**	***V*$_S$** **(*m*/*s*)**
1	38	1.78	1,478	170
2	132	1.81	1,559	242
3	118	1.88	1,782	443
4	186	1.92	1,916	564
5	292	2.01	2,253	868
6	*half space*	2.38	3,737	2,205

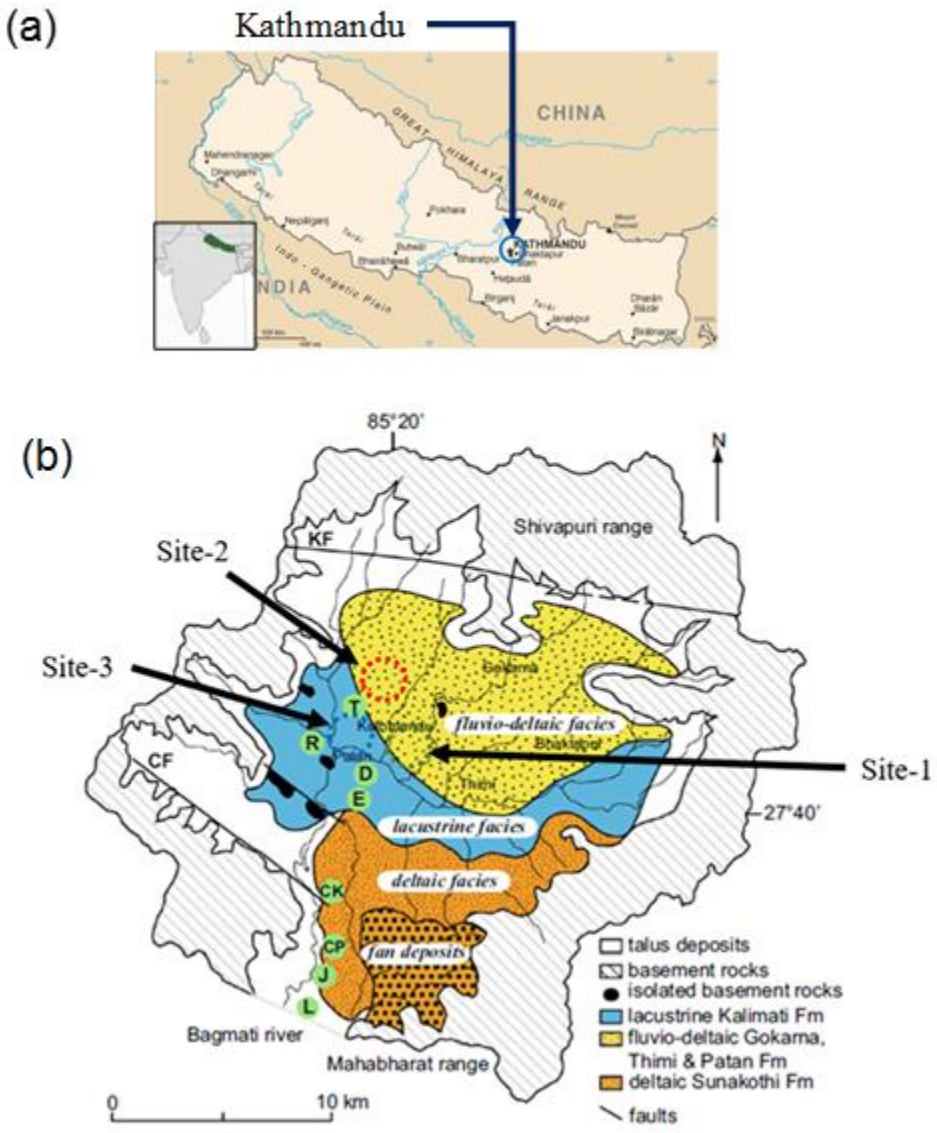

Figure 5.1 (a) Index map of Kathmandu, Nepal. (b) Locations of the three study sites on a surface geology and geomorphology map of the Kathmandu valley, Nepal (modified from Sakai *et al*., 2016).

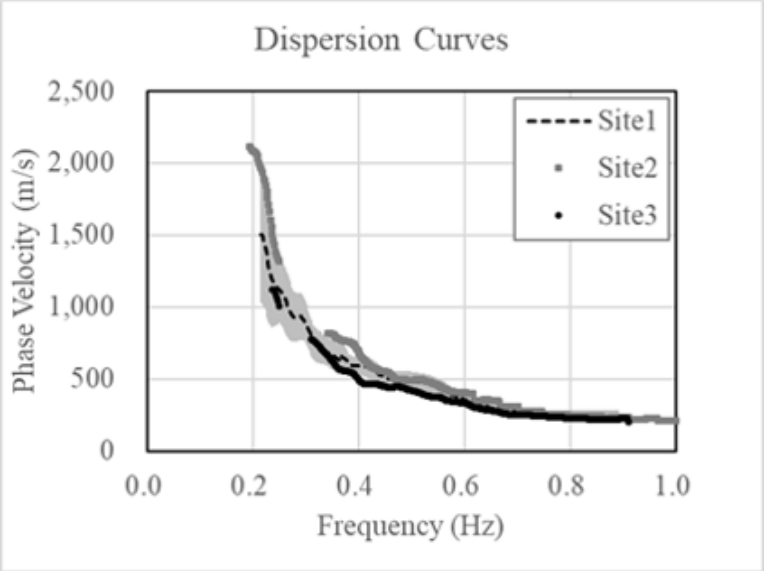

Figure 5.2 Dispersion curves determined in this study for the three sites at the central part of the Kathmandu valley using SPAC of regular and irregular shape arrays. Gaps in the curves of sites 2 and 3 were caused by anomalous behavior of the coherence function, as explained below. The light grey shadow shows the range of the phase velocity ± 1 standard deviation of site 1.

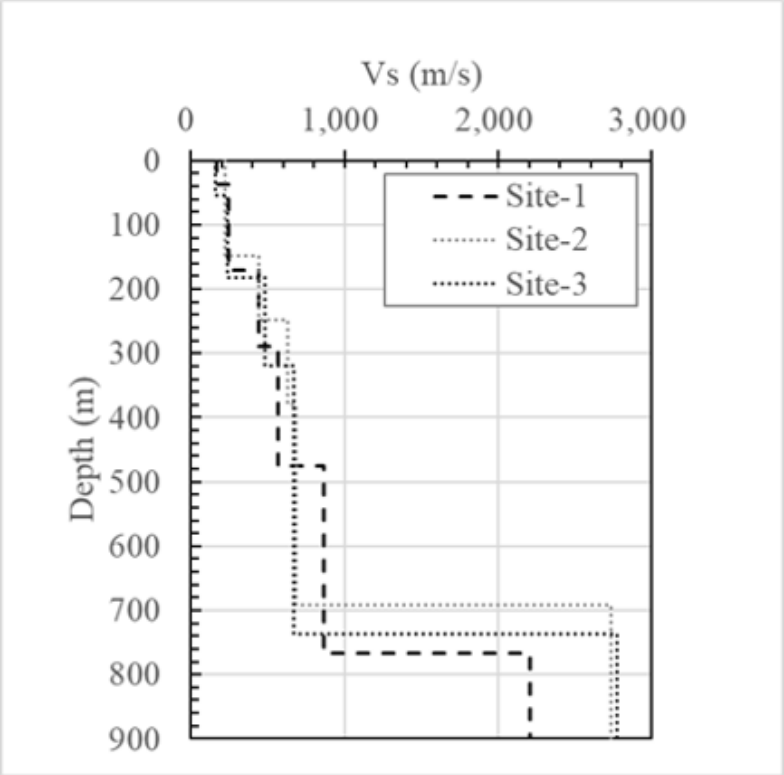

Figure 5.3 V_S structure estimated in this study for the three sites at the central part of the Kathmandu valley using the SPAC of regular and irregular shape arrays. A considerable uncertainty; however, must be considered at layers deeper than around 500 m.

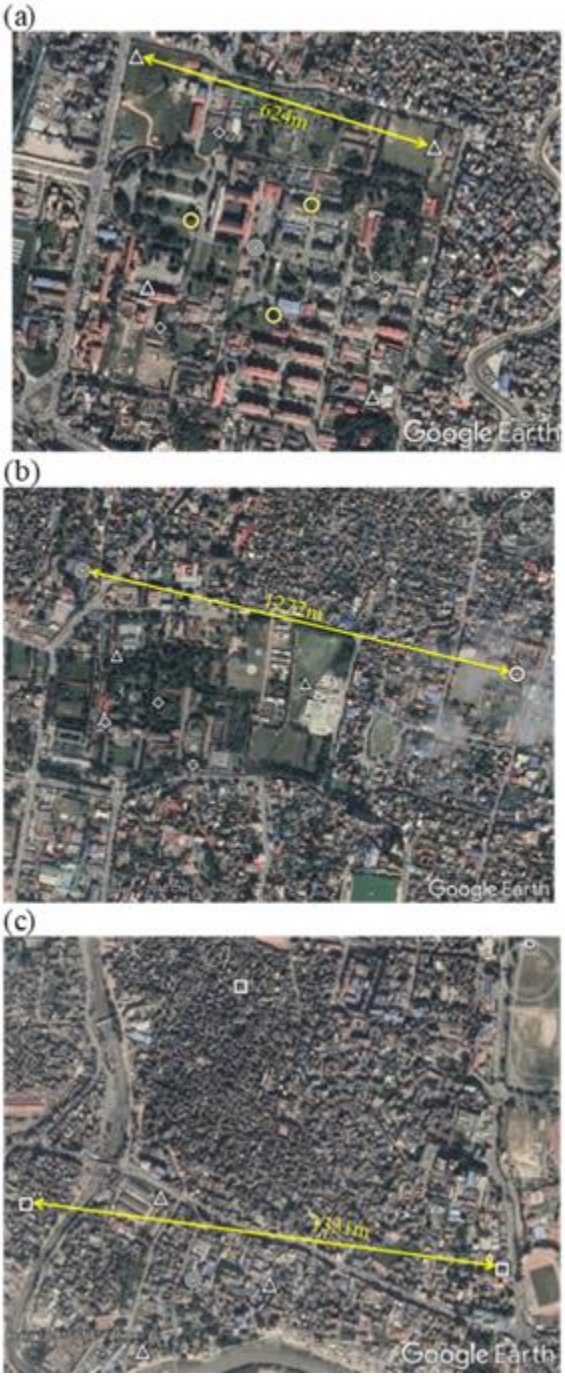

Figure 5.4 Configurations of the deployed arrays (a) site 1, (b) site 2, and (c) site 3. These are drawn using google earth.

(a)

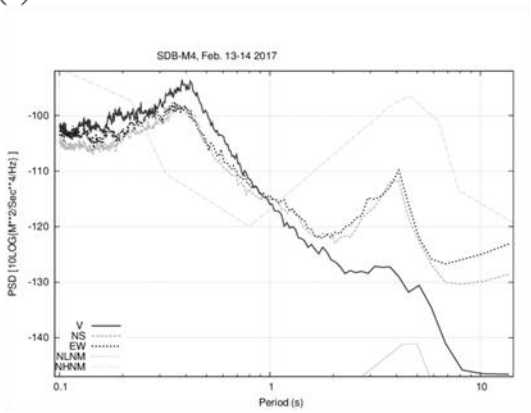
SDB-M4, Feb. 13-14 2017
PSD [10LOG(M**2/Sec**4/Hz)]
Period (s)
V
NS
EW
NLNM
NHNM

(b)

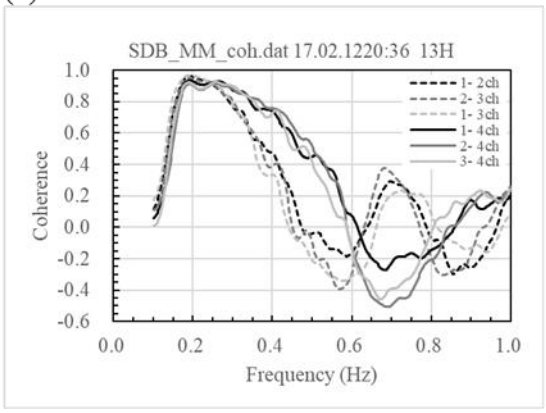
SDB_MM_coh.dat 17.02.1220:36 13H
Coherence
Frequency (Hz)
1- 2ch
2- 3ch
1- 3ch
1- 4ch
2- 4ch
3- 4ch

(c)

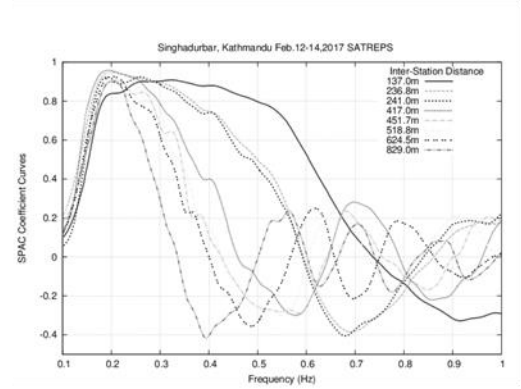
Singhadurbar, Kathmandu Feb.12-14,2017 SATREPS
SPAC Coefficient Curves
Frequency (Hz)
Inter-Station Distance
137.0m
236.8m
241.0m
417.0m
451.7m
518.8m
624.5m
829.0m

(d)

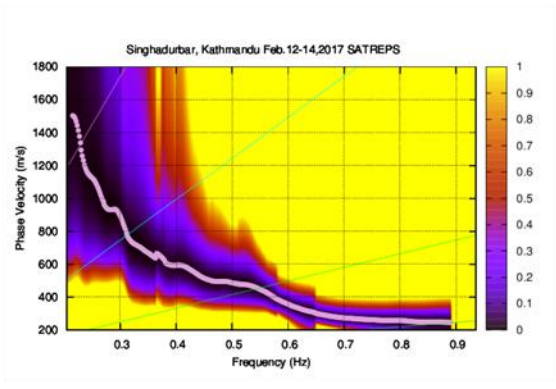
Singhadurbar, Kathmandu Feb.12-14,2017 SATREPS
Phase Velocity (m/s)
Frequency (Hz)

(e)

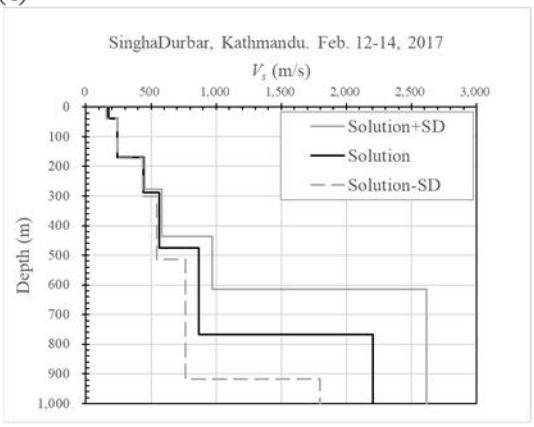
SinghaDurbar, Kathmandu. Feb. 12-14, 2017
V_s (m/s)
Depth (m)
Solution+SD
Solution
Solution-SD

(f)

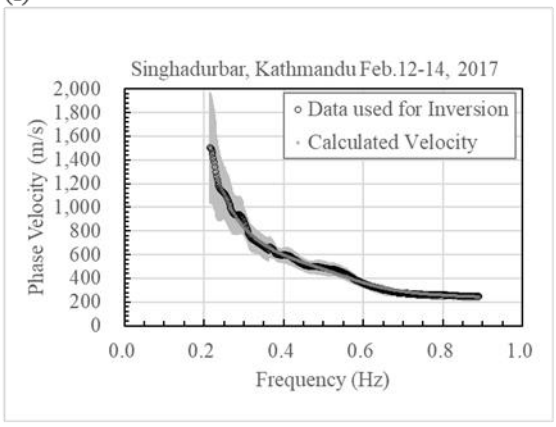
Singhadurbar, Kathmandu Feb.12-14, 2017
Phase Velocity (m/s)
Frequency (Hz)
Data used for Inversion
Calculated Velocity

Figure 5.5 Data processing and the results for site 1 (a) Power spectral density of acceleration at M4-S4 (triple concentric circle in Figure 4a). Any smoothing filter was not applied. Solid and dashed curves show the vertical and two horizontal components, respectively. Two thin curves are NLNM and NHNM of Peterson (1993). (b) Solid curves show the coherence functions among three vertices (open circles in Figure 4a) of equilateral triangular M array, whereas the dashed curves show those between the vertices and the central point M4. (c) SPAC coefficient of all station pairs used in analysis. (d) Misfit function and the determined dispersion curve. (e) V_S structure inverted from the dispersion curve shown with standard deviation (f) Comparison of the observed dispersion curve (black circles) and the curve calculated based on the estimated structure (grey circles). Light grey shadow shows the SD of the observed dispersion curve (Bhattarai *et al*. (2017a)).

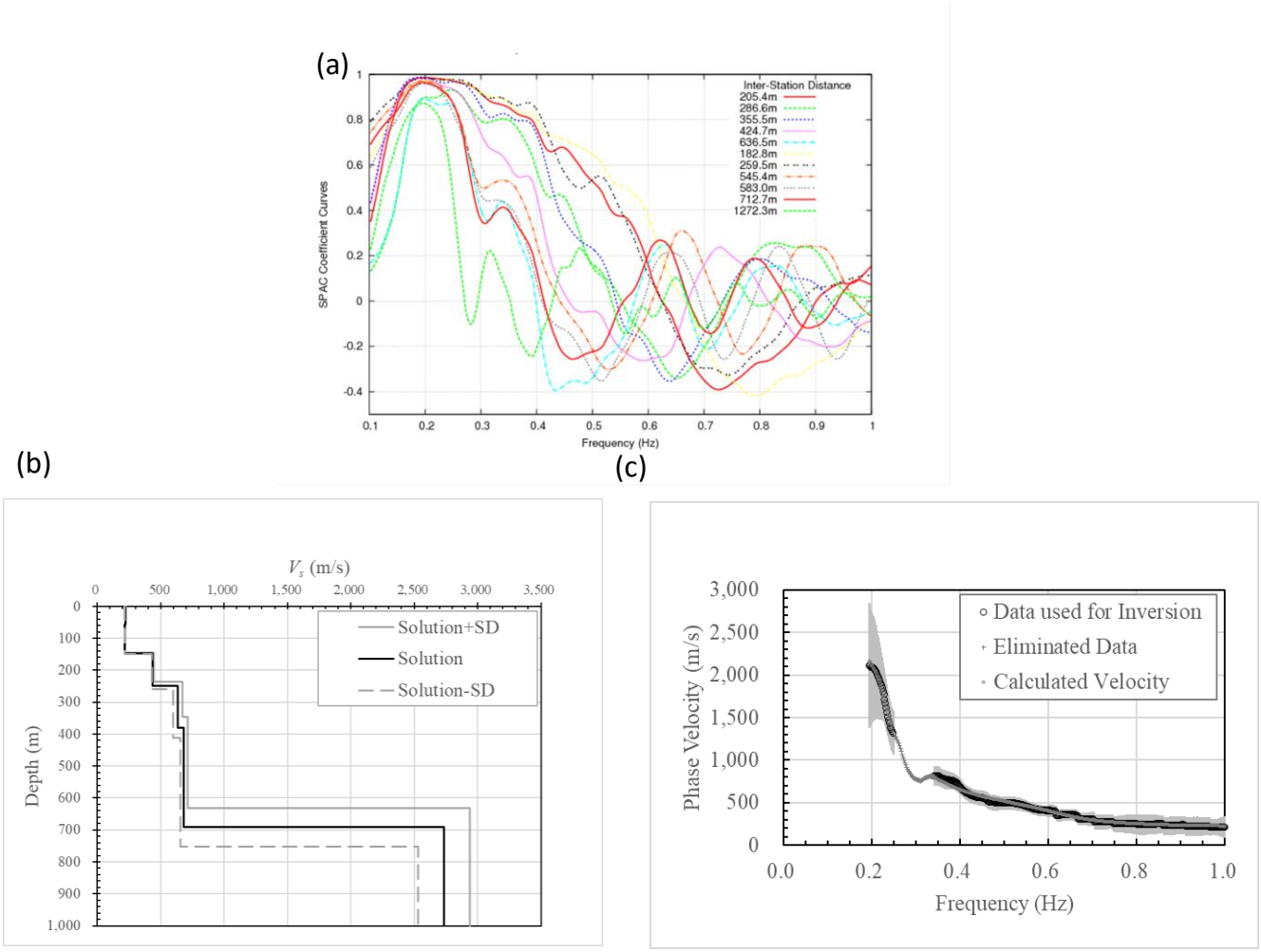

Figure 5.6 Results for site 2 (DMG-Narayanhiti): (a) SPAC coefficient curves of all station pairs used in analysis. (b)*Vs* structure inverted from the dispersion curve shown with standard deviation. (c) Comparison of the observed dispersion curve (black circles) and the curve calculated based on the estimated structure (grey small circles). Small "+" mark denotes the phase velocity data that were eliminated from inversion because of their anomalous behavior. Light grey shadow shows the SD of the observed dispersion curve (Bhattarai *et al*., 2017a)).

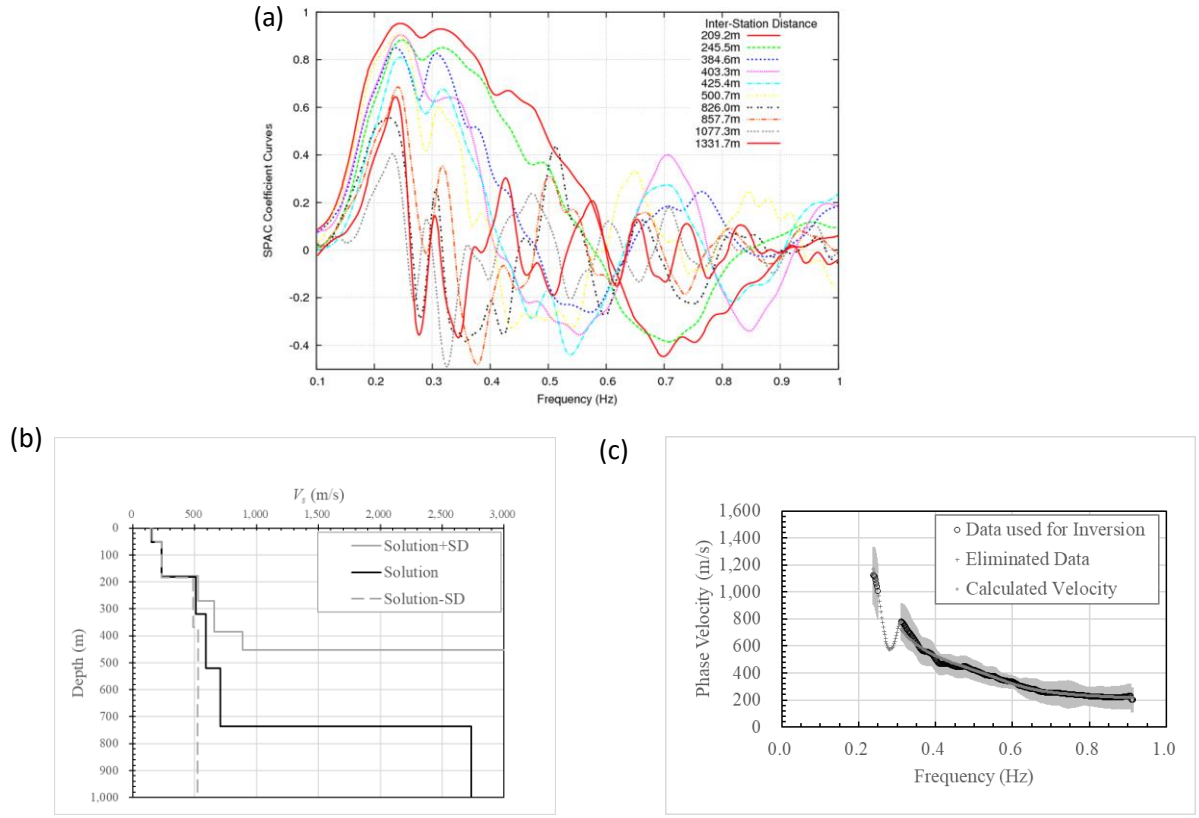

Figure 5.7 Results for site 3 (Teku-Kalimati): (a) SPAC coefficient curves of all station pairs used in analysis. (b) V_S structure inverted from the dispersion curve shown with standard deviation. (c) Comparison of the observed dispersion curve (black circles) and the curve calculated based on the estimated structure (grey small circles). Small "+" mark denotes the phase velocity data that were eliminated from inversion because of their anomalous behavior. Light grey shadow shows the SD of the observed dispersion curve (Bhattarai *et al*. (2017a)).

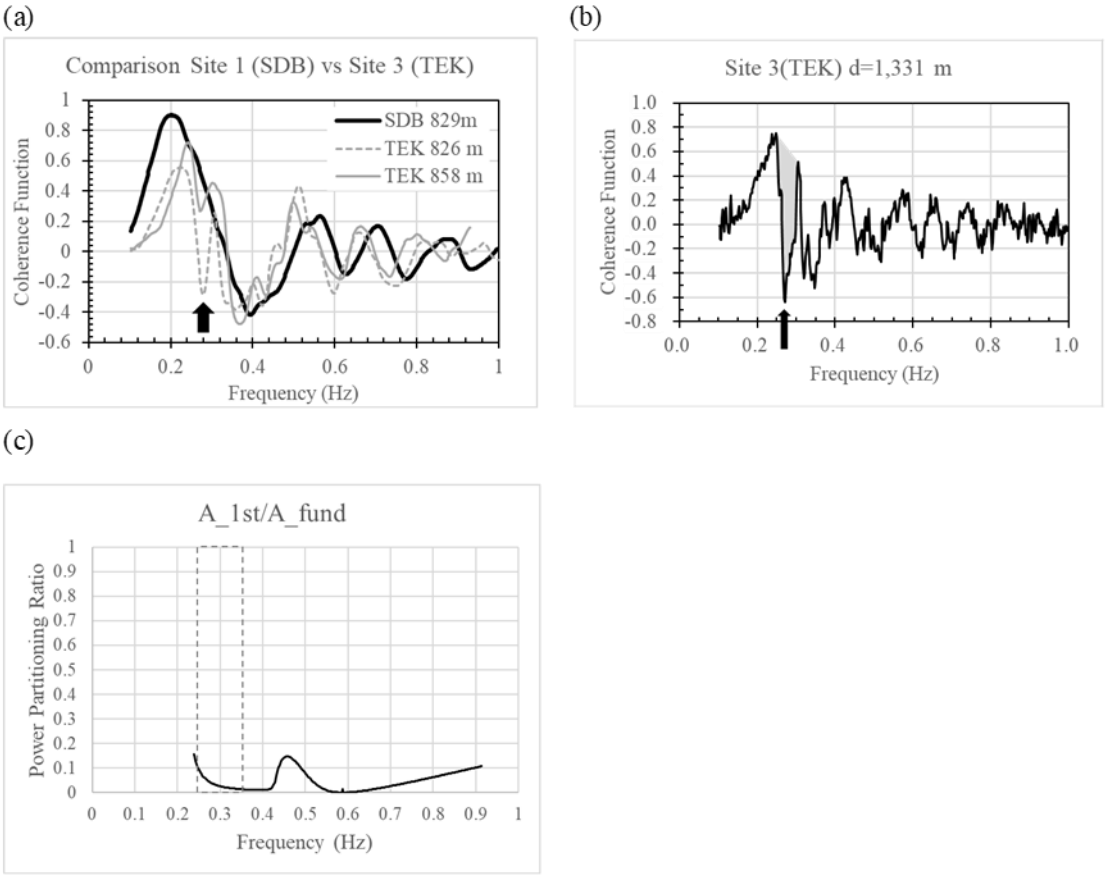

Figure 5.8 Anomalous behavior of coherence functions that causes the winding of dispersion curves of site 2 and 3. (a) Sags of the coherence functions of two station pairs at the site 3 in comparison of a station pair at the site 1 that has similar inter-station distance. Parzen window was applied as shown in Table 5.4. Black arrow indicates the negative peak of the grey dashed curve -0.284 at 0.271 Hz. (b) Coherence function of a station pair in site 3 (TEKU) with inter-station distance 1,331 m. Any smoothing filter was not applied. Grey shadow shows the sag. Black arrow indicates the negative peak of the value -0.637 at 0.271 Hz. (c) Power partitioning ratio of the first higher mode to the fundamental mode for the V_S structure of site 3. Rectangle of dashed lines shows the frequency range of the problem around 3.0 Hz.

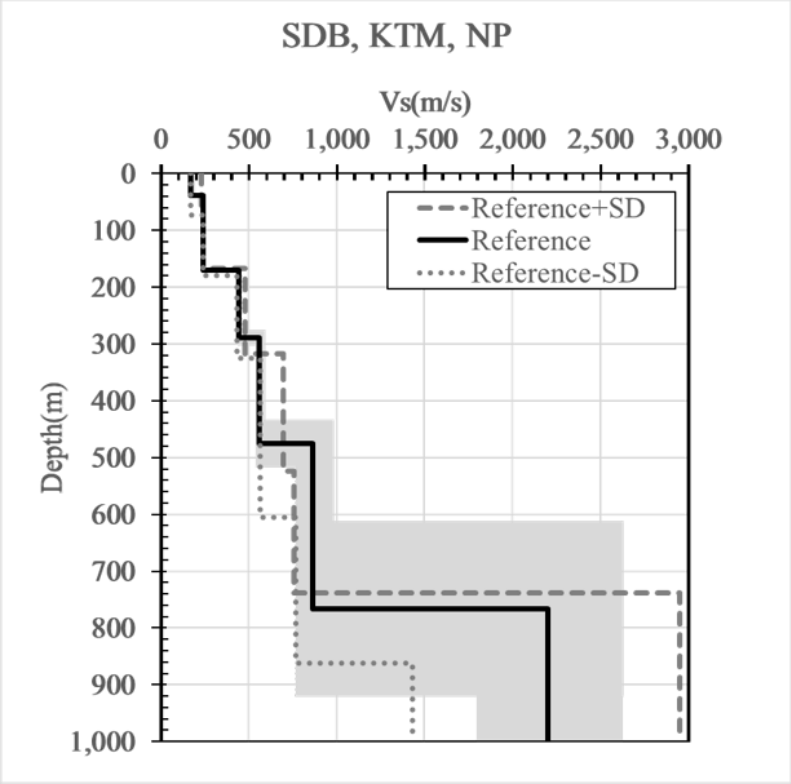

Figure 5.9 Analysis of uncertainty due to the estimation error of dispersion curve using site 1. Solid black curve is the reference structure inverted from the dispersion curve of site 1, i.e., the dashed curve in Figure 5.2. Light grey shadow is the range of the SD of structural parameters estimated from the SD of the average dispersion curve of site 1 (Solid black curve). Dashed grey curve is the structure inverted from the upper limit of the grey shadow in Figure 5. 2, i.e., the average dispersion curve plus one SD. Dotted grey curve is the structure inverted from the lower limit of the grey shadow in Figure 5.2, i.e., the average dispersion curve minus one SD.

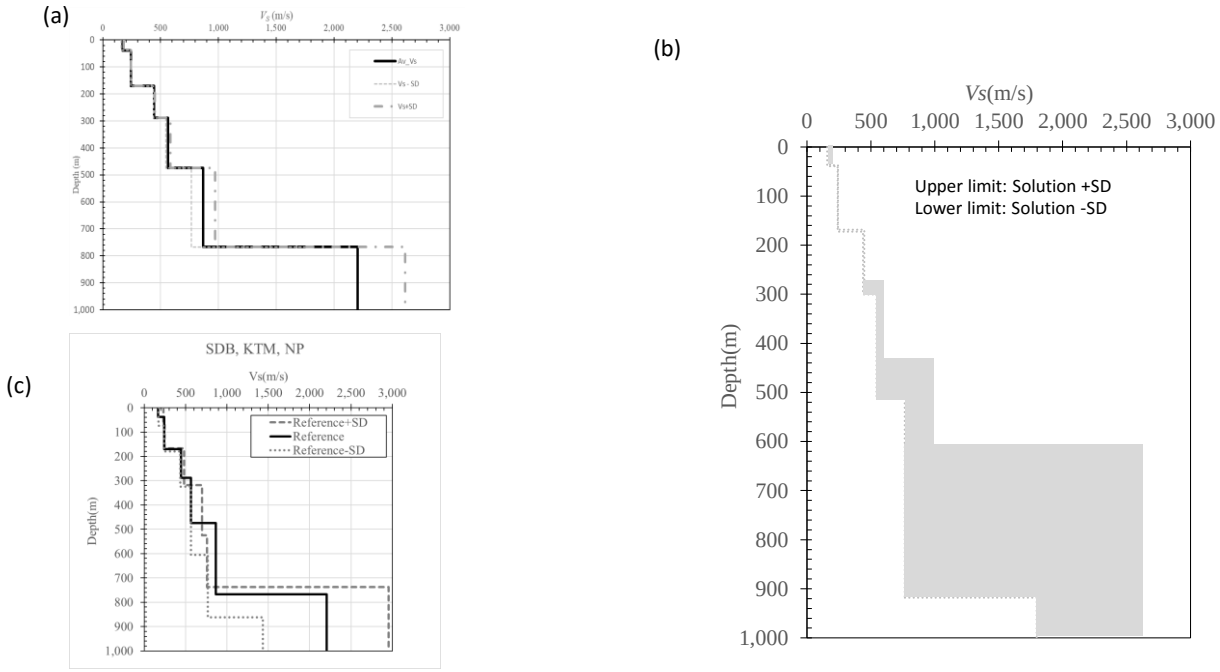

Figure 5.10 (a) The standard deviation of the V_S structure of site 1 plotted against the average depth. (b) Light grey shadow is the range of the standard deviation of the structural parameter estimated from the standard deviation of the average dispersion curve of site 1. (c) Dashed grey curve is the structure inverted from upper limit of the uncertainty of site1 and dotted grey curve is the structure inverted from the lower limit of uncertainty of site 1 (these are the structures obtained by plotting different V_S with different depths).

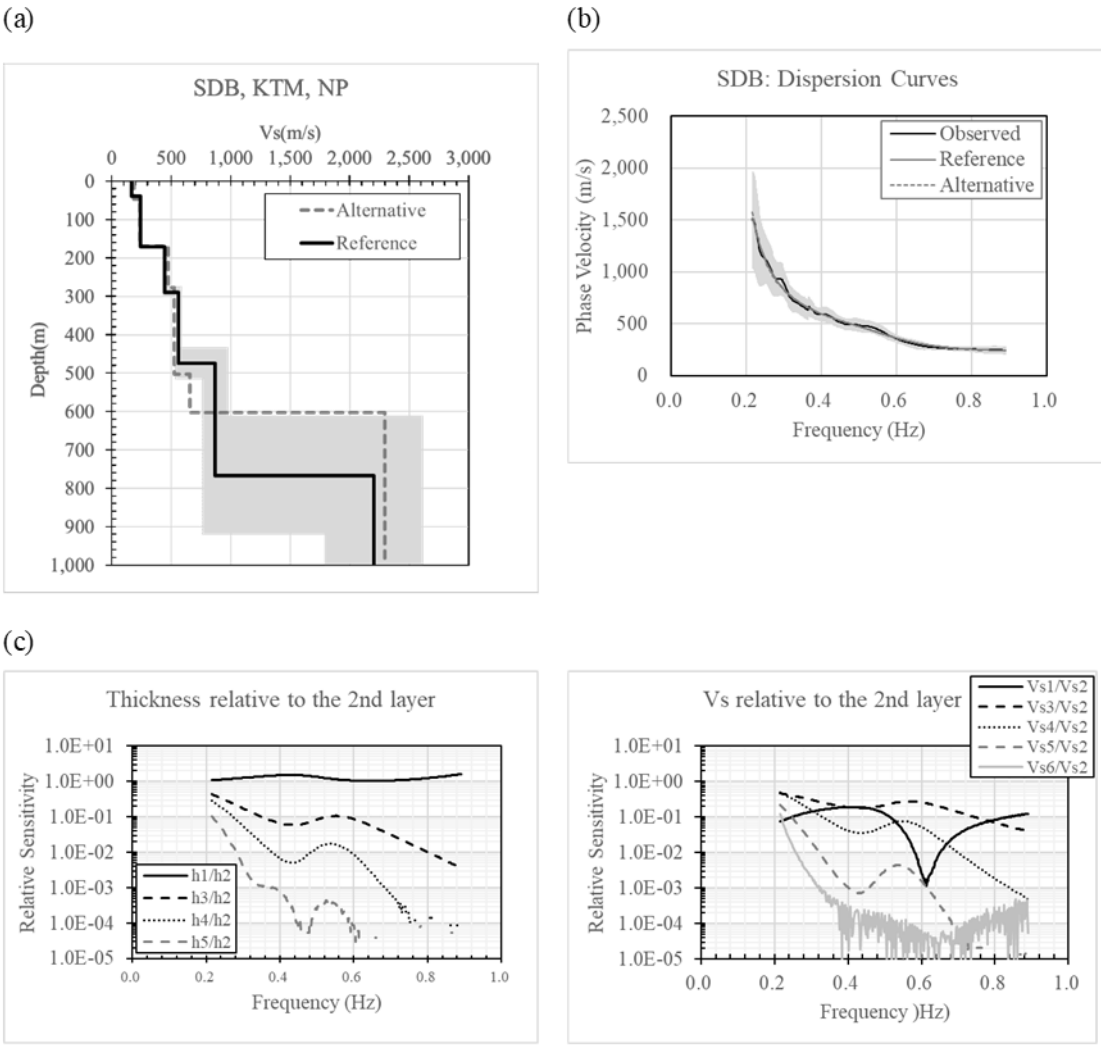

Figure 5.11 Analysis of uncertainty due to the low sensitivity of dispersion curve to the structural parameters of the deepest part using site 1 (a) Comparison of Reference and Alternative structures. Light grey shadow shows the range of the SD of structural parameters estimated from the SD of the dispersion curve of Reference structure of site 1 (Solid black curve). (b) Comparison of Observed dispersion curve and those of Reference and Alternative structures. (c) Sensitivity of dispersion curve of Reference structure, i.e., the partial derivatives of the phase velocity to the structural parameters normalized by the values of layer's thickness (left) and V_S (right) of the second layer. V_S6 means the V_S of the underlying half-space. The disturbed curve of V_S6/V_S2 is caused by the insufficient precision of calculation.

Chapter 6

Extensions to the exploration of deeper structures

6.1 Introduction

The Kathmandu valley is the largest administrative, economic, historical, and cultural capital of the Federal Democratic Republic of Nepal which was originated from the lake deposits and later filled with sediment overlying basement rocks. The basement topography of the basin is not homogeneous and detailed study of the subsurface structures by using active sources that are quite impossible and expensive being highly urbanized and environmentally sensitive issues. Therefore, different trails are considered to analyze the microtremor data acquired in Chapter 5.

Long-period microtremors observed at the various sites in the central part of the Kathmandu valley (Bhattarai *et al*., 2017a) (Figures 5.1) in Chapter 5 are re-analyzed. The Centerless Circular Array (CCA) (*e.g*., Cho *et al*., 2004) method with an emphasis on scalene triangle arrays is used. To grasp the shear wave velocity of the most surficial layer, the existing data of the L-shape SPAC using 4.5 Hz geophones and CCA method using 2 Hz seismometers are also analyzed. Some additional observations are also realized. Particularly, for sites 2 and 3 among three, the dispersion curves determined by 2ST-SPAC in the previous chapter have a winding part in the frequency range from 0.25 Hz to 0.35 Hz. This disturbance is examined using the CCA method and compared with the 2ST-SPAC method. However, the dispersion characteristics below 0.2 Hz remains unrevealed due to the weak power of ambient noise. Additionally, the performance of seismic interferometry is tested with small to moderate-sized microtremor array recordings from the same data set. Furthermore, to obtain the dispersion curve in the lower frequency range below 0.2 Hz for better estimation of bedrock depth, a temporary network of four continuous broadband seismic observation stations was realized since 2018 and changed its configuration a few months later. The inter-station distances among four sites are from 4.6 to 14.7 km (left panel) as shown in Figures 6.1 Hayashida *et al*. (2018b); Yokoi *et al*. (2018). During the observation period, signals from

shallow, local, and teleseismic events of the various magnitude was detected and surface wave component of the recordings (M > 6.0) are used for the estimation of Rayleighwave phase velocities in the lower frequencies. The estimated phase velocities are compared with those derived from the newly proposed seismic velocity structure model of Nepal (Yamada *et al*., 2018) and existing velocity model as shown in Table 6.3 (Pandey *et al*., 1995). Moreover, microtremor observation sites inside the Kathmandu valley is enlarged and results from other exploration techniques (e.g., gravity survey and seismic reflection survey) are discussed.

The aim of this chapter is to compare, validate, expand, and tune the velocity structure model derived in Chapter 5 with various exploration techniques/trails (e.g., CCA, Seismic interferometry, analysis of teleseismic records etc.). These data will be integrated with connection to (*e.g*., Gravity survey, seismic reflection survey etc.) in the Kathmandu valley for the 3-D basin modeling for future earthquake disaster studies. Such comparative studies for validating the results will enlighten the effectiveness, limitation, and advantages of these new methods in consideration of the conventional SPAC method. The results obtained/confirmed from the various techniques discussed above could be used for seismic microzonation, land use planning, and various stages of risk applications.

6.2 Method of Analysis

6.2.1 Centerless Circular Array (CCA) method

The CCA method originally proposed by Cho *et al*. (2004, 2006) is based on the theory of circular array given by Henstridge (1979) and stands for the Fourier transform of microtremor wavefield over the azimuth. This method is quite similar to the circular array of SPAC method but no sensor at the center of the circle; however, based on completely different principle. The CCA coefficient is given by the spectral ratio of the power of the zero order Fourier coefficient over azimuth to that of the first order and expected to converge to the known function as follows,

$$s(r,\omega) = \frac{PSD\langle \int_{-\pi}^{\pi} Z(t,r,\phi)d\phi \rangle}{PSD\langle \int_{-\pi}^{\pi} Z(t,r,\phi)\, exp(-j\phi)d\phi \rangle} = \frac{J_0^2(r\omega/c)}{J_1^2(r\omega/c)}, \quad (6.1)$$

where *PSD*<> denotes the power spectral density, $J_0(\ )$ and $J_1(\ )$ the zero and the first order Bessel functions of the first kind, *r* the radius of circular array, ω the angular frequency, *c* the phase velocity of Rayleigh waves, φ the azimuth from the center of the array to a station on the peripheral circle, Z(t, r, φ) time series of vertical component of microtremor observed at distance (r,φ) and time t.

In this study, the calculation of the CCA coefficient was done in the frequency domain using the following formula.

$$s(r,\omega) = \frac{\sum_{i=1}^{M}\sum_{k=1}^{M}[C_{ik}(r,\omega)]}{\sum_{i=1}^{M}\sum_{k=1}^{M}[C_{ik}(r,\omega)]\, exp\{-j(\phi_i-\phi_k)\}}, \quad (6.2)$$

Where $C_{ik}(r,\omega)$ denotes the cross spectra of the records obtained at the *i*-th and the *k*-th stations on the peripheral circle and $j^2 = -1$.

The array pattern of the de-fact standard is a regular polygon, for example, equilateral triangle, with a station at the center that is not essential. Using only three stations among four that we have deployed, an array of three stations on the same circle can be formed but with un-even azimuthal distribution. Three stations at each site were selected to form a triangle of which circumscribed circle's center is located within this scalene triangle; namely, we avoid using acute-angled scalene triangle array. The circumscribed circles of the selected arrays at the three sites are shown in Figures 6.2a, b, and c whereas their corresponding dispersion curves are shown in Figures 6.2d, e, and f respectively. The problematic feature detected at site 3 in chapter 5 (Figure 6.2g) is compared with site 1 (Figure 6.2h). The applicability of array geometry is supported by the isometric nature of the coherence function derived from site 1. The determined dispersion curves cover the frequency range lower than 1 Hz and higher frequency is covered, by seismic interferometry and by the 24 channels L-shape array (LS-SPAC) using 4.5 Hz Geophone for site 1 and site 2. For site 3 small regular CCA arrays of radii 10 m to 20 m and LS-SPAC is used. The summarized dispersion curves are shown in Figure 6.3a and their inverted velocity structures at shallow and deeper part are shown in

Figures 6.3b and c. Which indicates the velocity structure focused for the deeper structure cannot be precise representative for the shallow structure.

6.2.2 Seismic interferometry

Seismic interferometry is a method that allows the retrieval of the seismic response at one receiver from a virtual source at the position of another receiver. Claerbout (1968) first proposed this method in the seismic exploration community for a horizontally layered surface. Yoshimi *et al*. (2012), Chimoto and Yamanaka (2013), Hayashida and Yoshimi (2014), and Tsuno *et al*. (2015) applied the seismic interferometry to microtremor array data. In this study we first applied the seismic interferometry method to existing microtremor array data observed at the site 1 in Chapter 5 for the estimation of surface wave group velocities (Rayleigh and Love waves) and subsequently performed the joint inversion of phase and group velocities of surface wave (especially of Rayleigh wave) to examine the accuracy of existing models.

At site 1, due to the security reason it is not easy to conduct additional measurement. In order to extend the analyzable frequency range to higher frequency, this method was applied in the frequency range from 0.6 to several Hz and the group velocity was determined. The stacked cross-correlation functions for (Z-Z) component for the medium and large sized arrays at site 1 (SDB) and that of (T-T) component are shown in Figures 6.4a and b. Not so much examples applied in this frequency range we can find among the existing studies. The joint inversion of the phase velocity determined by 2ST-SPAC at lower frequency range and the group velocity determined by the seismic interferometry shows a good fitting among the calculated and two observed ones as shown in Figure 6.5.

6.2.3 Analysis of regional and teleseismic earthquakes

To obtain the dispersion curve in the lower frequency range below 0.2 Hz which was not detected by the SPAC, CCA, and seismic interferometry methods a set of 4 seismographs have been deployed in the Kathmandu valley (Figure 6.1) since early 2018 by the aim of long term continuous microtremor observation as well as to record the earthquakes of local, regional, and teleseismic distances in the valley covering the wider range. So far, 5 regional and teleseismic earthquakes have been recorded as shown in Table 6.2. Among them, an earthquake of regional distance occurred on 9 May, 2018 and is recorded by four

seismographs; however, surface wave has not clearly been detected at all stations. The wave packet in the *S*-wave part at site DMG01 seems higher amplitude in comparison to other three sites. The Fourier amplitude spectra of this event show the clear peak above frequency 0.2 Hz. Moreover, the unknown event No. 4 is not used for analysis. Thus, we only used the remaining 3 events of teleseismic distances from Table 6.2.

For the 2-point array (Figure 6.6a) the phase velocity of Rayleigh wave is estimated as follows,

$$C_{app}(f) = \frac{d}{\Delta t(f)}, C(f) = C_{app}(f)\, Cos\theta \qquad (6.3)$$

where the distance between the observation points is d, and the difference in the arrival time of the surface wave at the frequency $\Delta t(f)$,

For error suppression, the azimuth of each observation points is less than or equal to 2, resulting in $\theta <$ 30 as shown in Figure 6.6a which is only applicable for pairs of seismic observation points. For the 3-point array (Figure 6.6b) the slowness and then phase velocity of Rayleigh wave is estimated as follows,

Slowness,

$$s_1 = \frac{\Delta t_1}{r_1}, s_2 = \frac{\Delta t_2}{r_2} \qquad (6.4)$$

and the Phase velocity c,

$$A = \frac{\mathrm{s1}\sin\theta 2 - s2 sin\theta 1}{\sin(\theta 2 - \theta 1)} \qquad (6.5)$$

$$B = \frac{s1 cos\theta 2 - s2 cos\theta 1}{\cos(\theta 2 - \theta 1)} \qquad (6.6)$$

$$c = \frac{1}{\sqrt{A^2 + B^2}} \qquad (6.7)$$

where the azimuth of P as seen from O: $\theta 1$; the azimuth of Q as seen from O: $\theta 2$ the phase difference of O-P(s) is Δt_1, and that of O-Q(s) is Δt_2.

6.3 Results comparing to CCA and 2ST-SPAC

The configuration of site 1 (SDB) includes three radii of the circular arrays starting from inside namely 136.5 m, 240.0 m, and 385.2 m respectively as shown in Figures 6.2a, where the first 2 indicates equilateral triangle with a station at the center. From the biggest 4 points irregular array a scalene triangle array of radius 328.5 m was selected. The phase velocity thus derived is plotted in Figure 6.2d. The widest angle from the center to a station pair on the circle gives 151.2 degree. The results from CCA (Yokoi *et al*., 2018) mentioned above are plotted together with the results obtained from 2ST-SPAC (Bhattarai *et al*. 2017a) and LS-SPAC (JICA *et al*., 2018). The records from latter one was acquired using L-shape array that consists of 24 vertical geophones of the natural frequency 4.5 Hz with sensor interval 2.5 m. The maximum phase velocity thus determined is above 2200 m/s at frequency 0.2 Hz. The gradual change in the dispersion curve depending upon the increase on array radius might indicate the dipping basement top. The gap around 1 Hz between the frequency range covered by CCA method and that of LS-SPAC method was later filled consistently by the application of the seismic interferometry to the same data set (Hayashida *et al*., 2018a).

The isotropic nature of coherence function at KTV was verified using the equilateral triangular array of radius 240 m at site 1 already confirmed in Chapter 5. The shown angle is the viewing angle from the center to 2 seismographs on the circumscribed circle. Variation of coherence function obtained using scalene triangle array of radius 328.5m (Figure 6.2d) is comparable with that obtained from the equilateral traingle at site 1 in Chapter 5 (Figure 5.5b). In both cases, a decay in the frequency range below 0.2 Hz is clearly shown.

The arrays in the site 2 (DMG) have radii 17.3 m, 153.5 m, and 365.4 m as shown in Figure 6.2b. The smallest one is an equilateral triangular mini-array deployed at the premises of DMG in December 2017, with a sensor at the center of the circle. The widest angles from the center to a pair of peripheral stations for the medium and large array are 177.1 and 139.6 degrees respectively. The data provided by JICA (2018) were also used with the LS-SPAC method too; however, the spacing of the geophone is 2 m in comparison to site 1. The maximum phase velocity determined in this configuration is about 2,400 m/s at around 0.2 Hz. The winding part of the dispersion curve in the frequency range from 0.25 to 0.35 Hz

detected by Bhattarai *et al.* (2017b) using 2ST-SPAC is observed in the dispersion curves determined by CCA method as shown in Figure 6.2e. The gap of the dispersion curve around 1 Hz similar to the site 1 is filled by the results of the Mini CCA-array of radius 17.3 m (Yokoi *et al*., 2018).

Site 3 Teku (Figure 6.2c) has a widest angle from the center to the pair of peripheral stations for four CCA arrays of radii 234.1 m, 441.6 m, 548.0 m and 667.3 m. The angles from the center to a station pair on the circle are 130.6, 152.4, 158.9 and 130.6 degree's respectively. The dispersion curve determined at site 3 Teku is shown in Figure 6.2f which is located at the north bank of Bagmati river close to the junction with Bishnumati river. It covers the Kathmandu Durbar square and gas well site of DMG in TEKU. We have deployed the irregular shape arrays due to non-grid like road pattern. They gave almost the same dispersion curves as that given by 2ST-SPAC (Bhattarai *et al.*, 2017a) with a sharp sag at around 0.3 Hz. At around 0.24 Hz the estimated dispersion curves stopped increasing toward lower frequency. A mini CCA-array of radius 10.8 m was also deployed at this site. This provides the dispersion curve in the high frequency range above the coverage of CCA arrays. The winding part of the dispersion curve in the frequency range from 0.25 to 0.35 Hz commonly appeared for CCA arrays similar to 2ST-SPAC determined by Bhattarai *et al*. (2017a)

The summary of the dispersion curve at three sites is plotted in Figure 6.3a and the inverted velocity structure in Figures 6.3b and c. Among the three sites considered for analyses site 3 does not have the increase of dispersion curve in the frequency range 0.2 to 0.23 Hz. Figure 6.2f shows the difference in two sites (1 and 3) at almost similar radius CCA (r = 240.1 m) at SDB and CCA (r = 234.1m) at TEKU in terms of the power of the zero order coefficient of Fourier expansion over azimuth (G0), and the denominator is that of the first order (G1), both normalized by total power. The range at low frequency where G0/All becomes significantly smaller than 1.0. This means the dominance of incoherent noise. In the frequency range above it, G0/All is almost flat and the minimum of G1/All controls the maximum of the CCA coefficient and then the low frequency limit of the estimable phase velocity. In site 1 G1/All decreases toward lower frequency and turn to grow at 0.181 Hz. In site 3 the turning point is at 0.23 Hz. It is guessed that their difference is due to the noise level at low frequency side. Additionally, G1/All of site 3 have a narrow sharp peak at around 0.3 Hz. Its G0/All has a sag at the same frequency as painted in grey in Figure 6.2f. This is the

same phenomenon as that we have detected in the 2ST-SPAC analysis that is a sharp sag of the SPAC coefficient and the coherence functions. These suggest the creation of G1 component in and around site 3 (Figure 6.2g). The similar phenomenon is observed at site 2, too (Figure 6.2e); However, it is left for future studies. The CCA method gives the high resolution of the depth considering the size of the geometry of the arrays in comparison to SPAC.

6.4 Results comparing to SPAC and seismic interferometry

The joint inversion was performed using the phase velocity information derived from 2ST-SPAC and the group velocity calculated from seismic interferometry using moderate to large arrays (Hayashida *et al*., 2018a). Site 1 (SDB) is selected for the data analysis. The data processing follows the following steps. The 1-hour microtremor data is divided into 351 segments (40.96 s) by overlapping 75% (1024 s). The DC component and linear trend is removed and one-bit normalization is applied. Next, the Fast Fourier Transform (FFT) is performed and spectral whitening is done. The band pass filter of the frequency range between 0.8-15 Hz is applied. The cross-correlation functions CCFs are calculated and the stacking is done. The stacked CCFs for (Z-Z) and (T-T) components are shown in Figures 6.4a and b. After applying a multi filtering technique (Dziewonski *et al.*, 1969) the signal to noise ratio of each frequency is derived. After that, the Group and phase velocities of large and medium array are calculated with the fine S/N ratio. The joint inversion of Group (Love wave) and phase velocity (Rayleigh wave) of surface wave calculated from seismic interferometry and the phase velocity obtained for the same data set using 2ST-SPAC Bhattarai *et al*. (2017a) is compared as shown in Figure 6.5. Results from the joint inversion are much more consistent in shallower part rather than the deeper part. Thus, the combinational use of phase and group velocities indicates the possibility that the accuracy of the derived model would be slightly improved (shallower part), due to the consideration of high-frequency component.

6.5 Results and comparison among SPAC, CCA, regional, and teleseismic earthquake analysis

So far studies using the 2ST-SPAC, CCA, and seismic interferometry methods could derive the dispersion curve in the frequency range from 0.2 to 5.0 Hz and even in the higher

frequencies; however, the frequency below 0.2 Hz remains unrevealed. To capture the dispersion curve below the above-mentioned frequency range long term continuous microtremor data observed at DMG01 (Figure 6.1) gas well site of DMG at TEKU is analyzed and the characteristics of the microtremor in all the 3 components are checked between the period 1 March 2018 to 31 March 2018 for about a month. The power of the microtremor was very weak and could not determine the dispersion curve with such a low power in the lower frequency range from 0.01 to 1 Hz in all the three components at the four observation stations. Fortunately, a regional earthquake was recorded at all the four stations and three teleseismic earthquakes were observed at three stations being one station out of order during that period (Table 6.2). The phase velocity was determined using both 2 and 3 stations using the methodology shown in Figures 6.6a and b. Finally, the broad band dispersion curve ranging from 0.01 to 0.1 Hz and above 0.2 Hz is derived using all those methods mentioned above (Figure 6.6c). However, the dispersion curve in the frequency range from 0.1 to 0.2 Hz has not been derived yet and still waiting for the strong local earthquake at short distances or the teleseismic earthquake in all the deployed stations. It seems that the gap in the dispersion curve mentioned above might cause some ambiguity in the derived velocity structure model. The broad band dispersion curve obtained in the lower frequency range below 0.1 Hz is inverted to derive the velocity structure and compared with the velocity structure model of central Nepal derived by Pandey *et al*. (1995) in Table 6.3 using the quarry blast. It is observed that the shear wave velocity structure at shallow depth below 10 km is underestimated compared to Pandey *et al*. (1995) and Yamada *et al*. (2018); however, the *Vs* values are larger between 10 to 30 km depth (Figures 6.8a and b).

6.6 Summary of the dispersion curves and comparisons with other subsurface velocity structures in the Kathmandu valley, Nepal

The Kathmandu valley occupies about 600 sq. km area and its basement topography is not homogeneous. Previous studies for e.g., Moribayashi and Maruo (1980) first conducted the gravity survey in the valley and reported the approximate depth of the bedrock at the deeper part of the basin is about 650 m almost at the center. However, none of the drillings has reached this depth so far. This is only the experimental result well documented and freely available. Moreover, we do not have the shear wave velocity profile up to the deeper part of the basin in other sites which should be accounted for the disaster mitigation issues and risk

evaluation studies. To grasp the better idea of the bedrock depth and shear wave velocity structure we extended our observation from 3 limited sites to various sites as shown in Figure 6.7a (Yokoi *et al*., 2019). However, none of the sites has given the dispersion curve in the lacking range from 0.1 to 0.2 Hz noticed in the previous chapter. Also, the derived velocity model shows some discrepancies to the bedrock depth as well as the shear wave velocities above this depth. To better have an idea about the structural parameters at the exposed weathered rock (limestone) we have conducted the microtremor survey at this particular site together with the other probable sites of the valley (Yokoi *et al*., 2019). The location of this site is indicated as Chobar (CHB) as shown in Figure 6.8a and lies about 9 km south-west of the Kathmandu valley. Whereas the sites 1 and 2 of the previous studies are denoted by upper most two yellow squares (right panel, Figure 6.1). The dispersion curve obtained at this site is quite distinct among others and having the shear wave velocity same as the weathered bedrock that has derived in the frequency range 0.19 to 3.0 Hz. It is clearly noticed that the dispersion curve obtained in the lower frequency range at the deeper part denoted by BDR, has a similar trend towards the higher frequency (Figure 6.7d). However, the dispersion curves of all other sedimentary sites are concentrated in the frequency range below 0.2 Hz following the missing part of the dispersion curve in the lower frequency range below 0.2 Hz and the gap of the dispersion curve between 0.1 to 0.2 Hz. To better understand the basement depth gravity survey in and around the valley (Pradhan *et al*., 2018) over 236 sites was conducted and seismic reflection survey was performed at the Tribhuvan International Airport (TIA), Gaucher Kathmandu and National Agriculture Research Institute (NARI) in Lalitpur as reported by Kosika *et al*., 2019. Long-period microtremor survey at these two sites with various array geometry was also performed. The integrated results from each of the survey will provide the complete database for the 3-D modeling of the Kathmandu basin in the near future**.** The heuristic search range for the underground structure set for SDB site 1 is shown in Table 6.1. The locations of the microtremor survey are shown in Figure 6.7a (Yokoi *et al*., 2019). The most prominent part of these results together with the previous ones in Chapter 5 is that the gap in the dispersion curve from 0.1 to 0.2 Hz is clearly evident at all sites. The bedrock depth at NAST and TIA are found higher values than we previously obtained at site 1 (SDB). However, there seems some similarity in the underground structure at a discontinuity between site 3 (TEKU), site 1 (SDB), and TIA about 400 m depth. The results of the Gravity survey show the down going basement at about 400 m below TIA which is also supported by the seismic reflection survey. However, the approximation of

bedrock shape is done by assuming the uniform density of the sediment layers while using Gravity survey and that of the constant velocity stack section 1400 m/s for shallow reflection and 1700 m/s for the deep reflection during the data processing.

The comparison between the microtremor survey and the seismic reflection survey shows a clear velocity discontinuity V_S at a depth of about 400 m from the microtremor survey at TIA is supported by the V_P discontinuity at this depth derived from the reflection survey which is consistent with the results of the gravity survey indicating the dipping basement at TIA. However, microtremor results give the bedrock depth at about 800 m which is about half that is obtained from the reflection survey. This comparison results also follow the trend at site 1 (SDB) and site 3 (TEKU) explained in the previous chapter. Thus, the clear impedance contrast detected by seismic reflection survey might not be the seismic bedrock but an intermediate V_P discontinuity that can correspond to the V_S discontinuity at around 400 m detected by microtremor exploration at TIA, SDB, and TEKU.

6.7 Conclusions

Long-period microtremor data observed in the central part of the Kathmandu valley at three sites processed by the SPAC method for the deep velocity structures are re-analyzed. The Centerless Circular Array (CCA), L-shape SPAC, and seismic interferometry methods are used. Moreover, the teleseismic earthquakes recorded at the four temporary continuous stations are analyzed to determine the dispersion curve in the broadband frequency range. Some additional measurements for CCA mini-array were also performed.

By the analysis using the CCA method with special consideration of the scalene triangle arrays of various sizes, the dispersion curves of 3 sites are determined in a broad frequency range. A good consistency is confirmed between SPAC and CCA methods in the lower frequency range with similar dispersion curves; however, with the higher phase velocity using CCA**.** This similarity of the summarized dispersion curves in the low-frequency range suggests a similar deep structure for 3 sites. However, by the clear difference of the dispersion curves at the frequency higher than 1.0 Hz, site 2 (DMG) is highlighted with higher shear wave velocity at shallow parts. Which is well supported by the existing geological and geographical location of the site 2 (DMG). Explored depth is constrained by the limit of available frequency range at around 0.2 Hz due to the low power of microtremor as indicated in Chapter 5. The sags in the coherence function detected by the SPAC method at sites 2 and 3 in the previous chapter are suppressed when the CCA method is applied, but detectable.

The results from the seismic interferometry method derived by the joint inversion of phase and group velocities using small and moderate-sized array shows the possibility of high accuracy of the derived velocity model at the higher frequency range.

The dispersion characteristics below 0.2 Hz are detected using the earthquakes at teleseismic distances. The dispersion curve at the high-frequency range is confirmed by the joint inversion of phase and group velocities. The estimated phase velocities using the teleseismic earthquake show dispersive characteristics from 0.01 to 0.13 Hz and the phase velocity at higher frequency side can be connected with the estimated ones from microtremor explorations. It is confirmed that the estimated shear wave velocity structure is comparable with those derived from the newly proposed seismic velocity structure model of Nepal

(Yamada *et al.*, 2018); however, smaller than those obtained from Pandey *et al*., 1995 in the shallower part but bigger in the range from 10 km to 18 km.

The high-velocity contrast at 400 m depth determined by the *Vp* wave (seismic reflection survey) at TIA is supported by the gravity survey at TIA (Kawasaki *et al*., 2019) and *Vs* discontinuity detected by the microtremor survey at TIA, SDB, and TEKU. The gap of the dispersion curve in the range from 0.1 to 0.2 Hz is also detected in the summary of dispersion curves observed at all sites in the Kathmandu valley. The power of long-period microtremor is weak in the Kathmandu valley to grasp the dispersion curve in the lower frequency range therefore, the geometry of the array of the ongoing continuous observation system in the Kathmandu valley should be periodically change considering the interstation distances and azimuthal coverage.

The results of the Gravity survey show the downgoing basement at about 400 m below TIA which is supported by the seismic reflection survey. A clear *Vs* discontinuity at a depth of about 400 m from the microtremor survey at TIA is supported by the *Vp* discontinuity at this depth derived from the reflection survey which is consistent with the results of the gravity survey indicating the dipping basement at TIA.

Difference in shallow part depth < 100 m, but not well constraint the results obtained from 2S-SPAC method is supported by the CCA method, seismic interferometry method and will be integrated with the awaited results of Gravity and Seismic Reflection surveys to construct a 3-D velocity structure of the Kathmandu valley. The maximum explored sediment depth of the Kathmandu valley derived from Chapters 5 and 6 are used in the GMPE (Abraham and Silva, 2008) in Chapter 4 to account for the basin effect in the observed mainshock record in the central part of the Kathmandu valley. The velocity structure models thus derived and validated from various exploration techniques are used for the ground motion simulation and building damage analysis in the following chapter.

6.8 References

Abrahamson, N., and W. Silva (2008). Summary of the Abrahamson and Silva NGA Ground-Motion Relations, Earthquake Spectra, *Earthquake Spectra*, **24(1)**, 67-97, doi: 10.1193/1.2924360.

Bhattarai, M., D. Nepali, S. Dhakal, S. Shrestha, T. Yokoi, and T. Hayashida (2017a). Microtremor array exploration for deep sedimentary layers in the central part of the Kathmandu valley, Nepal, *Proceedings of the 13th Annual Meeting of Japan Asoc. Earthq. Eng.*, 4-32.

Chimoto, K., and H. Yamanaka (2013). Applicability of estimation of Rayleigh-wave group velocities by using seismic interferometry in the short-period range, *BUTSURI-TANSA* (*Geophysical Exploration*), **66(3)**, 179-188 (in Japanese with English abstract).

Cho, I., T. Takada, and Y. Shinozaki (2006). Centerless circular array method: Inferring phase velocities of Rayleigh waves in broad wave length ranges using microtremor records, *J. Geophys. Res.*, doi: 10.1029/2005JB004235.

Cho, I., T. Tada, and Y. Shinozaki (2004). A new method to determine phase velocities of Rayleigh waves from microseisms, *Geophysics*, **69**, 1535-1551.

Clerbout, J. F. (1968). Synthesis of a layered medium from its acoustic transmission response, *Geophysics*, **33**, 264-269.

Dziewonski A., S. Bloch, and M. Landisman (1969). A technique for the analysis of transient seismic signals, *Bull. Seismol. Soc. Am.*, **59**, 427- 444.

Hayashida, T, T. Yokoi, M. Bhattarai, S. Dhakal, S. Shrestha, T. Pokharel, N. Maharjan, and C. Timsina (2019). Estimation of Bedrock Depth in the Kathmandu Valley, Nepal, Using Ambient Noise and Teleseismic Data, *SSA annual meeting*, Seatle USA.

Hayashida, T., T. Yokoi, and M. Bhattarai (2018a). Estimation of shear wave velocity structure from joint inversion of surface-wave phase and group velocities, *Proc. 15th Japan Earthq. Eng. Symp.*, (in Japanese with English abstract).

Hayashida, T., T. Yokoi, and M. Bhattarai (2018b). Phase velocity of long period surface waves in the Kathmandu Valley, Nepal, inferred from continuous broadband seismic data, *SSJ Fall Meeting*.

Hayashida, T., and M. Yoshimi (2014). Validation of S-wave velocity structure by application of seismic interferometry and SPAC method to long-term microtremor array data, *Proc. 14th Japan Earthq. Eng. Symp*., OS3-Thu-PM1-5, 9pp (in Japanese with English abstract).

Henstridge, J. D. (1979). A signal processing method for circular arrays, *Geophysics*, **44(2)**, 179-184.

Japan International Cooperation Agency (2018). THE PROJECT FOR ASSESSMENT OF EARTHQUAKE DISASTER RISK FOR THE KATHMANDU VALLEY IN NEPAL FINAL REPORT VOLUME 2, MAIN REPORT.

Koshika, K, Y. Kawasaki O. Pradhan, M. Yamamoto, D. Nobuoka, Y. Matsubara, J. Monika, C. Timsina, S. Shrestha, M. Bhattarai, D. Nepali, S. N. Sapkota, M. Hisanori, H. Miyake, and K. Koketsu (2019). Seismic reflection survey in the Kathmandu Valley, Nepal, *JpGU* (Japanese with English abstract).

Moribayashi, S., and Y. Maruo (1980). Basement Topography of the Kathmandu valley, Nepal, An application of gravitational method of the survey of the tectonic basin in the Himalayas, *J. Japan Soc. Eng. Geol*., **21(2)**, 30-37.

Pandey, M. R., and R. P. Tandukar (1995). Interseismic strain Accumulation on the Himalayan crustal ramp (Nepal), *Geophys. Res. Lett*., **22**, 751-754.

Pradhan, O., M. Shimoyama, K. Koshika, T. Kobayashi, S. Dhakal, S. Shrestha, M. Komazawa, K. Nozaki, S. N. Sapkota, D. Nepali, M. Hisanori, H. Miyake, and K. Koketsu (2018), *JpGU*.

Tsuno S., N. Iwata, H. Miyakoshi, S. Yamamoto, and K. Chimoto (2015). An application case of seismic interferometry to exploration of subsurface layer, using short-period microtremor, *Japan Asso. Earthq. Eng*., **15(7)**, 454-462 (in Japanese with English abstract).

Yamada, M., T. Kandel, and K. Tamaribuchi (2018). Automatic hypocenter determination for the aftershocks of the 2015, Gorkha earthquake Nepal, *AGU fall meeting*, Washington D.C.

Kawasaki, Y., K. Kota, O. Pradhan, H. Kurosawa, K. Abe, M. Yamamoto, D. Nobuoka, Y. Matsubara, M. Jha, C. Timsina, S. Shrestha, P. Pokhrel, D. Nepali, M. Bhattarai, S. N. Sapkota, H. Matsuyama, H. Miyake, and K. Koketsu (2019). Subsurface Structure of the Kathmandu Valley Revealed by Seismic Reflection and Gravity Surveys, *AGU*.

Yoshimi, M., T. Hayashida, and T. Sugiyama (2012). Microtremor array survey in active fold area Niigata Japan-Using SPAC and V-method, *Proc. 15th World Conf. Earthq. Eng*., Paper No. 2987, 10 pp.

Yokoi, T., T. Hayashida, M. Bhattarai, T. Pokharel S. Shrestha, C. Timsina, S. Bhattarai, and D. Nepali (2019). Broadband Microtremor Array Exploration at and around Tribhuvan International Airport, Kathmandu, Nepal, *JpGU*.

Yokoi, T., T. Hayashida, M. Bhattarai, T. Pokharel, S. Dhakal, S. Shrestha, C. Timsina, and D. Nepali (2018). Deep Exploration using Ambient Noise in Kathmandu Valley, Nepal-with an emphasis on CCA method using irregular shape Array, *Proc. 13th SEGJ Int. Symp*.

Table 6.1 Search range for the Heuristic search for site 1 (SDB)

No. of Layers	Thickness h_min (km)	Thickness h_max (km)	Shear wave velocity *Vs*_min (km/s)	Shear wave velocity *Vs*_max (km/s)
1	0.001	0.020	0.090	0.120
2	0.001	0.100	0.120	0.150
3	0.010	0.100	0.150	0.400
4	0.010	0.300	0.400	0.700
5	0.010	0.300	0.700	0.900
6	0.010	0.300	0.900	2.470
7	6.000	7.360	2.470	2.730
8	3.253	3.560	2.993	3.308
9	4.714	5.210	3.534	3.906
10	998.0	999.0	4.370	4.830

Table 6.2 Teleseismic Earthquakes used for the analysis of broadband dispersion curve

S.No.	Date and time (UTC)	Latitude	Longitude	Depth (Km)	Magnitude *Mw*	Epicenter
1.	2018/02/25 17:44:44	-6.070	142.754	25.2	7.5	Papua New Guinea
2.	2018/03/02 22:32:54	27.70	86.33	2.1	6.9	Hawaii
3.	2018/05/04 06:19:05	19.313	-164.998	18.0	6.1	Philippines
4.	2018/05/05	14.571	123.919	Unknown	4.1	----------
5	2018/05/09 10:41:45	36.994	71.382	116	6.2	Tajikistan

Table 6.3 Velocity model for Nepal Himalaya (Pandey *et al*. 1995)

Layer (Km)	*Vp* (Km/s)	*Vs* (km/s)
0-23	5.6	3.2
23-32	6.5	3.7
>55	8.1	4.6

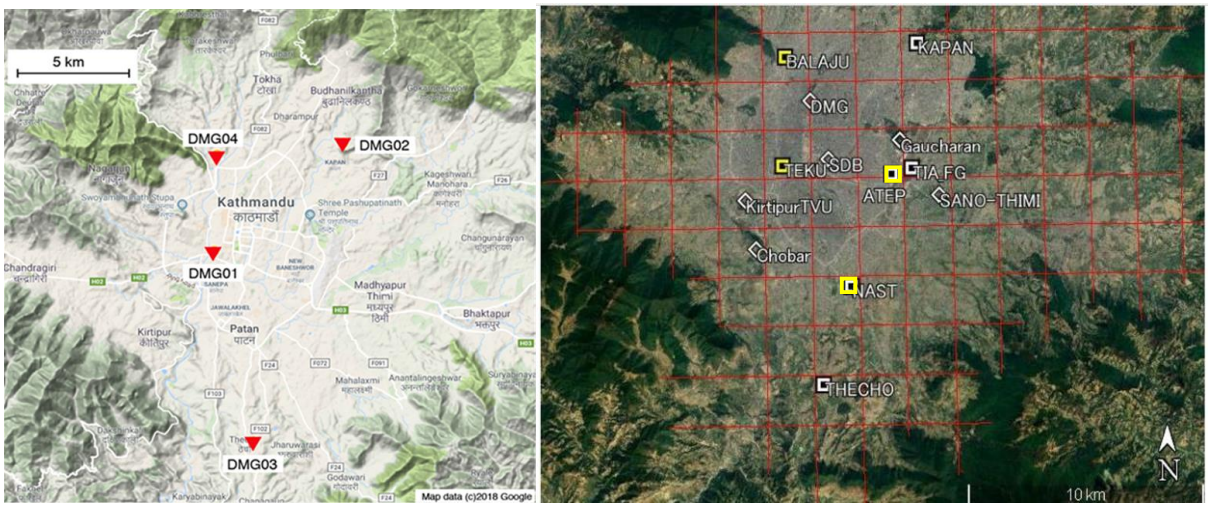

Figure 6.1 The geometry of the continuous temporary observation sites in the Kathmandu valley at the beginning (left panel) and the current configuration (right panel). The configuration has been modified to capture the long period microtremor arriving from various azimuth and interstation distances. This array geometry has also been used to observe local, regional, and teleseismic events of various magnitudes (modified after Hayashida *et al*. (2018b) and Yokoi *et al*. (2018)).

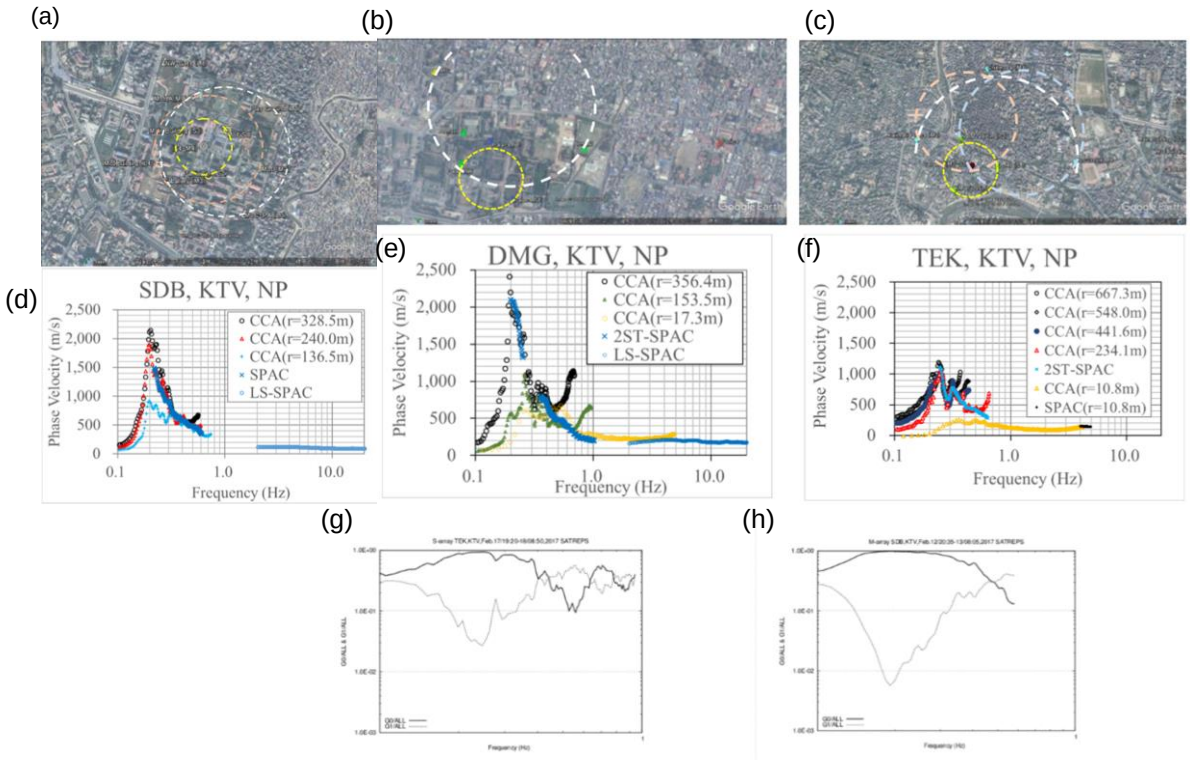

Figure 6.2 (a) Configuration of the array at site 1 (SDB), (b) site 2 (DMG), and (c) site 3 (TEKU). Their combined dispersion curves obtained from analysis of the array of various radius are plotted in Figures (d), (e), and (f) respectively. (g) The power of the zero order Fourier coefficient over azimuth (G0, black) and that of the first order (G1, gray) normalized by the total power (ALL) plotted against the frequency (Hz). (g) Shows those of site 3 TEKU CCA (r = 234.1 m), whereas (h) site 1 SDB CCA (r = 240.0 m) (Yokoi *et al*, 2018).

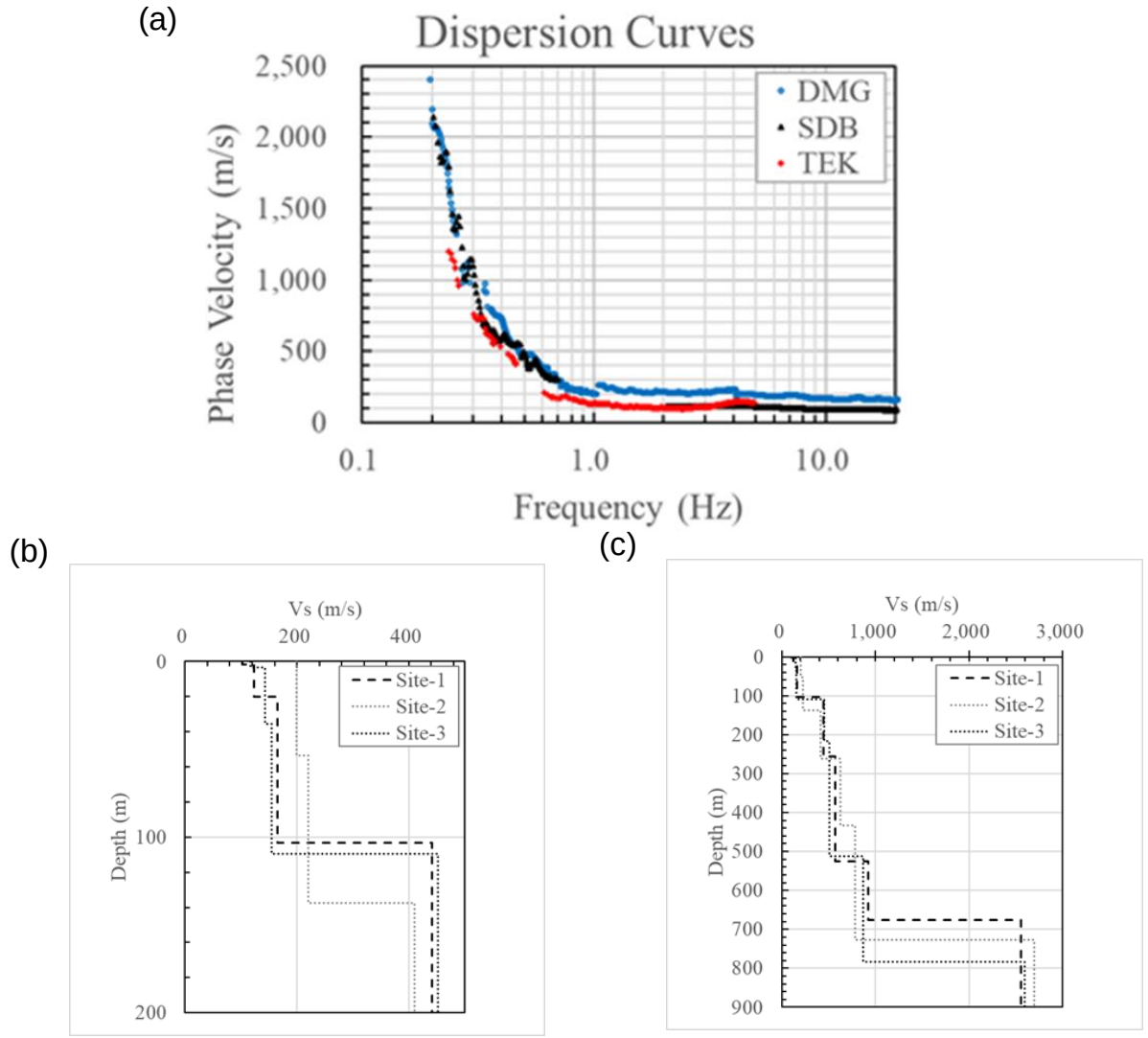

Figure 6.3 (a) Combined dispersion curves obtained from the analysis of various radii from all the 3 sites of various radii, (b) The shear wave velocity structures inverted at shallow depth, and (c) its continuation up to the deeper part (Yokoi *et al*., (2018)).

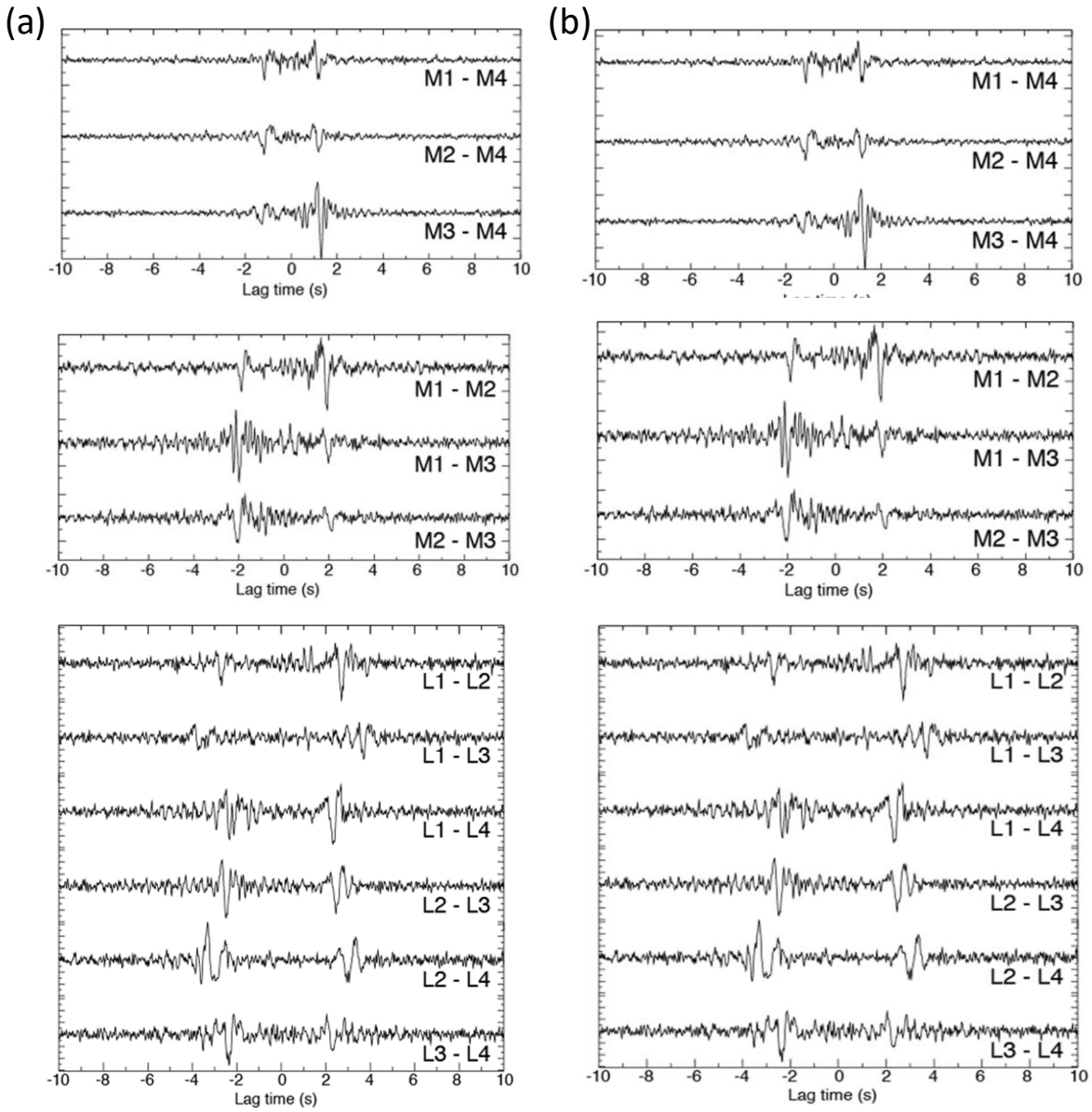

Figure 6.4 The stacked cross-correlation functions (CCFs) for the medium (M) and large (L) sized arrays at site 1 (SDB) (a) (T-T) component and (b) (Z-Z) component (Hayashida *et al*. 2018a)).

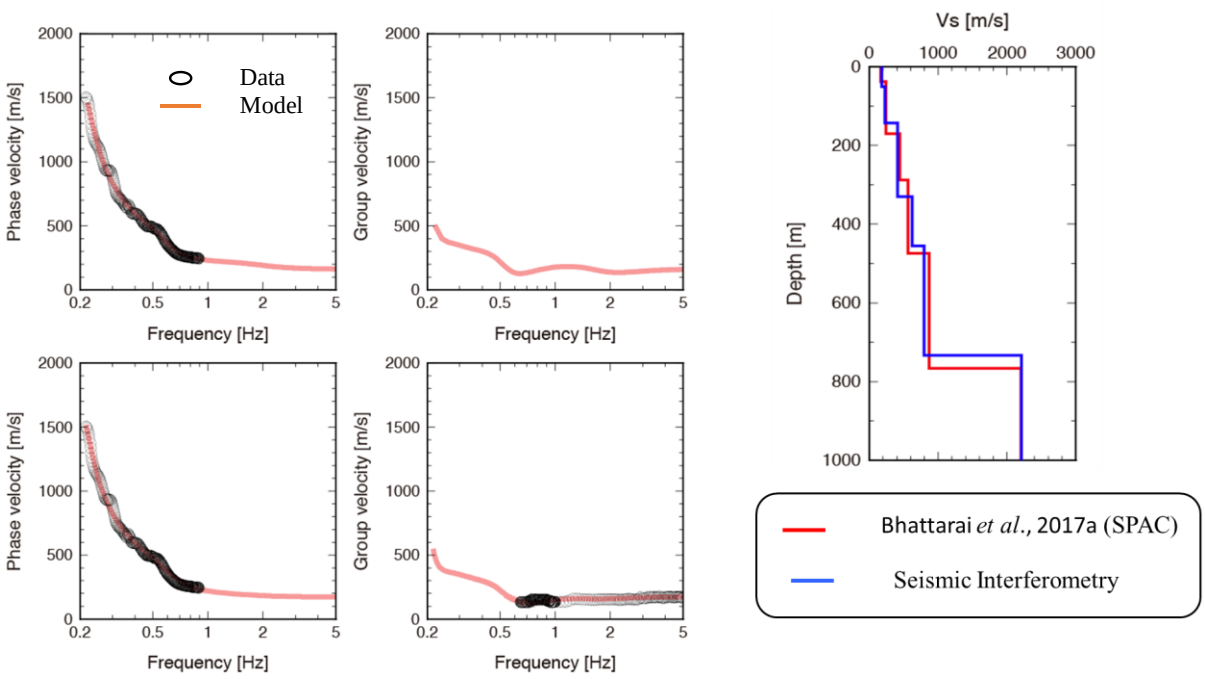

Figure 6.5 Comparison of the velocity structures obtained from 2ST-SPAC (upper panels) and seismic interferometry method (lower panels) at site 1 (SDB) (Hayashida *et al*. (2018a)).

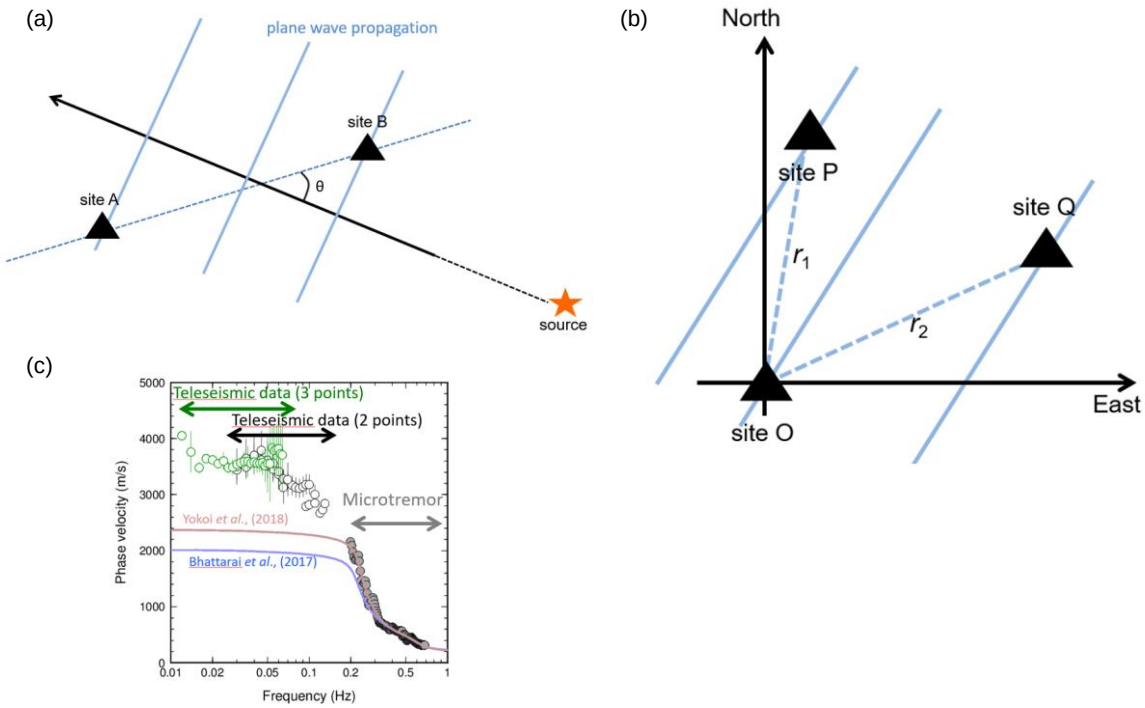

Figure 6.6 Method of calculating the phase velocity of Raleigh wave using (a) 2 stations and (b) 3 stations. (c) Phase velocity derived from the dispersion curve combined from SPAC, CCA, seismic interferometry, and analysis of teleseismic records (Hayashida *et al*. (2018b)).

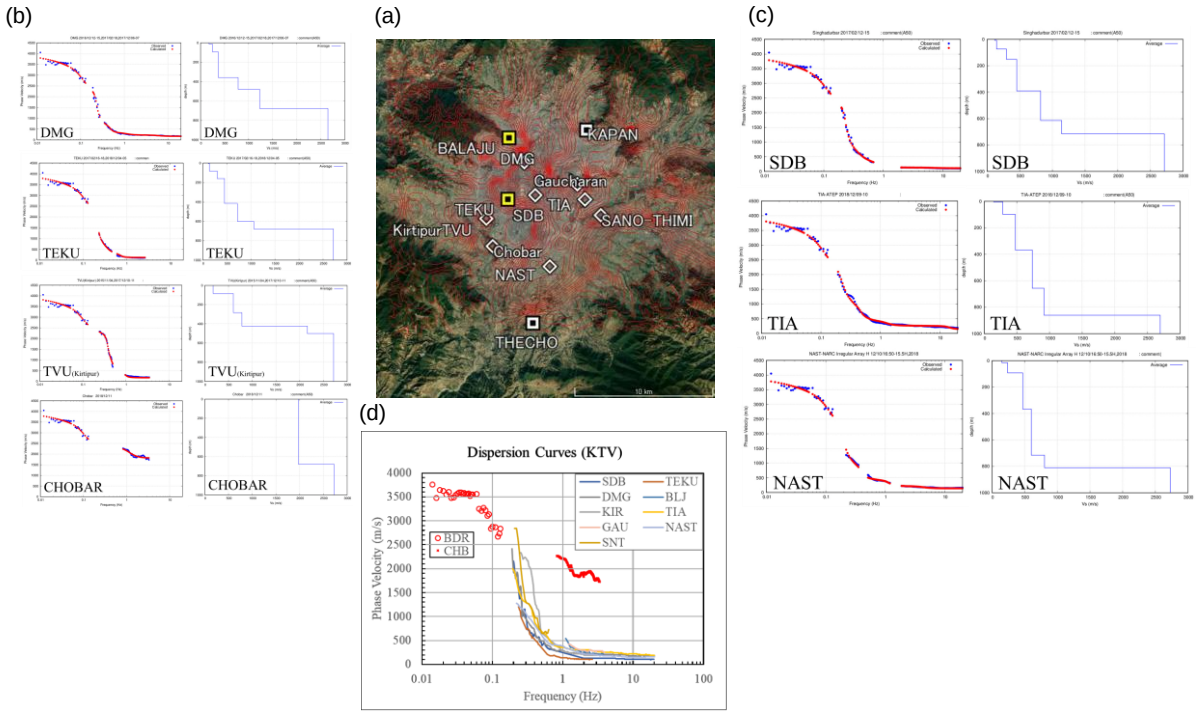

Figure 6.7 (a) Location of the observation sites in the KTV. (b) and (c) Dispersion curves obtained from analysis (left panels) and their inverted velocity structures (right panels). (d) Summary of the dispersion curves obtained from all the considered sites (Yokoi *et al.* (2019)).

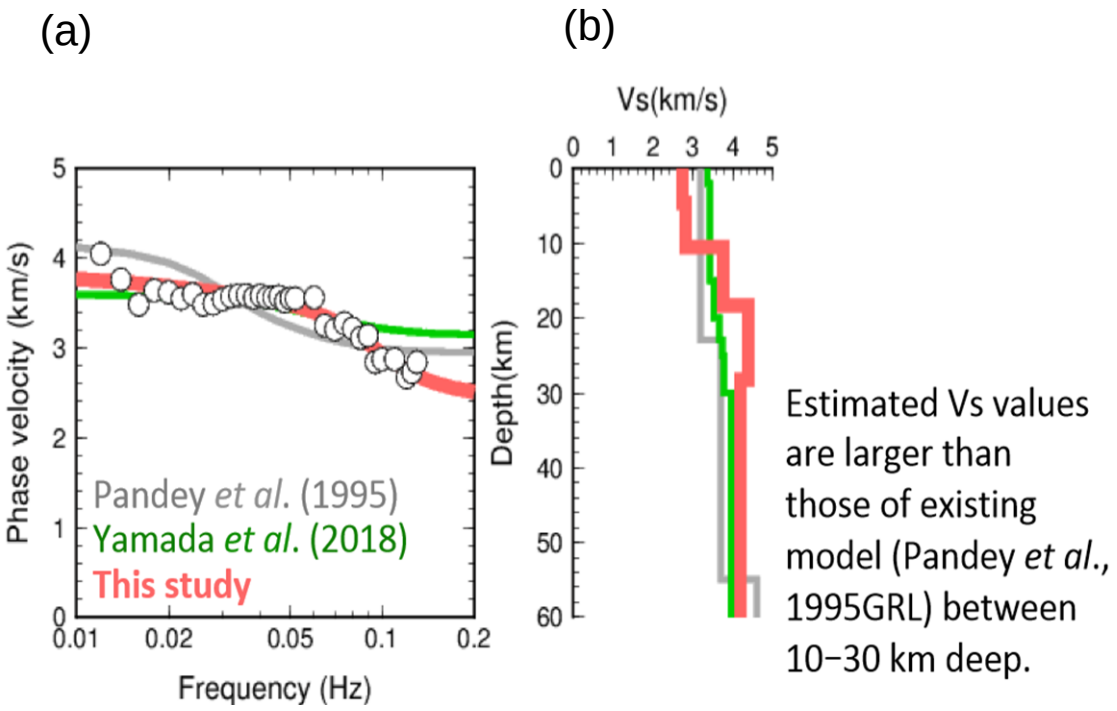

Figure 6.8 (a) Dispersion curves obtained from the analysis of microtremor and teleseismic records (b) The velocity structures obtained from the inversion of dispersion curves (Hayashida *et al*. (2019)).

Chapter 7

Implication of site effect studies for understanding of building damage

7.1 Introduction

The propagation characteristics of seismic waves are essential for understanding seismic damage in the sedimentary filled basins. The long-period ground motion in the sedimentary basin is of great engineering concern as most of the high-rise buildings, long-spanned bridges, and huge oil tanks are located there. Therefore, it is necessary to derive the underground structures as many as possible sites in the basin to understand the propagation characteristics of long-period ground motions. The study of local site effects based on the subsurface ground structure is essential for the evaluation of the seismic hazard of a region.

It is well known that damage due to an earthquake may vary even within a short distance, because of the variation in local site conditions e.g., thickness of soil layers, type of soil, topography, and basement undulations. Theoretical analysis and observed data have shown that each site has a resonance frequency at which ground motion gets amplified. Besides the estimation of deep *Vs* structure, the shallow to intermediate depth structures are also very important because of their influence on the ground motion of the frequency range that is important for building design.

After the pioneering work of Kanai *et al*. (1954) site effect studies based on the propagation of microtremor (ambient noise) has been widely used. Later the array measurement of microtremor has gained its approval for the ascertainment of deep subsurface velocity structures for e.g. (Aki, 1957, 1965; Okada 2003). Chavez-Garcia and Cardenas (2002) have concluded that surface wave generated by soil-structure interaction must have a very long-period, and might be guided by basin deep structure, and could be relevant in terms of seismic risk. Nepal has suffered various large earthquakes over the past centuries that have resulted in the loss of life and substantial damage. The earliest recorded earthquake occurred in 1255 and produced, near Kathmandu, a Maximum Modified Mercalli Intensity (MMI) of X (Chitrakar and Pandey, 1986). The great 1934 (M_W 8.1) Bihar-Nepal earthquake was

located north of Chainpur in the eastern Nepal. This earthquake devastated eastern and central Nepal including the Kathmandu valley, (Rana, 1935) whereas the majority of destruction and damage reportedly occurred in the Kathmandu valley. The 1988 (M_L 6.5) Udaypur earthquake occurred in the Udayapur district of eastern Nepal and resulted in 721 death and destruction of damage about 66382 private and residences and buildings (Chamlagain and Gautam, 2015). The damage was concentrated in the eastern Terai, in a pattern similar to the 1934 earthquake. The historic and past damaging earthquake, and in particular, the 1988 Udayapur earthquake have shown how vulnerable residences and other structures in Nepal are to earthquake loading. Thus, following the 1988 earthquake, Nepal elected to address the basic weakness in the country's construction and housing sectors and to seek the development and implementation of building code. The Gorkha earthquake is the most destructive one in Nepal's history since 1934 which causes about 9000 deaths and damaged about 498,582, buildings and infrastructures (NPC, 2015). After this earthquake Nepal's existing building code is under revision taking in to account the observed ground motion records and damage.

The National Earthquake Hazard Reduction Program (NEHRP) defined six different soil and rock types based on the average shear wave velocity on the 30 m depth (AV_S30), in order to determine the amplification effects: Type A, hard rock (igneous rock), $AV_S30 > 1500$ m/s, type B, rock (volcanic rock) $760 < AV_S30 \leq 1500$ m/s, type C, very dense soil and soft rock (sand stone) $360 < AV_S30 \leq 760$ m/s, type D, stiff soil (mud) $180 < AV_S30 \leq 360$ m/s, type E, soft soil (artificial fill) amplification $AV_S30 < 180$, type F, soils requiring site-specific evaluations. The earlier in the alphabet type A indicates the hardest soil and results in the least wave amplification whereas type E is the softest soil with the most amplification. The central part of the Kathmandu valley falls in type D based on NEHRP site classification (BSSC, 2000).

In the recent building construction practices, the soil investigation at a site in the Kathmandu valley, Nepal comprises of percussion drilling, Standard Penetration Test (SPT), Laboratory tests and prediction of the allowable bearing capacity of the site under investigation. The SPT is carried out on both disturbed and un-disturbed soil samples at regular intervals and depth. The samples thus drawn at the site is taken to the laboratory for the appropriate tests. Moreover, the material properties mostly used are Ordinary Portland

cement (OPC), concrete grade M20 (20 MPa) for all beams, columns, slab, and staircase and steel grade for reinforcement is Fe500, Thermo Mechanically Treated (TMT) steel. Generally, as structural concrete M15 (15 MPa) and M20 (20 MPa) are used in residential and M25 (25 MPa) and M30 (30 MPa) are used in larger structures. For the residential purposes, M20 is suitable and Fe415 grade of steel is commonly used until few years ago; however, Fe500 is more common eventhough Fe550 is also available.

The location map of accelerometers DMG, KKA, PKI, and KTP and the highly damaged areas during the Gorkha earthquake inside the Kathmandu valley are shown in Figure 7.1. The DMG site lies almost at the central part of the valley as indicated by (black triangle) whereas KKA about 10 km north-west of DMG (yellow triangle), KTP about 8 km south-west of DMG (Black triangle), and PKI about 15 km south-east of DMG (gray triangle) are rock sites. The star indicates the aftershocks observed inside the Kathmandu valley after the Gorkha earthquake and the black square indicates the approximate locations of the observed damage inside the Kathmandu valley during the Gorkha earthquake. The site indicated by the black square and marked as new bus park is the heavily damaged site commonly known as Gongabu bus terminal.

The purpose of this chapter is to simulate the ground motions to predict building damage levels for non-specific RC buildings of various height designed by the Nepalese building code under consideration (NBC, 1994). The simulated ground motion is used to analyze building damage using the capacity spectrum method. For the simulation of ground motion where the seismic observation system does not exist the shear wave velocity structure model is used to calculate the theoretical response at the site using any rock and soil motions. Any rock motion can be used to calculate the theoretical response of the site that exists the velocity structure model. Similarly, the theoretical response of the site is evaluated using the sediment motion at any site, a basic requirement is a shear wave velocity structure model or observed ground motion records or both. The existing building code and building damage reports after the Gorkha earthquake are reviewed. Mainly the results obtained from the observed ground motion at DMG is compared with the observed damage at Gongabu area (new bus park) as recommended by AIJ, Japan. Comparisons are realized among the observed damage and computed damage. Tables 7.1 and 7.2, shows the search range and the velocity structures obtained from a Heuristic search at the site 1 (DMG) for numerical simulation.

7.2 Overview of Nepal National building code NBC 105, 1994

After resulting heavy loss of life and numerous buildings damage including the important type of buildings (e.g., hospital, school) in the eastern Udayapur district of Nepal in 1988 by an earthquake (M_L 6.5) National Building code was realized in Nepal. During this earthquake, it was evident that most of the houses were highly vulnerable to earthquakes even in such a moderate magnitude earthquake. To address the lack of understanding of earthquake safety measures the Ministry of Housing and Physical Planning (MHPP) in collaboration with Department of Urban Development and Building Construction drew attention to the urgent need for national building code. In 1988 the MHPP, conscious of the growing needs of Nepal's urban and shelter sectors requested technical assistance from the United Nations Development Programme (UNDP) and their executing agency, United Nations Centre for Human Settlements (UNCHS). A programme of Policy and Technical Support was set up within the Ministry (UNDP Project NEP/88/054) and a number of activities have been carriedout within this framework. Consequently, the Nepal National Building Code (NBC) was developed by the Department of Urban Development and Building Construction (DUDBC) under the Ministry of Physical Planning and Works (MPPW) with the assistance of the United Nation Development Programme (UNDP) and United Nations Human Settlements Programme (UN-HABITAT) and enacted in 1994. The code was made mandatory in all municipalities in 2003 as a legally binding document. In the Kathmandu valley, Lalitpur sub-metropolitan city and Kathmandu metropolitan city started implementing the National Building Code (NBC, 1994) in 2003 and 2006, respectively.

The present code (NBC, 1994) mimics two methods for calculation of design seismic force: Seismic Coefficient Method and Model Response Spectrum Method. The former is stationary; however, the latter is vigorous. The existing building code abides the use of seismic coefficient method for structures up to 40 m heigh that designates the condition of regularity. This method is easy to apply, transparent, and provides equilibrium of actions at a joint (NHSSP, 2017).

The Modal Response Spectrum Method is inherently used for simple structures over 40 meters high designating the configuration of irregularity. Due to default on assignment of indentation, the users of the code will be troubled. The dynamic analysis is inadequate to the

response spectrum method. The Nepalse code do not account the time history time history analyses (NHSSP, 2017).

For the Seismic Coefficient Method:

The design horizontal seismic force coefficient, C_d shall be taken as,

$$C_d = CZIK \tag{7.1}$$

Where C is the basic seismic coefficient for the fundamental translational period in the direction under consideration, Z is the seismic zoning factor, I is the importance factor for building, and K is the structural performance factor specified by (NBC, 1994).

For the Modal Response Spectrum Method**:**

The design spectrum, $C_d\,(T_i)$, shall be taken as,

$$C_d\,(T_i) = C\,(T_i)\,ZIK \tag{7.2}$$

where, $C\,(T_i)$ is the ordinate of the basic response spectrum for translational period, T_i and the other parameters are as stated above. Its value is determined by using the appropriate site subsoil category, and period, T_i from the design response spectra of Nepal (Figure 7.3). In this figure red curve denotes the subsoil type I and indicates hard rock which is derived from (0.032/T), T = 0.4 s. Similarly, the green curve denotes the subsoil type II and indicates the medium type soil which is derived from (0.04/T), T = 0.5 s and blue curve indicates the subsoil type III and indicates the soft soil which is derived from (0.08/T), T = 1.0 s. The basic seismic coefficient for the design response spectra in the Nepalese code is considered as 0.08*g*. The response spectra of the mainshock and largest aftershock of the Gorkha earthquake are compared with the design spectra of the building code and are shown in the Figures 7.4a and b. It clearly indicates that long-period ground motion during the mainshock exceeds the period limit of the code; however, the largest aftershock fits on it well. The same trend is appeared while comparing with the acceleration displacement response spectra in Figures 7.5a and b. Design response spectra designated for the Nepalese building code can be modified by changing the values of I (Importance factor of building) and K (structural performance factor) for different purposes. In particular, construction practices in Nepal are based on code spectrum corresponding to actual resistance of structures of minimal ductility. Figure 7.6a Bijukchhen *et al*. (2017) shows actual demand for the brittle buildings and Figure 7.6b Williams *et al*. (2016) shows

actual minimum demand for the important but brittle buildings. In usual horizontal components of ground motions are used for the codal provisions considering their higher PGA's in the horizontal components in comparision to the vertical ones. However, during the mainshock of the Gorkha earthquake, the PGA in the vertical component, recorded at the central part of the Kathmandu valley at DMG, shows a high PGA value in the vertical component (Figures 7.7), unlike the same ground motion recorded at the rock site KTP. Considerations are needed for the future studies on codal provisions.

For the design analyses based in the Kathmandu valley the seismic zoning factor $Z = 1$, Importance factor $I = 1$, and sub soil type III (soft soil) is used. In this study we have used the value of the structural performance factor $K = 1, 2, 3$, and 4 to analyse the building damage. Different values of K are used to examine the performance of the different types of structures and materials during past earthquakes. The minimum permissible value of the structural performance factor K, and associated detailing is shown in Table 7.3.

Where the numbers 1 and 2 represent as follows,

1. These factors shall apply only if the steel bracing members, the shear walls and/or the infill panels are taken into consideration in both the stiffness and lateral strength calculations.

2. These factors shall apply only if the frame acting alone is capable of resisting at least 25 percent of the design seismic forces.

7.3 Building typology in the Kathmandu valley

Ordinary buildings in Kathmandu valley based on earthquake performance are classified into the following five types (UNDP, 2014).

(1) Adobe, stone- in-mud, brick-in-mud

Adobe buildings are constructed in sun-dried bricks (earthen) with mud mortar for the construction of structural walls. The wall thickness is usually more than 350 mm. Stone-in-mud buildings are constructed using dressed and undressed stones with mud mortar. These types of buildings usually have flexible floor and roof. Brick-in-mud is constructed with fired bricks in mud mortar. These are low-strength masonry buildings.

(2) Brick in cement, Stone in cement

These are brick masonry buildings with fired bricks in cement or lime mortar and stone-masonry buildings using dressed and undressed stones with cement mortar.

(3) Non-engineered reinforced concrete Moment-Resisting-Frame buildings.

These are the buildings with reinforced concrete frames and unreinforced brick masonry infill in cement mortar. The thickness of the infill walls is 230 mm (9") or 115 mm (41/2") and column size is predominantly 9" × 9". The prevalent practice in the most urban areas of Nepal for the construction of residential and commercial complexes generally falls under this category. These buildings are not structurally designed and supervised by engineers during construction. This category also includes buildings with architectural drawings prepared by engineers.

(4) Engineered reinforced concrete Moment-Resisting-Frame buildings

These buildings consist of the frame assembly of cast-in-place concrete beams and columns. Roof and roof framings consist of cast-in-place concrete slabs. Lateral forces are resisted by concrete moment frames that develop their stiffness through monolithic beam-column connections. These are engineered buildings with structural design and construction supervision is made by engineers. Some of the newly constructed reinforced concrete buildings are of this type.

(5) Others

Wooden buildings are mixed building (e.g., stone and adobe), stone and brick in mud, brick in mud and brick in cement, etc. are another building type in the Kathmandu valley and other parts of the country as well.

Among the mentioned buildings above, stone-in-mud, brick-in-mud i.e., the first one has weak performance while the 4th one has the best performance during an earthquake.

Since the 1970's to today number of RC buildings of type 4 is increasing in Nepal usually in the Kathmandu valley. The design of these building is mainly dominated by seismic coefficient method explained in the above section. National Housing and Building Census (CBS, 2011) shows that the percentage of RC buildings in Nepal is 10% among them, 40% of RC constructions are concentrated in the Kathmandu valley as shown in Figure 7.2

(Chamlagain *et al*., 2013). The damage analyses of buildings of type 4 are considered in the following sections.

7.4 Method of ground motion simulation

7.4.1 Propagator Matrix Method

Semi-analytical methods such as Propagator Matrix Method (PMM) (Aki and Richards, 2000) are used to calculate the responses of plane-waves in horizontally layered media to estimate the incident wave from surface displacement. On the other hand, it can be used to estimate surface displacement when the incident wave is known (Bijukchhen *et al*., 2017). When a waveform incident at angle j propagates through a layer with density ρ, the motion stress vector **f**(z) at depth z can be related to motion vector at surface **f**(z_0) by a matrix **P**, known as the propagator matrix.

$$\boldsymbol{f}(z) = \boldsymbol{P}(z, z_0)\boldsymbol{f}(z_0) \tag{7.3}$$

For the horizontal component of S-wave, the Propagator Matrix for a layer is

$$\boldsymbol{P}(z, zo) = \begin{bmatrix} \cos[\omega\eta(z - z_0)] & (\omega\mu\eta)^{-1}\sin[\omega\eta(z - z_0)] \\ -(\omega\mu\eta)\sin[\omega\eta(z - z_0)] & \cos[\omega\eta(z - z_0)] \end{bmatrix} \tag{7.4}$$

Where $\eta = \frac{\cos j}{V_s}$ and $\mu = \rho {V_s}^2$

For n layers above a half space, equation (7.1) becomes

$$\boldsymbol{f}(z_n) = \boldsymbol{P}(z_n, z_{n-1})\boldsymbol{P}(z_{n-1}, z_{n-2}) \dots\dots\dots\dots\dots\dots \boldsymbol{P}(z_1, z_0)\boldsymbol{f}(z_0)$$

$$\boldsymbol{f}(z_n) = \widehat{\boldsymbol{P}}(z_n, z_0)\boldsymbol{f}(z_0) \tag{7.5}$$

The motion stress vector ***f****(z)* can be written in terms of amount of down going (refracted) $\grave{S}$ wave and amount of up going (incident) wave $\acute{S}$ as,

$$\boldsymbol{f}(z_n) = \boldsymbol{F}(z_n)\begin{pmatrix}\hat{S}\\ \acute{S}\end{pmatrix} \tag{7.6}$$

From equation (7.5) and (7.6) we get,

$$\begin{pmatrix}\hat{S}\\ \acute{S}\end{pmatrix} = \boldsymbol{E}^{-1}(z_n)(\widehat{\boldsymbol{P}}(z_n, z_0)\begin{pmatrix}l_0\\ 0\end{pmatrix}_{z=z_0} \tag{7.7}$$

where $\boldsymbol{E}^{-1}(z_n)$ is defined as

$$\boldsymbol{E}^{-1}(z_n) = \begin{bmatrix}\frac{1}{2} & \frac{-i}{2\omega\mu\eta}\\ \frac{1}{2} & \frac{i}{2\omega\mu\eta}\end{bmatrix}$$

From equation (7.7) we get,

$$\begin{pmatrix}\hat{S}\\ \acute{S}\end{pmatrix} = \boldsymbol{B}(z_n, z_0)\begin{pmatrix}l_0\\ 0\end{pmatrix}_{z=z_0} \tag{7.8}$$

when the incident wave is known, its surface displacement, l_0 after passing through the n layers can thus be estimated by,

$$l_0 = \frac{\acute{S}}{\boldsymbol{B}_{21}}. \tag{7.9}.$$

7.4.2 Mathematical Method

The procedure for the ground motion simulation at the site where the observation system does not exist but the underground velocity structure and observed records at some of the rock and soil sites in the vicinity are available. For the simulation of ground motion at the site 1 (SDB).

SDB simulated ground motion

$$= DMG\ observed\ ground\ motion \times \frac{(SDB,\ theoritical\ Response)}{(DMG,\ theoritical\ Response)}$$

$$\frac{SDB,\ theoritical\ Reponse}{DMG,\ theoritical\ Response} = \frac{(SDB,\ theorictical\ Response)\times(Any\ input\ Motion)}{(DMG,\ theoritical\ Response)\times(Any\ input\ motion)}$$

Where, the KTP rock site observed ground motion can be used as any input Motion.

DMG theoretical response multiplied by the KTP observed ground motion is the output from Propagator Matrix Method using DMG velocity structure and KTP observed ground motion as the input.

For the simulation of ground motion at site 3 (TEKU),

TEKU simulated Ground Motion

$$= DMG\ observed\ ground\ motion \times \frac{(TEKU,\ theoritical\ Response)}{(DMG,\ theoritical\ Response)}$$

$$\frac{TEKU,\ theoritical\ Reponse}{DMG,\ theoritical\ Response} = \frac{(TEKU,\ theorictical\ Response)\times(Any\ input\ Motion)}{(DMG,\ theoritical\ Response)\times(Any\ input\ motion)}$$

In this method, any input motion is considered as the available ground motion records at the rock site (KTP). The theoretical response at each site is calculated by inputting the rock site motion (KTP) under the velocity structure available at the site of interest i.e., sites SDB, DMG, and TEKU. We mainly used this procedure to simulate the ground motions at the SDB and TEKU sites using mainshock records observed at sedimentary site DMG and rock site KTP.

7.5 Method of building damage analyses

7.5.1 Capacity Spectrum Method (CSM)

To estimate the maximum displacement, the Capacity Spectrum Method (CSM) (Freeman *et al*., 1975; Freeman, 1978) is a non-linear static process that uses the interaction of the capacity curve derived from a pushover analysis and a reduced response spectrum. This method provides a graphical representation of the global force-displacement capacity curve of the structure (i.e., pushover) and compares it to the response spectra representation of the earthquake demand. It is widely used as a useful tool for the evaluation and retrofit design of existing concrete buildings.

In the traditional force-based design procedures, force related quantities are used to judge the performance of a structure whereas, displacement-based quantities are used to judge in the recent displacement-based seismic design. To prevent the collapse of the structure during strong earthquakes the ductility demand of the structural elements and the overall deformation of the structure should be accounted for and well addressed only by the displacement-based design procedure. The capacity spectrum method (CSM), first introduced in the 1970's is a practical, widely accepted and well-established performance-based seismic analysis technique for accessing the seismic vulnerability of buildings (Freeman *et al*., 1975). Later it was used as the procedure to find the correlation between seismic ground motion and building performance in the 1980s (ATC, 1892). The manual "Seismic Design Guidelines for Essential Buildings" (Freeman *et al.,* 1984; Army, 1986) is developed to design verification procedures based on Performance-Based Seismic Design (PBSD). CSM is used for identifying earthquake damage to buildings caused by various amplitudes of ground motion. The schematic diagram for the CSM method is shown in Figure 7. 8 (Kusunoki *et al*., 2017). This method requires that both the capacity curve and the demand curve be represented in response spectral ordinates and compares the capacity of the structure (in the form of pushover curve) with the demands on the structures (in the form of response spectra). The capacity curve used in Figure 7.8 is for the Single Degree of Freedom (SDOF) system, is simplified down from the Multiple Degree of Freedom (MDOF) system by using the model analysis method. The curve 1 represents the demand curve with 5% vicious damping. The point A denotes the yield point after the building yielded, the point B is the initiation point of demand reduction whereas the point C represents the intersection point when the capacity

curve intersects the demand curve. The maximum response of the mainshock is predicted from the intersection at point C of the capacity curve and the reduced demand curve (curve 2). The intersection of these two curves approximates the response (performance) of the structure and the safety limit is described by the ultimate point (E). The capacity curve, which describes the ability of a building to resist an earthquake, will be superimposed with a response spectrum, which represents the demand of an earthquake for the judgement procedure. Precise estimation of equivalent period, damping ratio and reduced demand spectrum are the key parameters for the accuracy of CSM. Once the building yields the damping will increase due to inelastic response to account for this the demand curve is often decrease. The CSM accounts the effect of non-linearity directly, cracking, and additional damping to the building soil structure interaction.

7.6 Procedure for building damage analysis

The mainshock recorded at the KTP rock site for the ground motion simulation is mainly used as a rock site motion for mainshock simulation. The largest aftershock observed at PKI and KTP rock sites are also used for the same purpose. The data for the same time window at the sedimentary site 2 (DMG) is prepared and damage caused by the simulated ground motions at sites 1, 2, and 3 are analyzed using horizontal components of ground motion. First the simulated ground motions for the Xizang, and Taplejung-Sikkim earthquakes are used for the damage analyses. The epicenter of the former one was above 100 km whereas that of the latter one was about 300 km. However, the epicentral distances of the mainshock and largest aftershocks of the Gorkha earthquake were about 80 km. The observed ground motion at site 2(DMG) is used to check the performance of 40 story buildings in and around the Kathmandu valley. The Capacity Spectrum Method is used to see the performance of the buildings for the different values of the structural performance factor (K = 1, 2, 3, and 4) and calculate the ductility demand. For this, we sampled three Reinforced Cement Concrete (RCC) buildings followed by the National Building Code of Nepal (NBC, 1994). The time periods of such buildings are calculated as per the code which is mentioned in equation 7.10. The performance of 1-, 2-, 3-, 6-, 18-, and 40-story RC buildings in the Kathmandu valley considering the growing trend and majority of constructions today are considered. This is chosen to account the impact of distant moderate-sized earthquakes in the Kathmandu valley for the low raised residential buildings and mainly to analyze the damage observed by the Gorkha earthquake in low, medium, and high raised buildings in the

Kathmandu valley. The fundamental natural period of the RC concrete moment resisting frame building (NBC 105, 1994) is given by

$$T_i = 0.06H^{\frac{3}{4}} \quad (7.10)$$

where H is the height of the building in meter excluding basement story, and in general the height of each floor is averagely considered as 3 m. The period used in the Acceleration-Displacement Response Spectra (ADRS) format is the period of the yielding structure instead of the initial period of an elastic structure. We assumed the yielding period of the structure is two times the initial period of the building calculated using the equation (7.10).

Thus, the yielding period can be calculated as follows,

The angular period $\omega_1 = 2\pi/ T_1$ similarly $\omega_y = 2\pi/ T_y$ also, from Figure 7.9 $(\omega_y/\omega_1)^2 = 1/2$,

so that $(\omega_y/\omega_1)^2 = T_1/T_y$, thus T_y can be expressed as,

$$T_y = 2 \times T_1 \quad (7.11)$$

where T_1 is replaced with T_i in this study considering the change in yielding period in connection with the natural period of the building based on story height and number of floors.

The equivalent damping h_{eq} (Gulkan and Sozen, 1974) and the reduction factor of the spectrum F_h according to Building Standard Law of Japan (MLIT 2000) is calculated using the following formulas,

Equivalent damping $h_{eq} = 0.25\,[1 - \frac{1}{\sqrt{\mu}}] + 0.05$ (7.12)

where μ is the ductility Factor, the response spectrum reduction factor is,

$$F_h = \frac{1.5}{1+10\,h_{eq}} \quad (7.13)$$

The yielding periods of 1-, 2-, 3-, 6-, 18-, and 40-story buildings under consideration are 0.2, 0.4, 0.6, 1.04, 2.3, and 4.3 s respectively. The amount of inelastic deformation is quantified by the displacement ductility factor μ, defined as the ratio of the maximum displacement to the

yield displacement. The design spectrum, $C_d(T_i)$ as specified by the Nepalese code in terms of yielding period now becomes

$$C_d(T_y) = C(T_y)\, ZIK \quad (7.14)$$

where $C(T_y)$ is an ordinate of the basic response spectrum for yielding period *Ty*, *Z* is zoning factor, *I* is the importance factor of the building, and *K* is the structural performance factor appropriate to the particular structural type under consideration.

The following criteria are used for analyzing the building damage analysis;

(i) If the ductility demand is greater than the ductility capacity required for the building, then the building is assumed to have collapsed.

(ii) If the ductility demand is greater than 1 but very close or equal to the ductility capacity of the building, then severe damage occurs.

(iii) If the ductility demand is greater than 1 but less than designed ductility capacity of the building, then moderate damage occurs.

(iv) If the ductility demand is less than 1 then the building remains safe, and minimal damage occurs.

7.7 Data processing for numerical simulation and building damage analysis

7.7.1 Numerical simulation of KKA motion at DMG (M_L 5.7)

The Xizang earthquake (M_L 5.7) occurred on 17, October 2010 in the Tibetan territory of China. It has recorded at DMG in the Kathmandu valley about an epicentral distance of 110 km apart from it. This is the first felt earthquake observed both in sediment and rock sites after installation of an accelerometric network of NSC. Its acceleration waveform, Fourier amplitude spectra, and H/V spectral ratios at DMG are shown in Figures 7.10a, b, and c. The PGA in the vertical component is larger than the horizontal components. The Fourier amplitude spectra show two peaks below 1 Hz. The H/V spectral ratios with both components of ground motion exhibit a peak at around 0.3 Hz reflecting the response of the basin

sediments. This earthquake has also been recorded at all the stations of the seismic network even though the epicenter was outside its geometry. The rock site KKA is located at a distance of 10 km north-west from DMG and its motion is used for the numerical simulation. The same earthquake recorded at DMG is prepared for the comparison between observed and simulated ones using the same time window (Figure 7.11a). In this figure only 22 s observed waveform data at DMG is plotted and PGA remains almost the same in both components of ground motion as of the whole waveform. The acceleration displacement response spectra (ADRS) representation shows that there is a sharp peak between 0.1-0.2 s and broad peak below 0.5 s (Figure 7.11b). The response spectra do not show any clear peak in the period range considered (Figure 7.11c). For the numerical simulation 22 s waveform from KKA rock motion starting 2 s before the *S*-onset from the Husid plot is used. The Propagator Matrix Method (PMM) is applied for numerical simulation considering the damping (Q =*Vs*/10, *Vs* in m/s) for each layer (e.g., Satoh 2005; Oslen *et al*., 2000) of the velocity structure model-derived at DMG. It is very essential for understanding the attenuation and dispersion of the media on seismic waves at soil layers and yet not available in the Kathmandu valley. Therefore, the same value of *Q* is used for the following sections. The simulated motions show slightly higher PGA's than the observed ones (Figure 7.12a). The ADRS of the simulated motion exhibits a wider peak between 0.1-0.2 s which approximately corresponds the yielding period of 1-story building (Figure 7.12b). This peak can also be seen in the acceleration response spectra at around 0.2 s (Figure 7.12c). The observed and simulated motions are superimposed in the ARDS format (Figure 7.13). The simulated spectra from 0.1 to 0.2 s follow the same trend individually shown above. The capacity curves of the non-specific RC buildings having the structural performance factor (K = 1, 2, 3, and 4) in the ARDS format are superimposed with the demand spectra and buildings are analyzed using the Capacity Spectrum Method (CSM) at around DMG as shown in Figures 7.14a and b. The capacity curves having structural performance factor values in the increasing order from bottom to top (K = 1, 2, 3, and 4) are denoted by the green color in different pattern. These are also used in the following sections

7.7.2 Numerical simulation of KKA motion at DMG (M_L 6.8)

The Taplejung-Sikkim, Nepal-India border earthquake (M_L 6.8) occurred on 18, September 2011 in the far-eastern toe of Taplejung district eastern Nepal. The Kathmandu

valley was well shaken by this earthquake; however, epicentral distance was 300 km apart from DMG. This earthquake has also been recorded by both the networks even though the epicenter falls outside the geometry of the network. Its acceleration waveform, Fourier amplitude spectra, and H/V spectral ratios at DMG are shown in Figures 7.15a, b, and c. The PGA's in both the horizontal components is larger than the vertical component. The later part of the waveform was clipped due to the insufficient setup of the post-recording window. The Fourier amplitude spectra show two sharp and broad peaks below 1 Hz. The H/V spectral ratios with both components of ground motion exhibit a sharp peak at around 0.3 Hz reflecting the response of the sedimentary basin. The input motion of KKA is used for the numerical simulation. The same earthquake recorded at DMG is prepared for the comparison between observed and simulated ones using the same time window (Figure 7.16a). In this figure only 32 s observed waveform at DMG is plotted and PGA remains almost the same in both components of ground motion as of the whole waveform. Acceleration displacement response spectra (ADRS) representation shows that there are sharp peaks at around 1 and 2 s especially in EW component (Figure 7.16b). This period nearly corresponds the yielding period of 6-story building. The response spectra do not show any clear overlapping peak in the period range considered (Figure 7.16c). For the numerical simulation 32 s waveform of KKA rock motion starting 2 s before the *S*-onset from the Husid plot is used. The same method mentioned above is used for the numerical simulation. The simulated records show higher PGA's than the observed ones (Figure 7.17a). The ADRS of the simulated motion exhibits a sharp peak at 0.2 s (Figure 7.17b). This peak can be clearly seen in the acceleration response spectra at the same period (Figure 7.17c). The observed and simulated motions are superimposed in ADRS format (Figure 7.18). The simulated spectra follow the same trend individually shown above. The demand spectra of the simulated ground motions are superimposed with the capacity curves of the 1-, 2-, and 3-story RC buildings with both components of ground motion. The capacity curves of the non-specific RC buildings having the structural performance factor (K = 1, 2, 3, and 4) in the ARDS format are superimposed with the demand spectra and buildings are analyzed using the Capacity Spectrum Method (CSM) at around DMG as shown in Figures 7.19.

7.7.3 Numerical simulation of KTP motion at DMG (M_L 7.6)

The Gorkha earthquake (M_L 7.6) occurred on 25, April 2015 in central Nepal with an epicentral distance 80 km north-west of the Kathmandu valley. The Kathmandu valley was shaken with the long-period ground motion. This earthquake recorded at Kirtipur (KTP) rock site (Takai *et al*., 2016), is used as an input motion for the numerical simulation in the sedimentary site 2 (DMG). This earthquake has solely recorded by both the networks since the epicenter falls almost at the centroid of the network. Its acceleration waveform, Fourier amplitude spectra, and horizontal to vertical spectral ratios at the DMG, are shown in Figures 7.20a, b, and c. The PGA in the vertical component is larger than both the horizontal components. The mainshock was recorded above 1 minute and strong shaking resulted in about 40 s. The Fourier amplitude spectra show a broad peak at around 0.25 Hz. The H/V spectral ratios with both components of ground motion exhibit a sharp peak at around 0.25 Hz reflecting the response of the deep sedimentary basin. The input motion of KTP rock site at a distance of 8 km south-west of DMG is used for the numerical simulation. The same earthquake recorded at DMG site is prepared for the comparison between observed and simulated ones using the same time window (Figure 7.21a). In this figure only 42 s observed waveform at DMG is plotted and PGA remains almost the same in both components of ground motion as of the whole waveform. Acceleration displacement response spectra (ADRS) representation shows that there is a wide and broad peak between 4-5 s which nearly represents the yielding period of 40-story building (Figure 7.21b). The response spectra show two peaks at around 0.5 s and from 4 to 5 s respectively (Figure 7.21c). The acceleration waveform, Fourier amplitude spectra, and the H/V spectral ratios at the KTP are shown in Figures 7.22a, b, and c. The PGA's in both the horizontal components are larger than the vertical component. The mainshock was recorded above 1 minute and strong shaking has resulted in about 40 s in the rock site as well. The Fourier amplitude spectra show a broad sharp peak at around 0.25 Hz. The H/V spectral ratios with both components of ground motion exhibit neither a sharp nor a broad peak without showing any basin response as the site is located on the shallow outcrop at the outer margin or the basin.

For the numerical simulation 42 s waveform from the KTP rock motion starting 2 s before the *S*-onset from the Husid plot is used. The same method mentioned above is used for the numerical simulation. The simulated records show higher PGA's than the observed ones

(Figure 7.23a). The ADRS of the simulated motion exhibits a peak at around 4-5 s (Figure 7.23b). This peak can be clearly seen in the acceleration response spectra in the same period whereas another peak around 0.3 s is also visible (Figure 7.23c). The observed and simulated motions are superimposed in ARDS format (Figure 7.24). The simulated spectra follow the same trend individually shown above reflecting the higher spectral values for the simulated ones. The demand spectra of the simulated ground motions are superimposed with the capacity curves of the 3-, 6-, and 18-story buildings with both components of ground motion. The capacity curves of the non-specific RC buildings having the structural performance factor (K = 1, 2, 3, and 4) in the ARDS format are superimposed with the demand spectra and buildings are analyzed using the Capacity Spectrum Method (CSM) taking in to account both components of ground motion at around the DMG as shown in Figures 7.25 to 7.30 and Tables 7.4 to 7.9. In the above-mentioned figures, the black curve represents the simulated ground motion and the red curve represents the response reduced simulated ground motion after applying the addition damping mentioned in equations (7.12 and 7.13). These are also used in the following sections. The unusual earlier peak in the simulated results in Figure 7.23b might reflect some limitation of 1-D simulation for such a long-period ground motion during the mainshock of the Gorkha earthquake in the central part of the Kathmandu valley at DMG.

7.7.4 Simulation of KTP and DMG motions at SDB and TEKU (M_L 7.6)

The sedimentary sites SDB and TEKU both are of their unique administrative as well as geological importance; however, continuous seismic observation systems around those sites are not available. The shear wave velocity structures at these sites have been recently derived. We simulate the ground motion at SDB by applying the observed ground motion records at DMG (basin site) and (KTP) rock site. The theoretical response at the SDB is calculated by inputting the KTP rock motion under the shear wave velocity structure at SDB. Similarly, the theoretical response at DMG is calculated by inputting KTP rock motion under the velocity structure at DMG. The simulated ground motion at SDB is calculated using a mathematical approach by multiplying the observed ground motion at DMG with the quotient of the theoretical response between SDB and DMG. The simulated waveform at SDB (Figure 7.31a), its Sa-Sd response spectra (Figure 7.31b), and acceleration response spectra are shown in Figure 7.31c. In the simulated waveform in the NS component has the higher value

of PGA in comparison to EW. The Sa-Sd response spectra shows clear peaks at around 2 s and around 5 s, approximating the yielding period below 18- and above 40-story buildings. However, the response spectra show multiple peaks at around 0.4 s, 0.6 s, 2 s, 4 s etc. The capacity spectrum method is used to analyze the 3-, 6-, and 18-story RC buildings with the structural performance factor K = 1, 2, 3, and 4 at around SDB site for the analyses of building damage using both components of ground motion. The superimposed capacity demand curves and the damage sheet are shown in Figures 7.32 to 7.37 and in Tables 7.10 to 7.15. By repeating a similar procedure, we have simulated the ground motion at TEKU. The simulated ground motion, its Sa-Sd response spectra, and acceleration response spectra are shown in Figures 7.38a, b, and c. The PGA in NS component is higher than the EW component. The Sa-Sd response spectra exhibits a clear peak at around 4-5 s, approximating the yielding period of buildings around 40-story and above; however, response spectra show unclear peak at around 0.7 s and clear broad peak at around 4-5 s. The capacity demand curves together with the damage sheet using both components of ground motion of the considered RC buildings are shown in Figures 7.39 to 7.44 and in Tables 7.16 to 7.21.

From this mathematical approach, we are benefited to simulate the long-period ground motion complementing the lack of a 3-D velocity structure model. The simulated waveform clearly shows the surface waves in the later part both at the SDB and TEKU sites. The simulated PGA in the NS component of SDB is similar to that of DMG; however, smaller than KTP. It is also observed that the simulated waveform in the EW component of SDB is larger than that of observed ground motion at DMG and KTP. The Sa-Sd curve at the SDB shows two peaks at around 2 s and 5 s. The former is not evident at DMG and TEKU; however, the latter is almost similar to the observed and simulated ground motion at DMG, and simulated ground motion at TEKU.

7.7.5 Numerical simulation of PKI motion at DMG (M_L 6.9)

The largest aftershock of the Gorkha earthquake (M_L 6.9) occurred on 12, May 2015 in the eastern tip of the mainshock rupture. Its epicentral distance was about 80 km south-east of the Kathmandu valley. The Kathmandu valley was shaken with its long-period motion and its characteristics are described in Bhattarai *et al*. (2015). This earthquake was recorded at PKI rock site located at about 15 km south-east of the Kathmandu valley. The rock motion at PKI is used as an input motion for the numerical simulation at the sedimentary site DMG.

The acceleration waveform, Fourier amplitude spectra, and H/V spectral ratios at DMG are shown in Figures 7.45a, b, and c. The PGA's in the EW component is significantly larger than the NS component; however, both the horizontal components have larger values than the vertical component. The later part of the waveform is missing as only 70 s was the total duration of the records. The Fourier amplitude spectra show a clear sharp peak at around 1 Hz; however, two consecutive peaks are noticed below it. The H/V spectral ratios with both components of ground motion exhibit a clear and broad peak around 0.3 Hz reflecting the response of the sedimentary basin. The input motion of PKI is used for numerical simulation and the same time window at DMG is prepared for the comparison (Figure 7.46). In this figure only 32 s observed waveform data at DMG is plotted and PGA remains almost the same in both components of ground motion as of the whole waveform. Acceleration displacement response spectra (ADRS) representation shows that there are wide and sharp peaks at around 1 s and other less significant peak below 2 s both are dominated in the EW component representing the yielding period of buildings below 6- and above 18-story (Figure 7.46b). The acceleration response spectra also show a clear peak of around 1 Hz (Figure 7.46c). For the numerical simulation 32 s waveform from PKI rock motion starting 2 s before the S-onset obtained from the Husid plot is used. However, the whole acceleration waveform, Fourier amplitude spectra, and H/V spectral ratios at PKI are shown in Figures 7.47a, b, and c. PGA's in both the horizontal components of ground motion is larger than the vertical one. The Fourier amplitude spectra show two non-overlapping broad peaks below 1 Hz. There are individual peaks in the H/V spectral ratios of ground motion as well; however, no coincidence in peaks among them. The same method mentioned above is used for the numerical simulation. The simulated records show higher PGA's than the observed ones in both components of ground motion (Figure 7.48a). It is noticed that the simulated ground motion in the EW component is extremely larger than the observed one. The ADRS of the simulated motion exhibits a broad large peak between 1-2 s in EW component (Figure 7.48b). This peak can be seen around 2 s in the acceleration response spectra (Figure 7.48c). Any building of this period has chance to yield and then collapse. The observed and simulated motions are superimposed in ARDS format (Figure 7.49). The simulated spectra follow the same trend individually shown above and dominated in both the components in comparison to the observed ones. The demand spectra of the simulated ground motions are superimposed with the capacity curves of the 3-, 6-, and 18-story RC buildings with both components of ground motion. The capacity curves of the non-specific RC buildings having the structural

performance factor (K = 1, 2, 3, and 4) in the ARDS format are superimposed with the demand spectra and buildings are analyzed using the Capacity Spectrum Method (CSM) at around the DMG as shown in Figures 7.50-7.55 the corresponding damage sheets are shown in Tables 7.22 to 7.27.

7.7.6 Numerical simulation of KTP motion at DMG (M_L 6.9)

The largest aftershock recorded at KTP rock site (Takai *et al*., 2016) is used for the numerical simulation using the shear wave velocity structure at DMG and the simulated motion is compared with the same record observed at DMG. The simulation is performed in a similar way as mentioned above with the choice of the time window 32 s before the *S*-onset. The acceleration waveform at DMG, their Fourier amplitude spectra, spectral ratios and choice of the window for comparison are shown and discussed in the previous section (Figures 7.45 and 7.46). The waveform of the observed rock motion at KTP, their Fourier amplitude spectra, and spectral ratios are shown in Figures 7.56a, b, and c. The horizontal components have larger PGA's than the vertical one. The Fourier amplitude spectra exhibits broad peak around 0.25 Hz; however, two other unclear peaks occurred below 1 Hz. The simulated ground motions are shown in Figure 7.57a. Both the horizontal components of simulated motion have larger PGA's than the observed ones. The ADRS of the simulated motion exhibits a non-overlapping peak among 0.5 to 1 s, and between 1 to 2 s indicating the yielding period of buildings above 2- and below 6-story (Figure 7.57b). None of the sharp peaks have observed; however, there exhibit some peaks in the acceleration response spectra below 2 s (Figure 7.57c). The observed and simulated spectra are superimposed in ARDS format (Figure 7.58). A clear broad peak exhibit at around 1 s. The observed ground motion in both the components is larger than the simulated ones. The demand spectra of the simulated ground motions are superimposed with the capacity curves of the 3-, 6-, and 18-story RC buildings with both components of ground motion. The capacity curves of the non-specific RC buildings having the structural performance factor (K = 1, 2, 3, and 4) in the ARDS format are superimposed with the demand spectra and buildings are analyzed using the Capacity Spectrum Method (CSM) at around the DMG are shown in Figures 7.59 to 7.64 and the damage sheets are shown in Tables 7.28 to 7.33.

7.7.7 Damage analysis of 40-story building using the mainshock at DMG

By considering the observed long-period (about 4-5 s) ground motion at DMG during the mainshock of the Gorkha earthquake we analyze the damage on the 40-story RC building at around DMG using the capacity spectrum method. The ground motion on both the components is used. The capacity curves fall at the bottom of the response spectra as shown in Figures 7.65a, and b. Its damage sheet is shown in Table 7.34 (upper part EW and lower part NS components of ground motion). It is observed that the long-period ground motion could not be resisted by the Nepalese RC buildings of 40-story even followed by the building code considering the code provisions.

7.8 Review on damage reports of the Gorkha earthquake in the Kathmandu valley

The Gorkha earthquake drew the attention of researchers from all over the world to find the cause of building damage. There are not many reports on the studies of the structural damage of the RC buildings; however, the following points are noted from various field reports in consideration with seismology and earthquake engineering.

(1) Due to the the dominance of long-period ground motion in the Kathmandu valley, damage to low-rise buildings was less than predicted from the Gorkha earthquake and its aftershocks, considering the large number of non-engineered buildings (Bijukchhen *et al*., 2017).

(2) The natural frequency of vibration of the sustained older buildings after the Gorkha earthquake in Patan were found smaller with reduction of the stiffness in comparision prior to the Gorkha earthquake eventhough they were not severely damaged or collapsed (Furukawa *et al*., 2017)

(3) The following points related to structures of buildings are indicated on the reconnaissance report of Gorkha earthquake presented by Architectural Institute of Japan (AIJ, 2016).

(i) Effect of increasing the number of floors without strengthening (retrofitting).

(ii) Poor detailig in Nepalese RC buildings in the Kathmandu valley.

(iii) The base shear coefficient from 0.21 to 0.22 of a 3-story RC building suffered with soft-story collapse, the building would have just yielded according to the capacity spectrum method; however, for the six-story building with a base shear coefficient from 0.25 to 0.29 should remain elastic (effect of poor construction materials).

(4) Limited building damage to engineered structures at some sites in the Kathmandu valley have occurred because these structures are not significantly excited by long-period ground motion of Gorkha earthquake; however, they were not tested for future similar earthquakes (Williams *et al*., 2016).

(5) The PGA recorded in the NQ.KATNP stations did not exceed the PGA estimates with 10% probability of exceedance in 50 years based on the seismic hazard studies resultedby JICA (2002), Thapa and Wang (2011); however, it is speculated that the local site effects might have contributed to the significant amplification of motions in the Kathmandu valley and make the effect of the earthquake more influential.

(6) The damage analysis in the Kathmandu valley mainly by Rapid Visual Damage Assessment (RVDA) was done and stickers were pasted in the buildings following the guidelines of Department of Urban Development and Building Construction (DUDBC) guidelines indicating the vulnerability of buildings are as follows: (i) Inspected, (ii) Limited entry, and (iii) Unsafe.

(7) Considering the damage depicted to specific high-rise structures like the Dharahara Tower and other high-rise apartment buildings by the Gorkha earthquake, valley resonance have occurred due to the long-period ground motion which is evidenced by the failure of Dharahara; however, Clock Tower sustained well as it has been strengthened before the earthquake. As both of these towers were rebuilt after the 1934 earthquake. Similar observations were made in the case of residential buildings too as most of the substandard buildings up to three stories performed very well, while many well-designed and detailed high-rise structures sustained substantial damage (Gautam *et al*., 2017).

(8) In the Kathmandu valley, Lalittpur Sub-metropolitan City (LSMC) and Kathmandu Metropolitan city (KMC) have adopted the (NBC 1994) in 2003 and 2006 respectively. During the Gorkha earthquake it has been evident that KMC and LSMC sustained 4 to 5

times less damage than the other areas of the Kathmandu valley where the building code has not been practiced (Yadav, 2015).

The observed damage in the Kathmandu valley is shown in Figures 7.69. The figures show both reinforced concrete and load bearing types. The heavily damaged buildings in the central part of the Kathmandu valley e.g., buildings inside Singhadurbar, Kathmandu durbar square, Durbar High school etc. are dominated by unreinforced concrete and irregular type, poses substantial damage. High rise buildings with masonry infill shows heavy diagonal and other non-diagonal cracks. Some residential RC buildings were pan cake collapsed. In the RC buildings substantial damages are found due to ponding effect, strong-beam weak column, first-soft story failure, insufficient length of the beam, and improper bonding between beam and column. During field visit violence of the building code and low quality of the construction materials is observed. The recommendations given by AIJ; Japan is compared with the observed demand curve at site 1 (DMG) Figures 7.66-7.68.

7.9 Results and discussion

Construction of Reinforced Cement (RC) buildings had begun in Nepal since the 1970s during that time there were no provisions for the earthquake resistance design and construction. Most of the buildings constructed were adobe, wooden, loadbearing, and unreinforced cement. Review on recent construction shows that among the 10% RC constructions in Nepal are confined with 40% in the Kathmandu valley (Chamlagain *et al*., 2013). The Gorkha earthquake is the most recent damaging earthquake in the Kathmandu valley. The mainshock and the largest aftershock of this earthquake is compared with the design response spectrum of the building code (NBC, 1994). Results show that the long-period peak of the mainshock recorded in the Kathmandu valley could not be addressed by the current building code; however, it works well for the largest aftershock (Figures 7.4). Similar results are obtained in comparision to the Sa-Sd response spectra (Figures 7.5). The PGA recorded during the mainshock at the DMG is dominated in the vertical component; however, that recorded at the KTP rock site is dominated in the horizontal components as shown in Figures 7.7. Also, there appearsa flexibility for building designs in Nepal. For example, the basic seismic coefficient varies based on the ductile, brittle, important and maximum resistant buildings. Considerations are needed in the building code based on the recently observed records mainly in terms of basic seismic coefficient and soil type.

In this study ground motions recorded at the rock sites are simulated in the sedimentary sites taking in to account the subsurface velocity structures. In the absence of the seismic observation system the theoretical response is calculated using any ground motion recorded at the rock and soil sites. Mathematical approaches have made it possible to simulate ground motion. In general, propagator matrix method is used to simulate the rock motion at the sedimentary sites. The simulated ground motions are used to calculate the ductility demand of the building collapse which is compared with the ductility capacity required for the building collapse.

The ground motion record from the 2010 Xizang, China earthquake recorded at the KKA rock site is considered for the numerical simulation at the sedimentary site DMG. The simulated results of the Xizang earthquake are used to analyze the damage of 1-story RC building in both horizontal components of ground motion. Results from the analyses show that none of the buildings having the structural performance factor (K = 1, 2, 3, and 4) reported any substantial damage or collapse. The demand curves did not show any overlapping with the capacity curves neither meet any performance points (Figures 7.14a, b)). This shows that none of the RC buildings in the Kathmandu valley are affected by this earthquake; however, the valley was well shaken. It might be due to the low magnitude earthquake coming from over 100 km epicentral distance could not activate the sediments of the basin.

Next, the 2011 Taplejung-Sikkim, Nepal-India border earthquake recorded at KKA is used for the numerical simulation at the sedimentary site DMG. The 1-, 2-, and 3-story RC buildings are taken into consideration for the damage analysis with the structural performance factor (K = 1, 2, 3, and 4). In the superimposed capacity-demand curves the demand curves fall at the bottom of the capacity curve not reflecting any damage (Figures 7.19a, b, c, d, e, and f)) using first EW and then NS components of ground motion. This shows that all the buildings considered behave elastically i.e., poses minimal damage in the Kathmandu valley during Taplejung-Sikkim earthquake. This moderate magnitude (M_L 6.5) earthquake occurred about 300 km east of the Kathmandu valley.

The strong motion records of the mainshock and the largest aftershock of the Gorkha earthquake observed both the rock sites (KTP and PKI) are simulated in the sedimentary site DMG. The comparison of ground motion of the mainshock at DMG with the simulated one

show that the simulated ground motion has higher PGA values compared to observed ones at DMG (Figure 7.23a). There might be several discrepancies for the mainshock simulation (e.g., limitation of 1-D simulation, non-linearity at DMG, lack of damping factor value *Q*, etc.); however, the performance of the buildings with their structural performance factors in NS and EW components show several states of damage or collapse (Tables 7.4 to 7.9). We considered 3-, 6-, and 18-story code compliance buildings having the structural performance factor (K = 1, 2, 3, and 4) for the analysis. The rock site KTP lies on the shallow depth weathered bedrock and situated at about 9 km south-west of DMG. We used damping parameter for each layer as V_S/10. A 3-story building with the structural performance factor K = 1 collapse, K = 2 severe damage; however, K = 3 sustained with moderate damage, and K = 4 shows the minimal damage using the EW component of ground motion (Figure 7.25, Table 7.4). Same buildings with the NS component of ground motion for K = 1, 2, and 3 sustained with moderate damage; however, building having K = 4 sustained with minimal damage (Figure 7.26, Table 7.5). The moderate and minimal damage occurs for the 6-story buildings with EW component of ground motion (K = 1, 2 moderate, K = 3, 4 minimal) (Figure 7.27, Table 7.6). For the NS component of ground motion K = 1 and 2 sustained with moderate damage whereas K = 3 and 4 minimal damage (Figure 7.28, Table 7.7). For 16-story building with EW component of ground motion K = 1 collapse, K = 2 sustained with moderate damage; however, K = 3 and 4 poses minimal damage (Figure 7.29, Table 7.8). For the NS component of ground motion (K = 1 and 2) collapse, K = 3 sustained with moderate damage; however, K = 4 sustained with minimal damage (Figure 7.30, Table 7.9).

Based on the damage analyses of the simulated mainshock at DMG, masonry buildings designed to code-level do not yield and thus have minimal damage. This is in contrast to masonry building performance observed during the earthquake. This is because in reality, masonry buildings are not designed to code-level. These may have similar strength to K = 1, 2, or 3, or lower. In most cases, these buildings would have yielded because masonry buildings are brittle, masonry building with this strength would therefore have likely collapsed as observed in reality.

The simulated ground motion of the mainshock at SDB (Figure 7.31) is analyzed using capacity spectrum method for understanding building damage. Results show mainly moderate and minimal damage for 3- and 6-story buildings with all the structural performance factor considered using both the components of ground motion (Figure 7.32,

Table 7.10, Figure 7.33, Table 7.11 and Figure 7.34, Table 7.12, Figure 7.35, Table 7.13). However, collapse has shown in the 18-story buildings with K = 1 and 2 whereas K = 3 and 4 sustained with moderate damage using the EW component of ground motion (Figure 7.36, Table 7.14). With NS component of ground motion buildings having K = 1 and 2 collapses, however, K = 3 and 4 sustained with minimal damage (Figure 7.37, Table 7.15).

A similar procedure mentioned above is used to analyze the simulated ground motion of the mainshockat TEKU (Figure 7.38). Results show moderate and minimal damage for 3- and 6-story buildings with both the components of ground motion and structural performance factor under consideration (Figure 7.39, Table 7.16, Figure 7.40, Table 7.17 and Figure 7.41, Table 7.18, Figure 7.42, Table 7.19). However, collapse has shown in the 18-story building with K = 1 and 2 whereas K = 3 and 4 sustained with moderate damage using the EW component of ground motion (Figure 7.43, Table 7.20). With NS component of ground motion buildings having K = 1 and 2 collapses; however, K = 3 sustained with moderate damage whereas K = 4 shows minimal damage (Figure 7.44, Table 7.21).

Based on the simulated results on buildings in SDB and TEKU 3- and 6-story yielding periods has very small effect on period elongation but is not as severe as 18-story which is weaker and yields earlier. The 3- and 6-story buildings have high-strength in most cases only K =4 yields so moderate or minimal damage occurred.

The simulated ground motion of the largest aftershock recorded at PKI is simulated at DMG as shown in Figure 7.48 and analyzed using capacity spectrum method for building damage studies. Results show moderate damage for 3-story buildings with K = 1; however, buildings having K = 2, 3, and 4 sustained with minimal damage using the EW component of ground motion (Figure 7.50, Table 7.22). Only the minimal damage occurs for all values of K under consideration (K = 1, 2, 3, and 4) using NS component of ground motion (Figure 7.51, Table 7.23). The state of collapse occurred for the 6-story building having K = 1 with EW component of ground motion; however, only moderate damage occurred for K = 2, 3, and 4 (Figure 7.52, Table 7.24). Using the NS component of ground motion, only moderate damage occurs for K = 1 whereas minimal damage occurred for rest values of K under consideration (Figure 7.53, Table 7.25). All states of collapse occurred in the 18-story building using the EW component of ground motion for K = 1, 2, 3, and 4 (Figure 7.54, Table 7.26); however,

moderate damage occurs with $K = 1$ and only minimal damage occurred for the rest of the K values using the NS component of ground motion (Figure 7.55, Table 7.27).

The simulated largest aftershock using KTP rock motion at DMG is shown in Figure 7.57a the results show neither of the collapse states nor damage with all types of buildings considered having the structural performance factor $K = 1, 2, 3,$ and 4. Only the moderate and minimal damages are reported for 3-, 6-, and 18-story buildings in both the components of ground motion (Figure 7.59, Table 7.28; Figure 7.60, Table 7.29; Figure 7.61, Table 7.30; Figure 7.62, Table 7.31, Figure 7.63, Table 7.32; and Figure 7.64, Table 7.33).

The largest aftershock observed at PKI and simulated at DMG shows collapse in 6-story ($K = 1$) and mainly with 18-story buildings with all values of K with the EW component of ground motion; however, same ground motion observed at KTP and simulated at DMG did not show any states of collapse. Further studies using numerical techniques are needed to confirm the simulated results of PKI at DMG. The higher values of PGA observed in the EW component has also reflected in the states of damage.

For the considered 40-story building full collapse occurred using both NS and EW components of ground motion and all types of structural performance values considered (Figures 7.65, Table 7.34).

Our results from the analyses of observed strong motion records at DMG during the mainshock are consistent with the recommendations from the report of Architectural Institute of Japan (AIJ) in the Kathmandu valley after the Gorkha earthquake. Both of the analysis shows strengthening on the structures is recommendable before adding the additional floors. The ductility value required for the building collapse is low due to the improper detailing of the design. Also, the poor/improper construction practices and the insufficient quality of the construction materials cause the building damage. The building failure during the earthquake might be strengthening using the good detailing. Also, the effectiveness of the 6-story building is doubled in comparison to 3-story building if the base shear capacity is increased (Figures 7.66, 7.67, and 7.68 respectively) taking in to account the better structural performance.

In reality we are using only few earthquakes records observed and simulated at the particular sites so it might not be the representative of the damage in the whole the

Kathmandu valley, also there might be some limitation of 1-D simulation. We are considering the code compliance buildings which do not say something about the weak and non-ductile buildings e.g., $K = 1$ which are similar to the vulnerable older buildings in the Kathmandu valley and were damaged during the mainshock and the largest aftershock. Also, there might have some limitations to follow of the code during construction design of the buildings and building material which has not been considered during these analyses; however, were noticed during the site visit. The overview of the observed damage in the Kathmandu valley is shown in Figures 7.69.

7.10 Conclusions

The Xizang, China earthquake, the Taplejung-Sikkim earthquake, the mainshock, and the largest aftershock of the Gorkha earthquake recorded at rock sites KKA, KTP, and PKI are simulated in the sedimentary site DMG where shear wave velocity structure as well as seismic observation system exists. The mainshock of the Gorkha earthquake is also simulated using mathematical approach at the sites where only the underground velocity structure exists but the seismic observation system does not exist.

The Xizang, China earthquake with an epicentral distance of about 110 km north from DMG recorded at the KKA rock site is used for simulation. The simulated results used for the damage analysis neither show any state of damage or collapse in 1-story RC building in both the components of ground motion and with all values of structural performance factor used. The Taplejung-Sikkim earthquake with an epicentral distance of about 300 km east of the Kathmandu valley recorded at the KKA rock site is used for simulation at DMG. None of the 1-, 2-, and 3-story RC building with the structural performance factor considered in both the components of ground motion does not show any states of damage or collapse. It is to say only the minimal damage.

The results of the mainshock from the damage analyses using simulated motion of KTP at DMG shows collapse, severe damage, moderate damage, and minimal damage i.e., all damage patterns while increasing the value of K considered in this analyses mainly for EW component of ground motion in the 3-story buildings; however, only moderate and minimal damage occurred with NS component of ground motion. Analyses shows in 6-story buildings moderate and minimal damage occurred in both the components of ground motion.

Especially, in 18-story buildings, $K = 1$ collapse with the EW component, however; $K = 1$ and 2 collapse in the NS component of ground motion. The simulated ground motion of the mainshock at SDB shows collapse only in 18-story buildings with $K = 1$ and 2 using both components of ground motion. Similar results of collapse are obtained while analyzing the simulated ground motion at TEKU. Considering the results of the simulated mainshock and values of K other buildings remain sustained with moderate and minimal damage.

The damage pattern with the simulated ground motion of the largest aftershock recorded at PKI shows all states of collapse in the 18-story building; however, that of collapse on 6-story building ($K = 1$) considering EW component of ground motion. Moderate and minimal damage is observed with other values of K in the buildings under consideration. In contrast, no states of collapse have resulted from the same record of ground motion observed at KTP and simulated at DMG.

Considering the long-period ground motion from 4 to 5 s with both the components of ground motion a 40-story building completely collapses while using the observed ground motion of the mainshock at DMG.

From the analysis of long-period ground motion, building with high story seems to behave more probability of collapse in comparison to low rise buildings. The analyses of the damage considering the mainshock ground motion supports the damage pattern during the Gorkha earthquake; however, the damage resulted by the largest aftershock might have been affected prior by the damage due to the mainshock record but not for all the structural performance factor K values. The results obtained from the analyses using the capacity spectrum method and mathematical method is well supported for the 18-story buildings. The damage observed in the Kathmandu valley considering the limited number of existing observation stations, shear wave velocity structures, and super high raised buildings during the Gorkha earthquake is supported by this study.

The design response spectra given by the Nepalese Building Code (NBC, 1994) could not address the long-period ground motion during the mainshock of the Gorkha earthquake; however, it suits well to the largest aftershock similar situation occurs with the ADRS. Considerations are needed in the design response spectra of the existing building code for the long-period ground motion of about from 4 to 5 s as provided by the Gorkha earthquake in

the Kathmandu valley. Also, the large value of PGA in the vertical component in comparison to the horizontal components at DMG suggests some correlation needs to be considered between the horizontal and vertical components of ground motion in the design response spectra. It is also recommended to follow the building code and strengthen the structural performance before adding the extra loads on structures.

Based on the results of the building damage analysis in this study weaker buildings are more likely to collapse, taller buildings are suspectable to long-period effects, masonry buildings design to code level do not yield causing minimal damage in contrast, with the observed damage in the masonry buildings. Both components of ground motion are significant for 3-, 6-, and 18-story buildings resulted from the mainshock in contrast, the largest aftershock is significant only with the EW component of ground motion. Also, smaller K factor resulted in more significant damage, however, masonry ($K = 4$) actually has resulted minimal damage.

Recommendations based on the observed damage and the observed and simulated ground motion records in this study support the reconnaissance report of AIJ. Which suggest strengthening of buildings before adding the extra loads, design with necessary detailing to meet the ductility capacity of the building collapse, maintain the necessary construction quality of the building materials, proper interaction between the soil foundation and structure, and construction without the violence of the building codes are the necessary measures to be taken for future RC building constructions in the Kathmandu valley.

In fact, we are considering the code compliance buildings which do not say something about the old and vulnerable buildings which were collapses during past earthquakes. Further studies are needed to address such issues.

This study shows the possibility of building damage analyses in a specific domain where either seismic observation system, or shear wave velocity structures or both exist.

7.11 References

Aki, K. (1957). Space and time spectra of stationary stochastic waves, with special reference to microtremor, *Bull. Earthq. Res. Inst*., Tokyo Univ., **35**, 415-456.

Aki, K. (1965). A note on the use of microseisms in determining the shallow structures of the earth'scrust, *Geophysics*, **30**, 665-666.

Aki, K., and P. G. Richards (2000). Quantitative seismology, University Science books, California.

Army (1986). "*Seismic Design Guidelines for Essential Buildings*", Department of Army (TM-5-809-10-1), Navy (NAVFAC P355.1), and Air Force (AFM 88-3, Chapter 13, Section A), Washington, D. C., U. S. A.

ATC (1982). "An investigation of the Correlation between Earthquake Ground Motion and Building Performance", Report ATC-40, Applied Technology Council, Red wood city, California U.S.A.

Bhattarai, M., D. Nepali, S. Dhakal, S. Shrestha, T. Yokoi, and T. Hayashida (2017a). Microtremor array exploration for deep sedimentary layers in the central part of the Kathmandu valley, Nepal, *13th Annual Meeting of Japan Assoc. Earthq. Eng*., Tokyo.

Bhattarai, M., L. B. Adhikari, U. P. Gautam, A. Laurendeu, C. Labonne, R. Hoste-Colomer, O. Sebe, and B. Hernandez (2015). Overview of the large 25 April Gorkha, Nepal, earthquake from accelerometric perspectives, *Seismol. Res. Lett*., **86**, 40-48.

Bijukchhen, S., N. Takai, M. Shigefuji, M. Ichiyanagi, and T. Sasatani (2017). Strong-Motion Characteristics and Visual Damage Assessment Around Seismic Stations in Kathmandu After the 2015 Gorkha, Nepal Earthquake, *Earthquake Spectra*, **33(S1)**, doi: 10.1193/042916EQS074M.

Building Seismic Safety Council (BSSC) (2001). NEHRP recommended provisions for seismic regulations for new buildings and other structures, 2000 Edition, Part 1: Provisions, prepared by the Building Seismic Safety Council for the federal emergency Management Agency (Report FEMA 368), Washington, D. C.

CBS (2011). National Population and Housing Census, Central Bureau of Statistics, Government of Nepal.

Chaulagain, H., H. Rodrigues, J. Jara, E. Spacone, and E. Varum (2013). Seismic response of current RC buildings in Nepal: a comparative analysis of different design/construction, *Eng. Struct*., **49**, 284-294.

Chavez-Garcia, F. J., and M. Cardenas-Soto (2002). The contribution of the built environment to the free-field ground motion in Mexico City, *Soil Dyn. Earthq. Eng*., **22**, 773-780.

Chitrakar, G. R., and M. R. Pandey (1986). Historical earthquakes of Nepal, *Bull. Nepal Geol. Soc*., **4**, 7-8.

Chamlagain, D., and D. Gautam (2015). Seismic Hazard in the Himalayan Intermontane Basins, An example from Kathmandu Valley, Nepal, R. Shaw; H. K. Nibanupudi (eds.), Disaster Risk Reduction, DOI: 10.1007/978-4-431-55242-0_5.

DUDBC (2015). Department of Urban Development and Building Construction, the Government of Nepal.

Freeman, S. A., J. P. Nicoletti, and G. Matsumura, (1984). "Seismic Design Guidelines for Essential Buildings", *Proceedings of 8th World Conference on Earthquake Engineering*, San Francisco, California, U.S.A.

Freeman, S. A. (1978). Prediction of response of concrete buildings to serve earthquake motion, Publ., SP-55, American Concrete Institute, Detroit, MI, 589-605.

Freeman, S. A., J. P. Nicoletti, and J. V. Tyrell (1975). Evaluations of Existing Buildings for Seismic Risk, A case study of Puget Sound Naval Shipyard, Bremerton, Washington, *Proceedings of U. S. National Conference on Earthquake Engineering*, EERI, Berkeley, U.S.A., 113-122.

Furukawa, A., J. Kiyono, R. R. Parajuli, and T. Kenjo (2017). Evaluation of damage to historic masonry buildings in Nepal through comparision of dynamic characteristics before and after the 2015 Gorkha earthquake, *Frontiers in Built Environment*, doi: 103379/fbuil2017.00062.

Galetzka, J., D. Melgar, J. F. Genrich, J. Geng, S. Owen, E.O. Lindsey, X. Xu, Y. Bock, J. -P. Avouac, L. B. Adhikari, B. N. Upreti, B. Pratt-Sitaula, T. N. Bhattarai, B. P. Sitaula, A. Moore, K. W. Hudnut, W. Szeliga, J. Normandeau, M. Fend, M. Flouzat, L. Bollinger, P. Shrestha, B. Koirala, U. Gautam, M. Bhattarai, R. Gupta, T. Kandel, C. Timsina, S. N. Sapkota, S. Rajaure, and N. Maharjan (2015), Slip pulse and resonance of Kathmandu basin during the 2015 Gorkha earthquake, Nepal, *Science*, **349(6252)**, 1091-1095, doi: 10.1126/science.aac6383, 2015.

Gulkan, P., and M. A. Sozen (1974). Inelastic Response of Reinforced Concrete Structures to Earthquakes Motions, Procedings to the ACI, 71(12).

Japan International Cooperation Agency (2002). *The study on earthquake disaster mitigation in the Kathmandu valley, Kingdom of Nepal*, Vols. I-III.

Kanai K., T. Tanaka, and K. Okada, (1954). Measurement of Microtremor, *Bull. Earthq. Res. Inst.*, **32**, 199-210.

Kusunoki, K., D. Hinata, Y. Hattori, and A. Tasai (2017). A new method for evaluating the real time residual seismic capacity of existing structures using accelerometers, Structures with multiple degree of freedom, *Japan Architectural review*, doi: 10.1002/2475-8876.1010.

MLIT (2000). Notification No. 1457-2000, Technical standard for structural calculation of response and limit strength of building, Ministry of Land, Infrastructure and Transport, Tokyo, Japan (in Japanese).

National Planning Commission (NPC, 2015). *Post Disaster Need Assessment Vols. A and B.* Kathmandu, Government of Nepal.

NBC (1994). Seismic Design of Buildings in Nepal, Government of Nepal, Ministry of Physical Planning and Works, Department of Urban Development and Building Construction.

NHSSP (2017). Nepal Health Sector Support Programe III (NHSSP-III), Retrofitting Codes and Practices Priliminary Report.

Okada, H. (2003). The Microtremor Survey Method, translated by Koya Suto, Geophysical Monograph Series, no 12, *Soc. Exp. Geophysics*.

Oslen, K. B., R. Nigbor and T. Konno (2000). 3-D viscoelastic wave propagation in the Upper Borrego Valley, California, constrained by bore hole and surface data, Seismol. Soc. Am., **90(1)**, 134-150

Parajuli (2018). Damages due to Gorkha earthquake 2015 and deficiencies in shree mahal, A Journal on Rural Infrastructure Development, Vol (**9**) (Issue 9).

Rana, Maj. Gen. Braham Sumsher (1935). Nepal ko Bhukampa (The great earthquake of Nepal), *Second ed., Jorganesh press*, 1-250 (in Nepali).

Reconnaissance Report on the 2015 Nepal Grorkha Earthquake (2016). Architectural Institute of Japan (AIJ).

Satoh, T. (2004). Inversion of incident angle and Q value of sediments from deep borehole seismograms using adaptive simulative annealing method, paper presented in: *13th world conf. earthq. Eng.*, Vancouver, Canada.

Takai, N., M. Shigefuji, S. Rajaure, S. M. Bijukchhen, S. Ichiyanagi, M. R. Dhital and T. Sasatani (2016). Strong Ground Motion in the Kathmandu Valley during the 2015 Gorkha, Nepal, Earthquake, *Earth Planets Space*, **68(10)**, doi: 10.1186/s40623-016-0383-7.

Takai, N., K. Swada, M. Shigefuji, S. M. Bijukchhen, M. Ichiyanagi, T. Sasatani, Y. P. Dhakal, S. Rajaure and M. R. Dhital (2015). Shallow underground structure of strong ground motion observation sites in the Kathmandu valley, *J. Nepal Geol. Soc*., **48** (Special issue).

Thapa D. R., and G. Wang (2013). Probabilistic seismic hazard analysis in Nepal, *Earthq. Eng. Eng. Vib*., **12**, 577-586.

UNDP (2014). Seismic Vulnerability Evaluation Guideline for Private and Public Buildings Pre-disaster Vulnerability Assesment) May, 2011, Reprinted by Comprehensive Disaster Risk Management Programme in Nepal.

UNDP (1994). "Seismic Hazard Mapping and Risk Assessment for Nepal", His Majesty's Government of Nepal, Ministry of Housing and Physical Planning, UNDP/ UNCHS (Habitat), Subproject NEP/88/054/21.03.

Williams, S., B. Gosh, S. Wilkinson, C. Fenton, P. Burton, M. Whitworth, S. Dalta, G. Franco, A. Trieu, M. Dejong, V. Novellis, T. White, and T. L. loyd (2016). Site Amplification in the Kathmandu Valley during the 2015 *M* 7.6 Gorkha, Nepal earthquake. *Bull. Earthq. Eng.*, **14(12),** 3301-3315.

Yadav (2015). Effectiveness of building code implementation in Nepal, *Master's thesis*, *GRIPS/BRI*, Japan.

Table 7.1 Search range for site 2 (DMG)

No. of Layers	Thickness hmin (km)	Thickness hmax (km)	Shear wave velocity V_S min (km/s)	Shear wave velocity V_S max (km/s)
1	0.001	0.030	0.150	0.200
1	0.010	0.100	0.200	0.350
2	0.010	0.100	0.200	0.350
3	0.010	0.300	0.350	0.700
4	0.010	0.300	0.700	0.900
5	0.010	0.300	0.900	2.470
6	6.000	7.360	2.470	2.730
7	3.253	3.560	2.993	3.308
8	4.714	5.210	3.534	3.906
9	998.0	999.0	4.370	4.830

Table 7.2 Velocity structure model derived from microtremor at site 2 (DMG)

No. of Layers	Thickness (km)	Density (g/cm^3)	Velocity of P wave *Vp* (km/s)	Shear wave velocity V_S (km/s)
1	0.0125	1.783	1.486	0.177
2	0.0801	1.808	1.563	0.246
3	0.265	1.850	1.697	0.367
4	0.121	1.987	2.157	0.781
5	0.198	2.124	2.565	1.230
6	6.026	2.470	4.232	2.651
7	3.316	2.578	4.900	3.253
8	4.897	2.663	5.566	3.852
9	999	2.732	6.388	4.548

Table 7.3 Structural performance factor *K* and other design requirements for horizontal load-resisting systems of buildings and other structures (NBC, 1994)

Item	Structural Type	Minimum Detailing Requirements	Structural Performance Factor *K*
1 (a)	Ductile moment-resisting frame	Must comply with the detailing for ductility requirements.	1.0
(b)	Frame as in 1(a) with reinforced concrete shear walls	For frames: as for 1(a). Reinforced concrete shear walls must comply with appropriate[3] detailing for ductility requirements.	1.0[1]
2 (a)	Frame as in 1(a) with either steel bracing members detailed for ductility or reinforced concrete infill panels	For frames: as for 1(a). Steel bracing members must comply with the detailing for ductility requirements NBC 111-94. Reinforced concrete infill panels must comply with the detailing requirements of NBC 109-94.	1.5[1,2]
(b)	Frame as in 1(a) with masonry infills	Must comply with the detailing for ductility requirements.	2.0[1,2]
3.	Diagonally-braced steel frame with ductile bracing acting in tension only	Must comply with the detailing for ductility requirements of Nepal Steel Construction Standard	2.0
4.	Cable-stayed chimneys	Appropriate materials Standard	3.0
5.	Structures of minimal ductility including reinforced concrete frames not covered by 1 or 2 above, and masonry bearing wall structures.	Appropriate materials Standard	4.0

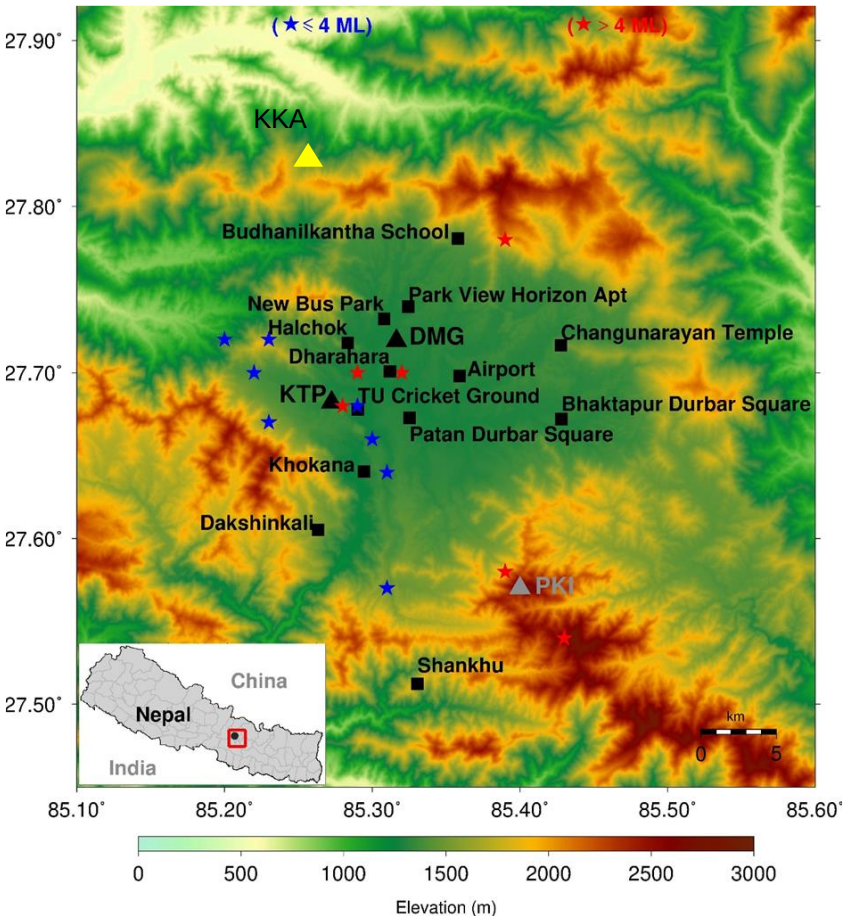

Figure 7.1 The strong motion stations in and around the Kathmandu valley used in this study are indicated by black tringles (DMG, KTP), yellow triangle (KKA), and grey triangle (PKI). Black squares denote the locaions of heavily damaged area in the Kathmandu valley during Gorkha earthquake and its aftershock sequence. Blue and red stars are the aftershocks after the Gorkha earthaquake recorded inside the Kathmandu valley. The black dot inside the red square in the lower right corner shows the epicenter of the Gorkha earthquake.

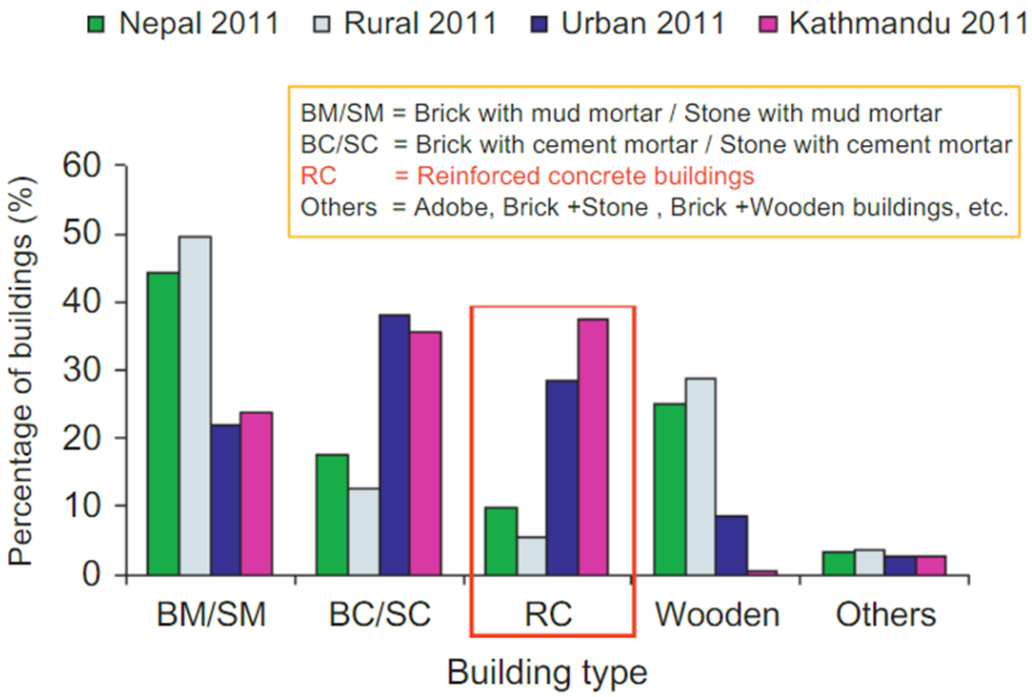

Figure 7.2 Building types in Nepal (Chamlagain *et al*., 2013).

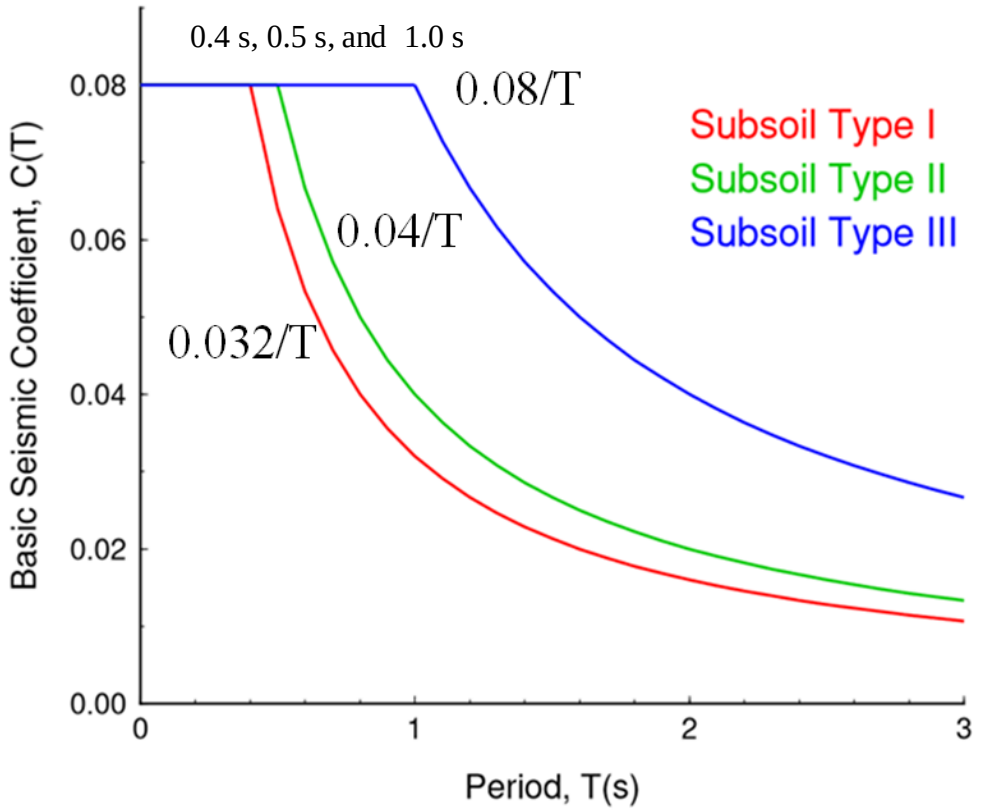

Figure 7.3 Design response spectra of Nepal's national building code. Red, green, and blue colors indicate hard rock, stiff soil, and soft soil respectively. Numbers represent the period and seismic coefficients of each sub soil type specified by the code (NBC, 1994).

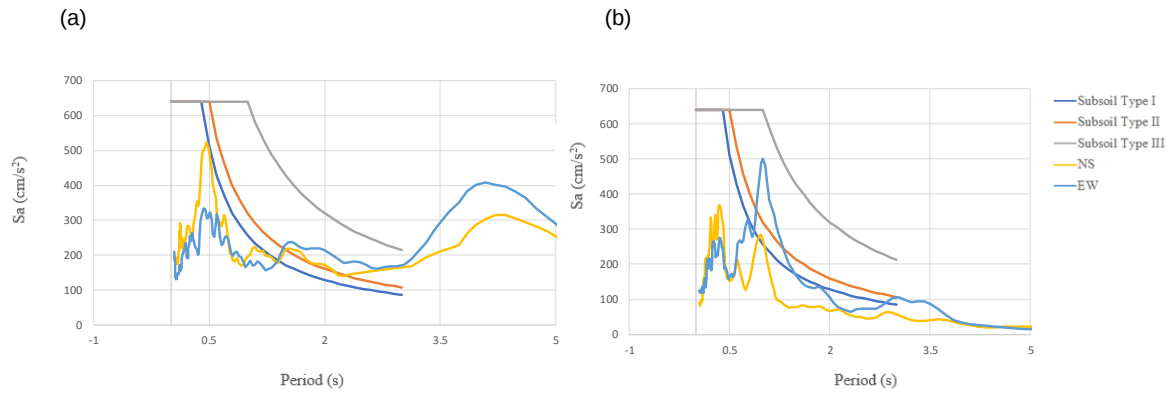

Figure 7.4 (a) Comparison of the response spectra of the mainshock and (b) the largest aftershock of the Gorkha earthquake recorded at DMG sedimentary site with the seimsic design code of Nepal.In the design response spectra of Nepal building code mentioned in this figure the basic seismic coefficient C = 0.08, structural performance factor K = 4 (maximum resistance of the structures for minimum ductility) and over strength factor 2 is used as a modification in Figure 7.3.

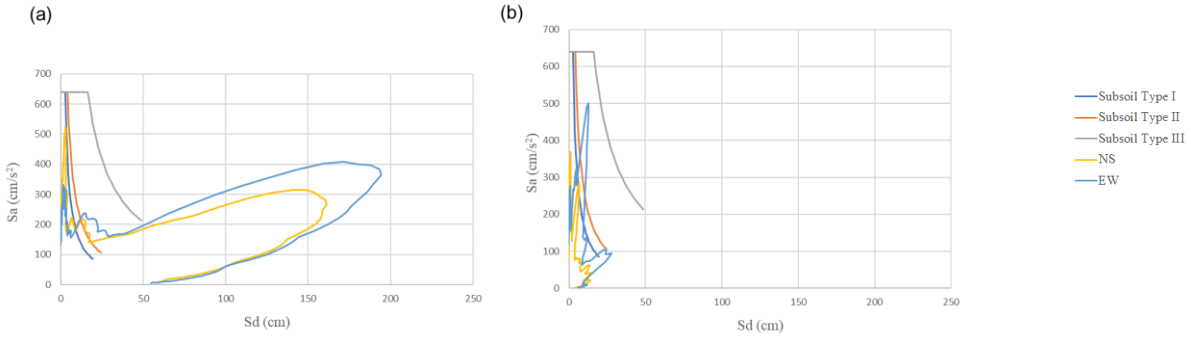

Figure 7.5 (a) Comparison of the acceleration displacement response spectra of the mainshock and (b) the largest aftershock at site 1 (DMG) with the design response spectra of the Nepalese building code.

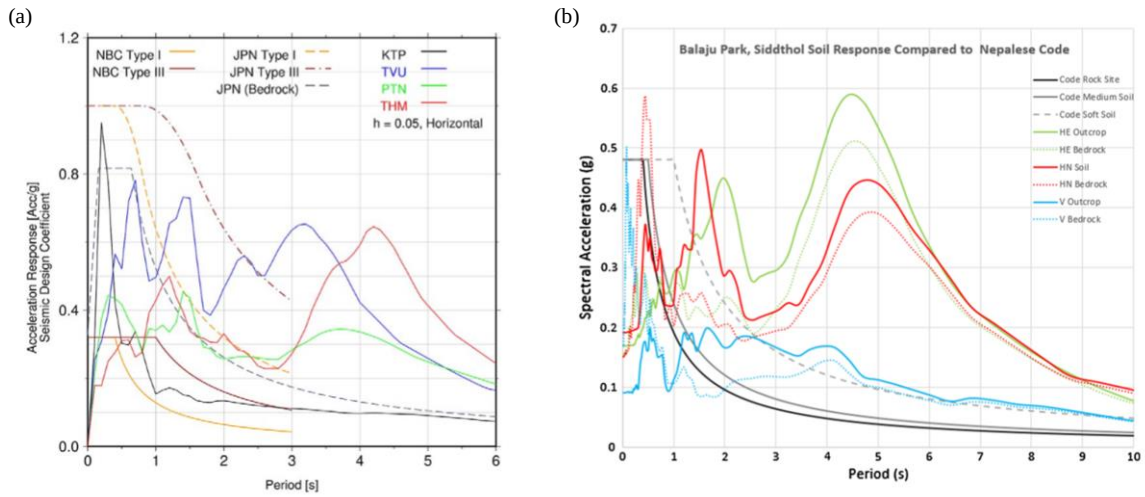

Figure 7.6 Design response spectra of Nepal can be modified by changing the values of *I* (Importance factor of building), and *K* (structural performance factor of building) for different purposes (a) Bijukchhen *et al*. (2017) actual demand for the brittle buildings and (b) Williams *et al*. (2016) actual minimum demand for the important but brittle buildings.

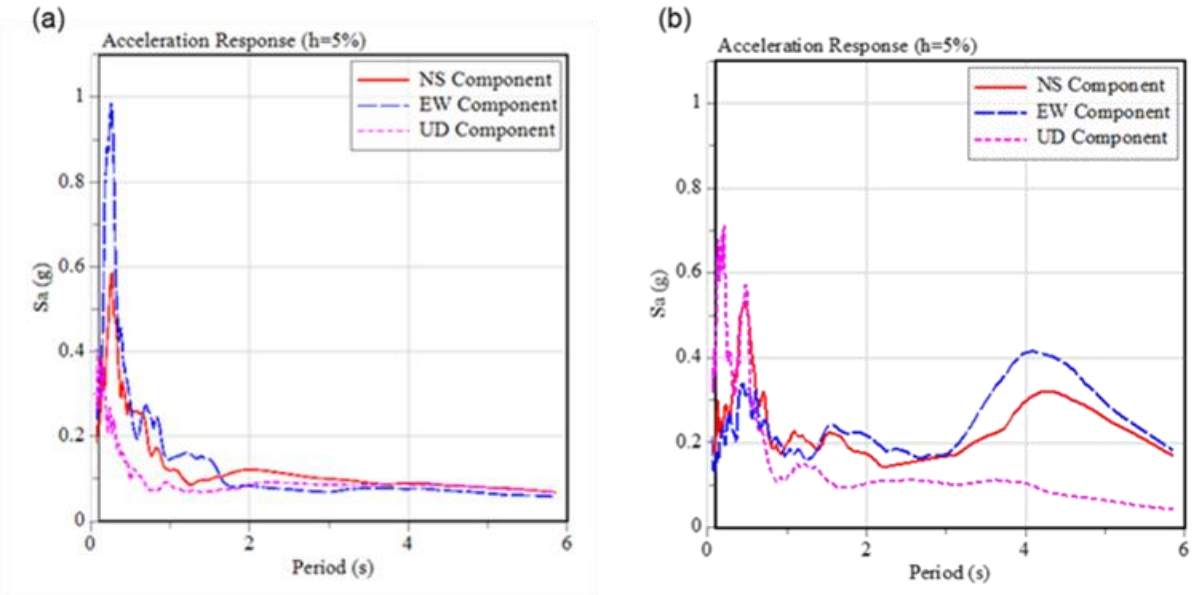

Figure 7.7 (a) Acceleration response spectra of the mainshock recorded at rock site (KTP). (b) That of sedimentary site (DMG).

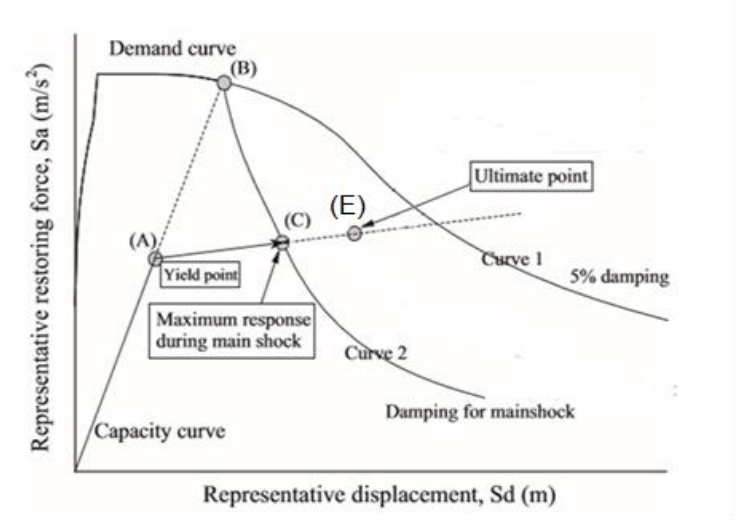

Figure 7.8 Outline of the capacity spectrum method (Kusunoki *et al*., 2017).

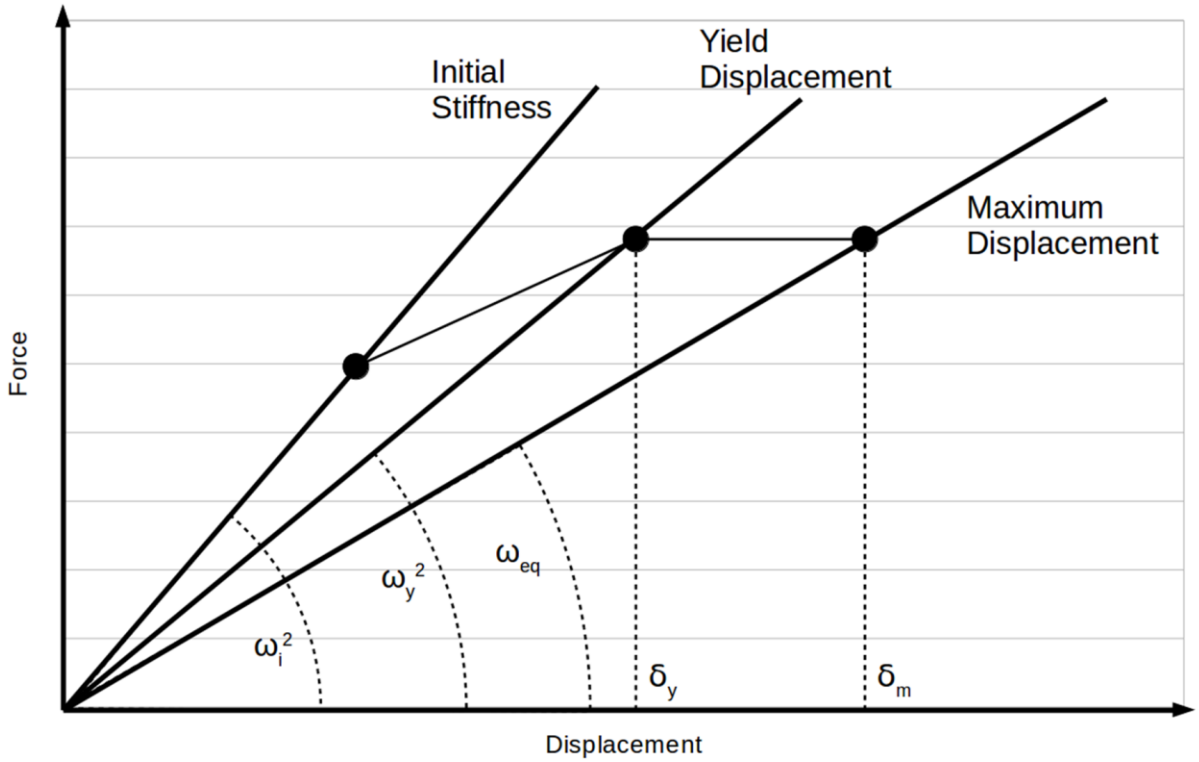

Figure 7.9 Schematic diagram for the initial angular period, yield period, and the equivalent period after additional damping.

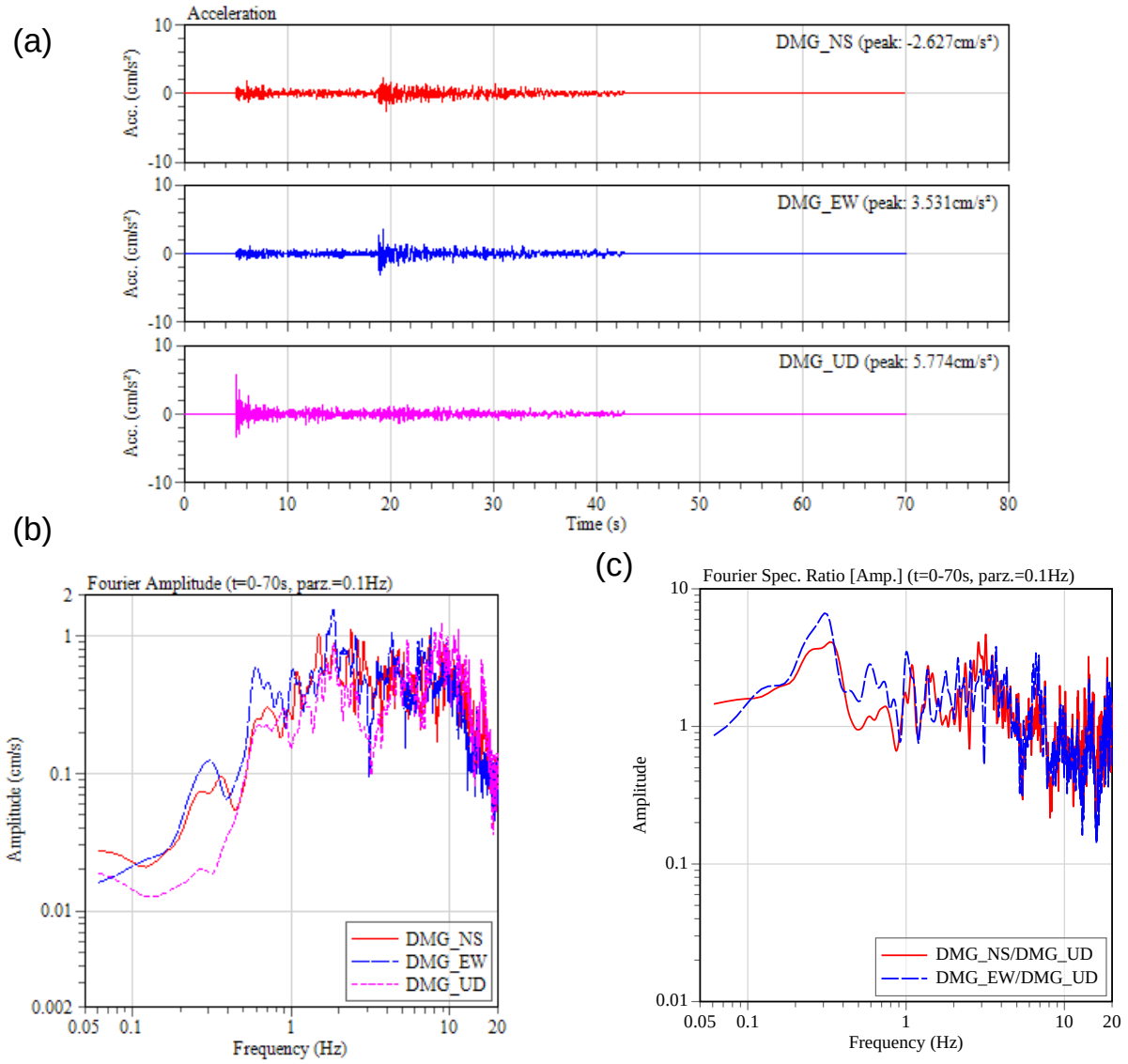

Figure 7.10 (a) Acceleration waveform of 2010 Xizang, China earthquake. (b) Its Fourier amplitude spectra, and (c) H/V spectral ratios.

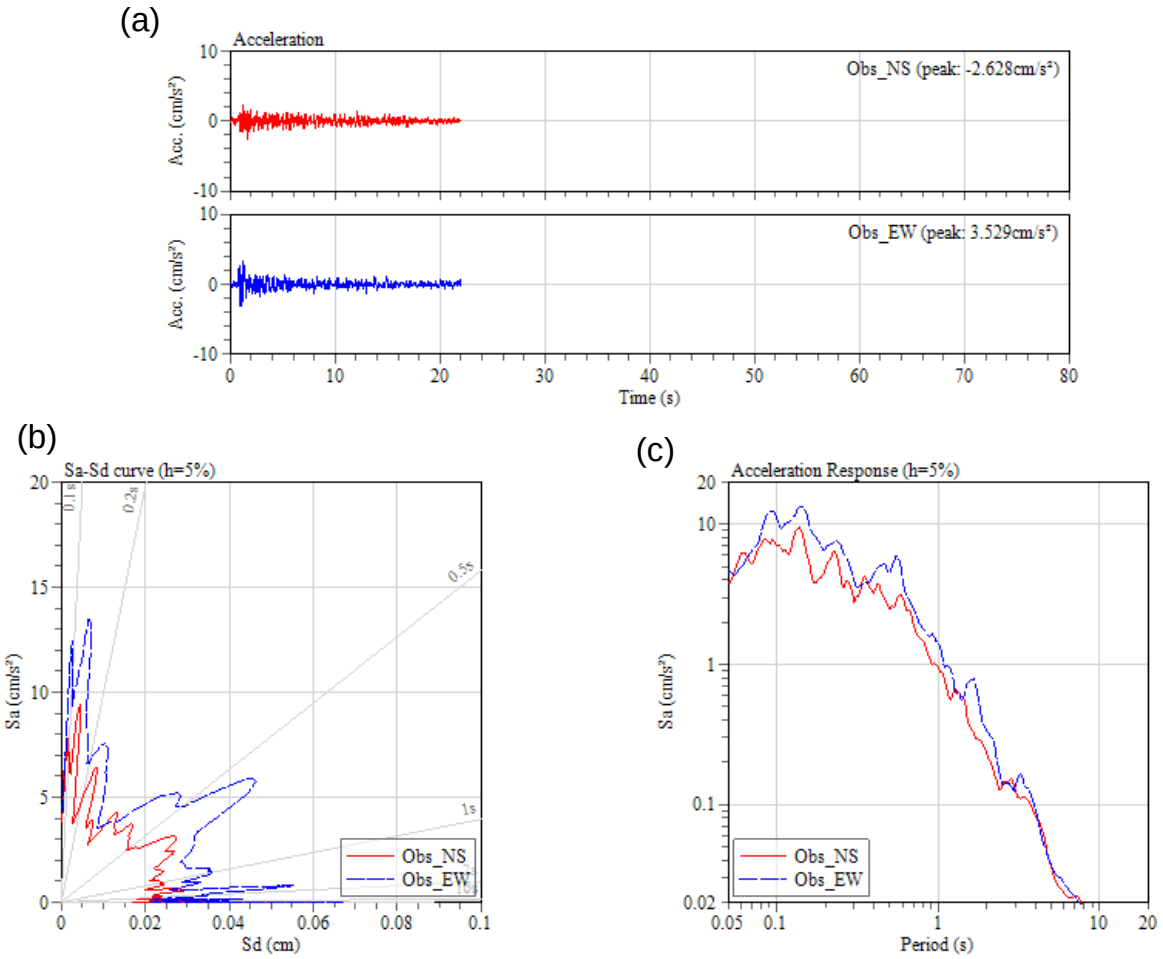

Figure 7.11 (a) Waveform of the Xizang, China earthquake used for comparison with simulation at DMG. (b) Sa-Sd response spectra, and (c) Acceleration response spectra.

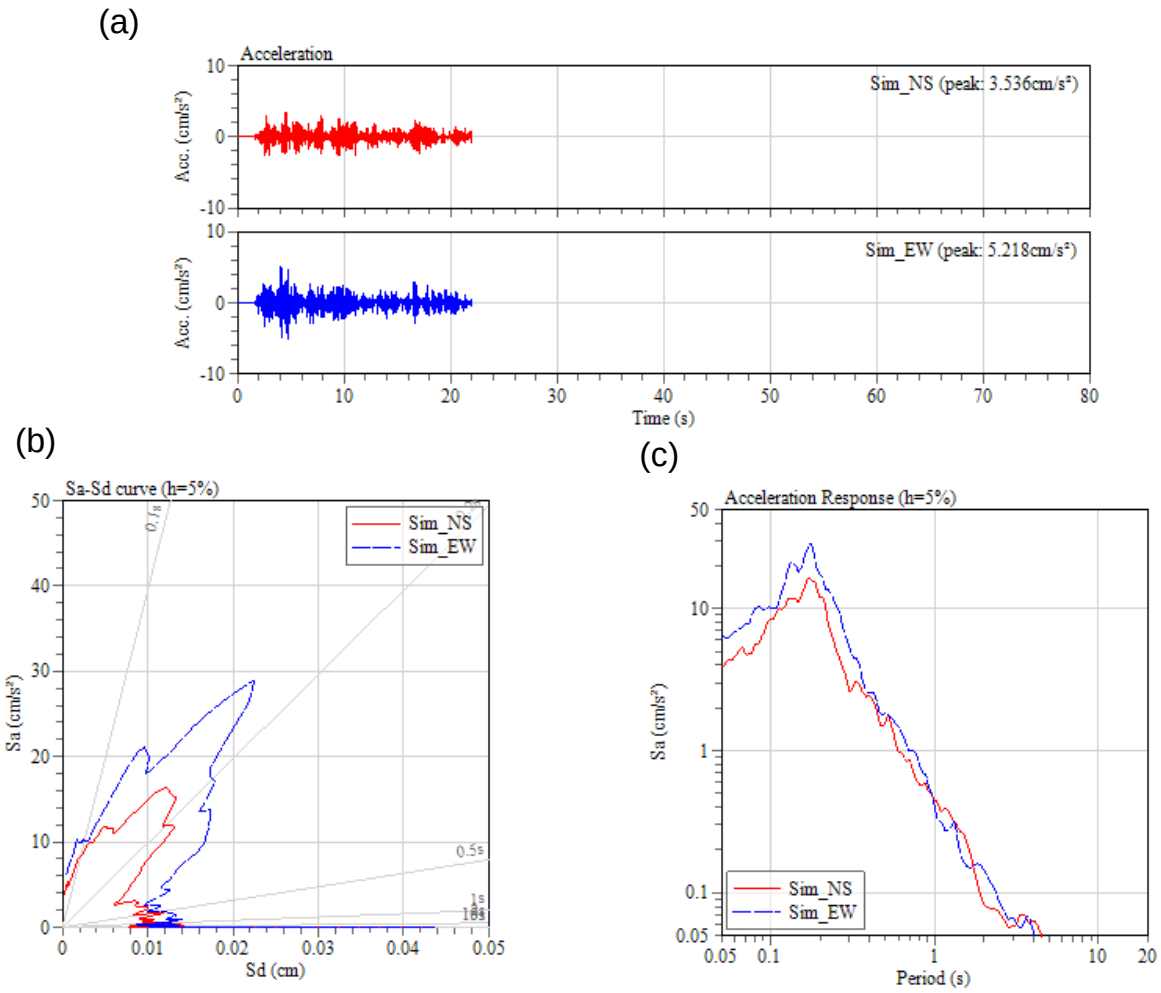

Figure 7.12 (a) Simulated waveform of the Xizang, China earthquake using the rock site motion KKA at DMG. (b) Sa-Sd response spectra, and (c) Acceleration response spectra.

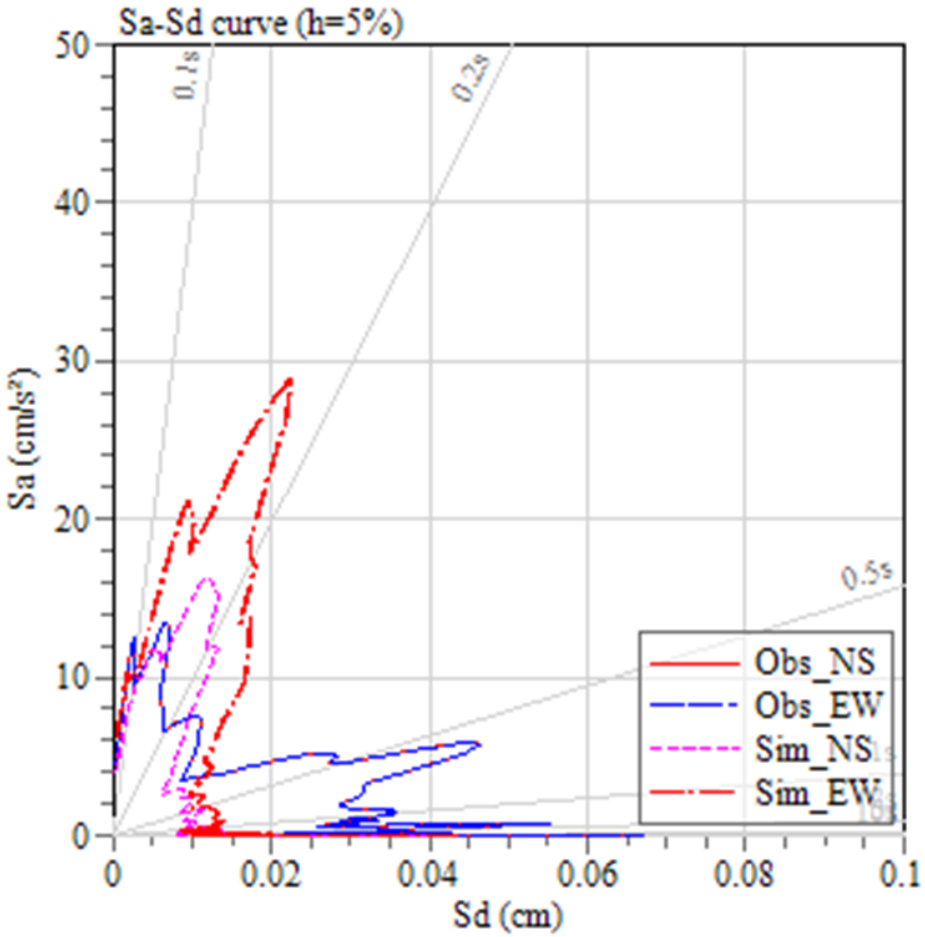

Figure 7.13 Comparison of the observed and simulated Sa-Sd response spectra of the Xizang, China earthquake.

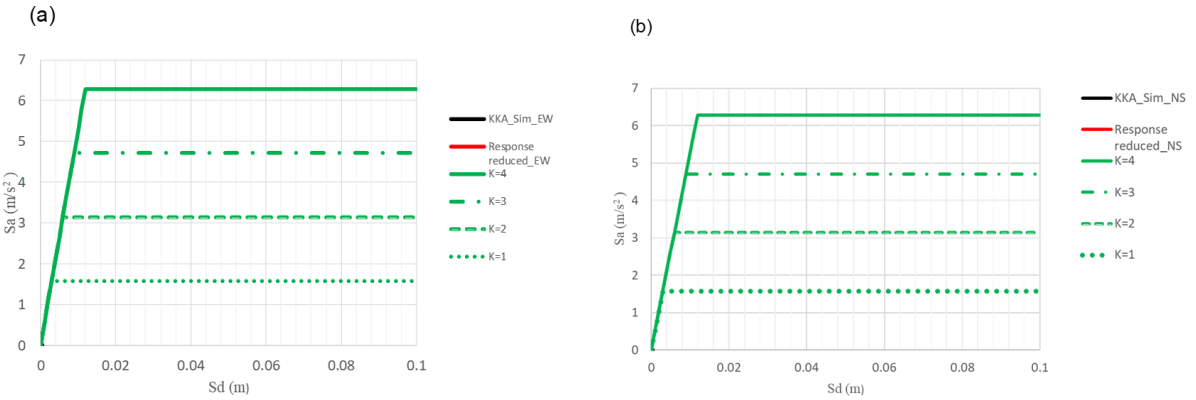

Figure 7.14 Capacity demand curves of the Xizang earthquake (a) 1-story RC building considered for damage analysis using EW component of ground motion. (b) 1-story RC building using NS component of ground motion.

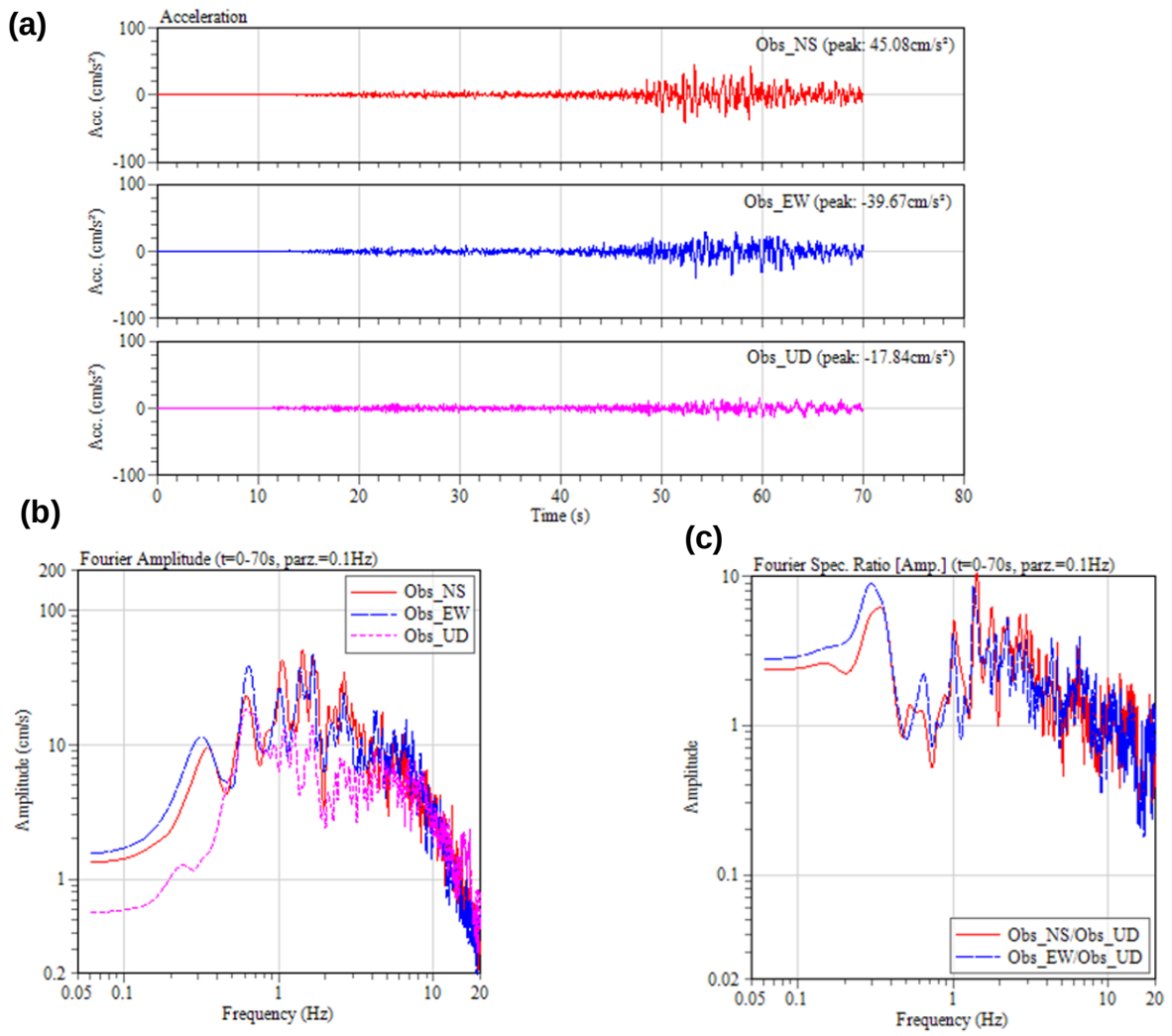

Figure 7.15 (a) Acceleration waveform of the Taplejung-Sikkim, border earthquake. (b) Its Fourier amplitude spectra, and (c) H/V Spectral ratios.

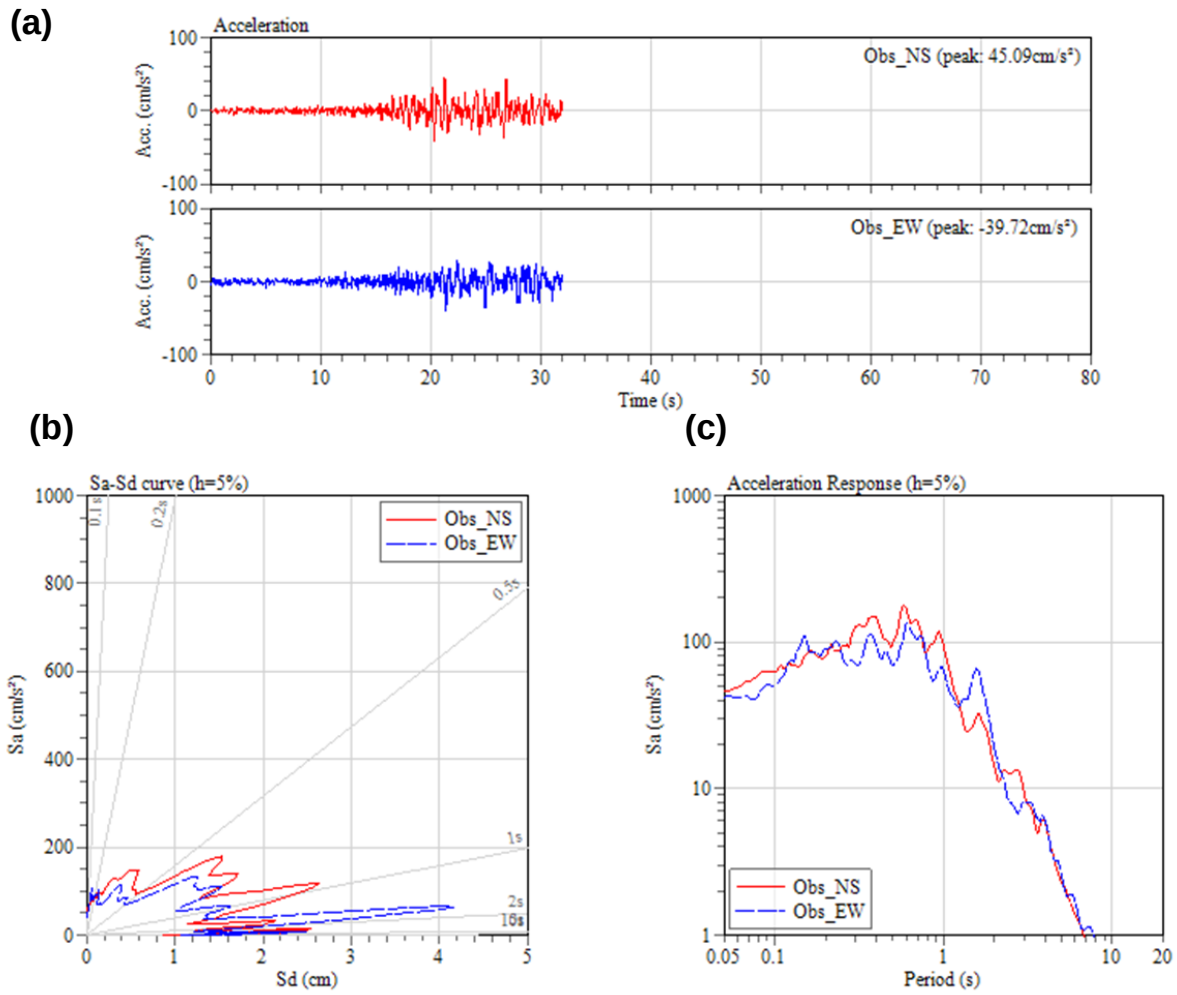

Figure 7.16 (a) Waveform of the Taplejung-Sikkim earthquake used for comparison with simulation at DMG. (b) Sa-Sd response spectra, and (c) Acceleration response spectra.

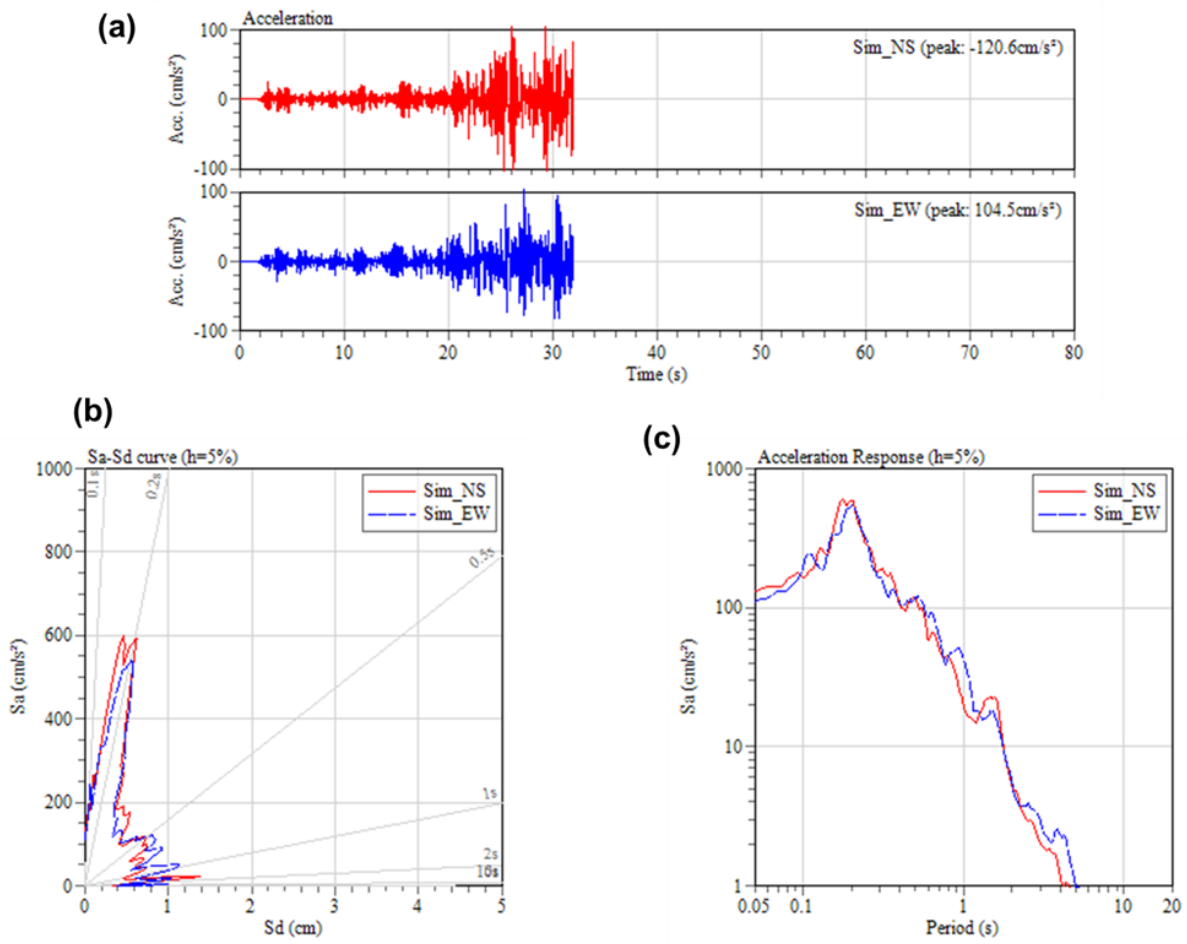

Figure 7.17 (a) Simulated waveform of the Taplejung-Sikkim, earthquake using the rock site motion KKA at DMG. (b) Sa-Sd response spectra, and (c) Acceleration response spectra.

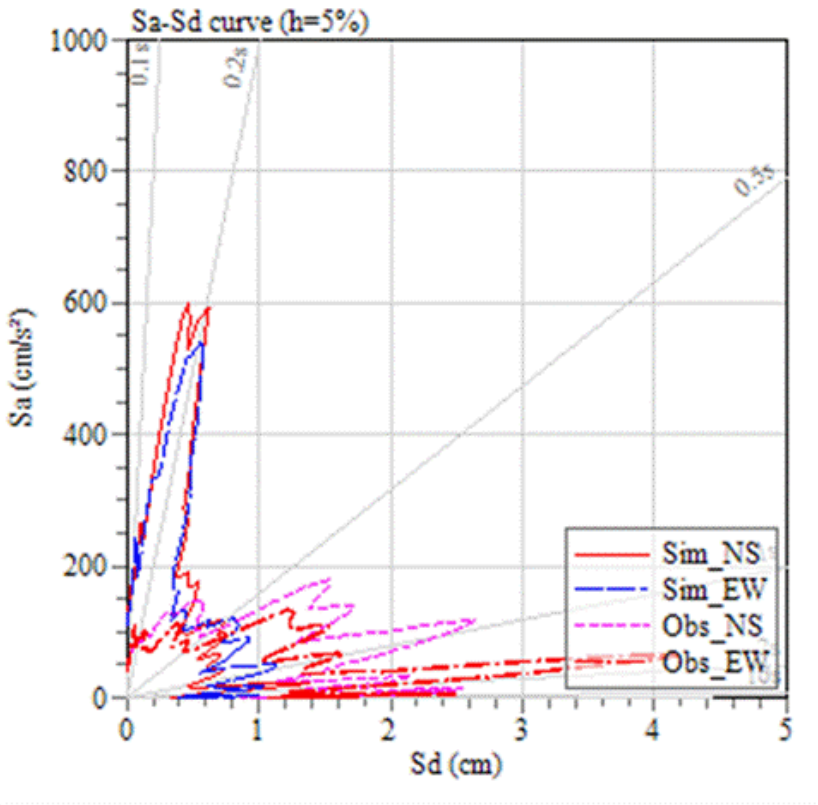

Figure 7.18 Comparison of the observed and simulated Sa-Sd response spectra at DMG of the Taplejung-Sikkim earthquake.

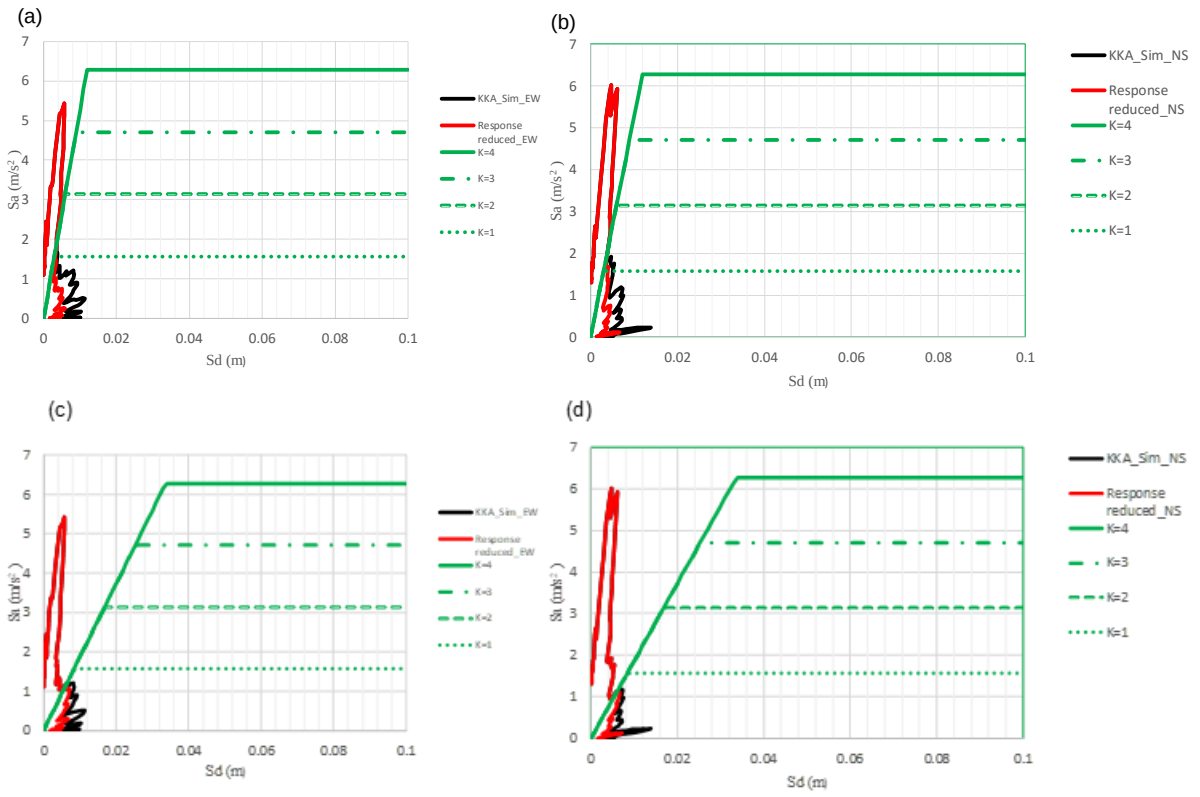

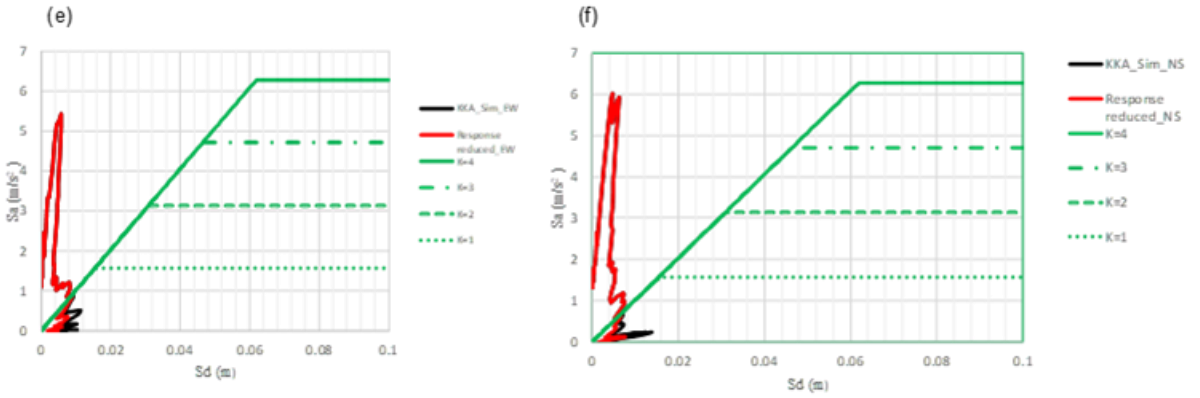

Figure 7.19 Capacity, demand curves of the Taplejung-Sikkim earthquake (a) 1-story RC building using EW component of ground motion, (b) 1-story RC building using NS component of ground motion, (c) 2-story RC building using EW component of ground motion, (d) 2-story RC using the NS component of ground motion, (e) 3-story RC building using the EW component of ground motion, and (f) 3-story RC building using the NS component of ground motion.

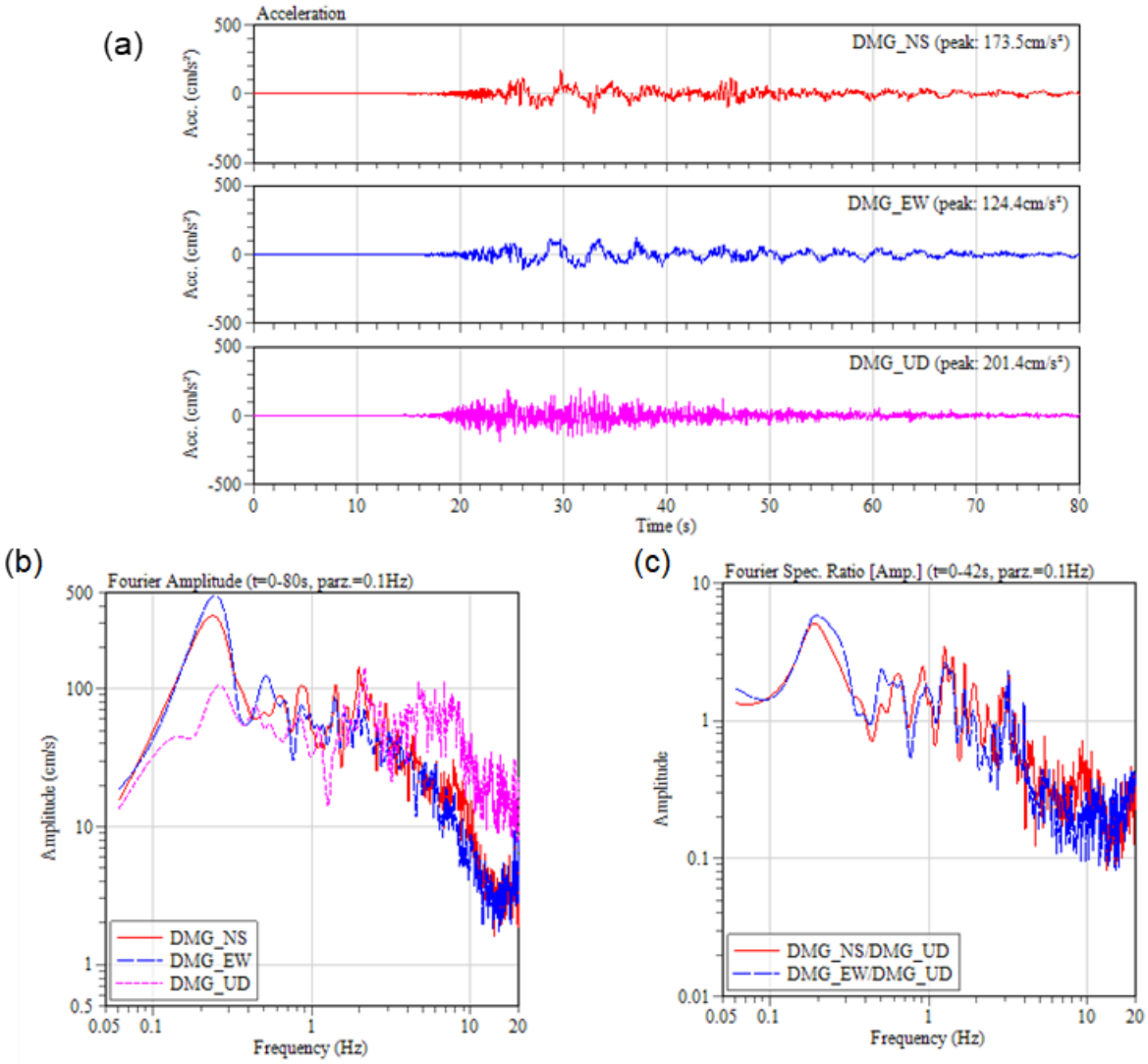

Figure 7.20 (a) The mainshock of the Gorkha earthquake observed at DMG. (b) Fourier amplitude spectra, and (c) H/V spectral ratios.

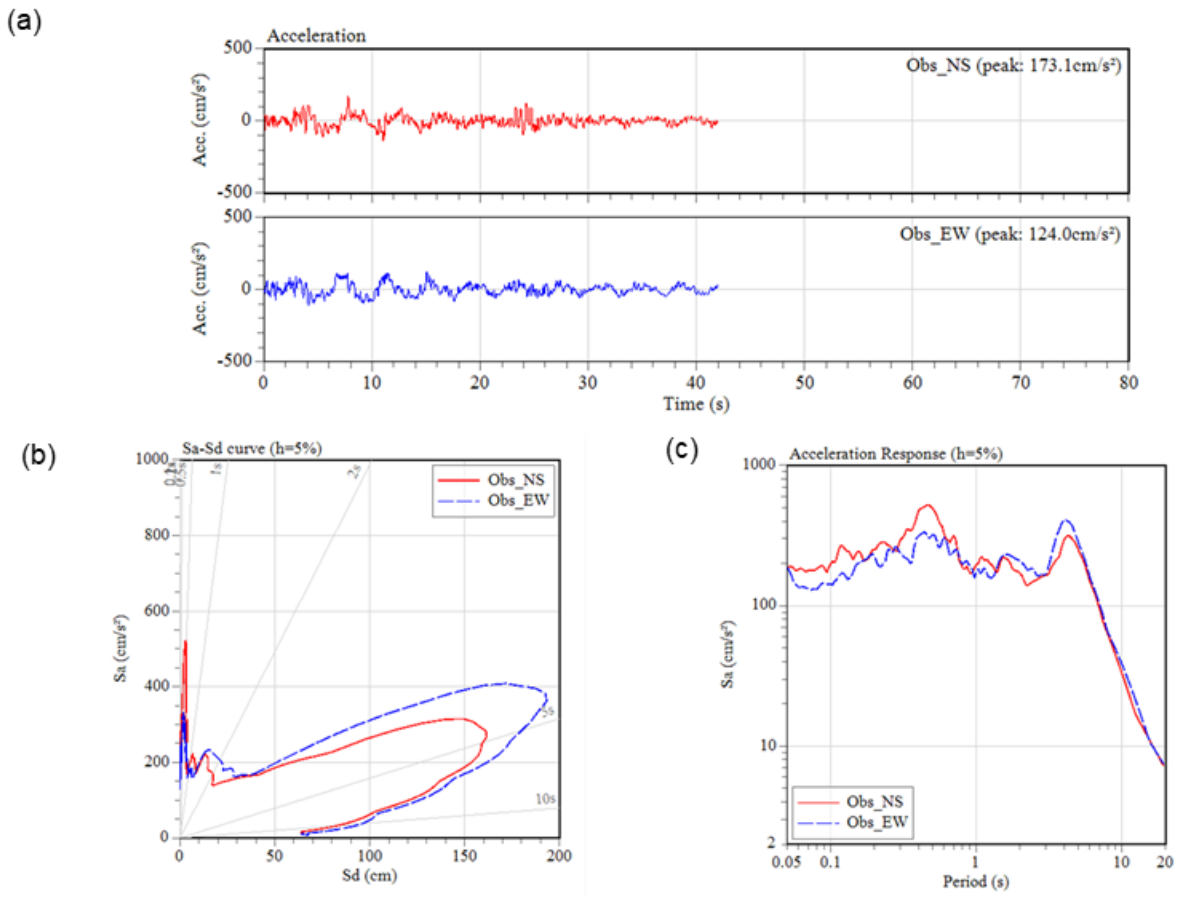

Figure 7.21 (a) Time window of the Gorkha earthquake observed at DMG used for comparison with the simulation. (b) Acceleration displacement response spectra, and (c) Its acceleration response. A time window of 40 s for both the horizontal components of ground motion are used to compare for the simulation staring 2 s before the *S*-onset. Note that the waveforms at DMG are resampled from 200 Hz to 100 Hz for the comparision with KTP having sampling frequency 100 Hz.

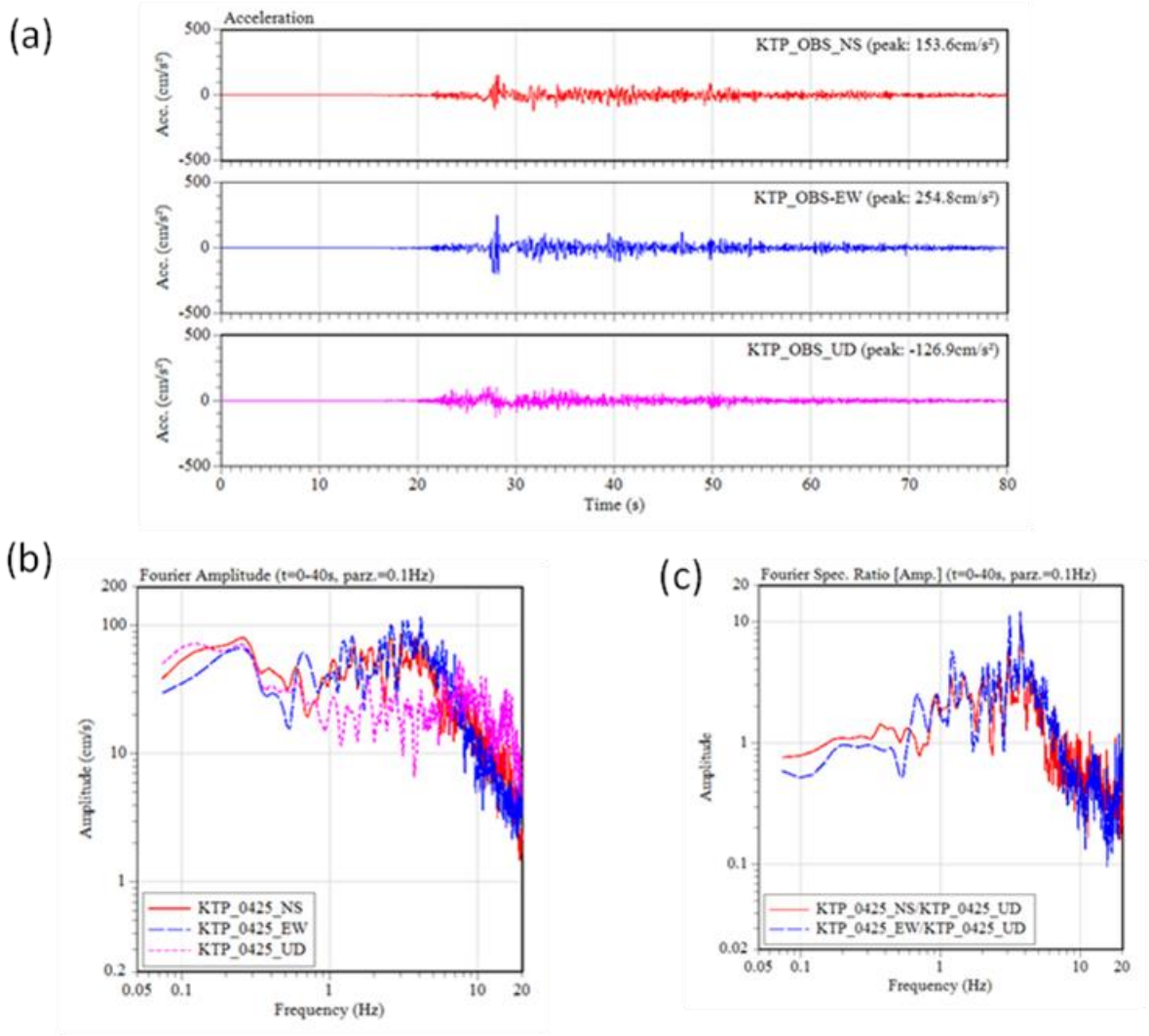

Figure 7.22 (a) The mainshock of the Gorkha earthquake observed at KTP (b) Its Fourier amplitude spectra, and (c) H/V spectral ratios. The sampling frequency of the KTP is set 100 Hz.

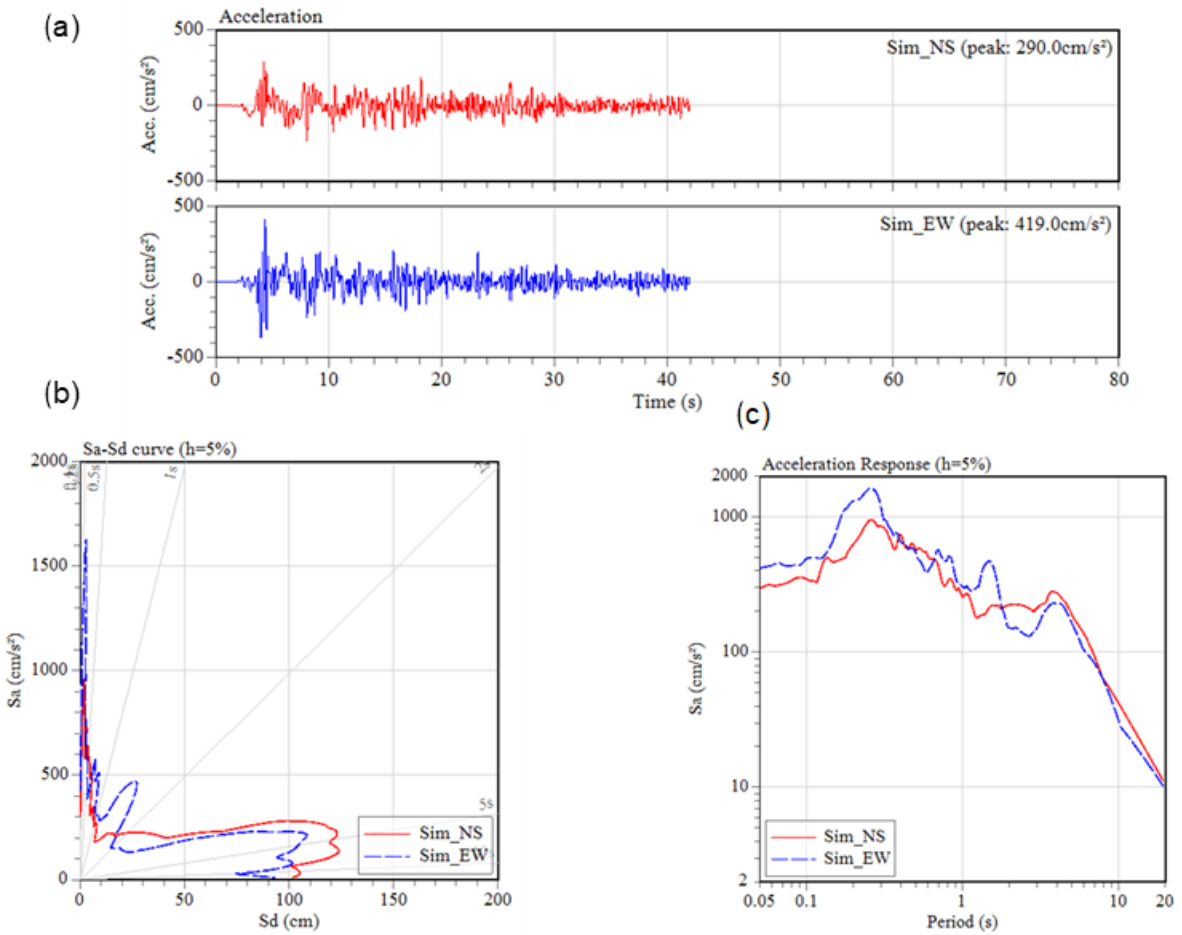

Figure 7.23 (a) The mainshock of the Gorkha earthquake observed at KTP and simulated at DMG. (b) Acceleration displacement response spectra, and (c) acceleration response spectra. A time window of 40 s for both the horizontal components of ground motion are used to compare with the observed ones staring 2 s before the *S*-onset.

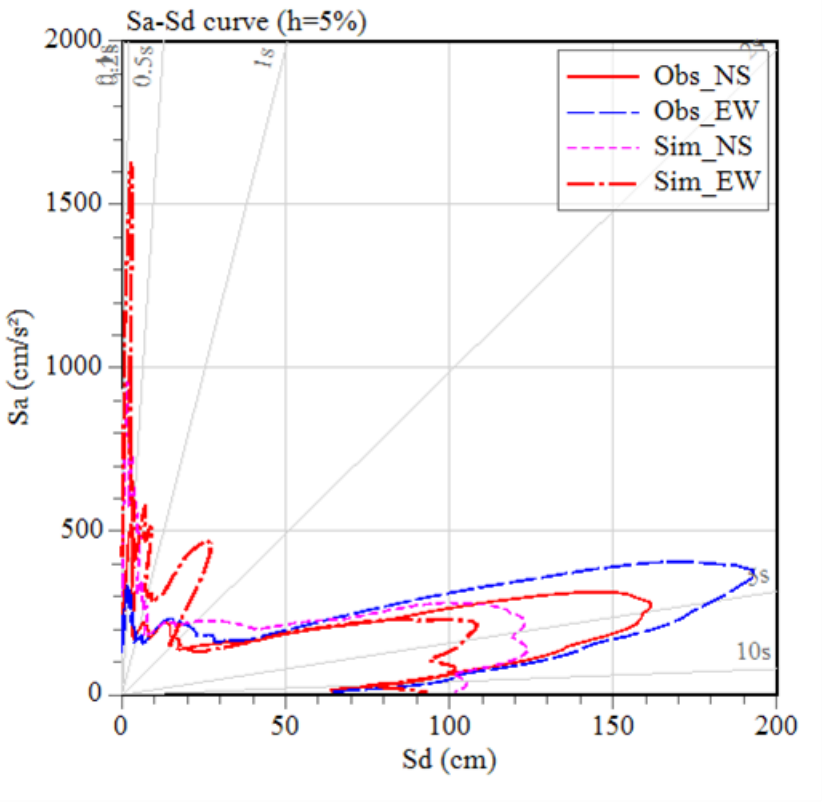

Figure 7.24 Comparison of the mainshock ground motion at DMG and simulated motion of KTP at DMG in the acceleration displacement response spectra (ADRS) format.

Figure 7.25 The capacity demand curves for the 3-story RC buildings considered for analysis using EW component of the simulated ground motion of the mainshock at DMG.

Table 7.4 Damage sheet of 3-story RC building using the EW component simulated ground motion of the mainshock at DMG

	Structural performance factor (K)	Ductility capacity of building collapse	Yield displacement (m)	Displacement demand (m)	Ductility demand	State of building
	1	4	0.015	0.11	7.333333333	Collapse
	2	2	0.031	0.06	1.935483871	Severe damage
	3	1.33	0.042	0.05	1.19047619	Moderate damage
	4	1	0.06	0.045	0.75	Minimal damage

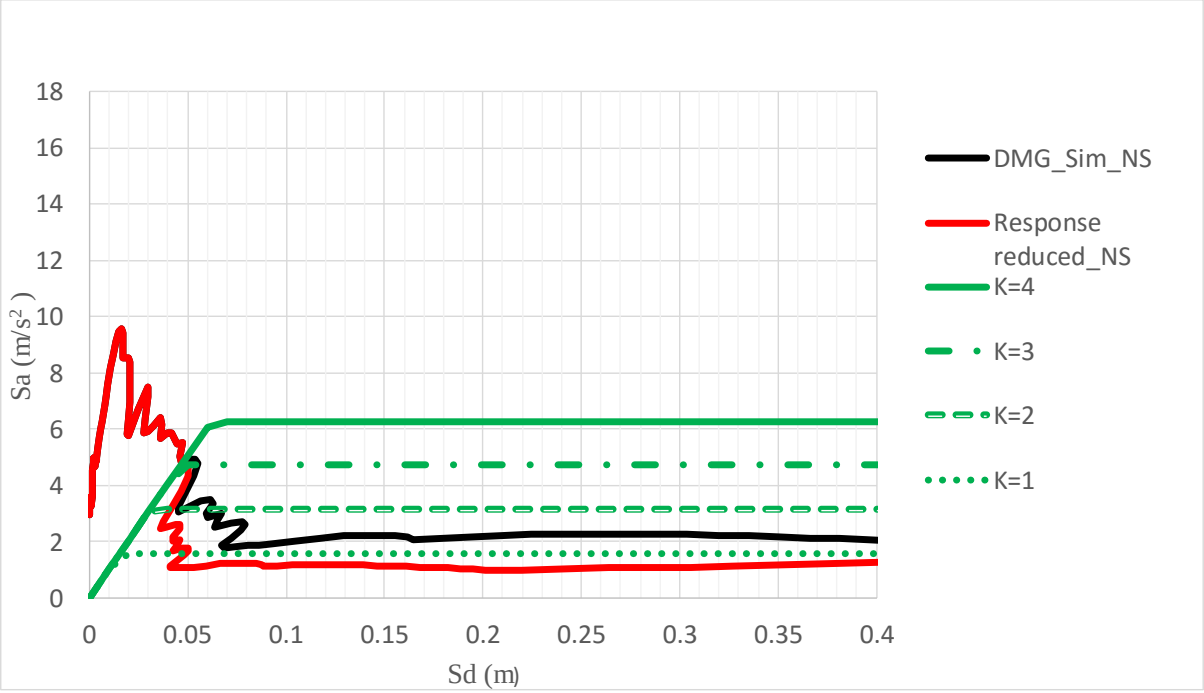

Figure 7.26 The capacity demand curves for the 3-story RC buildings considered for analysis usingNS component of the simulated ground motion of the mainshock at DMG.

Table 7.5 Damage sheet of 3-story RC building using the NS component simulated ground motion of the mainshock at DMG

Structural performance factor (K)	Ductility capacity of building collapse	Yield displacement (m)	Displacement demand (m)	Ductility demand	State of building
1	4	0.015	0.05	3.33333333	Moderate damage
2	2	0.031	0.04	1.29032258	Moderate damage
3	1.33	0.042	0.048	1.14285714	Moderate damage
4	1	0.06	0.048	0.8	Minimal damage

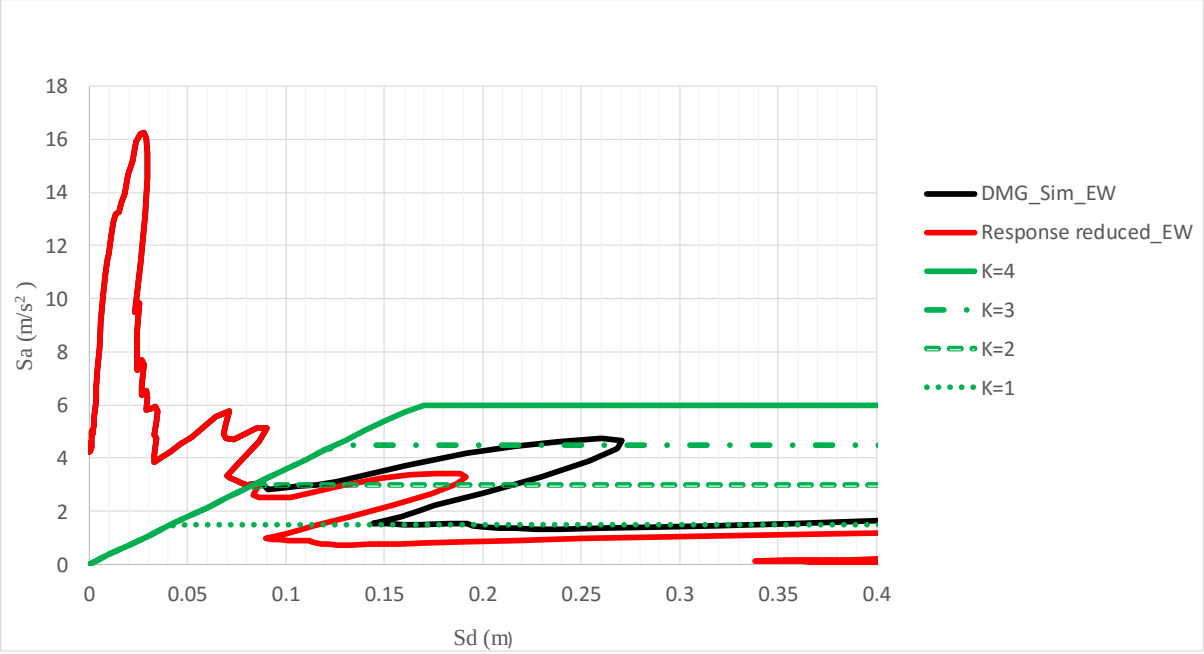

Figure 7.27 Capacity demand curves for the 6-story RC buildings considered for analysis using EW component of the simulated ground motion of the mainshock at DMG.

Table 7.6 Damage sheet of 6-story RC building using the EW component simulated ground motion of the mainshock at DMG

Structural performance factor (K)	Ductility capacity of building collapse	Yield displacement (m)	Displacement demand (m)	Ductility demand	State of building
1	4	0.04	0.11	2.75	Moderate damage
2	2	0.08	0.08	1	Moderate damage
3	1.33	0.13	0.08	0.615384615	Minimal damage
4	1	0.17	0.08	0.470588235	Minimal damage

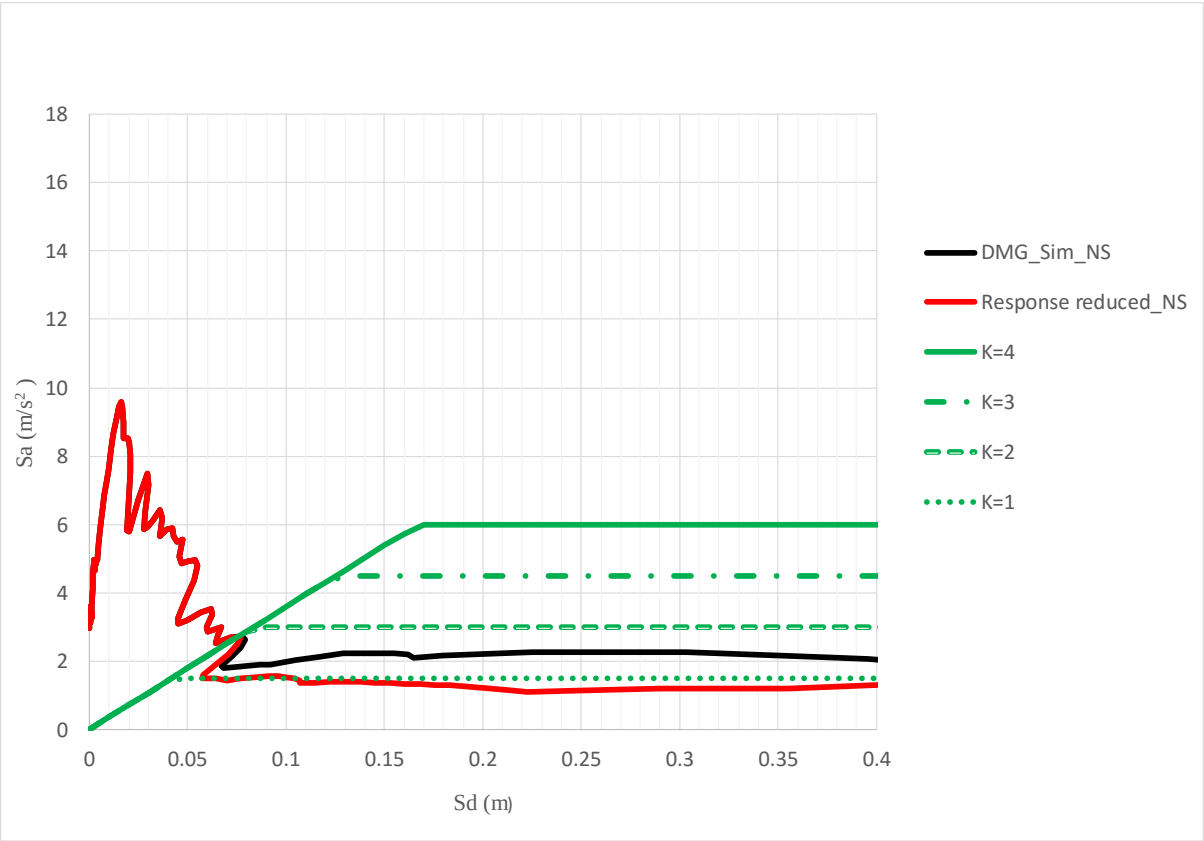

Figure 7.28 Capacity demand curves for the 6-story RC buildings considered for analysis using NS component of the simulated ground motion of the mainshock at DMG.

Table 7.7 Damage sheet of 6-story RC building using the NS component simulated ground motion of the mainshock at DMG

	Structural performance factor (K)	Ductility capacity of building collapse	Yield displacement (m)	Displacement demand (m)	Ductility demand	State of building
	1	4	0.04	0.052	1.3	Moderate damage
	2	2	0.08	0.08	1	Moderate damage
	3	1.33	0.13	0.08	0.61538462	Minimal damage
	4	1	0.17	0.08	0.47058824	Minimal damage

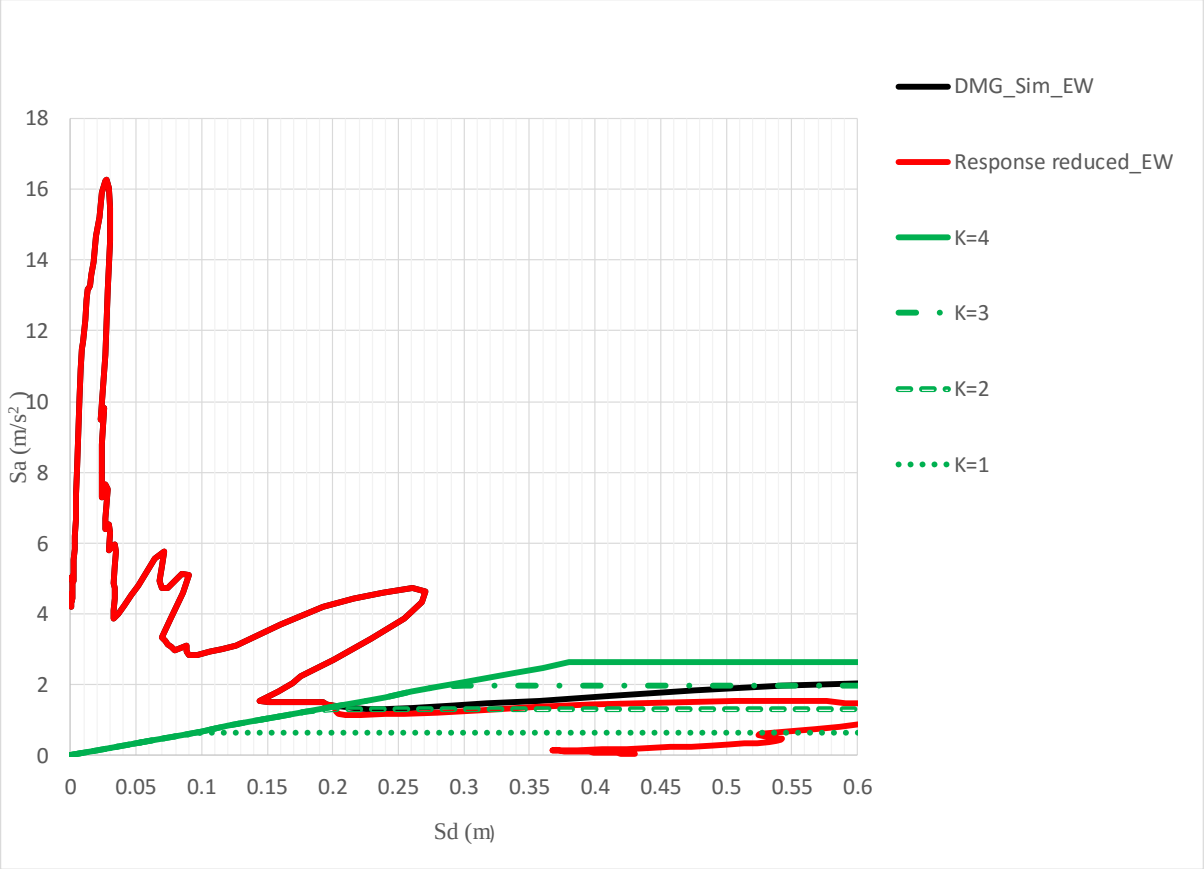

Figure 7.29 Capacity demand curves for the 18-story RC buildings considered for analysis using EW component of the simulated ground motion of the mainshock at DMG.

Table 7.8 Damage sheet of 18-story RC building using the EW component simulated ground motion of the mainshock at DMG

	Structural performance factor (K)	Ductility capacity of building collapse	Yield displacement (m)	Displacement demand (m)	Ductility demand	State of building
	1	4	0.1	0.52	5.2	Collapse
	2	2	0.2	0.2	1	Moderate damage
	3	1.33	0.3	0.2	0.666666667	Minimal damage
	4	1	0.38	0.2	0.526315789	Minimal damage

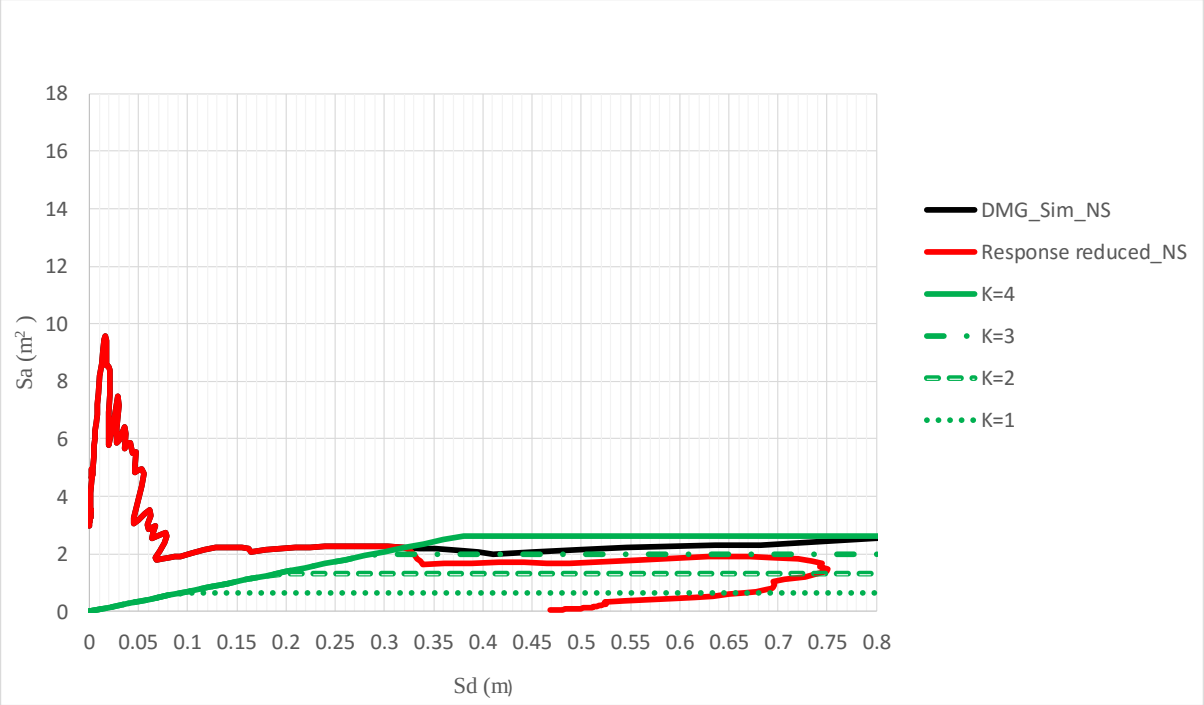

Figure 7.30 Capacity demand curves for the 18-story RC buildings considered for analysis using NS component of the simulated ground motion of the mainshock at DMG.

Table 7.9 Damage sheet of 18-story RC building using the NS component simulated ground motion of the mainshock at DMG

Structural performance factor (K)	Ductility capacity of building collapse	Yield displacement (m)	Displacement demand (m)	Ductility demand	State of building
1	4	0.1	0.66	6.6	Collapse
2	2	0.2	0.72	3.6	Collapse
3	1.33	0.3	0.32	1.066667	Moderate damage
4	1	0.38	0.32	0.842105	Minimal damage

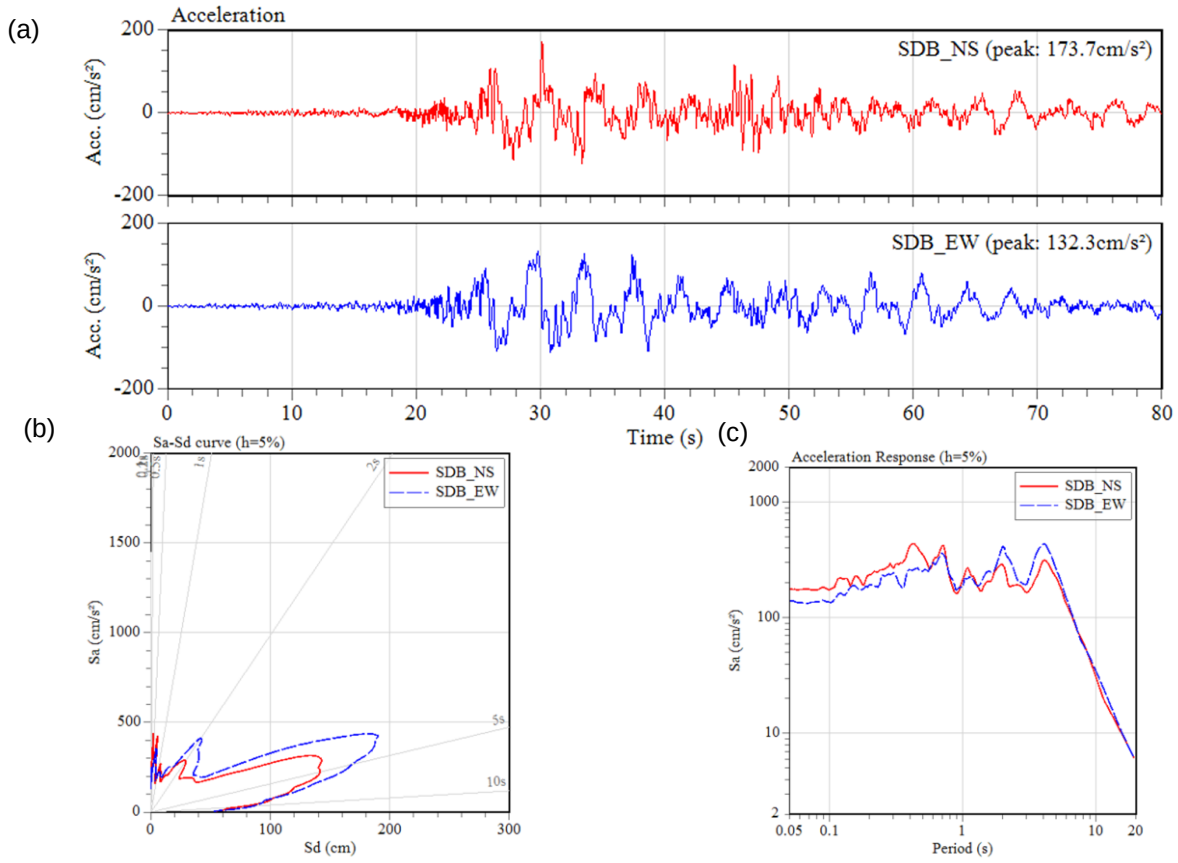

Figure 7.31 (a) Simulated ground motion at SDB using the observed records at DMG and theoretical response of DMG and SDB using the derived velocity structure model at SDB. (b) Acceleration displacement response spectra, and (c) Acceleration response spectra.

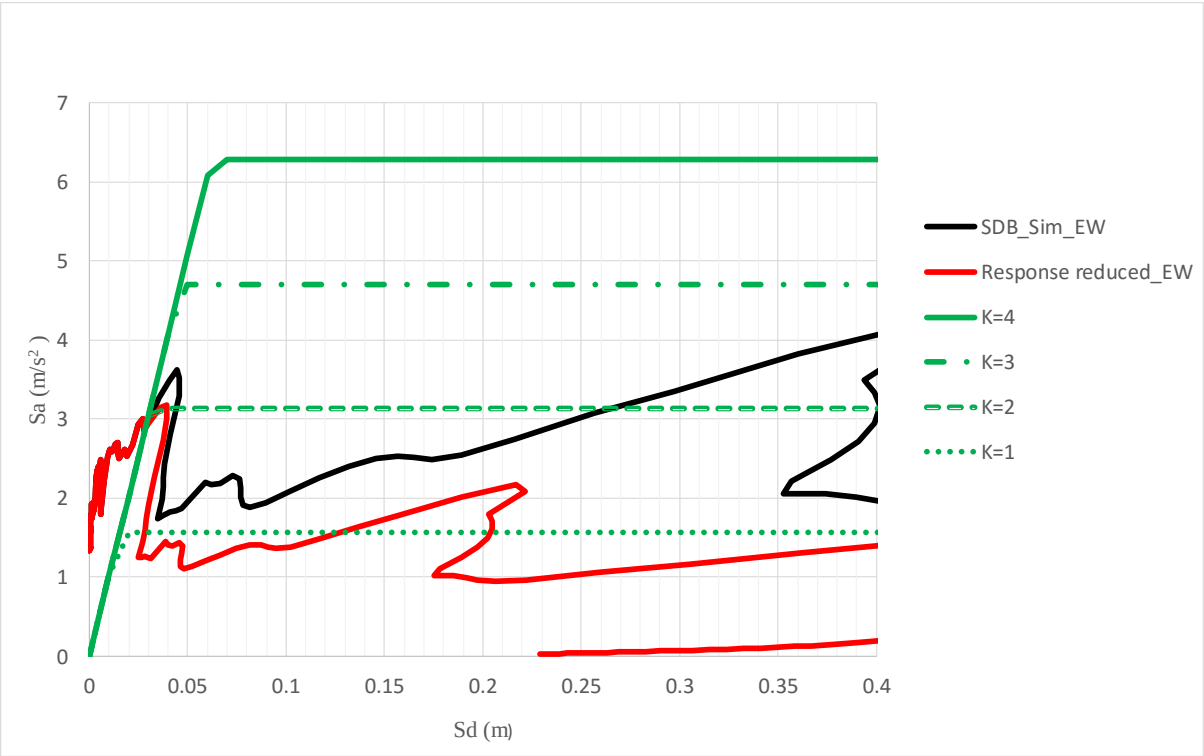

Figure 7.32 Capacity demand curves for the 3-story RC buildings considered for analysis using EW component of the simulated ground motion of the mainshock at SDB.

Table 7.10 Damage sheet of 3-story RC building using the EW component simulated ground motion of the mainshock at SDB

Structural performance factor (K)	Ductility capacity of building collapse	Yield displacement (m)	Displacement demand (m)	Ductility demand	State of building
1	4	0.02	0.025	1.25	Moderate damage
2	2	0.03	0.03	1	Moderate damage
3	1.33	0.05	0.03	0.6	Minimal damage
4	1	0.06	0.03	0.5	Minimal damage

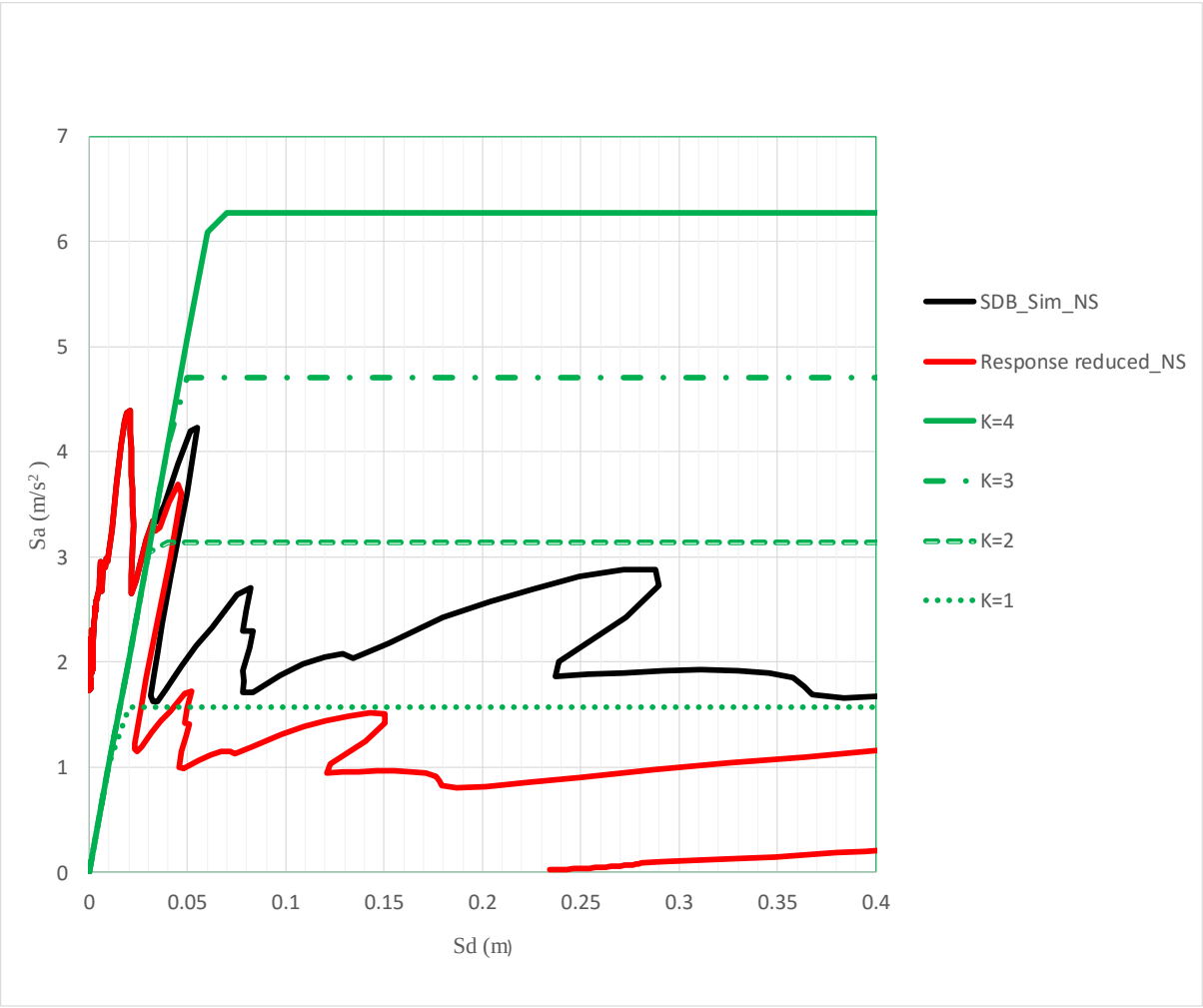

Figure 7.33 Capacity demand curves for the 3-story RC buildings considered for analysis using the NS component of the simulated ground motion of the mainshock at SDB.

Table 7.11 Damage sheet of 3-story RC building using the NS component simulated ground motion of the mainshock at SDB

Structural performance factor (K)	Ductility capacity of building collapse	Yield displacement (m)	Displacement demand (m)	Ductility demand	State of building
1	4	0.02	0.023	1.15	Moderate damage
2	2	0.03	0.04	1.333333333	Moderate damage
3	1.33	0.05	0.04	0.8	Minimal damage
4	1	0.06	0.04	0.666666667	Minimal damage

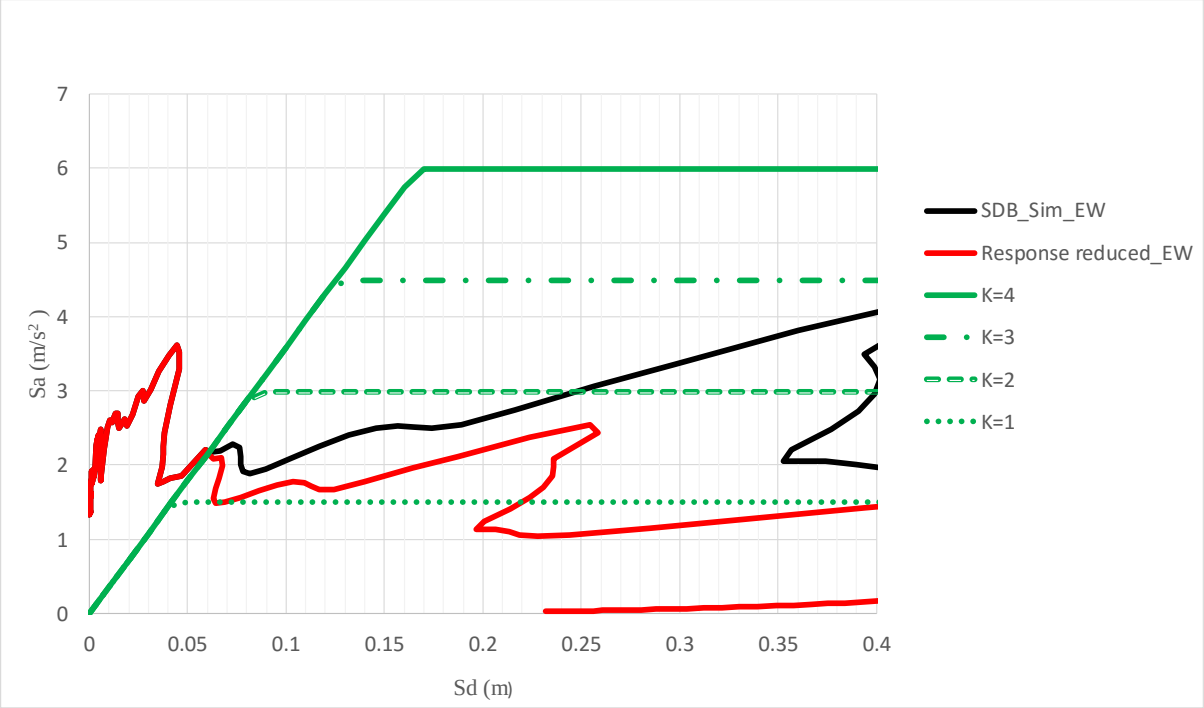

Figure 7.34 Capacity demand curves for the 6-story RC buildings considered for analysis using EW component of the simulated ground motion of the mainshock at SDB.

Table 7.12 Damage sheet of 6-story RC building using the EW component simulated ground motion of the mainshock at SDB

Structural performance factor (K)	Ductility capacity of building collapse	Yield displacement (m)	Displacement demand (m)	Ductility demand	State of building
1	4	0.04	0.07	1.75	Minimal damage
2	2	0.08	0.06	0.75	Minimal damage
3	1.33	0.13	0.06	0.461538462	Minimal damage
4	1	0.17	0.06	0.352941176	Minimal damage

Figure 7.35 Capacity demand curves for the 6-story RC buildings considered for analysis using NS component of the simulated ground motion of the mainshock at SDB.

Table 7.13 Damage sheet of 6-story RC building using the NS component simulated ground motion of the mainshock at SDB

Structural performance factor (K)	Ductility capacity of building collapse	Yield displacement (m)	Displacement demand (m)	Ductility demand	State of building
1	4	0.04	0.06	1.5	Moderate damage
2	2	0.08	0.07	0.875	Minimal damage
3	1.33	0.13	0.07	0.538462	Minimal damage
4	1	0.17	0.07	0.411765	Minimal damage

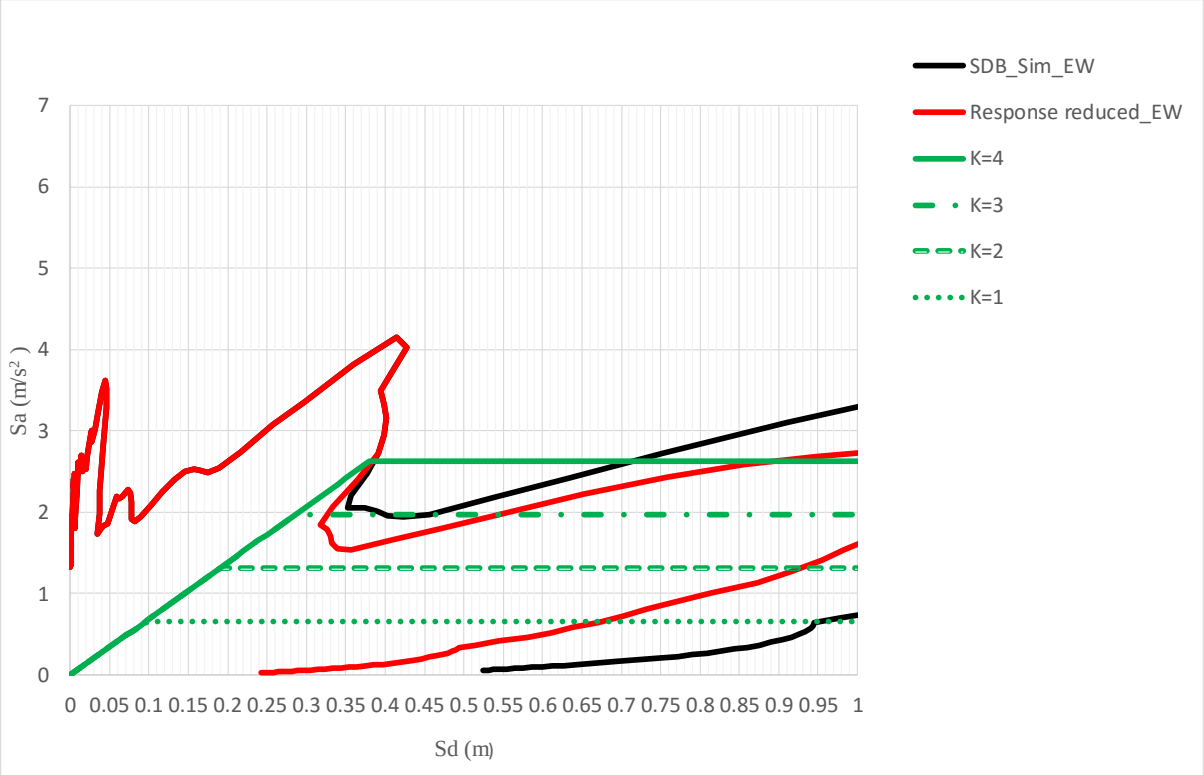

Figure 7.36 Capacity demand curves for the 18-story RC buildings considered for analysis using EW component of the simulated ground motion of the mainshock at SDB.

Table 7.14 Damage sheet of 18-story RC building using the EW component simulated ground motion of the mainshock at SDB

Structural performance factor (K)	Ductility capacity of building collapse	Yield displacement (m)	Displacement demand (m)	Ductility demand	State of building
1	4	0.11	0.65	5.90909091	Collapse
2	2	0.19	0.92	4.84210526	Collapse
3	1.33	0.29	0.32	1.10344828	Moderate damage
4	1	0.38	0.38	1	Moderate damage

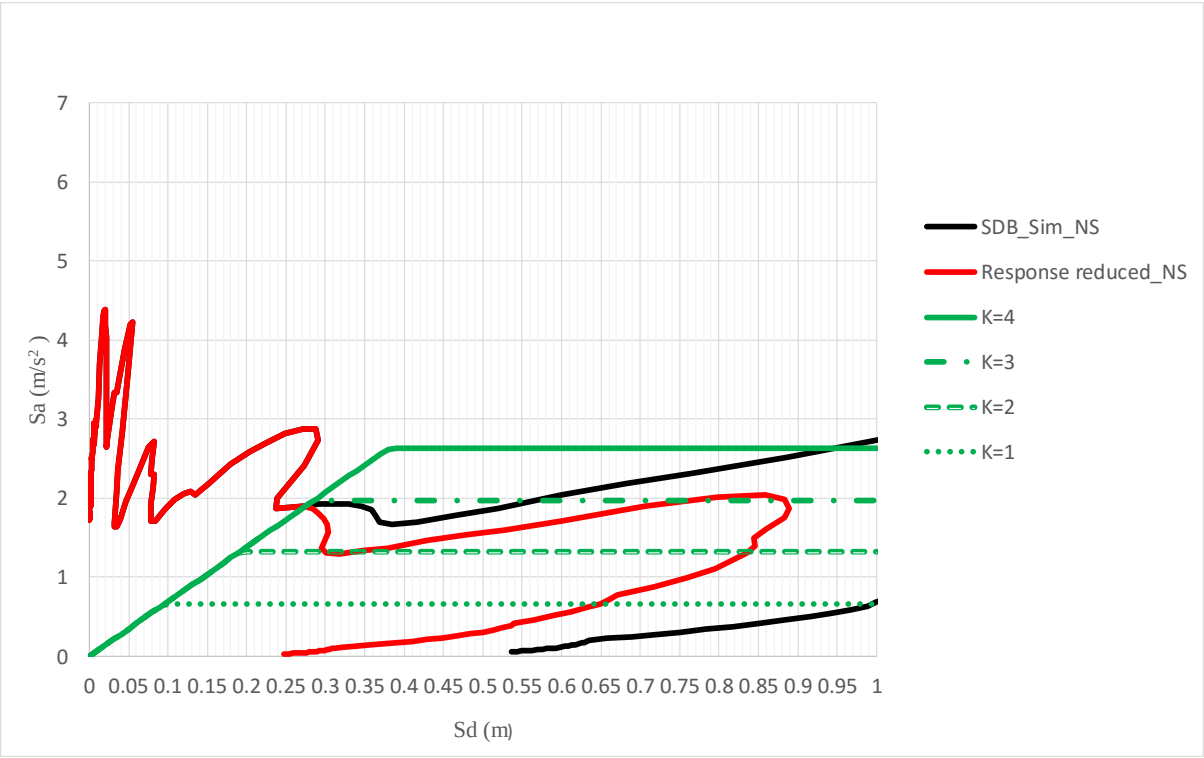

Figure 7.37 Capacity demand curves for the 18-story RC buildings considered for analysis using NS component of the simulated ground motion of the mainshock at SDB.

Table 7.15 Damage sheet of 18-story RC building using the NS component simulated ground motion of the mainshock at SDB

Structural performance factor (K)	Ductility capacity of building collapse	Yield displacement (m)	Displacement demand (m)	Ductility demand	State of building
1	4	0.11	0.63	5.727272727	Collapse
2	2	0.19	0.83	4.368421053	Collapse
3	1.33	0.29	0.27	0.931034483	Minimal damage
4	1	0.38	0.27	0.710526316	Minimal damage

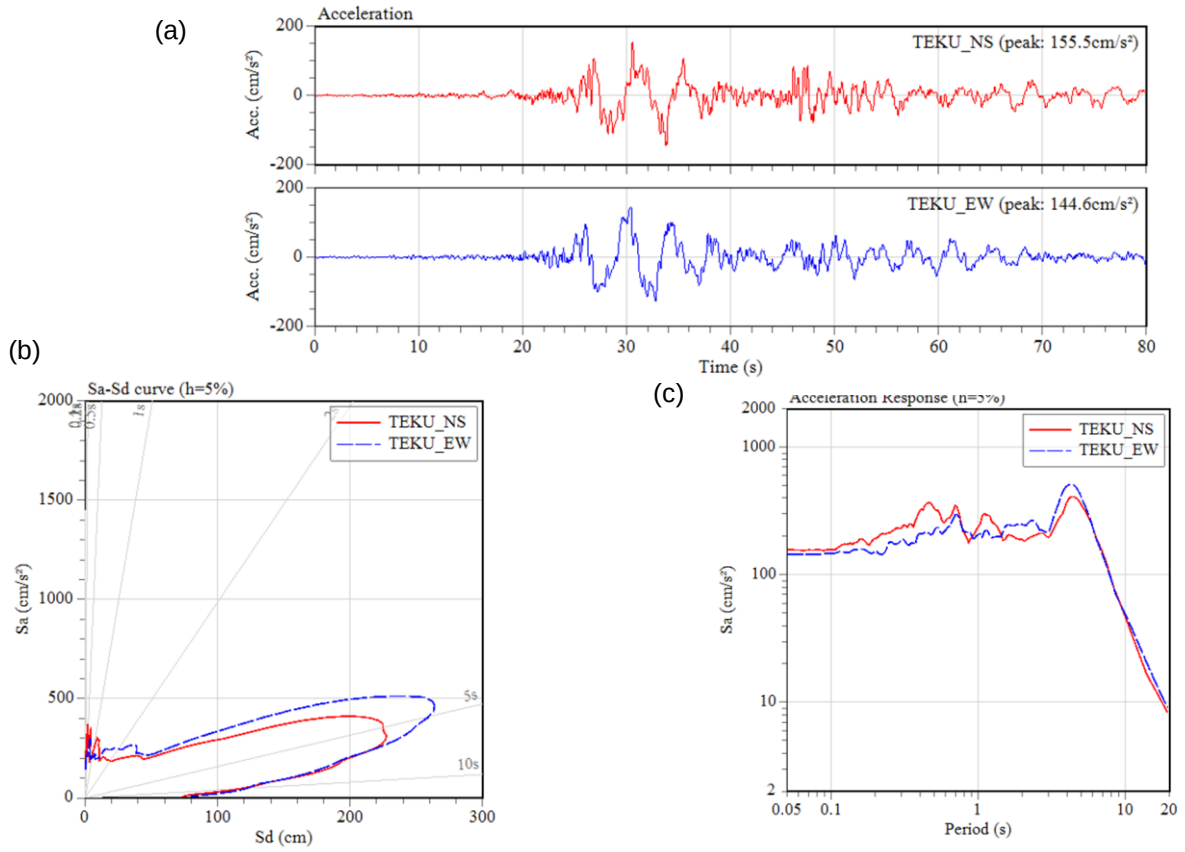

Figure 7.38 (a) Simulated ground motion at TEKU using the observed records at DMG and theoretical response at DMG and TEKU using with the derived velocity structure at TEKU. (b) Acceleration displacement response spectra, and (c) Acceleration response spectra.

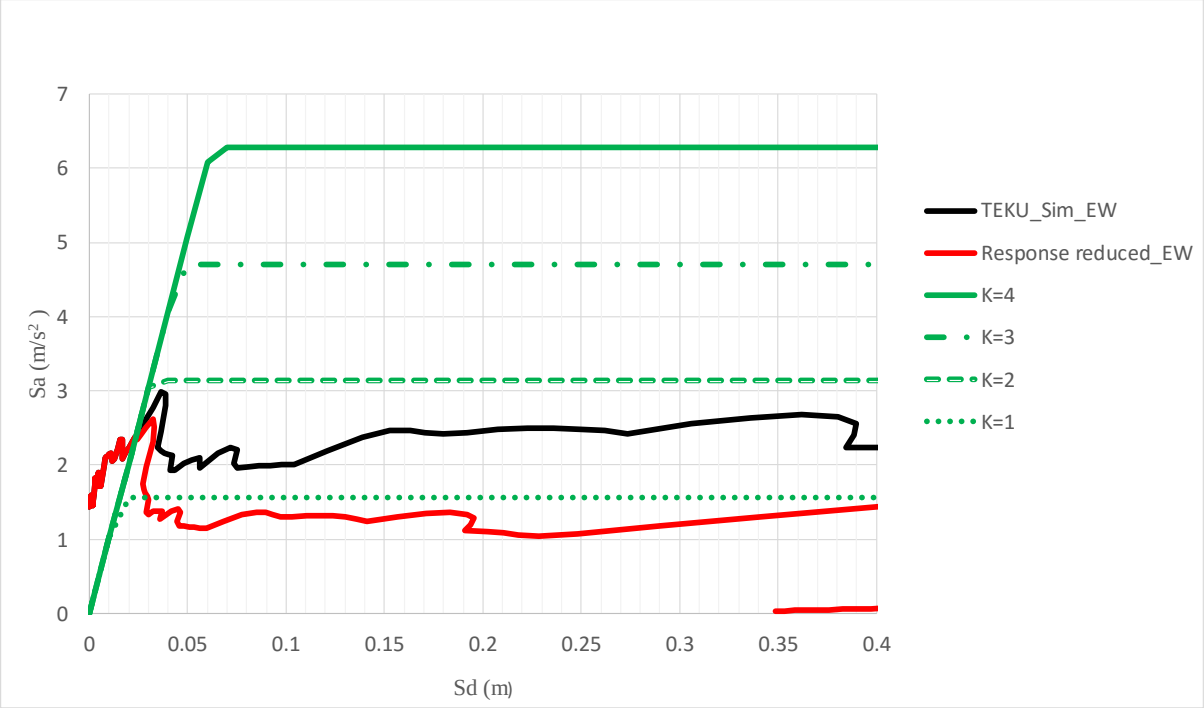

Figure 7.39 Capacity demand curves for the 3-story RC buildings considered for analysis using EW component of the simulated ground motion of the mainshock at TEKU.

Table 7.16 Damage sheet of 3-story RC building using the EW component simulated ground motion of the mainshock at TEKU

Structural performance factor (K)	Ductility capacity of building collapse	Yield displacement (m)	Displacement demand (m)	Ductility demand	State of building
1	4	0.02	0.028	1.4	Moderate damage
2	2	0.03	0.03	1	Moderate damage
3	1.33	0.05	0.03	0.6	Minimal damage
4	1	0.06	0.03	0.5	Minimal damage

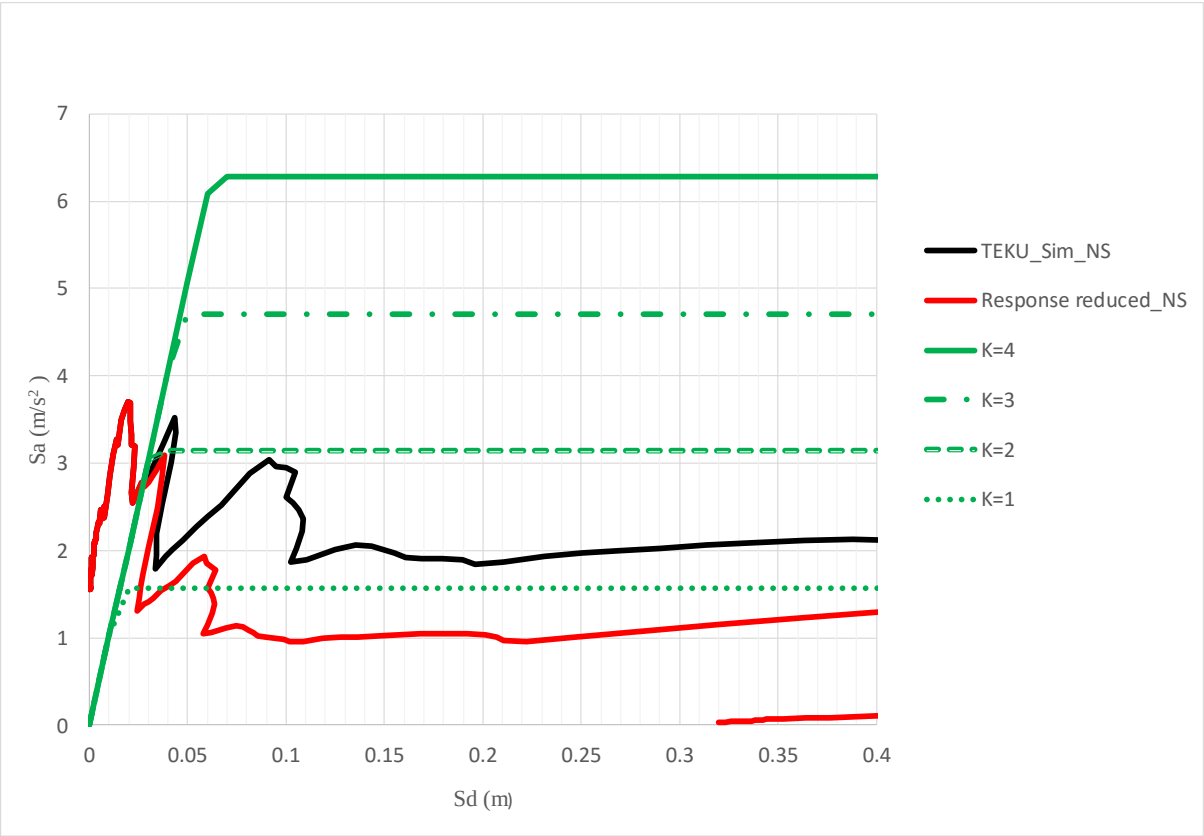

Figure 7.40 Capacity demand curves for the 3-story RC buildings considered for analysis using NS component of the simulated ground motion of the mainshock at TEKU.

Table 7.17 Damage sheet of 3-story RC building using the NS component simulated ground motion of the mainshock at TEKU

Structural performance factor (K)	Ductility capacity of building collapse	Yield displacement (m)	Displacement demand (m)	Ductility demand	State of building
1	4	0.02	0.025	1.25	Moderate damage
2	2	0.03	0.03	1	Moderate damage
3	1.33	0.05	0.03	0.6	Minimal damage
4	1	0.06	0.03	0.5	Minimal damage

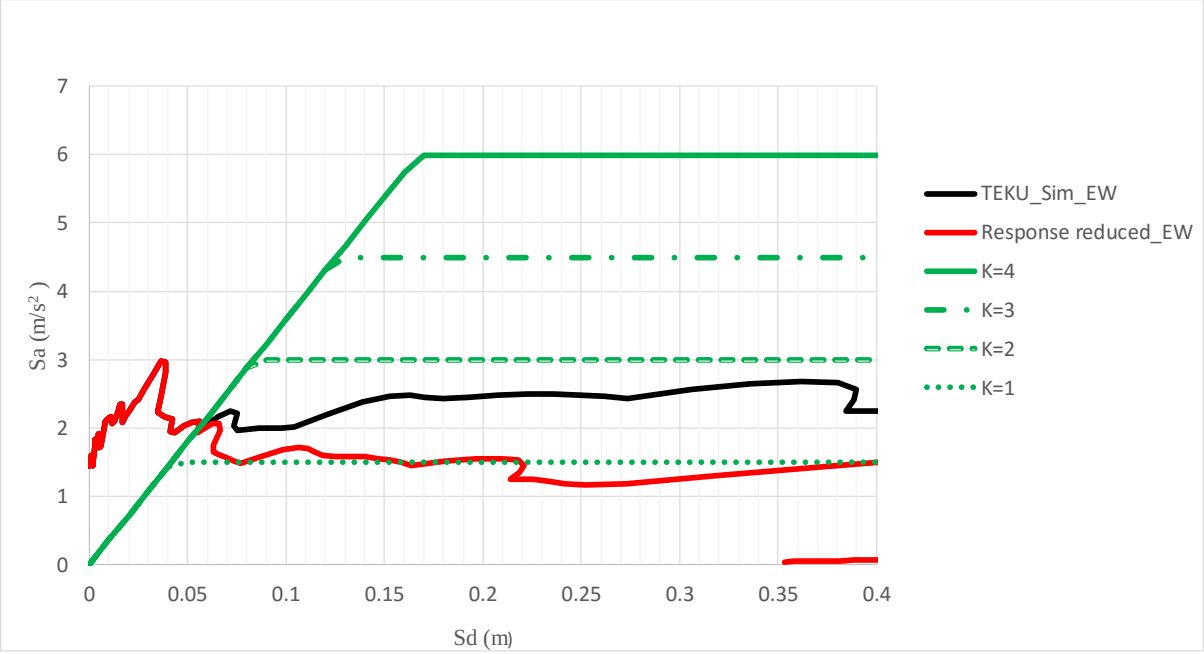

Figure 7.41 Capacity demand curves for the 6-story RC buildings considered for analysis using EW component of the simulated ground motion of the mainshock at TEKU.

Table 7.18 Damage sheet of 6-story RC building using the EW component simulated ground motion of the mainshock at TEKU

Structural performance factor (K)	Ductility capacity of building collapse	Yield displacement (m)	Displacement demand (m)	Ductility demand	State of building
1	4	0.04	0.08	2	Moderate damage
2	2	0.08	0.06	0.75	Minimal damage
3	1.33	0.12	0.06	0.5	Minimal damage
4	1	0.17	0.06	0.35294118	Minimal damage

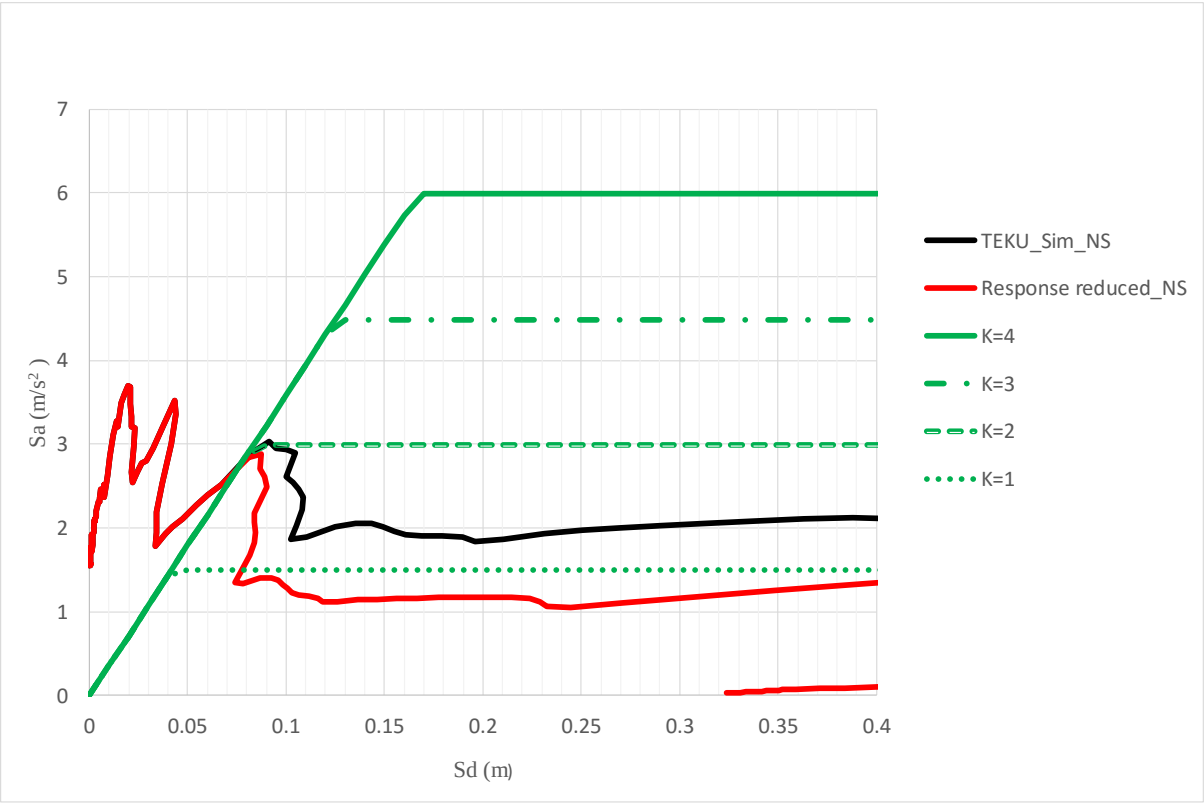

Figure 7.42 Capacity demand curves for the 6-story RC buildings considered for analysis using NS component of the simulated ground motion of the mainshock at TEKU.

Table 7.19 Damage sheet of 6-story RC building using the NS component simulated ground motion of the mainshock at TEKU

Structural performance factor (K)	Ductility capacity of building collapse	Yield displacement (m)	Displacement demand (m)	Ductility demand	State of building
1	4	0.04	0.08	2	Moderate damage
2	2	0.08	0.08	1	Moderate damage
3	1.33	0.12	0.08	0.666666667	Minimal damage
4	1	0.17	0.08	0.470588235	Minimal damage

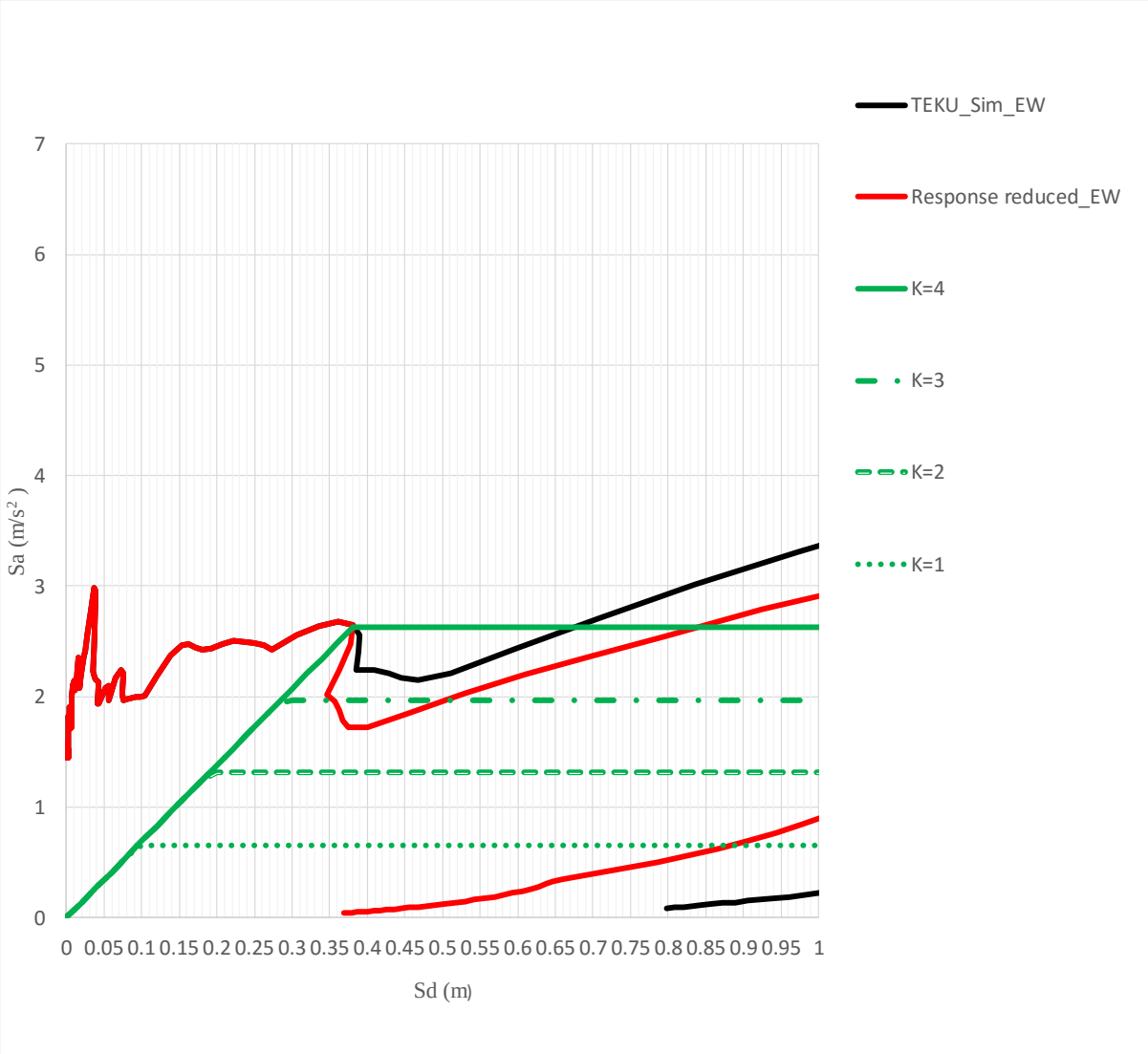

Figure 7.43 Capacity demand curves for the 18-story RC buildings considered for analysis using EW component of the simulated ground motion of the mainshock at TEKU.

Table 7.20 Damage sheet of 18-story RC building using the EW component simulated ground motion of the mainshock at TEKU

Structural performance factor (K)	Ductility capacity of building collapse	Yield displacement (m)	Displacement demand (m)	Ductility demand	State of building
1	4	0.09	0.86	9.555555556	Collapse
2	2	0.18	1.18	6.555555556	Collapse
3	1.33	0.28	0.36	1.285714286	Moderate damage
4	1	0.38	0.38	1	Moderate damage

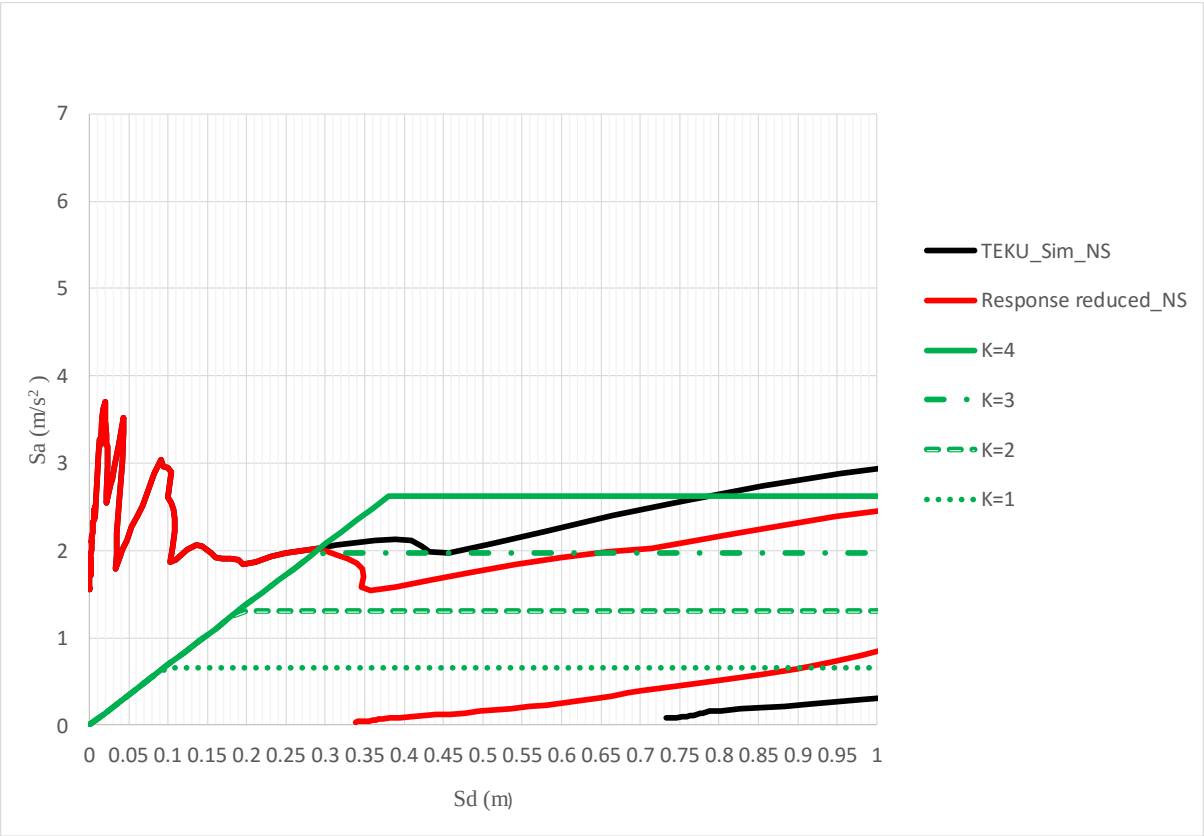

Figure 7.44 Capacity demand curves for the 18-story RC buildings considered for analysis using NS component of the simulated ground motion of the mainshock at TEKU.

Table 7.21 Damage sheet of 18-story RC building using the NS component simulated ground motion of the mainshock at TEKU

Structural performance factor (K)	Ductility capacity of building collapse	Yield displacement (m)	Displacement demand (m)	Ductility demand	State of building
1	4	0.09	0.9	10	Collapse
2	2	0.18	1.18	6.55555556	Collapse
3	1.33	0.28	0.3	1.07142857	Moderate damage
4	1	0.38	0.3	0.78947368	Minimal damage

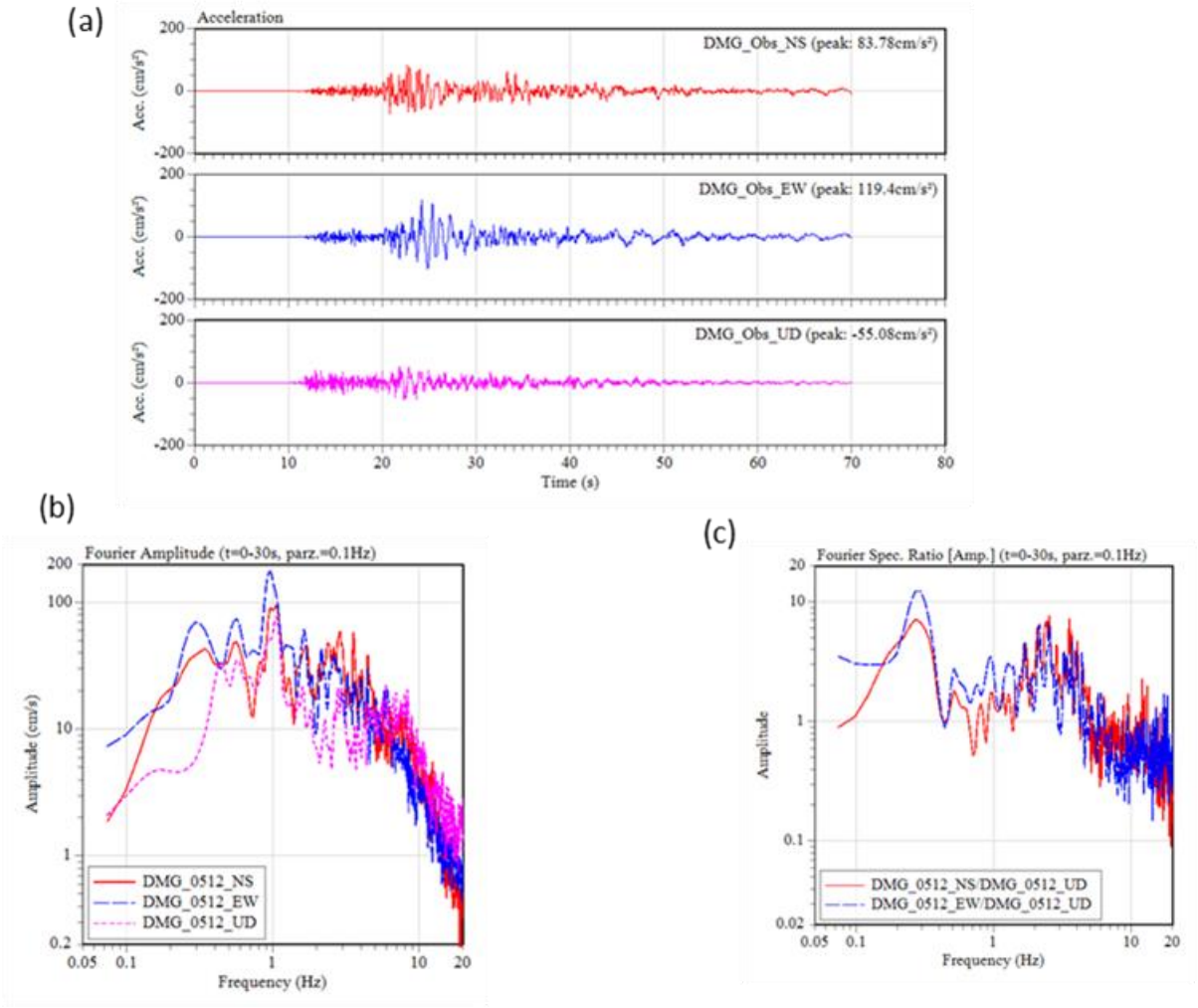

Figure 7.45 (a) The largest aftershock (*Mw* 7.3) of the Gorkha earthquake observed at DMG. (b) Fourier amplitude spectra, and (c) H/V spectral ratio. 30 s time window form both the horizontal components are used for the comparison with simulation at the site DMG staring 2 s before the *S*-onset.

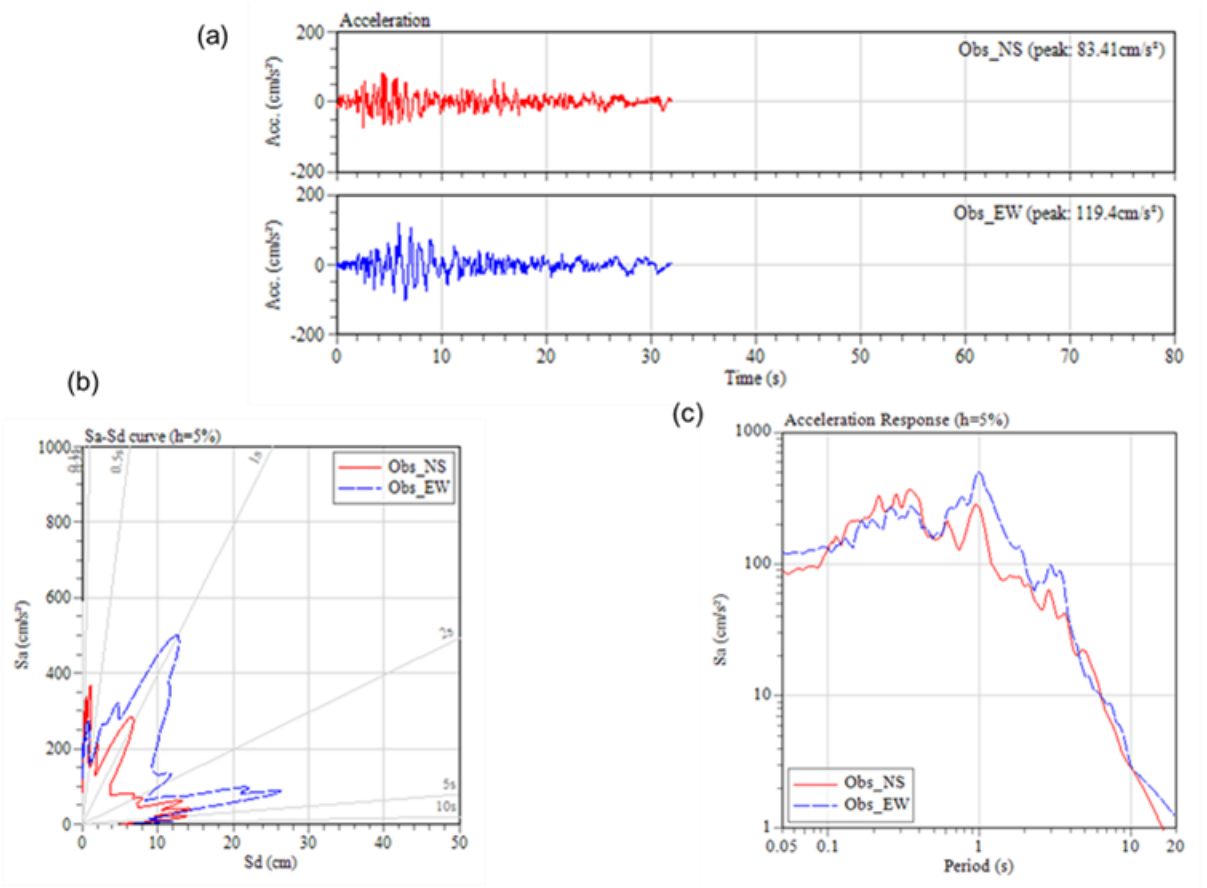

Figure 7.46 (a) The largest aftershock of the Gorkha earthquake observed at DMG and used for the comparision with simulation. (b) Acceleration displacement response spectra, and (c) Acceleration response spectra. 30 s time window for both the horizontal components are used to compare with the the simulated ground motion staring 2 s before the *S*-onset.

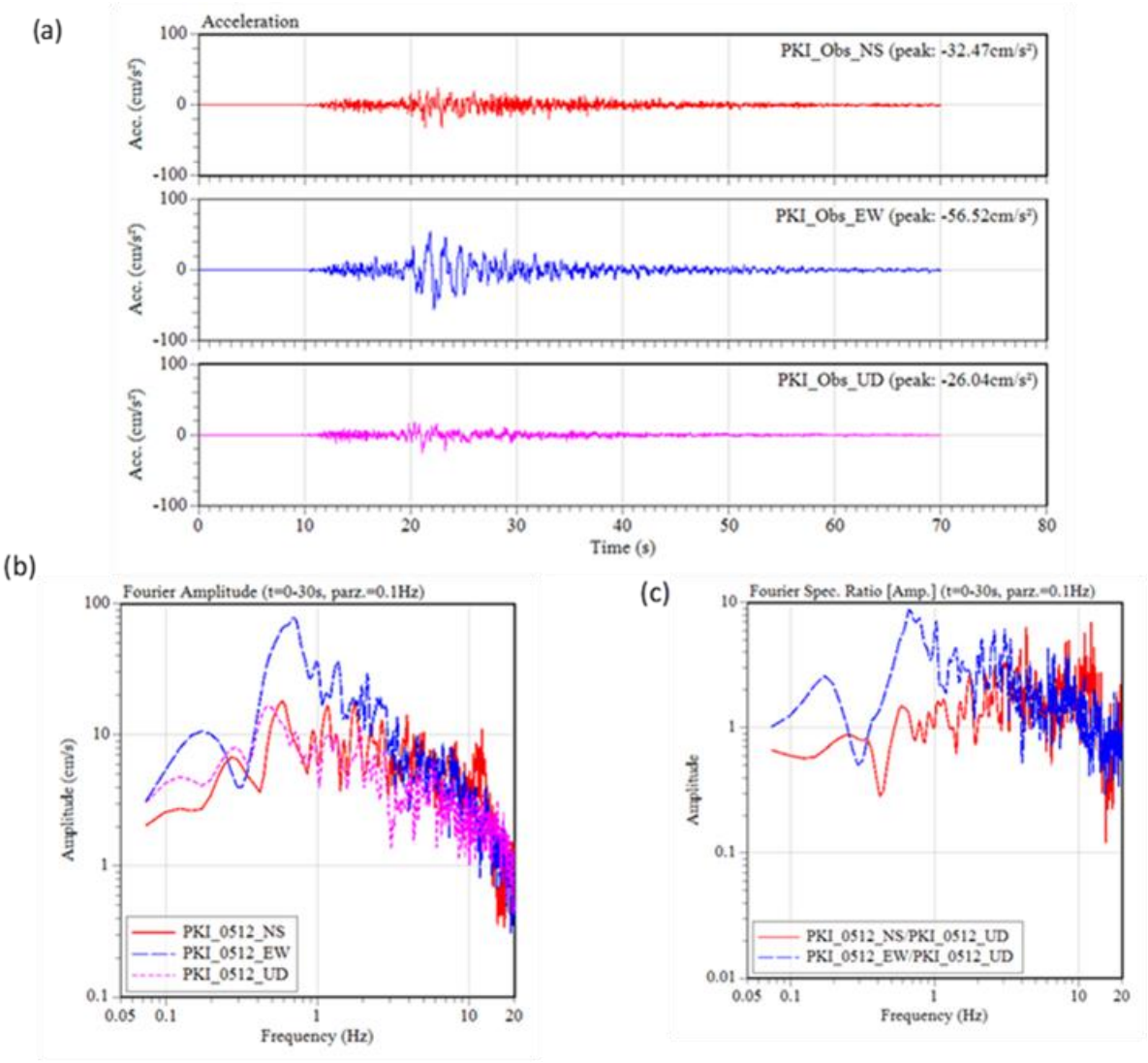

Figure 7.47 (a) The largest aftershock of the Gorkha earthquake observed at PKI rock site. (b) Fourier amplitude spectra, and (c) H/V spectral ratio. 30 s time window form both the horizontal components are used for the simulation staring 2 s before the *S*-onset.

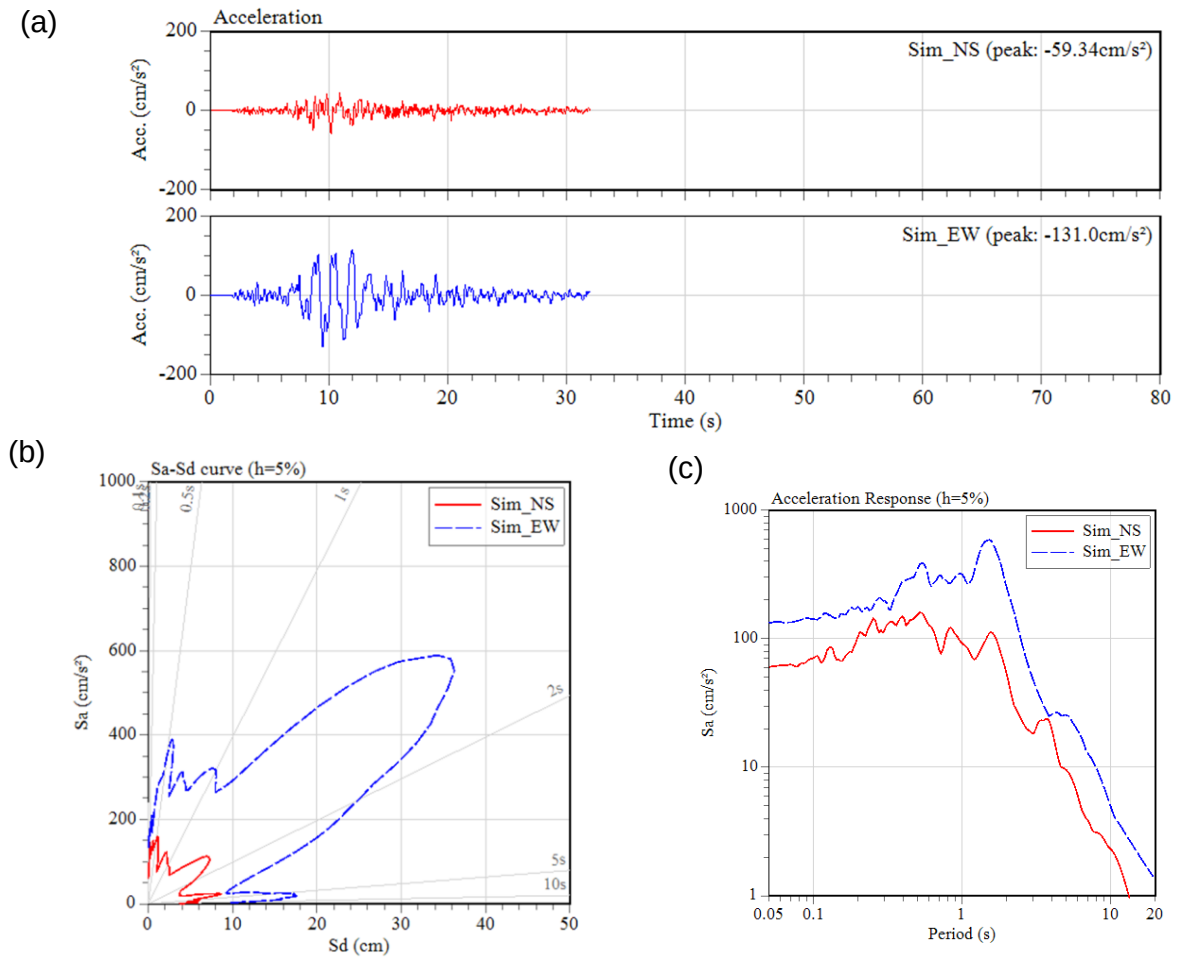

Figure 7.48 (a) The largest aftershock of the Gorkha earthquake observed at PKI and simulated using the velocity structure model derived at DMG. (b) Acceleration displacement response spectra, and (c) Acceleration response spectra. 30 s time window for both the horizontal components are used to compare with the observed ground motionstarting 2 s before the *S*-onset.

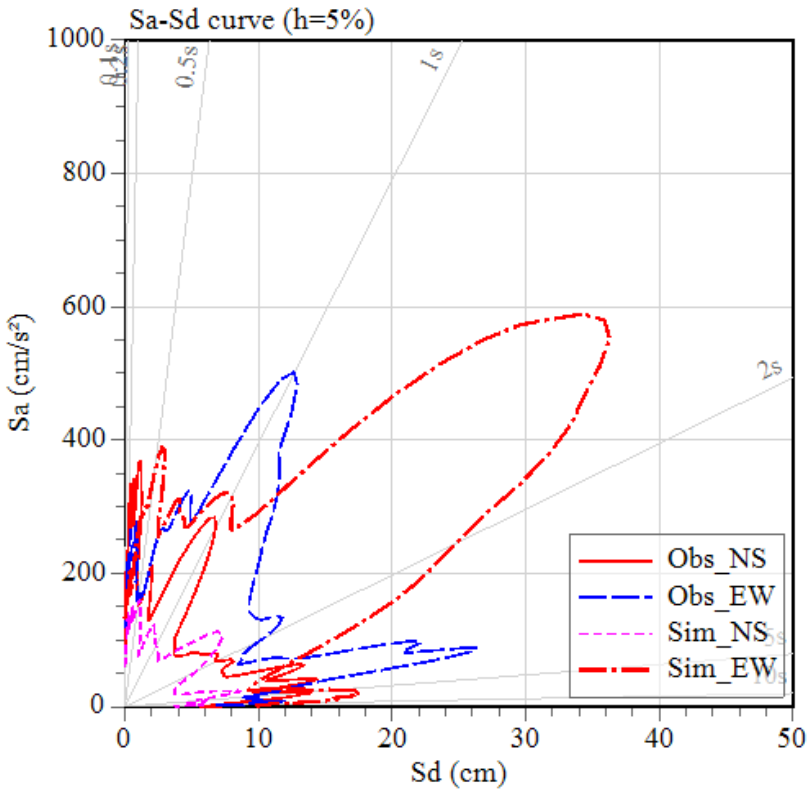

Figure 7.49 Observed (DMG) and simulated (PKI at DMG) are plotted in the Acceleration displacement response spectra (ADRS) format. The simulated waveform in the EW component is larger than the observed one. Both the observed and simulated motion in the NS component shows smaller values.

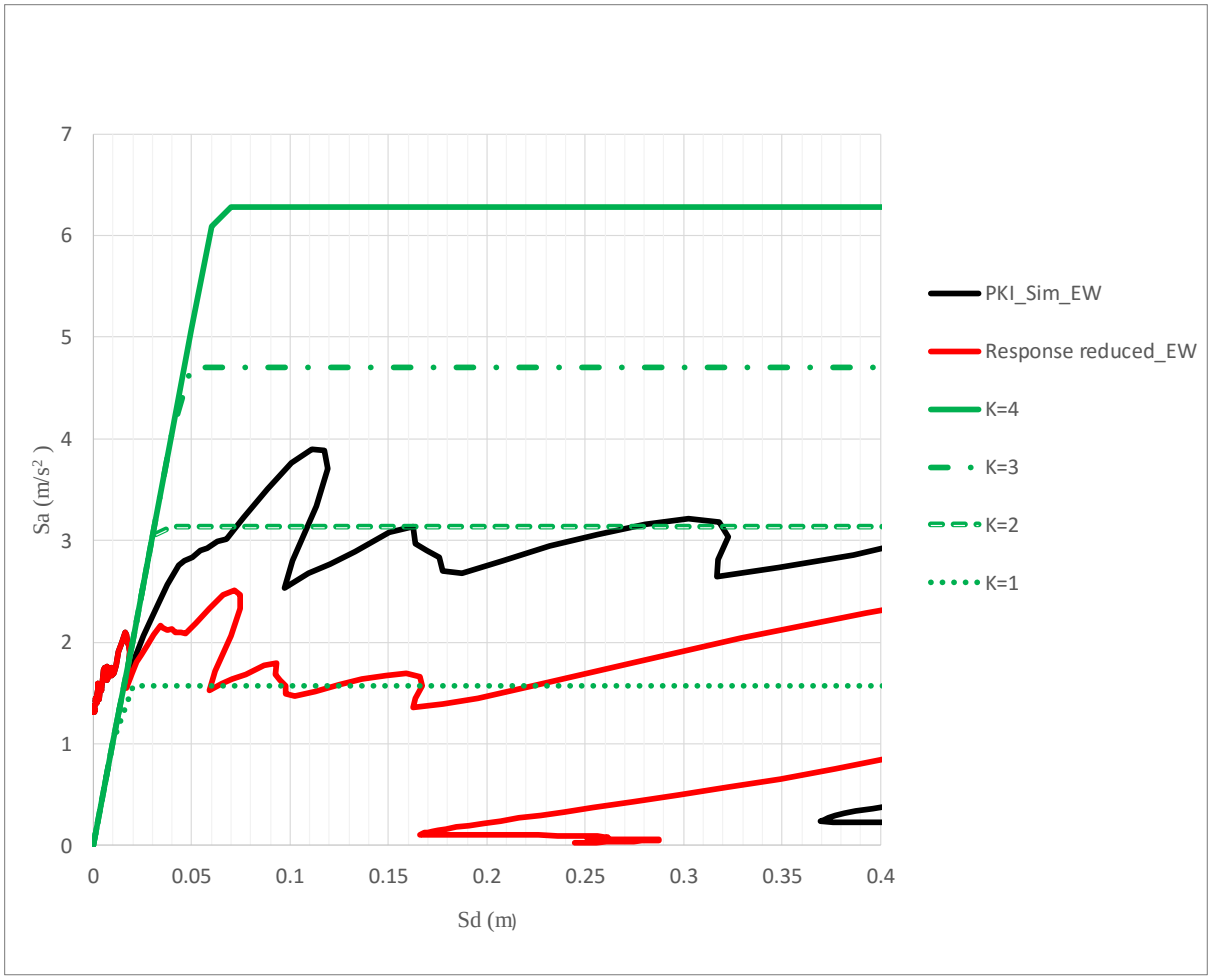

Figure 7.50 Capacity demand curves for the 3-story RC buildings considered for analysis using EW component of the simulated ground motion of the largest aftershock PKI at DMG.

Table 7.22 Damage sheet of 3-story RC building using the EW component simulated ground motion of the largest aftershock PKI at DMG

Structural performance factor (K)	Ductility capacity of building collapse	Yield displacement (m)	Displacement demand (m)	Ductility demand	State of building
1	4	0.02	0.02	1	Moderate damage
2	2	0.03	0.02	0.66666667	Minimal damage
3	1.33	0.05	0.02	0.4	Minimal damage
4	1	0.06	0.02	0.33333333	Minimal damage

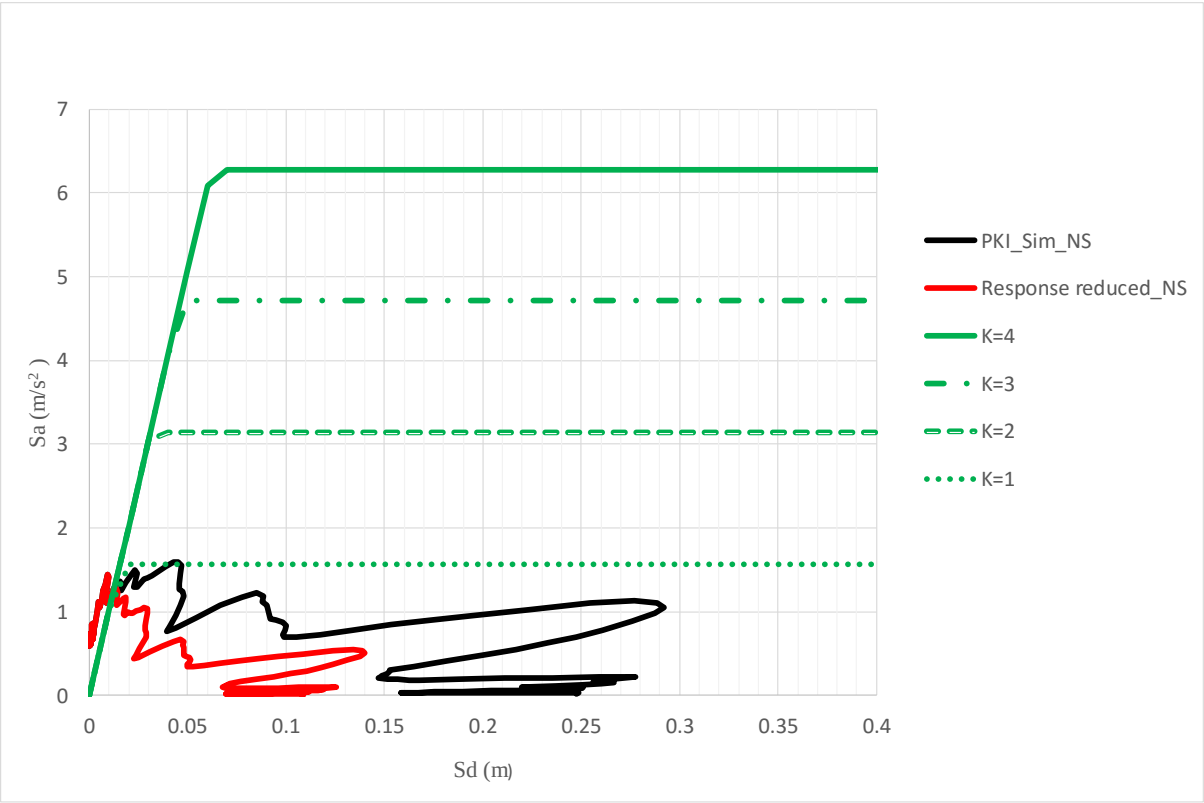

Figure 7.51 Capacity demand curves for the 3-story RC buildings considered for analysis using NS component of the simulated ground motion of the largest aftershock PKI at DMG.

Table 7.23 Damage sheet of 3-story RC building using the NS component simulated ground motion of the largest aftershock PKI at DMG

Structural performance factor (K)	Ductility capacity of building collapse	Yield displacement (m)	Displacement demand (m)	Ductility demand	State of building
1	4	0.02	0.01	0.5	Minimal damage
2	2	0.03	0.01	0.333333333	Minimal damage
3	1.33	0.05	0.01	0.2	Minimal damage
4	1	0.06	0.01	0.166666667	Minimal damage

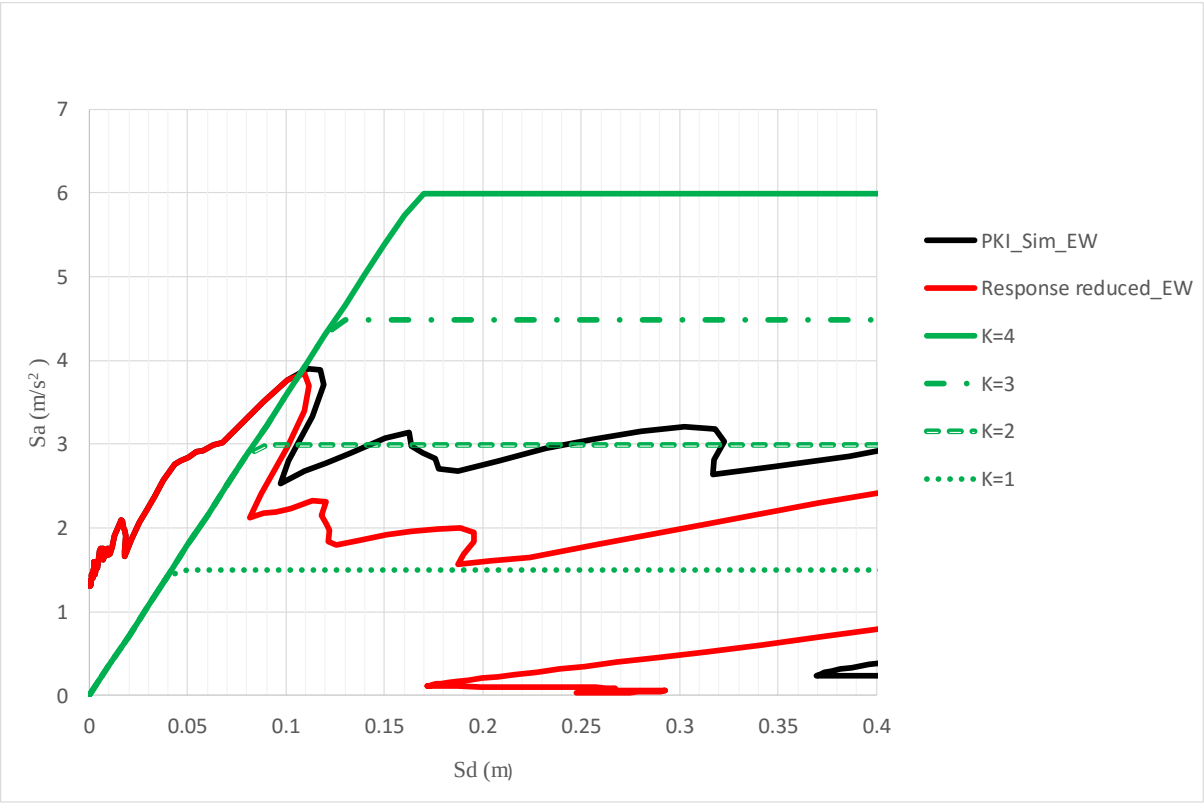

Figure 7.52 Capacity demand curves for the 6-story RC buildings considered for analysis using EW component of the simulated ground motion of the largest aftershock PKI at DMG.

Table 7.24 Damage sheet of 6-story RC building using the EW component simulated ground motion of the largest aftershock PKI at DMG

Structural performance factor (K)	Ductility capacity of building collapse	Yield displacement (m)	Displacement demand (m)	Ductility demand	State of building
1	4	0.04	0.248	6.2	Collapse
2	2	0.08	0.1	1.25	Moderate damage
3	1.33	0.11	0.11	1	Moderate damage
4	1	0.11	0.11	1	Moderate damage

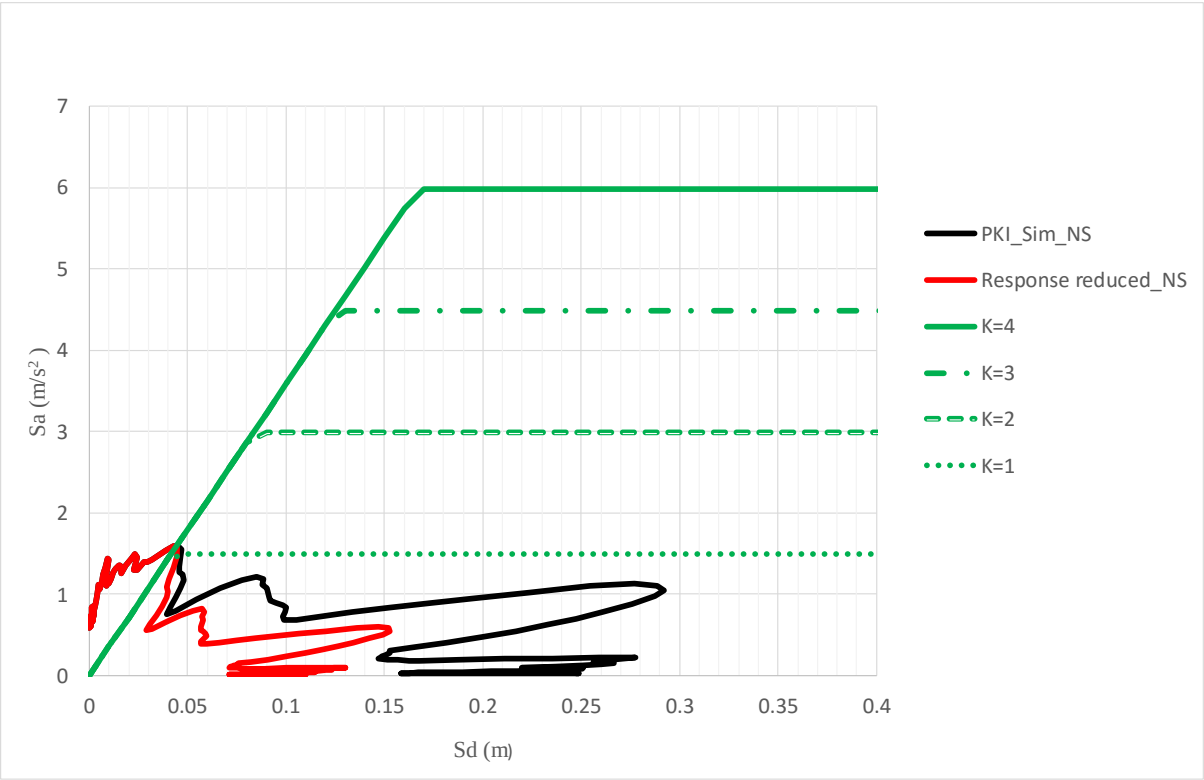

Figure 7.53 Capacity demand curves for the 6-story RC buildings considered for analysis using NS component of the simulated ground motion of the largest aftershock PKI at DMG.

Table 7.25 Damage sheet of 6-story RC building using the NS component simulated ground motion of the largest aftershock PKI at DMG

Structural performance factor (K)	Ductility capacity of building collapse	Yield displacement (m)	Displacement demand (m)	Ductility demand	State of building
1	4	0.04	0.04	1	Moderate damage
2	2	0.08	0.04	0.5	Minimal damage
3	1.33	0.11	0.04	0.363636364	Minimal damage
4	1	0.11	0.04	0.363636364	Minimal damage

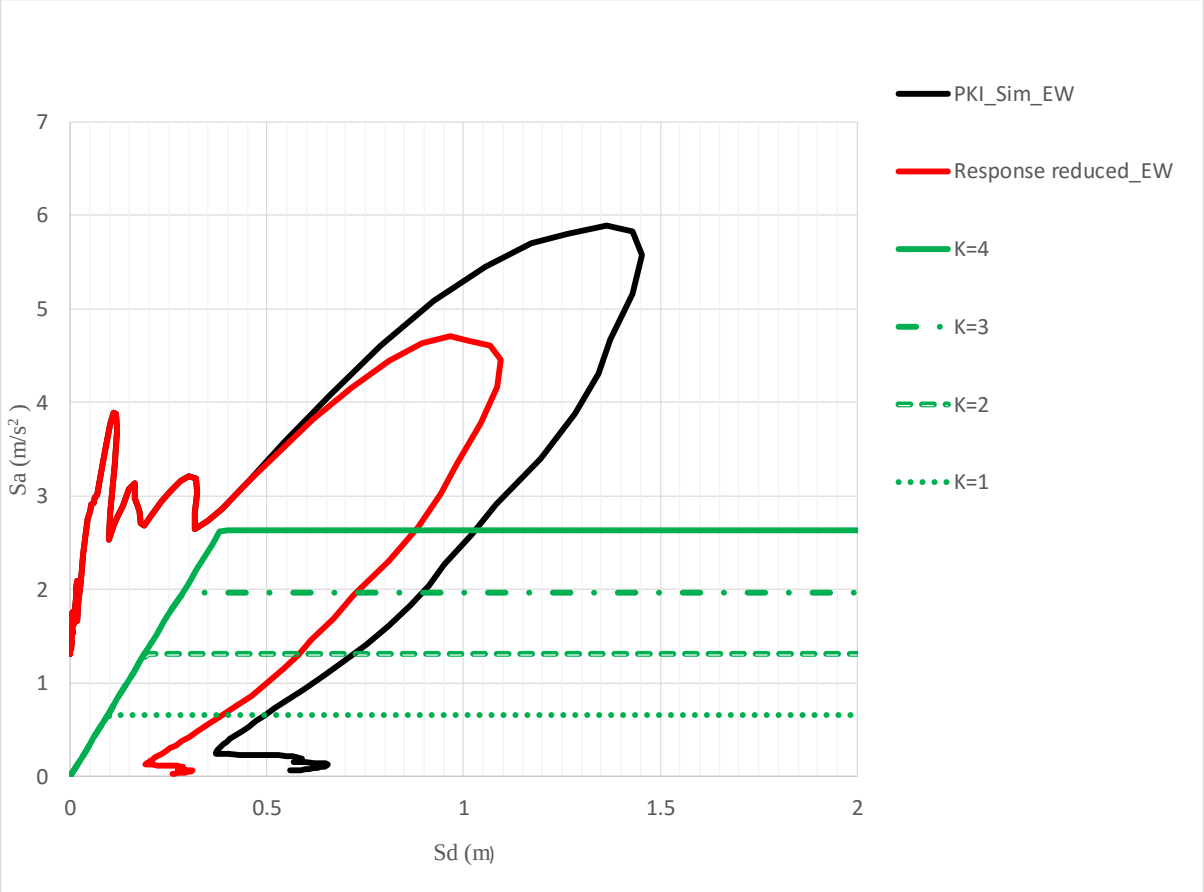

Figure 7.54 Capacity demand curves for the 18-story RC buildings considered for analysis using EW component of the simulated ground motion of the largest aftershock PKI at DMG.

Table 7.26 Damage sheet of 18-story RC building using the EW component simulated ground motion of the largest aftershock PKI at DMG

Structural performance factor (K)	Ductility capacity of building collapse	Yield displacement (m)	Displacement demand (m)	Ductility demand	State of building
1	4	0.1	0.4	4	Collapse
2	2	0.2	0.58	2.9	Collapse
3	1.33	0.28	0.72	2.571428571	Collapse
4	1	0.4	0.88	2.2	Collapse

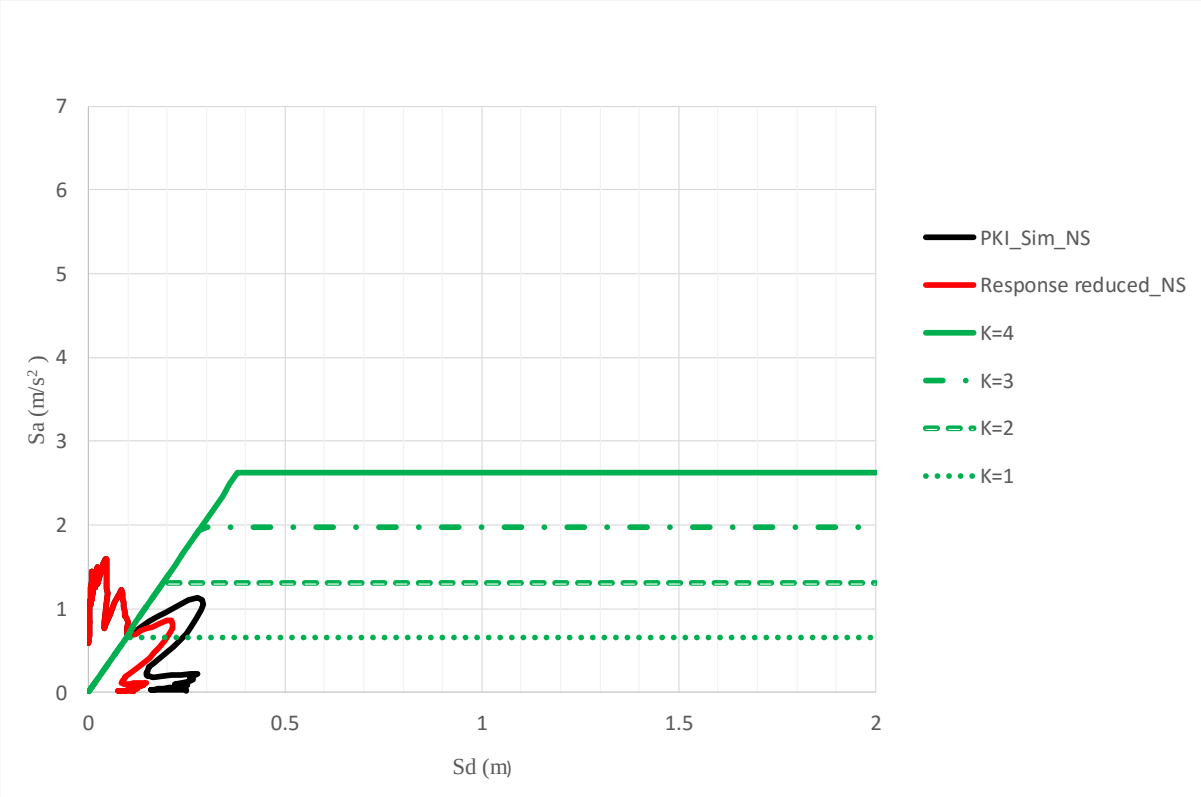

Figure 7.55 Capacity demand curves for the 18-story RC buildings considered for analysis using NS component of the simulated ground motion of the largest aftershock PKI at DMG.

Table 7.27 Damage sheet of 18-story RC building using the NS component simulated ground motion of the largest aftershock PKI at DMG

Structural performance factor (K)	Ductility capacity of building collapse	Yield displacement (m)	Displacement demand (m)	Ductility demand	State of building
1	4	0.1	0.12	1.2	Moderate damage
2	2	0.2	0.12	0.6	Minimal damage
3	1.33	0.28	0.12	0.428571429	Minimal damage
4	1	0.4	0.12	0.3	Minimal damage

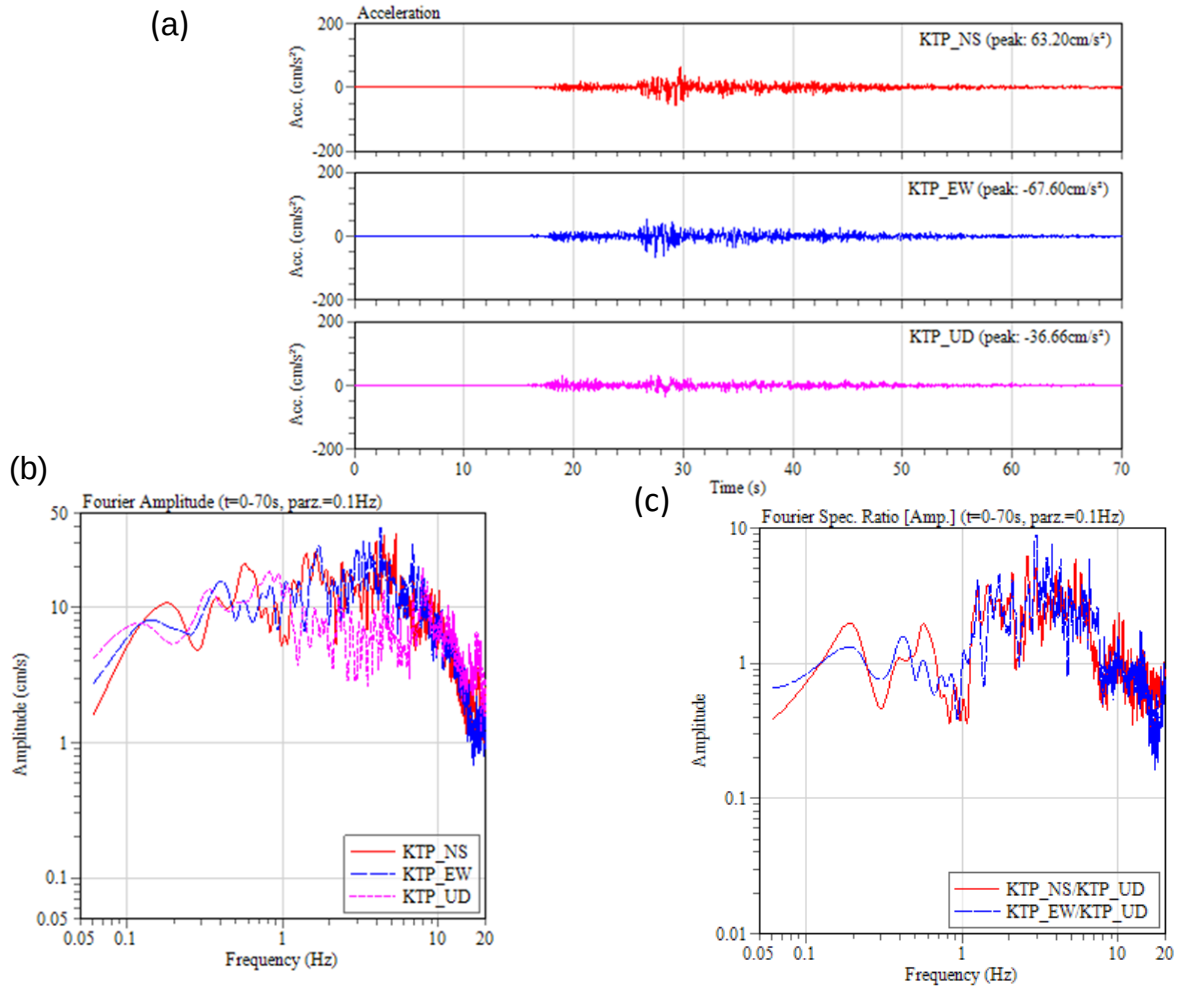

Figure 7.56 (a) The largest aftershock of the Gorkha earthquake observed at KTP (b) Fourier amplitude spectra, and (c) H/V spectral ratio.

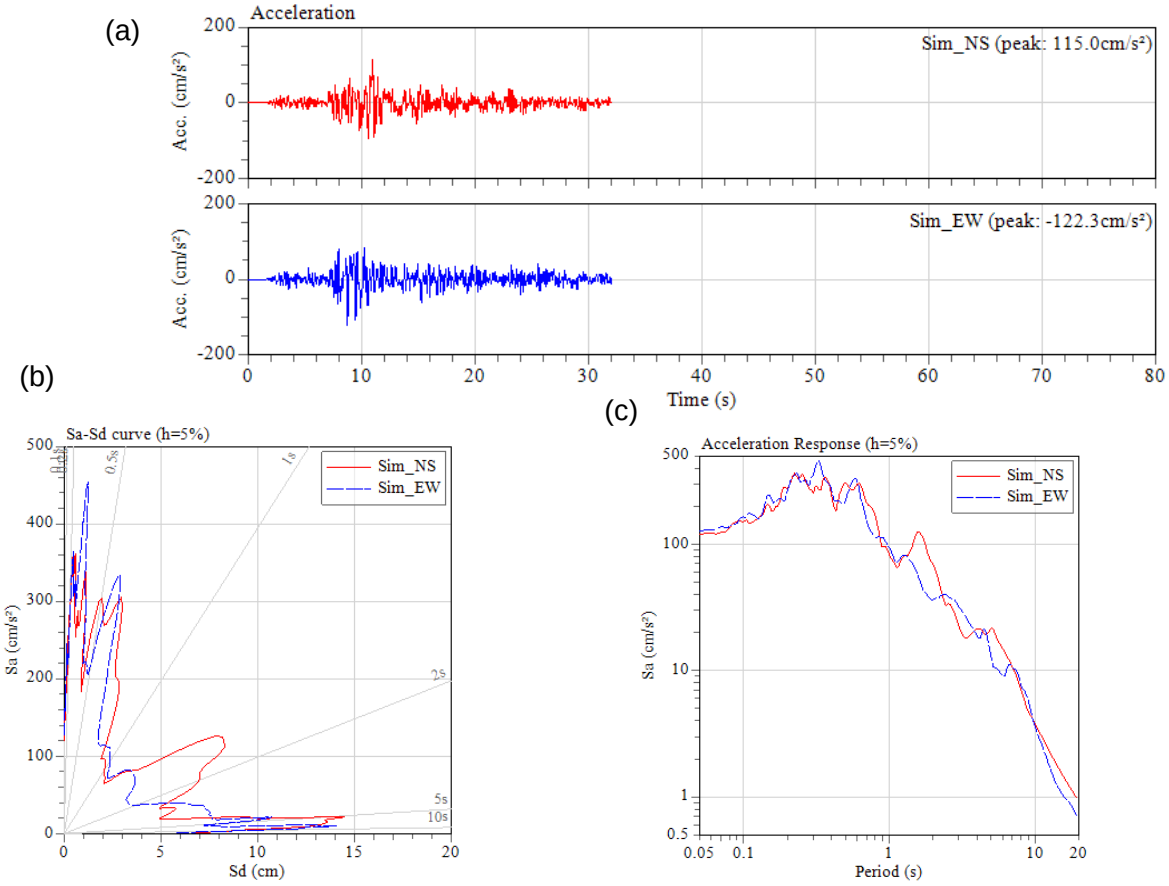

Figure 7.57 (a) The largest aftershock of the Gorkha earthquake observed at the KTP rock site and simulated at the DMG using underground velocity structure. (b) Acceleration displacement response spectra, and (c) Acceleration response spectra.

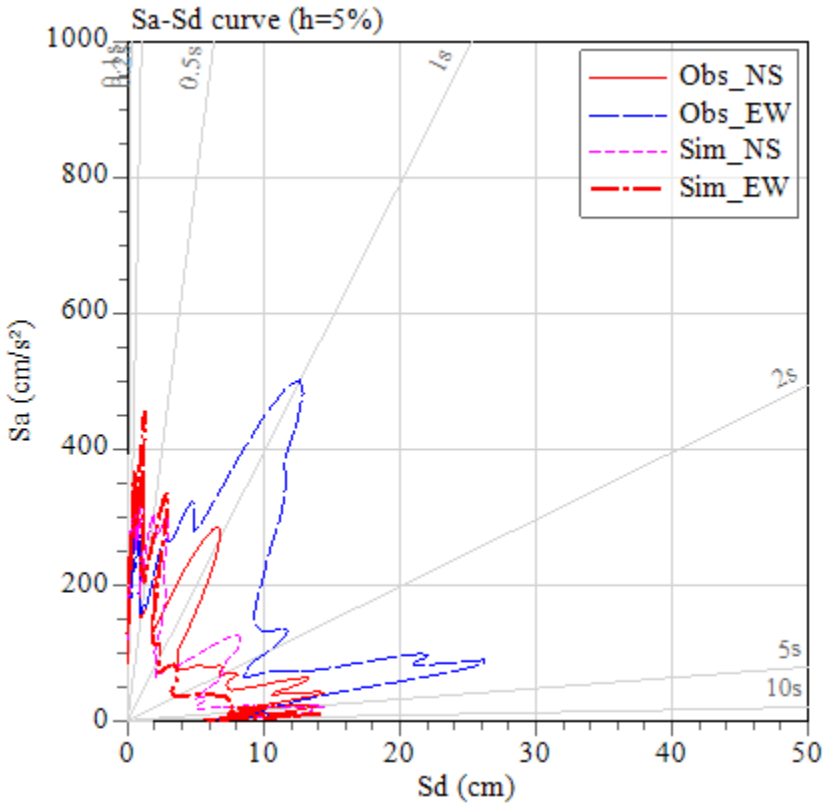

Figure 7.58 Comparision of the acceleration displacement response spectra of the largest aftershock observed at KTP and simulated at DMG.

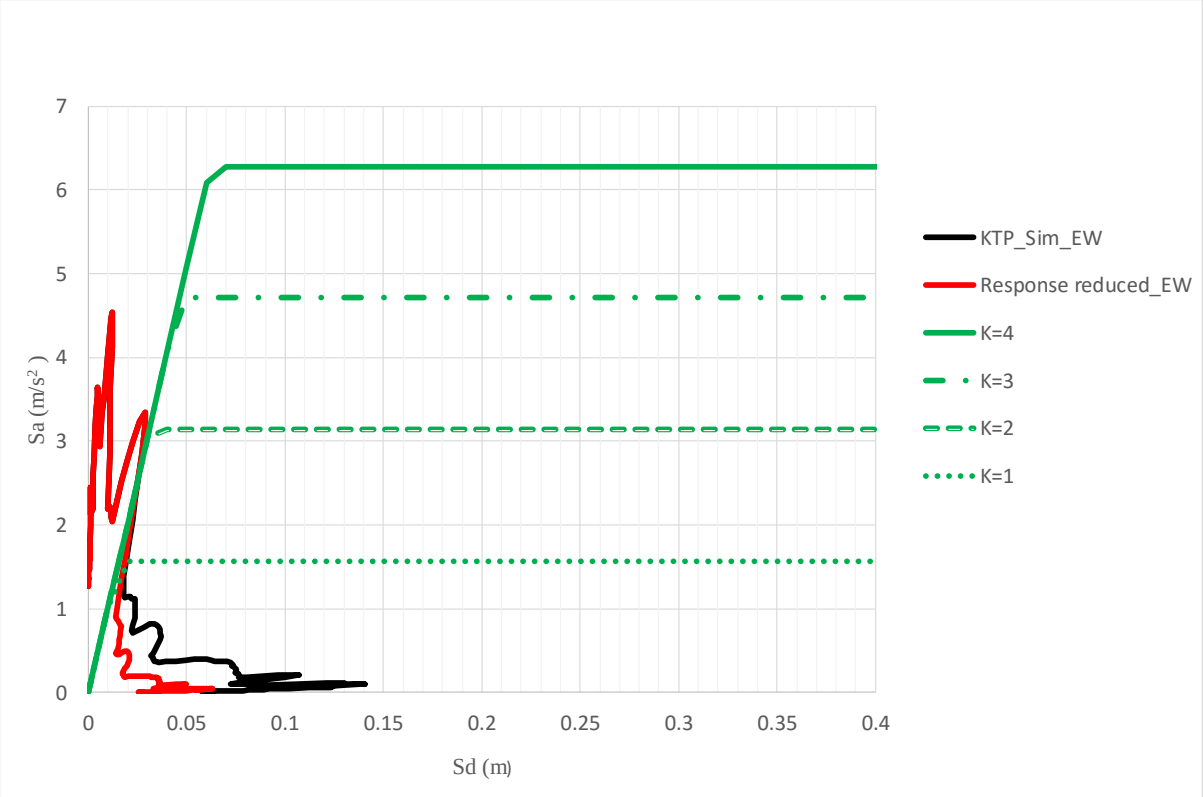

Figure 7.59 Capacity demand curves for the 3-story RC buildings considered for analysis using EW component of the simulated ground motion of the largest aftershock KTP at DMG.

Table 7.28 Damage sheet of 3-story RC building using the EW component simulated ground motion of the largest aftershock KTP at DMG

Structural performance factor (K)	Ductility capacity of building collapse	Yield displacement (m)	Displacement demand (m)	Ductility demand	State of building
1	4	0.02	0.02	1	Moderate damage
2	2	0.03	0.02	0.666666667	Minimal damage
3	1.33	0.05	0.02	0.4	Minimal damage
4	1	0.06	0.02	0.333333333	Minimal damage

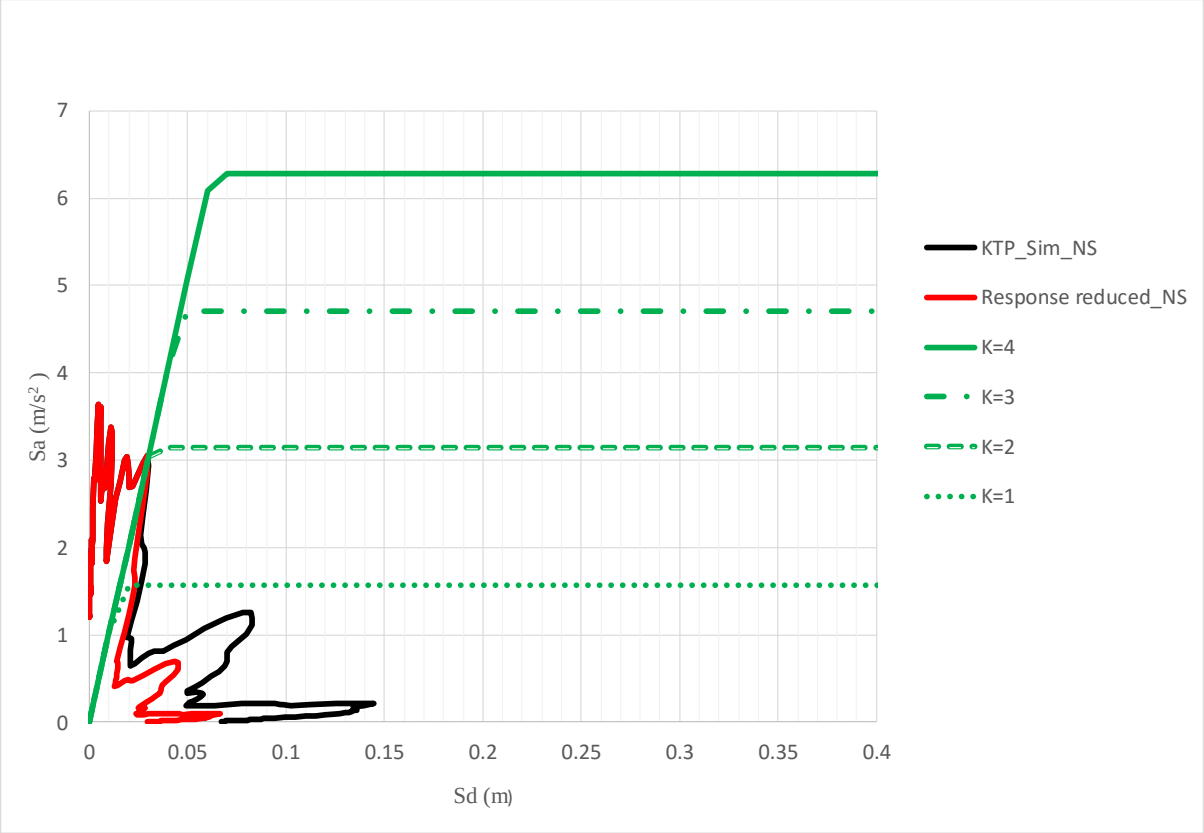

Figure 7.60 Capacity demand curves for the 3-story RC buildings considered for analysis using NS component of the simulated ground motion of the largest aftershock KTP at DMG.

Table 7.29 Damage sheet of 3-story RC building using the NS component simulated ground motion of the largest aftershock KTP at DMG

Structural performance factor (K)	Ductility capacity of building collapse	Yield displacement (m)	Displacement demand (m)	Ductility demand	State of building
1	4	0.02	0.02	1	Moderate damage
2	2	0.03	0.03	1	Moderate damage
3	1.33	0.05	0.03	0.6	Minimal damage
4	1	0.06	0.03	0.5	Minimal damage

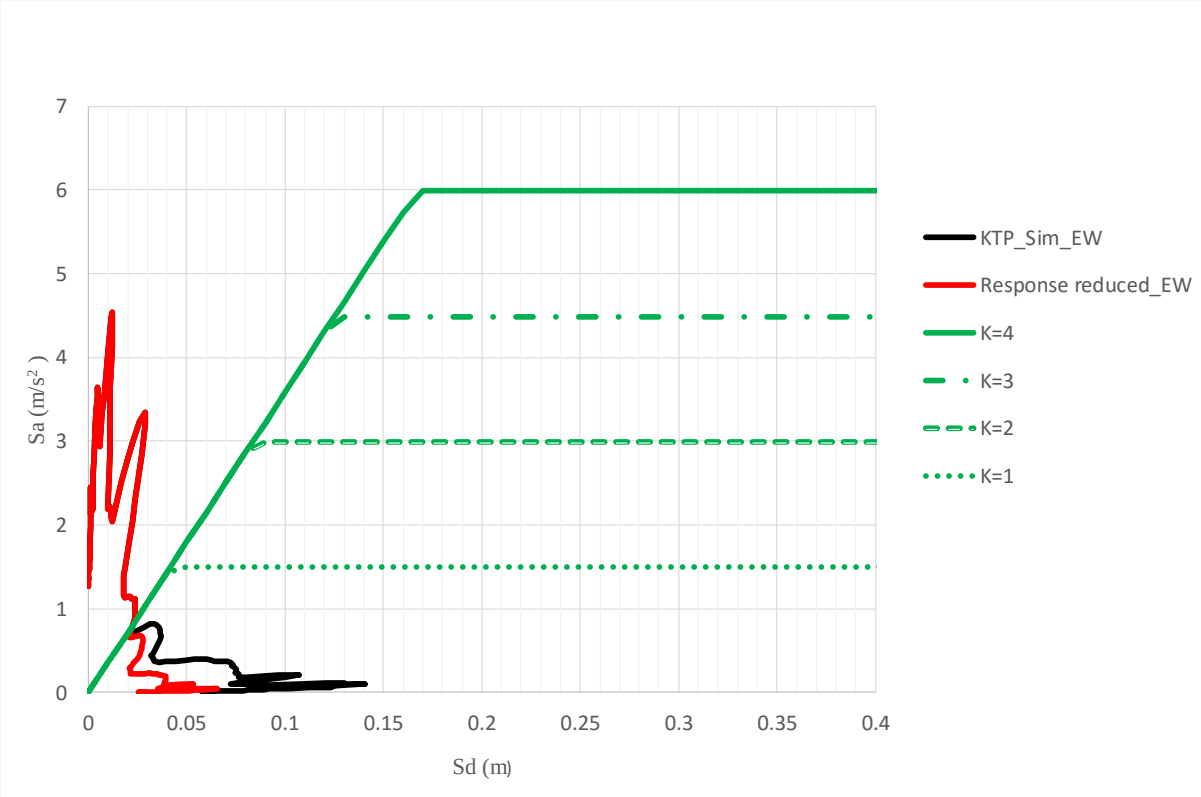

Figure 7.61 Capacity demand curves for the 6-story RC buildings considered for analysis using EW component of the simulated ground motion of the largest aftershock KTP at DMG.

Table 7.30 Damage sheet of 6-story RC building using the EW component simulated ground motion of the largest aftershock KTP at DMG

Structural performance factor (K)	Ductility capacity of building collapse	Yield displacement (m)	Displacement demand (m)	Ductility demand	State of building
1	4	0.04	0.02	0.5	Minimal damage
2	2	0.08	0.02	0.25	Minimal damage
3	1.33	0.12	0.02	0.166666667	Minimal damage
4	1	0.17	0.02	0.117647059	Minimal damage

Figure 7.62 Capacity demand curves for the 6-story RC buildings considered for analysis using NS component of the simulated ground motion of the largest aftershock KTP at DMG.

Table 7.31 Damage sheet of 6-story RC building using the NS component simulated ground motion of the largest aftershock KTP at DMG

Structural performance factor (K)	Ductility capacity of building collapse	Yield displacement (m)	Displacement demand (m)	Ductility demand	State of building
1	4	0.04	0.02	0.5	Minimal damage
2	2	0.08	0.02	0.25	Minimal damage
3	1.33	0.12	0.02	0.166666667	Minimal damage
4	1	0.17	0.02	0.117647059	Minimal damage

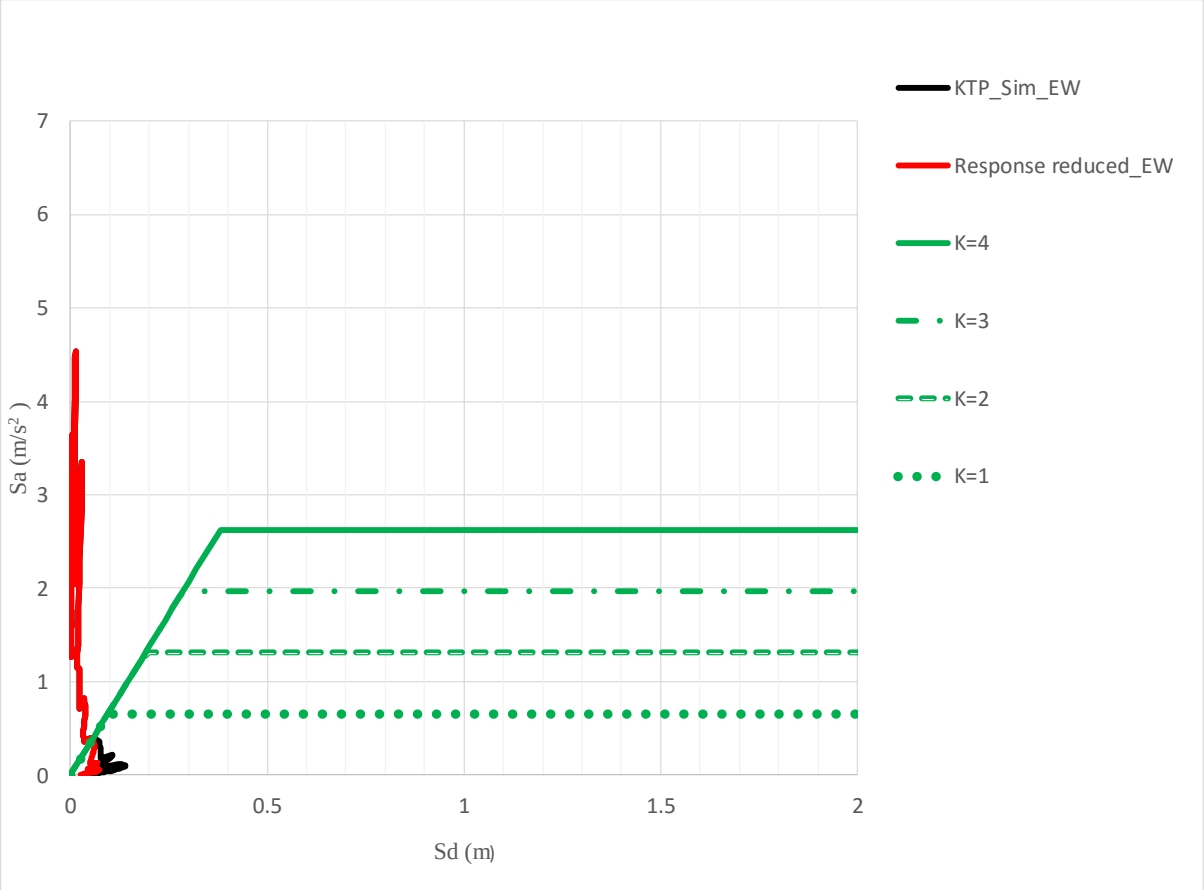

Figure 7.63 Capacity demand curves for the 18-story RC buildings considered for analysis using EW component of the simulated ground motion of the largest aftershock KTP at DMG.

Table 7.32 Damage sheet of 18-story RC building using the EW component simulated ground motion of the largest aftershock KTP at DMG

Structural performance factor (K)	Ductility capacity of building collapse	Yield displacement (m)	Displacement demand (m)	Ductility demand	State of building
1	4	0.08	0.06	0.75	Minimal damage
2	2	0.2	0.06	0.3	Minimal damage
3	1.33	0.28	0.06	0.214285714	Minimal damage
4	1	0.38	0.02	0.052631579	Minimal damage

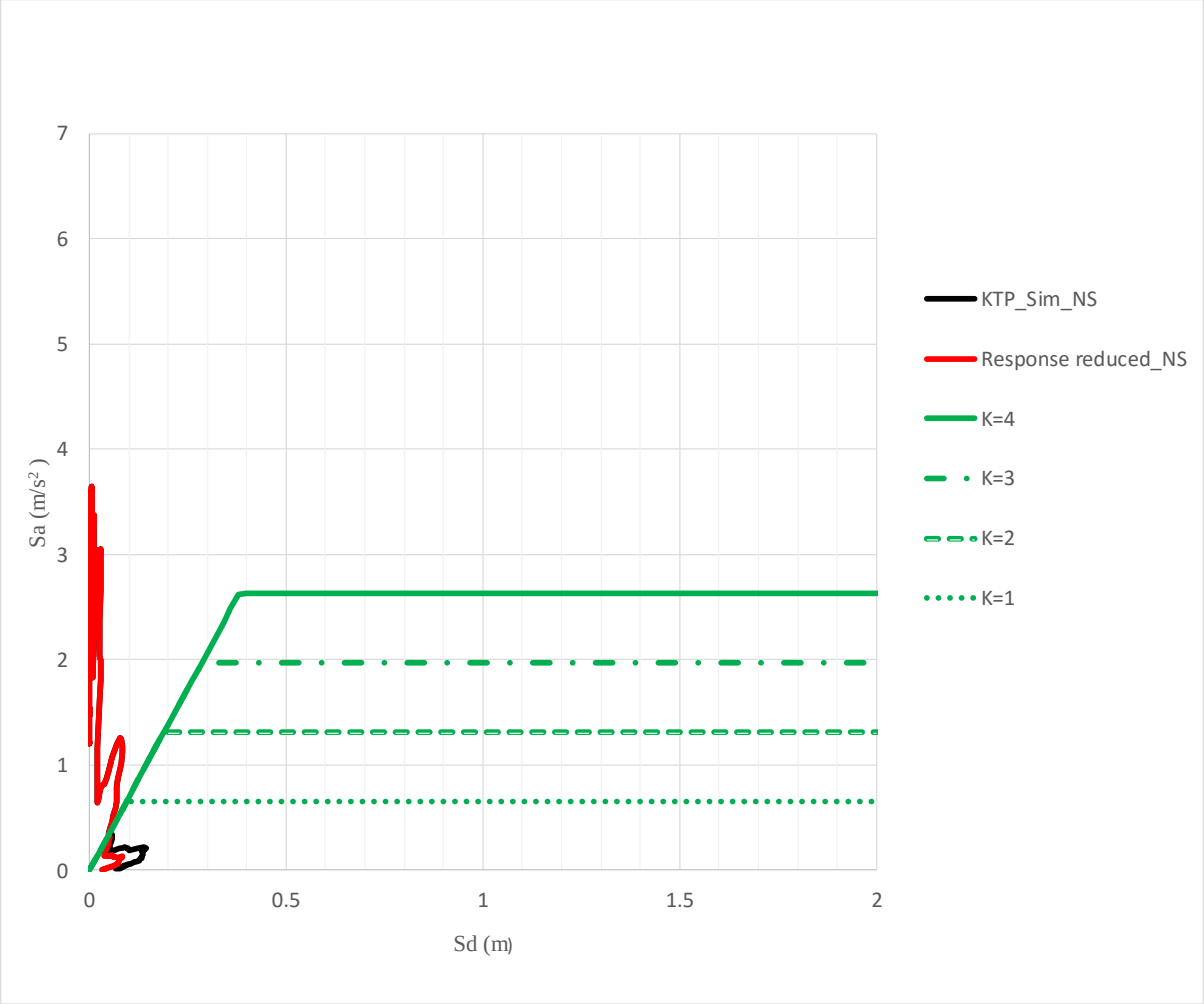

Figure 7.64 Capacity demand curves for the 18-story RC buildings considered for analysis using NS component of the simulated ground motion of the largest aftershock KTP at DMG.

Table 7.33 Damage sheet of 18-story RC building using the NS component simulated ground motion of the largest aftershock KTP at DMG

	Structural performance factor *K*	Ductility capacity of building collapse	Yield displacement (m)	Displacement demand (m)	Ductility demand	State of building
	1	4	0.12	0.04	1.72	Moderate damage
	2	2	0.2	0.04	1.244	Moderate damage
	3	1.33	0.28	0.04	1.06	Moderate damage
	4	1	0.4	0.04	0.9	Minimal damage

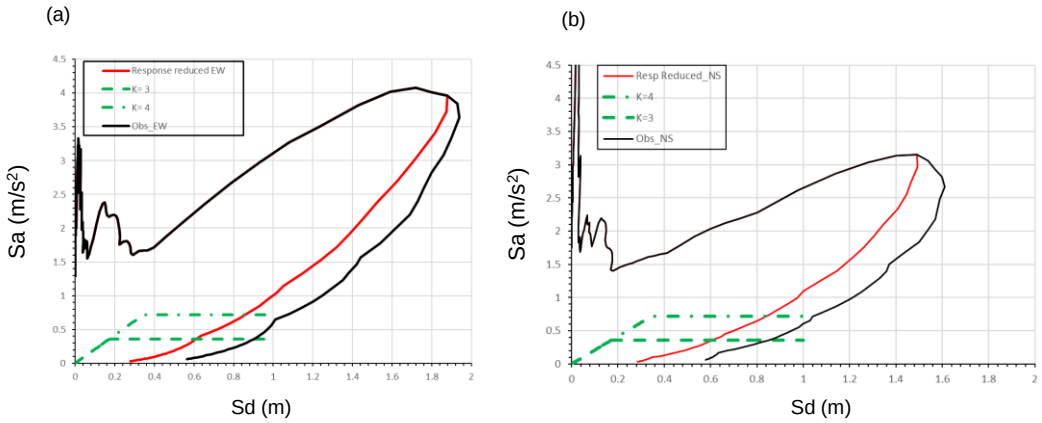

Figure 7.65 Capacity spectrum method considered with the 40-story code complaince building to check the possible damage at around from 4 to 5 s and their response sheet in both (a) EW and (b) NS components of ground motion.

Table 7.34 Damage sheet of 18-story RC building using both the EW (upper part) and NS (lower part) components simulated ground motion of the largest aftershock KTP at DMG

Structural performance factor (K)	Ductility capacity of building collapse	Yield displacement (m)	Displacement demand (m)	Ductility demand (μ)	State of building
1	4	-----	…….	…….	……
2	2	……..	……..	……..	……..
3	1.33	0.19	0.62	3.2	Collapse
4	1	0.36	0.85	2.3	Collapse

Structural performance factor (K)	Ductility capacity of building collapse	Yield displacement (m)	Displacement demand (m)	Ductility demand (μ)	State of building
1	4	-----	…….	…….	……
2	2	……..	……..	……..	……..
3	1.33	0.19	0.61	3.2	Collapse
4	1	0.38	0.82	2.1	Collapse

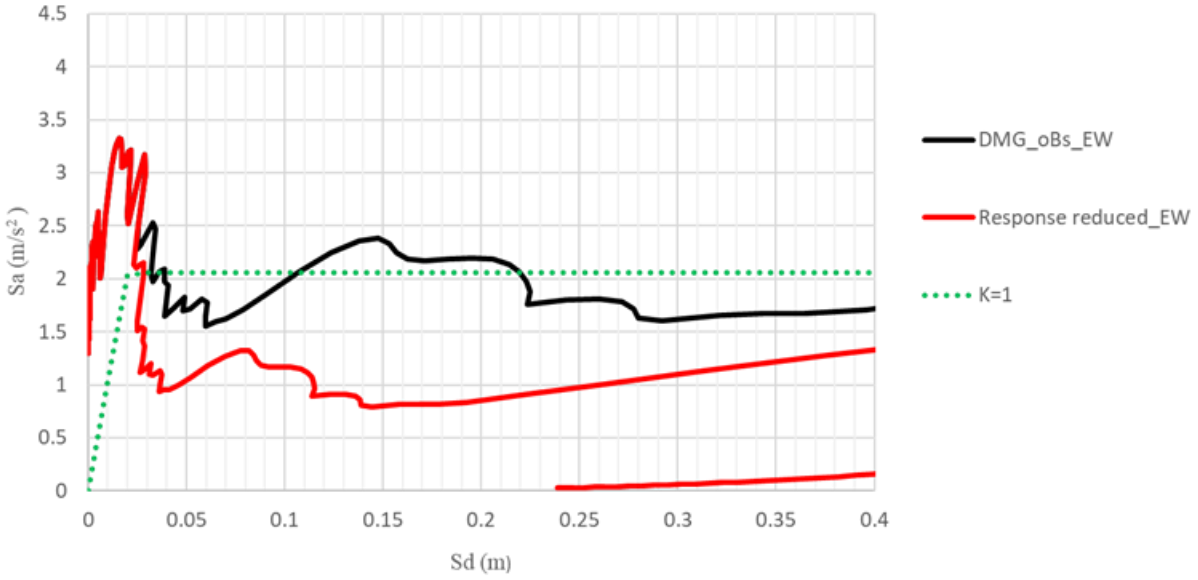

Figure 7.66 Observed Sa-Sd response spectra of the mainshock recorded at DMG with K = 1 (for the discussion in the specific domain, Gongabu area/new bus park, Figure 7.1).

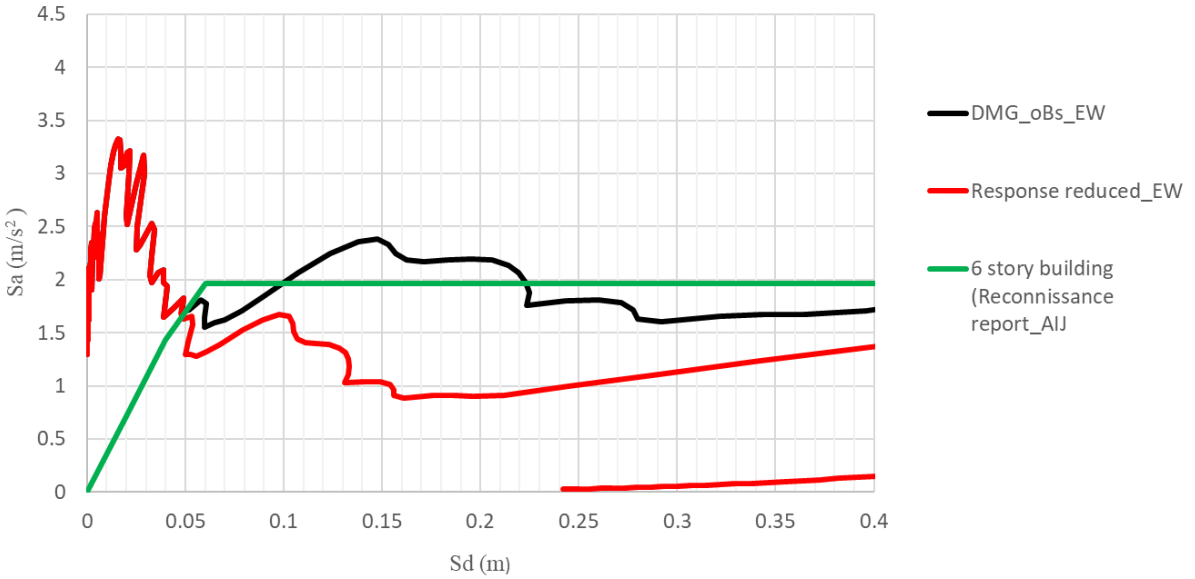

Figure 7.67 Observed Sa-Sd response spectra of the mainshock recorded at DMG with in consideration with 6-story damaged buildings for K = 1 reported by reconnaissance report of AIJ (for the discussion in the specific domain, Gongabu area/new bus park, Figure 7.1)

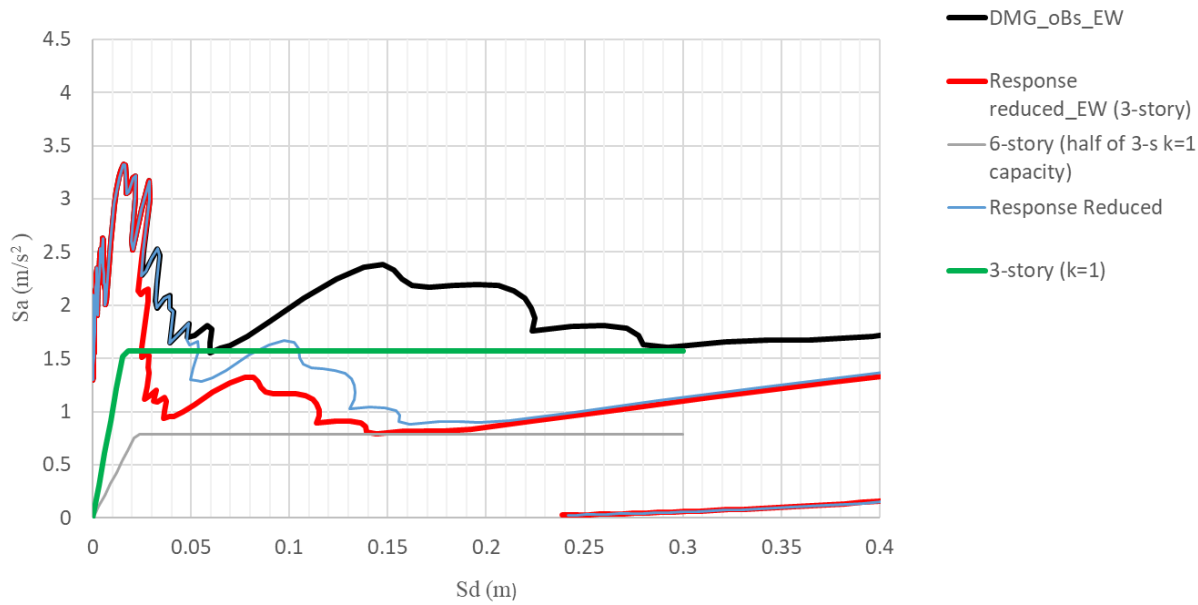

Figure 7.68 Observed Sa-Sd response spectra of the mainshock recorded at DMG in consideration with 3-, and 6-story buildings for K = 1 reported by reconnaissance report of AIJ (for the discussion in the specific domain, Gongabu area/new bus park, Figure 7.1).




Damage in the various RC and load bearing buildings

Damage in the RC buildings

Damage observed in the historical mounements at Kathmandu durbar square

Cracks on the infill walls

Cracks on the infill walls

Damaged observed in Hanuman dhoka durbar in Kathmandu Durbar square (online khabar.com)

Damaged School Building (Durbar High School) in the central part of the Kathmandu valley at a distance of 527 m south-west of the Kantipath (NQ.KATNP) strong motion station.

Damage and cracks in the high-rise buildings

Damage in high-rise buildings

Tilted buildings after Gorkha earthquake

Pan-cake Collapse of the residential building in the Kathmandu valley

Damaged buildings in the perifery of Singhadurbar

Damaged buildings in Singhadurbar

Damage of the main administrative building at Singhadurbar in the Kathmandu valley under retrofitting.

Severe structural damage in the Government irregular shaped building Shreemahal in patan (Parajuli, 2015).

Figure 7.69 Examples of the severly damaged and collapse buildings in the Kathmandu valley during the Gorkha earthquake (from government agencies e.g., DUDBC and Nepalese national newspapers daily).

Chapter 8

General conclusions and future studies

8.1 General conclusions

The study of site effects on the seismic ground motion has been a topic of great importance in the field of seismology and earthquake engineering in recent years. Ground motions in the sedimentary basin are significantly affected by the site effects. These ground motions can potentially cause building damages. The M_L 5.7 Xizang, China earthquake of 17 October 2010, the M_L 6.8 Taplejung-Sikkim border earthquake of 18 September 2011, and the M_L 7.6 Gorkha, Nepal earthquake of 25 April 2015 and its aftershocks are some of the recent earthquakes that have shaken the Kathmandu valley. Among them, the Tibet earthquake is one of the first earthquakes to be captured by the seismic and accelerometric networks of NSC whereas the Gorkha earthquake is the most recent damaging one. During the Tibet earthquake and the Taplejung-Sikkim earthquake, none of the buildings were reportedly damaged in the Kathmandu valley. However, the retaining wall was collapsed in the premises of the British Embassy nearby DMG during the Taplejung-Sikkim earthquake. The consequence of this collapse resulted in spot loss of 3 lives at that site. The Gorkha earthquake resulted in widespread building damage, several collapses, and thousands of losses of lives in the Kathmandu valley. This study mainly focused on the Gorkha earthquake. To explain the building damages that have occurred in the Kathmandu valley, this study is based on simulated ground motion derived from shear wave velocity structures using long-period microtremor based on the capacity spectrum method.

In Chapter 2, this study mainly focused to differentiate the ground motions recorded by the short-period seismic and accelerometric network in the vicinity of the Kathmandu valley to study the site amplification in the valley with reference to the nearby rock site. The results showed that the strong motion instruments complement well the pre-existing seismic network. The potentials of the seismic stations, with low gain and then high gain velocimetric channel, overlap very well with the large dynamic range of the accelerometric stations. The low gain channel will perfectly complement the high gain channel when they get saturated. The absence of *S*-waves onset in the vertical component of the accelerogram at DMG during the M_L 5.7 Xizang, China earthquake suspected the sedimentary effect at this site. The site

over reference spectral ratios of the records at the sedimentary site DMG with reference to the rock site KKA shows larger amplitudes towards lower frequencies below 4 Hz. However, in the frequency range from 4 to 10 Hz the spectral ratios exhibited large amplitude troughs suggesting its own site response. This study suspects that the site amplification would be inaccurate if the self-response of the reference rock site exists for the estimation of seismic hazard and resulting damage analysis in the mentioned frequency range. The damage analysis considering the Xizang, China earthquake is described in Chapter 7.

In Chapter 3, this study proposed an alternate reference rock site (PKIN) as a proxy of the reference site (KKA) described in Chapter 2. The site amplification at the DMG site is thoroughly checked to take into account both the reference points using the acceleration data of nine earthquakes of magnitude M_L greater than 5.0 coming from various azimuth and epicentral distances. The anomaly detected before re-reappeared for all the analyzed earthquakes and the site amplification of the rock site KKA in comparison to DMG is confirmed. The spectral ratios of DMG with reference to PKIN for all the considered earthquakes showed that DMG site has site amplification from 1 to 10 times in the frequency range from 0.5 to 10 Hz. On the other hand, the spectral ratios of KKA with referenced to PKIN showed that the KKA site has amplification from 4-10 Hz with the peak value at most 10. It is confirmed that the consideration of the KKA site as a reference will underestimate the site amplification of the Kathmandu valley in the frequency range from 4-10 Hz. Additionally, the long-period site response due to thick sediments in the Kathmandu valley has been detected by the spectral ratios of DMG compared to KKA considering the largest earthquake (M_L 6.8) used in this chapter. Based on the analysis and interpretations PKIN is proposed as a reliable reference site for the estimation of the seismic hazard and building damage analysis in the Kathmandu valley. Additionally, the reliability of PKIN as a reference site is confirmed by the records simultaneously observed among DMG and PKI. The reference rock site PKI has been established nearby the PKIN site after the Gorkha earthquake. Damage analysis considering the Taplejung-Sikkim earthquake is described in Chapter 7.

In Chapter 4, this study obtained the behavior of the site effects of the Kathmandu valley using the mainshock (M_L 7.6), the largest aftershock (M_L 6.9), and other aftershocks recorded mainly at the DMG site. The time histories, frequency content, and time-frequency decomposition suggested that the mainshock records have PGA of 0.15 g for the geometrical

mean of two horizontal components and larger PGA of 0.21 g on the vertical component. The significant relative duration D_{sr}(5-95%) is around 42 s for the horizontal components and around 35 s for the vertical one. The energy is mainly accumulated from 21 to 37 s. The horizontal components are mainly characterized by low-frequency signals from 23 s. The predominant frequency of the horizontal component at about 0.23 Hz is related to the site effect of the Kathmandu valley. The horizontal-to-vertical spectral ratio (HVSR) exhibits a clear peak at 0.2 Hz. The polarization characteristics were evident in the largest aftershock only among the considered earthquakes which might have affected by the source effect in the mainshock and lower power in the considered smaller aftershocks. The comparison with the Boore and Atkinson (2008) GMPE showed that the mainshock has large amplification in the lower frequency range. However, this phenomenon is suppressed taking in to account the basin effect using the GMPE (Abrahamson and Silva, 2008). The spiky pulses observed at the second negative and positive peaks in the NS component at DMG were suspected as an effect of liquefaction or source effects; however, none of the field studies suggested the phenomenon of liquefaction around that site. Neither the similarity in the observed ground motion at the same component in the nearby NQ.KATNP site at a distance of about 800 m from DMG. The building damage resulted from the Gorkha earthquake and its aftershock are described in Chapter 7.

In Chapter 5, this study conducted mainly long-period microtremor (ambient noise) array exploration for the deep sedimentary layers at 3 locations inside the Kathmandu valley assuming the deepest sediment at almost the central part of the valley taking into account mainly the nature of the long-period ground motion of the Gorkha earthquake. The SPatial Auto Correlation method (SPAC) of regular and the 2ST-SPAC with irregular shape arrays in the frequency below 1 Hz is the main target of this research. The appropriateness of 2ST-SPAC was supported by the isotropic characteristics of the coherence functions checked using the records of regular shape array at site 1. We; however, detected an anomaly of the dispersion curves in sites 2 and 3 that were caused by sharp sags of the coherence functions in the frequency range at around from 0.25 to 0.35 Hz. The power partitioning ratio did not support for the influence of the higher modes in the mentioned frequency range where the clear peaks of H/V spectral ratio and power spectra exist. Then the influence of a lateral variation of the underground structure was guessed. Especially for site 1, we conducted a virtual blind test, i.e., we executed the inversion without using the existing geological

information from drilling and estimated the basement depths of over 770 m, showing a notable discrepancy with the observed geological information. A detailed consideration of the Standard Deviation (SD) and the sensitivity of dispersion curves, however, showed considerable uncertainty for the V_S and thickness of the underlying half-space and the layer immediately above it. From the sensitivity of the dispersion curve to the structural parameters, we surmised that this uncertainty was caused not only by the SD of dispersion curve but also by the lack of the determined phase velocity below 0.2 Hz. For the other two sites, this uncertainty may present in a similar way. Further studies are required using different methods, for example, utilization of tectonic earthquakes' records or measurement of long-term ground vibrations to determine the dispersion curves below this current frequency limit of analysis.

In Chapter 6, this study re-analyzed the data acquired in Chapter 5 using different techniques for e.g., Centerless Circular Array (CCA), L-shape SPAC, and seismic interferometry methods. Moreover, few teleseismic earthquakes recorded at the four temporary continuous broadband stations were analyzed to determine the dispersion curve in the wide range towards the lower frequency. Some additional measurements for the CCA mini-array were also conducted. The sags in the coherence function detected by the SPAC method at sites, 2 and 3 were suppressed when the CCA method was applied, but detectable. Various methods mentioned above were applied intensively to obtain broadband dispersion curves from 0.2 Hz to the frequency higher than 5 Hz at three sites where a good consistency was confirmed between the SPAC and CCA methods in the lower frequency range with similar dispersion curves but with the higher phase velocity using CCA. The dispersion characteristics below 0.2 Hz were detected using the earthquakes at regional and teleseismic distances recorded from the temporary continuous broadband network of 4 stations. The dispersion curves at the high-frequency range were confirmed by the joint inversion of phase and group velocities. The estimated phase velocities using teleseismic earthquakes showed dispersive characteristics from 0.01 to 0.13 Hz and the phase velocity at a higher frequency side can be connected with the estimated ones from microtremor explorations. It is confirmed that the estimated phase velocities are comparable with those derived from the newly proposed seismic velocity structure model of Nepal (Yamada *et al*., 2018); however, smaller than those obtained from Pandey *et al.,* 1995 at the shallow depth but larger at the depth from 10 to 30 km. The high-velocity contrast at 400 m depth determined by the V_P wave (seismic reflection survey) at TIA is supported by the gravity survey at TIA and *Vs* discontinuity

detected by the microtremor survey at the TIA, SDB, and TEKU sites. The gap of the dispersion curve in the range from 0.1 to 0.2 Hz is also detected in the summary of dispersion curves observed at all sites considered so far in the Kathmandu valley.

In Chapter 7, this study simulated the ground motions (Xizang, China earthquake, Taplejung-Sikkim earthquake, the Gorkha earthquake, and its largest aftershock) observed at rock sites by using propagator matrix method and some mathematical approach at the sedimentary sites where the shear wave velocity structures and seismic observation system both exist (e.g., DMG) or the sites where only the velocity structure exist but not the seismic observation system (e.g., SDB and TEKU). The buildings under consideration were examined using the structural performance factor (K = 1, 2, 3, and 4 respectively) in the capacity curves. We mainly analyzed 1-story building using both NS and EW components of ground motions taking in to account the Xizang, China earthquake (Chapter 2). Similarly, 1-, 2-, and 3-story buildings were analyzed for the Taplejung-Sikkim earthquake considering both components of ground motions (Chapter 3). The mainshock and the largest aftershock of the Gorkha earthquake were examined considering 3-, 6-, and 18-story RC buildings. The long-period ground motion of 4-5 s is also examined for the 40-story buildings using both the components of ground motion.

Also, the design response spectra specified by the code (NBC, 1994) is compared with the response spectra of the mainshock and the largest aftershock recorded at DMG for the overview of possible causes of building damage. The simulated records are plotted in the acceleration displacement response spectrum format. The comparison between the capacity curve with the demand curve was done based on the capacity spectrum method to find the performance of the considered buildings. These performed well elastically both in the NS and EW components of ground motions taking in to account the Xizang, China and Taplejung-Sikkim earthquakes which are strongly supported by the damage reports issued after these earthquakes. The simulated ground motion at the site 2 (DMG) using the observed mainshock record at KTP resulted in several stages of collapse on 18-story high-raise buildings both in the EW and NS components of ground motion mainly with K = 1 and 2; however, collapse is also resulted with the EW component of ground motion with K = 1. Also, the assumed 40-story building considering the long-period ground motion from 4 to 5 s observed at DMG completely collapsed using the mainshock observed motion at DMG. The simulated ground motion at the site 1 (SDB) and site 3 (TEKU) shows several states of collapse in 18-story

buildings using both components of ground motion mainly with K = 1 and 2. However, moderate and minimal damages were reported in both the components of ground motion for 3-, and 6-story buildings with all values of K under consideration. All states of collapse were resulted using the simulated ground motion of the largest aftershock PKI at DMG with the EW component of ground motion for 18-story buildings with all values of K under consideration. However, for K = 1 there resulted collapse for 6-story building with EW component of ground motion. In contrast, only the moderate and minimal damages have been resulted from the simulated ground motion at the site 2 (DMG) considering the largest aftershock recorded at KTP. It is noticed that most of the collapse and severely damaged buildings are fallen in the structural performance factor (K =1 and 2); however, K =3 and 4 buildings performed well. Field observation has shown that lack of ductile detailing, poor construction practices, use of poor-quality construction materials and violence of the building code are major problems in the RC buildings at the severely damaged domain (Gongabu/new bus park area). Our results support the reconnaissance report based on observed damage presented by the Architectural Institute of Japan (AIJ) in the Kathmandu valley after the Gorkha earthquake.

The comparisons of the acceleration response spectra of the mainshock with the design response spectra given by the code (NBC, 1994) at the site 1 (DMG) shows 4 to 5 s predominant in the range of longer natural period, and 0.4 s predominance in the range of shorter natural period. This shorter-period component buildings were influenced mostly by the mainshock ground motion as the dominance of the existing RC buildings in the Kathmandu valley was low and medium-rise. Considering with design input of 0.08g given by the seismic design code, this value should be revised taking in to account, the long-period ground motion of the Gorkha earthquake considering the ongoing sky-rocking constructions and possible measures of hazard estimation through damage analysis.

The improper damage pattern in the Kathmandu valley as reviewed by damage reports during the Gorkha earthquake is partially supported by the building analyses using the mainshock and the largest aftershock for the whole Kathmandu valley in consideration with the limited number of seismic observation system. Studies are needed to address discrepancies in building collapse using 3-D modeling of the basin structure. The basic seismic coefficient given by the Nepalese code should be revised in consideration with the vertical component of ground motion for the seismic design spectra. This study shows the

possibility of building damage analysis in a particular domain where either observed/simulated ground motions or shear wave velocity structure or both exist.

8.2 Future studies

This study presented the comparative study between the national seismic network (NSC) and the newly established accelerometric network in Chapter 2. This thesis showed the dynamic range of the accelerometric signals recorded at sedimentary sites increases up to about 100 m/s^2 complementing well with the velocimetric stations and there is no gap between the velocimetric and accelerometric data in this range. This study carried out the site effect studies on the ground motion records observed at the sedimentary site DMG with reference to the rock site KKA. The site over reference spectral ratio of DMG with KKA detected KKA's high amplification in the frequency range from 4 to 10 Hz. Several records should be examined at this site considering the focal mechanism, depth, and source-station azimuth to properly characterize the particular site effect and differentiate it from the path effect and topographic effect. More accurate site effects should be estimated at KKA through the parallel measurement of ambient noise or geophysical explorations. Several accelerometric stations should be established in the Kathmandu valley at both the rock and sediment sites with the online data transmission and acquisition facility at NSC to study and constrain a strong motion database and study the variability of strong ground motion and its effect on building damage at different sites in and around the Kathmandu valley.

This study established a reliable reference rock site PKIN as a proxy of the rock site KKA considered in Chapter 3. The KKA site located at a distance of about 10 km north-west of the Kathmandu valley is equipped with an accelerometer whereas PKIN about 15 km south-east is equipped with short-period velocimeter. The amplification due to thick sediment in the Kathmandu valley as revealed by the spectral ratios of DMG with reference to KKA during the 2011 Taplejung-Sikkim earthquake (M_L 6.8) should be further studied to understand the long-period response of the Kathmandu valley below 0.5 Hz for such an earthquake over 300 km epicentral distance. Few more reference rock sites should be tested and established at various interstation distances from the Kathmandu valley sedimentary sites for better understand the variation of the site effects and resulting in building damage. It is recommended to install a bore-hole sensor at the base layers nearby the DMG site for further comparision with the observed records at the ground surface.

This study obtained the behavior of the long-period site effects in the Kathmandu valley based on the mainshock, the largest aftershock, and other aftershocks. The strong motion record in the NS component of the mainshock recorded at the DMG site exhibits spiky pulses in the second negative and positive pulse, however, such behavior did not obtain at the station about 600 m away from it at NQ.KATNP. The cause of such peaks should be studied to differentiate it either from liquefaction effect or source effect. The aftershock of M_L 4.1 occurred inside the Kathmandu valley shows quite different behavior in the Fourier amplitude spectra and HVSRs in comparing to the mainshock and other aftershocks occurred outside the Kathmandu valley. Such studies should be repeated focusing on the larger magnitude earthquakes occurring inside the Kathmandu valley. The building damage due to long-period ground motion in the frequency range from 0.25 to 3.0 Hz should be further studied using different numerical methods.

Chapters 2, 3, and 4 are basically based on site effects using the H/Href and HVSR spectral ratios. However, these studies could not always provide satisfactory results and more information at some particular sites having complex geological conditions. More studies are needed to accurate site effects estimation based on numerical analysis of soil response based on soil profiles.

This study constructed the shear wave velocity structures at different sedimentary sites and outcrop in and around the Kathmandu valley focusing the deeper part of the valley based on the long-period microtremor observations in Chapters 5 and 6. This study mainly used SPAC and 2S-SPAC methods. However, the sags of the coherence functions and resulting SPAC coefficients showed the uncertainty in the structural parameters in the deeper part and the layer just above it at sedimentary sites 2 and 3. The cause of such an unusual phenomenon affecting the velocity structures should be studied further. The CCA method, seismic interferometry method, and analysis of the teleseismic records are used to re-analyze the same dataset, check the sags and refine the velocity structure models taking in to account the deeper part; however, they could not suppress well the sags detected before. Long-period observation should be continued in the Kathmandu valley to obtain the lacking part of the dispersion curve in the frequency range from 0.1 to 0.2 Hz. Deriving the velocity structures at the arbitrary sites should be continued for the numerical simulation of the ground motion to understand building damage at the sites where the seismic observation system does not exist. This study mainly focused on long-period microtremor; however, for the seismic

microzonation and other engineering applications we should extend short-period measurements for shallow velocity structures using H/V, MASW, L-shaped array, T-shaped array, etc. at various sites inside the valley. Further extension of this work is to evaluate the building and structures using microtremor measurements. Also, comparisons are needed to verify the time-period given by the building code and those observed from microtremor.

This study predicted the damage levels of RC buildings of different structural performance factor (K = 1, 2, 3, and 4) designed based on the Nepalese building code (NBC, 1994) which was formulated in 1994 and recently under revision. This study mainly examined the damage observed in the Kathmandu valley due to the Xizang earthquake (M_L 5.7), the Taplejung-Sikkim earthquake (M_L 6.8), the most recent damaging Gorkha earthquake (M_L 7.6), and its largest aftershock (M_L 6.9). This study reduced the demand curve using additional damping from the elastic demand curve with 5% damping when using the capacity spectrum method. This study used the 1-D velocity structure model constructed in Chapters 5 and 6 for the numerical simulation and analyzed the buildings based on the ductility capacity of the building collapse and demand ductility. Further studies are needed taking in to account the revised building code of Nepal and 3-D modeling of the Kathmandu valley for the damage studies. The excess level of damage resulted based on the simulated ground motion observed from PKI rock motion during the largest aftershock of the Gorkha earthquake at the site DMG using the EW component of ground motion should be studied further. The provisions of the building code related to the earthquake resistance buildings should be revised periodically taking in to account the observed ground motion records of the recent damaging earthquakes. This study only focused on the code compliance buildings in the Kathmandu valley for the damage evaluation further studies are needed for the non-code compliance old buildings, load bearing buildings, heritage buildings, essential facilities (e.g., medical institutions, health care facilities, fire rescue houses, police services, communication facilities, emergency response and recovery preparedness centers etc.). This study used damping value (Q) as Vs/10; however, future efforts are needed to develop the Q values of the Kathmandu valley and other cities of Nepal.